Interaction of compact object with the surrounding matter in Symbiotic Stars, Be/X-ray binaries, and Quasars

Radoslav K. Zamanov

Institute of Astronony, Bulgarian Academy of Sciences

Sofia, Bulgaria

for the degree of

Doctor of Physical Sciences

10 Dec 2009

Contents

Chapter 1

Introduction

1.1 Be/X-ray Binaries

The Be stars are massive stars surrounded by an equatorial disk of material (a circumstellar disk). Roughly 2/3 of all high-mass X-ray binary systems consist of a Be star and a compact object (neutron star or black hole) in orbit around each other and, not surprisingly, these systems are known as Be/X-ray binaries.

The Be/X-ray binaries are generally quiescent, exhibiting low-luminosity (in a few cases) or no X-ray emission. The transient X-ray outbursts are thought to be due to interactions between the compact object and the circumstellar disk surrounding the Be star, and two different types of outburst have been identified:

Type I outbursts tend to be short and periodic, occurring around periastron when the two objects are at their closest approach. This would suggest that the orbit of the compact object around the Be star is wide and highly eccentric, limiting interactions with the circumstellar disk to when the objects are closest. Type I outbursts typically last only a few days and are the result of an increase in the amount of material impacting the compact object as it passes through, or close to the circumstellar disk.

Type II outbursts are much larger than Type I outbursts and can last for several weeks. They are not linked to the orbital period of the system but tend to be preceeded by increased activity in the Be star. This can change the density, size and other characteristics of the circumstellar disk, which in turn will affect the X-ray emission as the compact object interacts with the disk material.

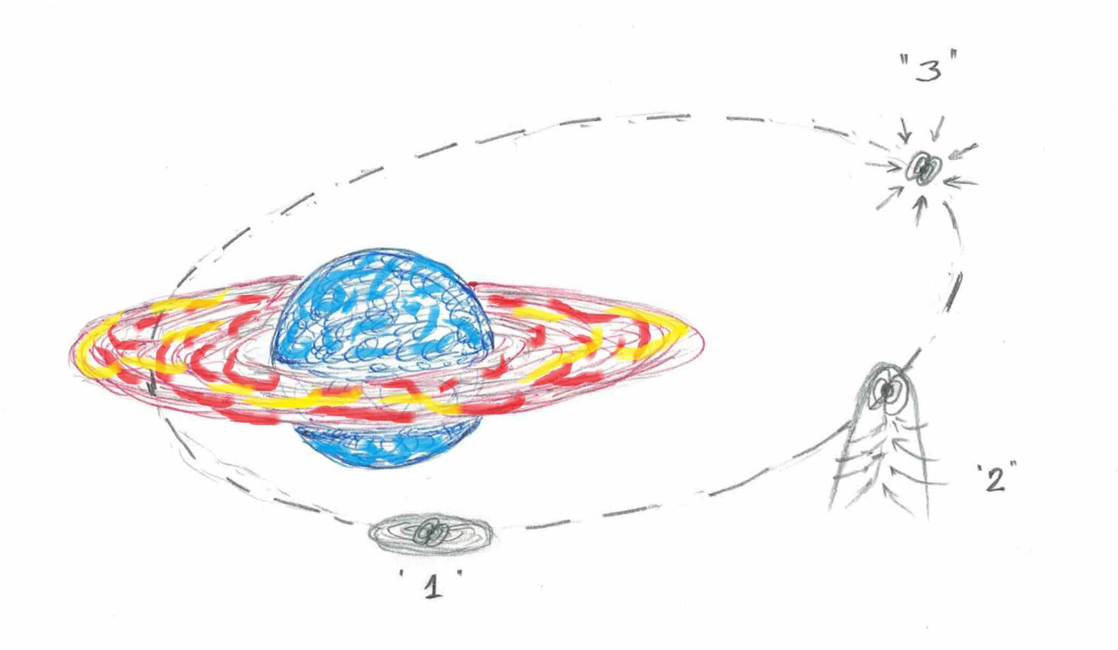

Figure 1.1: A sketch representing a Be/X-ray binary. The mass donor is a rapidly rotating Be star with a circumstellar disc. The neutron star is accreting material from the wind and the circumstellar disc of the Be star. Depending on the mass capture rate and magnetic field of the neutron star, an accretion disc can be formed ("1"), and/or an accretion wake ("2") or spherical accretion ("3").

1.2 Symbiotic stars

The symbiotic stars are binary star systems, the combined spectrum of which includes a molecular absorption band component, typically involving the presence of TiO bands and emission lines. The prominent emission component includes Balmer emission lines and HeI as well as emission lines of ions of higher ionization such as He IIλ4686 Å and [O III]λ5007 Å. The components of a symbiotic star are a red giant and a small hot star, surrounded by nebulosity. The mass donor can be a late giant, a supergiants, or an asymptotic giant branch star (Mira-type). The hot component is in the most cases white dwarf, although it can also be a main sequence star, hot subdwarf, neutron star, even black hole. On Fig. 1.2 is plotted accretion through inner Lagrangian point. on Fig. 1.3 – accretion from stellar wind.

Spectra of symbiotic stars suggest that there are three regions which emit radiation: the individual stars themselves and the nebulosity that surrounds them both. The nebulosity is thought to originate from the red giant, which is in the process of losing mass either through a stellar wind or through pulsations. The symbiotic phase represents a late stage in stellar evolution and a brief span in the life of the binary. Because of the short timescale involved, symbiotic stars are rare objects. About 200 are known. The majority of these are in our own galaxy, the Milky Way, although some extragalactic are already identified: in the Draco dwarf galaxy, in the Small Magellanic Cloud, and in the Large Magellanic Cloud. The symbiotic stars represent an unique laboratory in which to study important physical processes:

(i) stellar evolution

(ii) emission line formation

(iii) mass loss

(iv) accretion from stellar wind

(v) ejection of matter from compact objects.

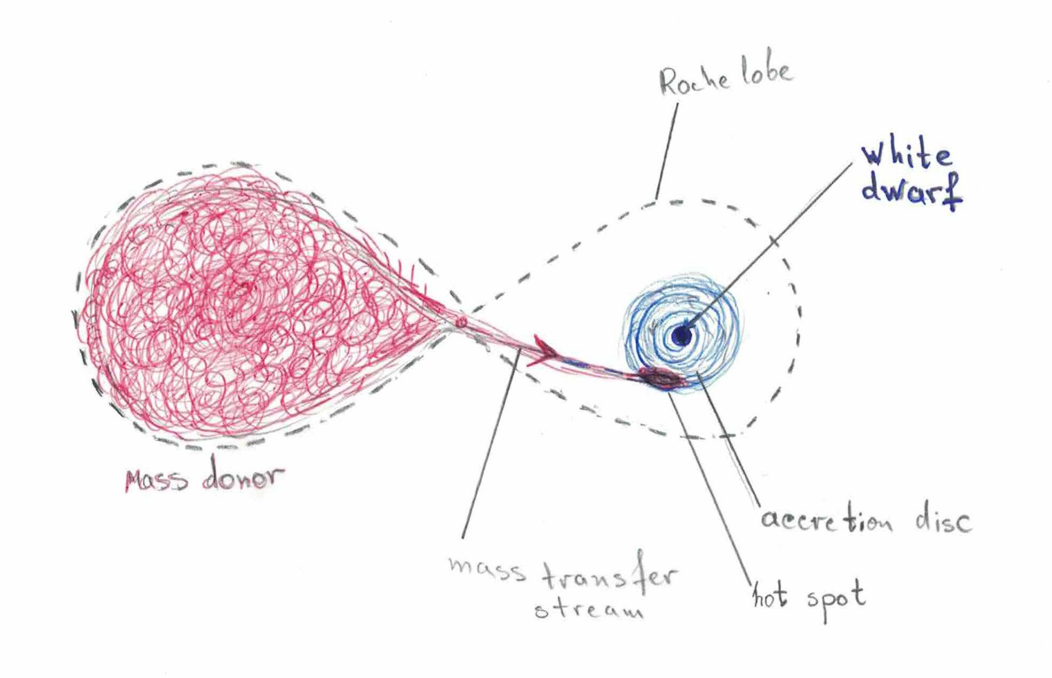

Figure 1.2: A sketch representing Roche lobe overflow in a symbiotic binary star. The mass donor is a red giant. In the most cases the hot component is a white dwarf.

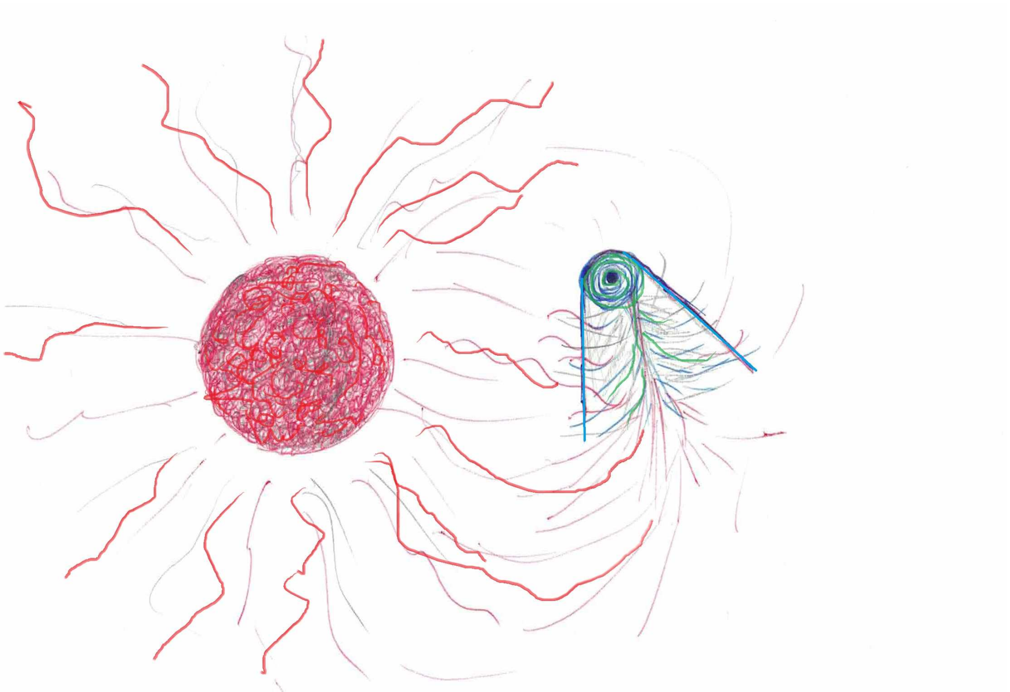

Figure 1.3: A sketch representing accretion from stellar wind. The supersonic motion of the compact object through the stellar wind creates shock front and accretion wake.

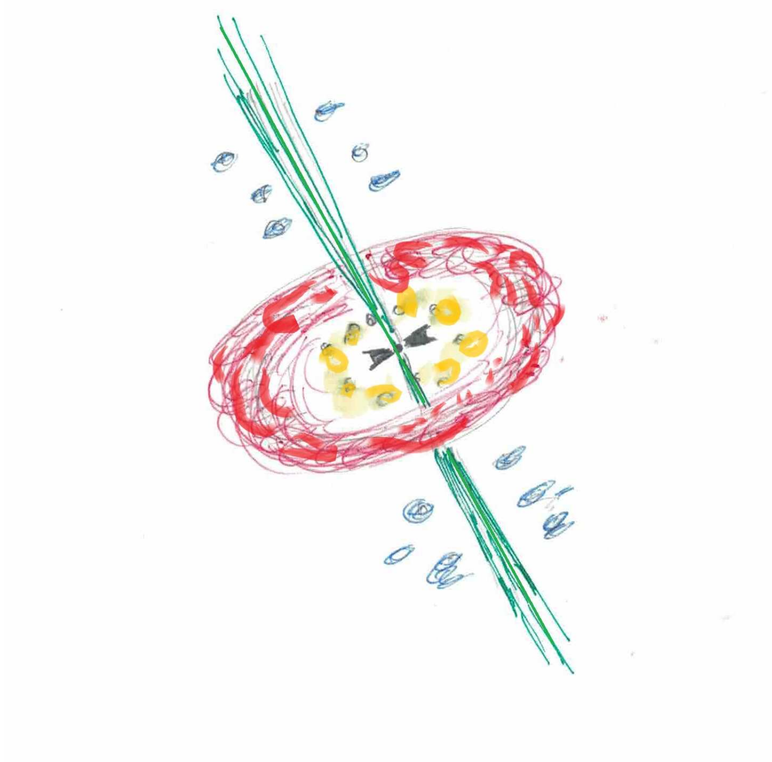

Figure 1.4: A sketch representing an Active Galactic Nuclei. The central engine is a massive black hole with an accretion disc. The broad line region (yellow) and the torrus (red) are around the disc. The jet (green) and narrow line region (blue) are also marked.

1.3 Active Galactic Nuclei

In some galaxies, known as "active galactic nuclei" (AGNs), the nucleus (or central core) produces more radiation than the entire rest of the galaxy! Quasars are very distant AGNs - the most distant quasars mark an epoch when the universe was less than a billion years old and a sixth of its current size. In some cases, the size of the AGN is smaller than the size of our solar system. Current theory suggests that there is a supermassive black hole ($M_{BH} \sim 10^6 - 10^9$ $M_\odot$) at the center of AGNs.

1.4 Aims of our study

Our aims are:

(1) to investigate the short term photometric and spectral variability, and long term behaviour of the brightness and emission lines of the recurrent nova T Coronae Borealis.

(2) to investigate the photometric and spectral variability of the recurrent nova RS Ophiuchi.

(3) to investigate the rotation of the giants in symbiotic binaries and to check is their rotation influenced by the compact companion.

(4) to investigate the photometric behaviour of interacting binaries.

(5) To investigate in details the Hα emission line in the Be/X-ray binary LS I+61°303, to search for connection between the variability of the circumstellar disk and the emission generated by the compact companion, to model the behaviour of this enigmatic object.

(6) To compare the circumstellar disks in the Be/X-ray binaries with those in normal Be stars and to understand are the disks in Be/X-ray binaries influenced by the presence of the compact object.

(7) To search for quasars with shifted [OIII] lines, and to find what is their nature. To find the influence of the physical parameter (accretion rate, black hole mass) on the [OIII] shifts and Hβ profile.

(8) To explore the emission line similarities between symbiotic stars and quasars and to use these similarities to through light on the Eigenvector-1 correlations in AGNs.

Chapter 2

Variability of the recurrent nova T CrB

2.1 Rapid Hα variability in T Coronae Borealis

Abstract: We report our search for variability in the Hα emission line of the recurrent novae T CrB with time resolution 10-15 minutes. This is comparable with the time scale of the photometric flickering observed in this object. This is the first time that observations of the short time scale variation in emission lines have been made in this object. On two nights (990106 and 990107) we detected statistically significant variability (at 0.99 confidence level) in the line profile of Hα. This variability is confined in the central part of the emission line ($\pm$100 km s^{-1}) although FWZI(Hα) is $\sim$800 km s^{-1}. The variability in the line profile is accompanied with variability of the total equivalent width, EW(Hα), $\pm$8% for 990106, and $\pm$6% for 990107 (calculated from the mean value of EW). Assuming Keplerian motion, the variability is generated at a distance $\sim$20-30R$_\odot$ from the white dwarf, which is approximately the radius of the ring the stream of gas forms as it flows away from L$_1$. On three other nights we are only able to put upper limits on the variability, ΔEW(Hα) $\pm$2% for 980415, $\pm$4% for 980802, and $\pm$3% for 980803.

Introduction: The short term photometric behaviour of symbiotic stars has been investigated in many systems (e.g. Dobrzycka et al. 1996; Sokoloski et al. 2001). However, there are no systematic searches for rapid *spectral* variations. Until now the search for rapid spectral variability has been undertaken in only three symbiotics: CH Cyg, MWC 560, and RS Oph. All three stars are known to exhibit flickering and have collimated outflows. Rapid spectral variability in the Balmer lines of CH Cyg on time scales of $\sim$1 hour have been detected and is probably connected with blobs ejected from a white dwarf, acting as a propeller (Tomov et al. 1996b). For RS Oph, Sokoloski (2003) reported variability on time scales of hours in the HeIIλ4686 line although no variability in Hβ was detected. No significant variability has been detected in MWC 560 (Tomov et al. 1995).

In a few cataclysmic variables (CVs), which are closely related to symbiotic stars, rapid spectral changes are visible in optical and UV lines as a result of a variable accretion disk wind: BZ Cam (Ringwald & Naylor 1998), V592 Cas (Witherick et al. 2003), RW Sex (Prinja et al. 2003), V 603 Aql (Prinja et al. 2000a), BZ Cam (Prinja et al. 2000b).

The detection of variability on time scales of tens of minutes in symbiotic stars and cataclysmic variables provides the motivation for this study. T CrB consists of a red giant and a hot component, most probably a white dwarf. T CrB can be classified as a cataclysmic variable, symbiotic star, and recurrent nova and accretes at a rate $1\times10^{-8}M_{\odot}$ yr^{-1} (Selvelli et al. 1992). This places it among the cataclysmic variables with the highest accretion rates (see Warner 1995, p.476) and for such high accretion rates an accretion disk wind could be expected. Here we report our search for signatures of variability in time-resolved optical spectroscopy in the Hα line of T CrB, with time resolution $\sim$10-15 minutes. This resolution is comparable with the time scale of flickering (see for example Zamanov et al. 2004).

Observations: The observations were performed with the Coudé spectrograph of the 2.0 m RCC telescope at the Bulgarian National Astronomical Observatory "Rozhen". The spectra have a dispersion of 0.2 Å pixel^{-1}. The normal CCD reduction procedures (i.e. bias subtraction, flat fielding, wavelength calibration, etc) have been undertaken in the IRAF environment. A journal of observations is given in Table 2.1. The signal to noise ratio (SNR) achieved on the individual exposures is 35-65.

The averaged spectra, normalised to the local continuum, are presented in Fig. 2.1, along with a comparison spectrum of the red giant HD135530.

2.1.1 Average, fractional and temporal variance spectra

The prominent emission line in Fig. 2.1 is Hα. On a time scale of years the intensity of the Hα line varies from EW=0.5 Å up to 35 Å (Iijima 1990, Anupama & Prabhu 1991, Zamanov & Martí 2001, Stanishev et al. 2004). During the search for rapid variability we have observed a range of different profiles. An atlas of the different Hα profiles is given in Stanishev et al. (2004). In the spectra obtained on 15th April 1998 the line is single peaked, and the central

Table 2.1: Hα observations of T CrB. In the table are given the date of observations, the beginning and the end of spectroscopic observations and truncated Julian Day. Orbital phase is calculated using the ephemeris of Fekel et al. (2000). The following columns give wavelength coverage, number of exposures in each night and the exposure time of the individual exposures. In the lower part, for the EW(Hα) we give the mean, standard deviation, plus the smallest and the largest values for each night.

Date yymmdd	UT_{start} - UT_{end} hh:mm - hh:mm	TJD mid	phase	wavelength coverage [Å]	N x Exp.time
980415	22:37 - 01:43	50919.512	0.187	6510 - 6620	10 x 15 min
980802	18:50 - 20:58	51028.328	0.665	6510 - 6620	12 x 10 min
980803	18:23 - 21:03	51029.305	0.669	6510 - 6620	15 x 10 min
990106	02:59 - 04:13	51185.652	0.356	6500 - 6700	7 x 10 min
990107	01:50 - 02:51	51186.598	0.360	6507 - 6707	3 x 20 min

	EW(Hα) [Å] mean±σ	EW_{min} – EW_{max} [Å]
980415	20.84 ± 0.31	20.39 – 21.36
980802	13.39 ± 0.23	12.72 – 13.81
980803	13.97 ± 0.25	13.63 – 14.45
990106	9.77 ± 0.62	8.90 – 10.51
990107	7.92 ± 0.45	7.45 – 8.36

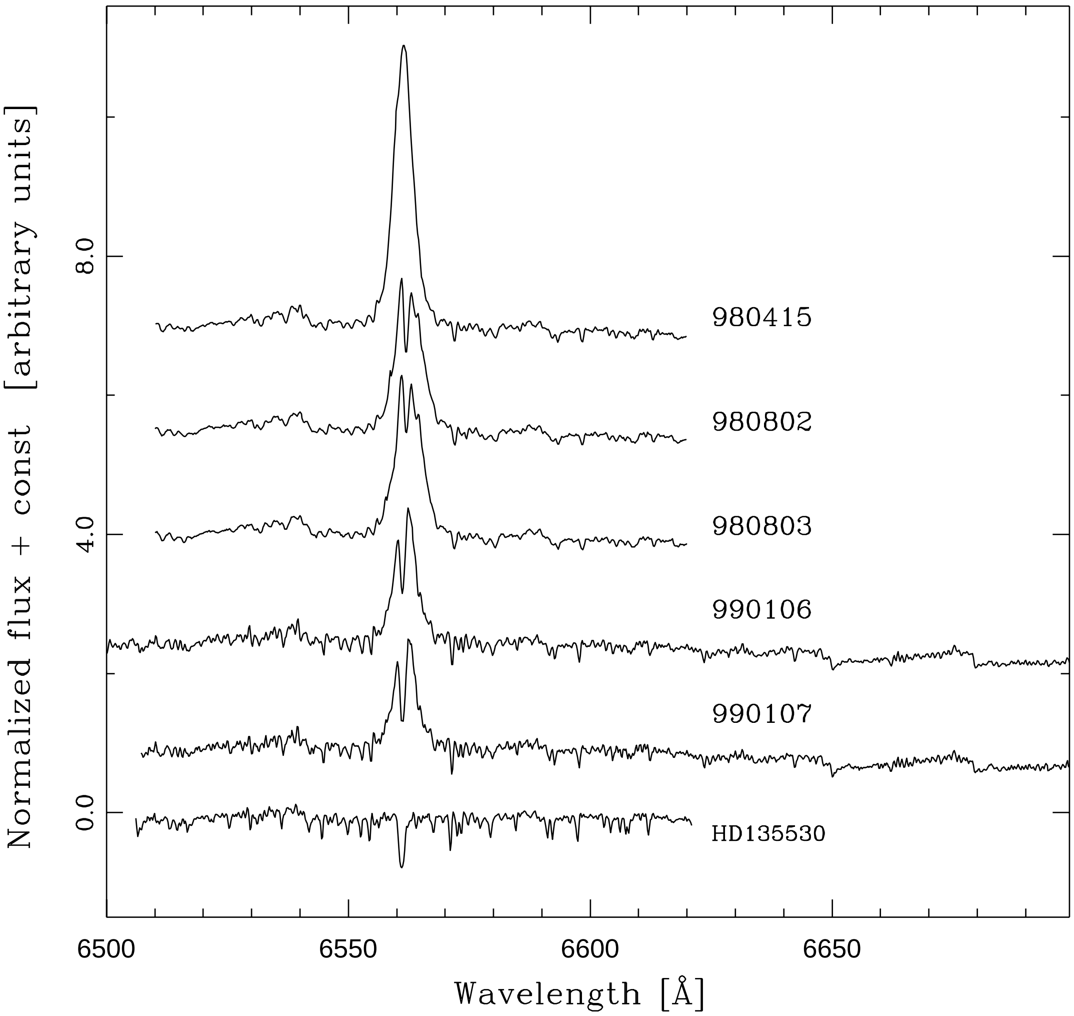

Figure 2.1: The nightly average spectra for all five nights. A spectrum of the red giant HD135530 (M2III) is shown for comparison at the bottom.

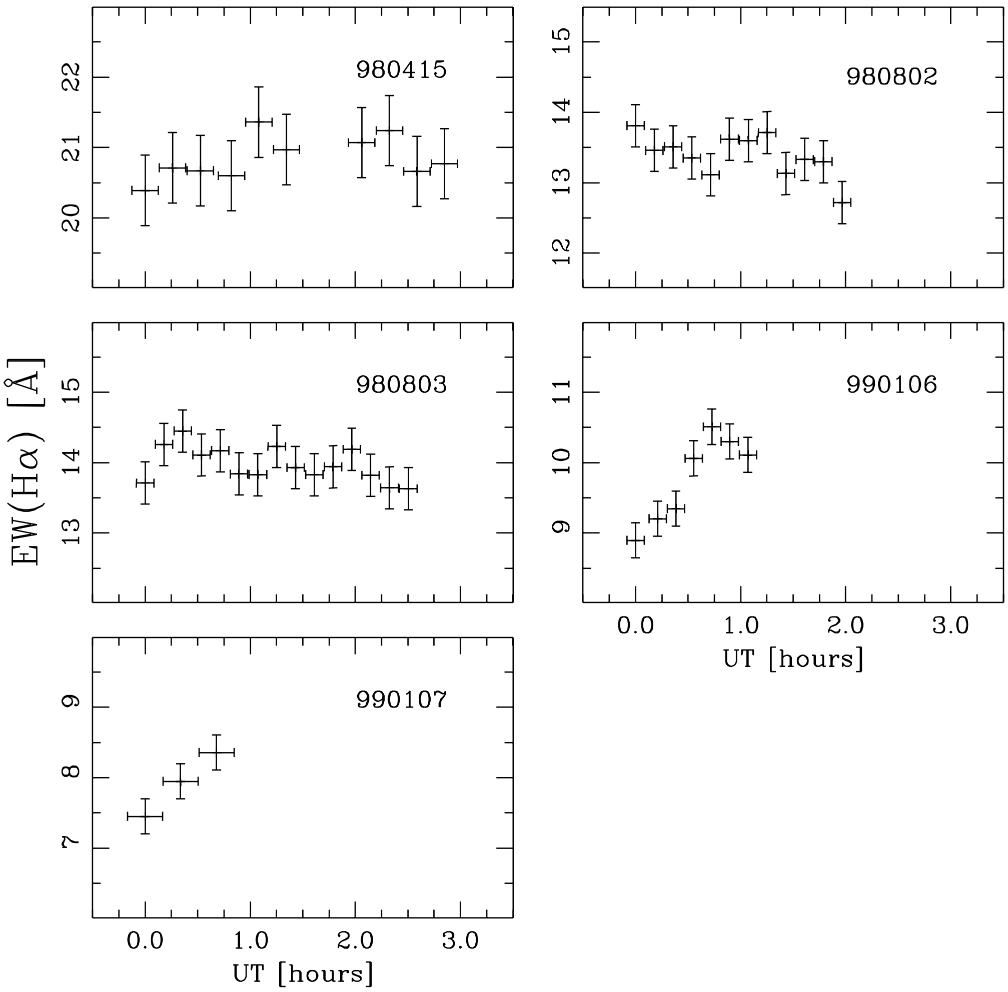

Figure 2.2: Measurements of the EW(Hα). The vertical error bars indicate the errors in EW measurements, the horizontal the exposure time of the spectra. In the first three nights the variability is of the order of the estimated errors. On 990106 and 990106 it is more or about 5 times the error of the measurements.

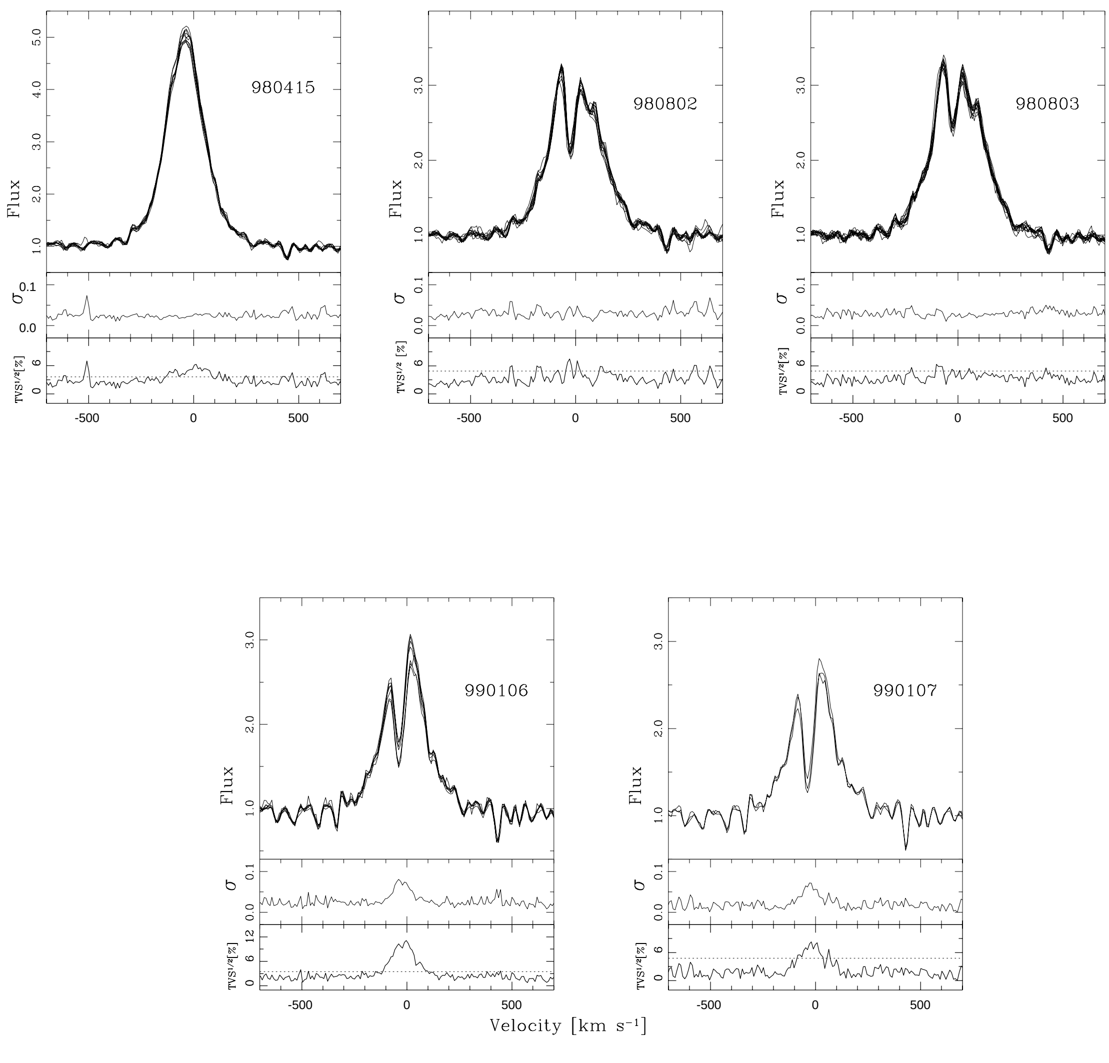

Figure 2.3: The Hα profiles of T CrB for 5 nights of observations, normalised to the local continuum. The X-axis is in heliocentric velocity. σ and the TVS for all nights are plotted. The dotted horizontal line indicates a 1% threshold for the detection of variability. For first 3 nights σ does not indicate any variability, while the TVS is marginally above the 1% significance level on the night of 980415. On 990106 and 990107 well defined peaks, both in σ and in the TVS, are clearly visible in the central part of the line, corresponding to velocity -100 to +100 km/s. This demonstrates that there is a statistically significant variability in the profile of Hα line with time resolution $\sim$10 min. The probability that this is a real variability is $\geq$0.99.

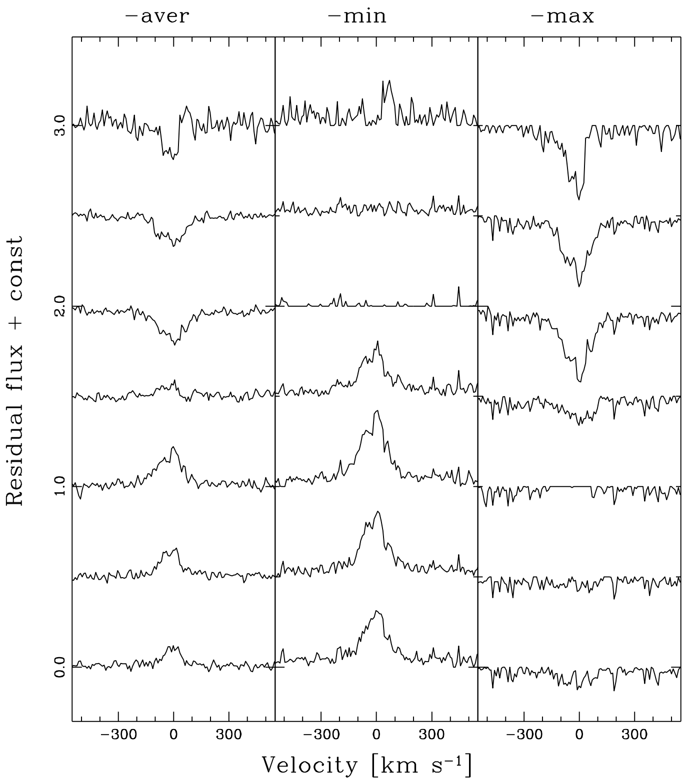

Figure 2.4: Night 990106: from the individual spectra have been subtracted the average spectrum (left panel), the minimum (middle panel), and the maximum spectrum (right panel). Zero of the velocity axis corresponds to the systemic velocity γ=-27.79 km s^{-1}(Fekel et al 2000).

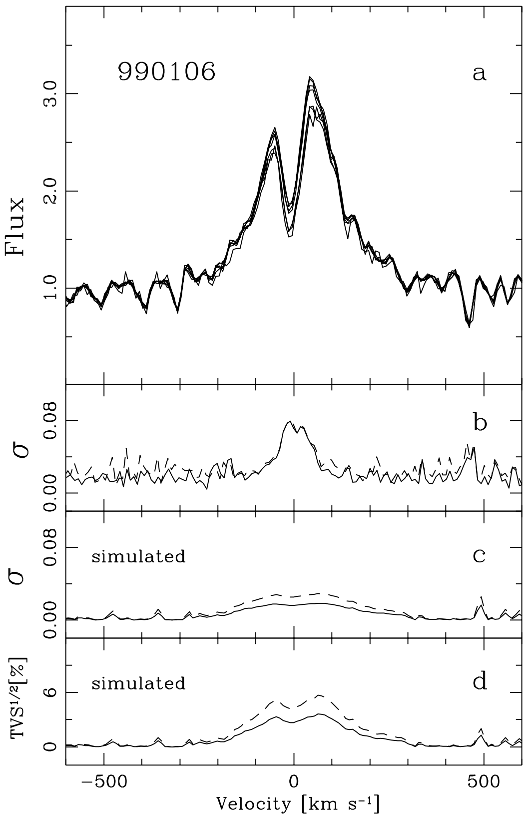

Figure 2.5: (a) Hα profiles observed on 990106 (the same as in Fig. 2.3). (b) σ for 990106, solid and dashed lines are for two deliberately different extraction and normalisation procedures. (c) simulated σ as a result of hot continuum variability. (d) simulated TVS as a result of hot continuum variability. During the simulation we assumed that the hot continuum contributes 15% of the flux on average and it varies with $\pm30\%$ (dashed line) and $\pm25\%$ (solid line). Zero of the velocity axis corresponds to the systemic velocity γ.

absorption dip is not visible. During August 1998, the profile is a little unusual, with 3 peaks or 2 absorption dips. During January 1999, the profile exhibits double peaks with a well defined central dip, which is partly due to the Hα absorption line of the red giant.

The total EW(Hα) was measured on each exposure in our sample. The results are presented in Fig. 2.2. In the first three nights the variability is less than three times the estimated errors. On 990106 and 990107 it is about 5 times the error of the individual measurements.

The measurements of the EW depend strongly on the continuum placement. The continuum was defined as a stright line or spline fitting, using parts of the spectrum located on both sides of Hα. We used different wavelength intervals to produce different normalisations. This leads to changes of the absolute value of EW, but keeps the relative distributions of the points the same. The errors of the EW have been calculated from four measurements, with different normalizations.

In order to search for the variability in the line profile of Hα line during an individual night, we calculate the fractional variance spectrum based on all the data in each night:

$$\sigma = \sqrt{\frac{1}{(N-1)\bar{f}_\lambda^2}\sum_{i=1}^{N}(f_{i\lambda}-\bar{f}_\lambda)^2}, \tag{2.1}$$

where N is the number of spectra, $f_{i\lambda}$ is the flux at wavelength λ of the i^{th} spectrum and $\bar{f}_\lambda$ is the flux at that wavelength averaged over all spectra. The σ in the continuum should correspond to (SNR)$^{-1}$, and hence a peak in σ should determine the significance of a variation.

One other statistical technique which is particularly useful to accurately determine the spectral location of variability is the temporal variance spectrum (Prinja et al. 2003; Fullerton, Gies & Bolton 1996):

$$(TVS)_\lambda = \frac{s_0^2}{(N-1)}\sum_{i=1}^{N}\frac{(f_{i\lambda}-\bar{f}_{w\lambda})^2}{s_i^2 f_{i\lambda}} \tag{2.2}$$

where $\bar{f}_{w\lambda}$ is the weighted mean of the normalised intensity, s$_i$ is the inverse of the SNR of spectrum i measured in the continuum, and $s_0^2 = [1/N\sum_{i=1}^{N} s_i^{-2}]^{-1}$.

The results of calculations are presented, together with all spectra, in Fig. 2.3.

As can be seen, the fractional variance spectra do not indicate variability in the first three nights (980415, 980802, and 980803), however the TVS indicates some variability in 980415. A clear peak in both σ and the TVS is visible on 990106 and 990107 at about velocity ≈0 km s^{-1}.

Following Fullerton, Gies & Bolton (1996), if the TVS for a spectral feature is above a specified level of significance then the null hypothesis of "no variability" can be rejected. The statistical distribution of the TVS is governed by the the reduced chi-squared distribution with N-1 degrees of freedom and scaled with SNR (TVS$\sim s_0^2\chi^2_{N-1}$). For the nights considered here, the statistical significance of 1% corresponds to TVS$^{1/2}$=3.6-5.0%, depending on the number of spectra and SNR. In the central part of the line the TVS is well above this level for 990106 and 990107 (Fig. 2.3). The peaks in σ correspond practically to the same confidence level of 3 standard deviations from the mean. This clearly shows that in these two nights there is statistically significant variability in the Hα line profile, at a confidence level of 0.99, at a time resolution of $\sim$10 min.

2.1.2 Variability in January 1999

For the two nights with detected variability, we subtract from the individual spectra the average spectrum, the minimum spectrum and the maximum spectrum. The average spectrum is defined as the average of the normalised flux for every pixel. The minimum (maximum) spectrum is defined as the minimal (maximal) value for each pixel. We do not know *a priori* whether we have variability due to a pure emission, pure absorption, or an admixture of both. The results for 990106 are presented in Fig. 2.4. As can be seen, variability exists in all three panels. This indicates additional absorption/emission with equivalent width of approximately 1 Å, located in the central part of the line.

To exclude the possibility that the observed variability is an artifact of data reduction we performed tests with data processing and normalisation, which showed that the detected variability on 990106 and 990107 is not an artificial result. Fig. 2.5b shows the results from two different extractions and normalisations which have identical σ peaks.

Although the sky conditions looked like photometric during the time of the observations we can not exclude the possibility that the variable atmospheric lines and small wavelength shifts from spectrum to spectrum can result in spurious variability. To test the variability these effects could produce, we artificially introduced random shifts in wavelength up to 3 km s^{-1}[the biggest shifts we detected were <0.25 px (2.5 km s^{-1})]. We also isolated athmosperic absorption lines from a high SNR spectrum of Spica (α Vir) and introduced variable atmospheric absorption in the spectra. We find that both efects can produce variability, but this variability is lower than the noise in TVS and σ and can not account for the observed peaks.

It is known (i.e. Zamanov & Bruch 1998) that the hot continuum, which flickers on time scales of minutes with amplitude 0.2-0.3 mag in U, contributes about 15% of the average flux in the V band. To check whether the variability detected in Hα is due to the changing continuum level caused by the flickering of the hot component, we simulate σ in such a case by supposing that the hot continuum flickers with amplitude $\pm$25-30% and contributes 15% of the flux in the continuum around Hα. The amplitude is chosen to be slightly higher than the highest one observed in the U band after the subtraction of the red giant contribution (see Zamanov& Bruch 1998). To this variable hot continuum we add constant red giant and Hα emission. The simulated σ and TVS are shown in Fig. 2.5. The simulated quantities are different from the "observed" ones as (i) they have smaller amplitude and (ii) they are wider and spread over the whole FWZI of the Hα emission, while the observed ones are located in the central part of the line only. This indicates that detected variability is not due to the continuum variability but is intrinsic to the line.

2.1.3 Origin of the rapid variability

The FWZI of the Hα emission line is 800 $\mathrm{km\,s^{-1}}$, with wings of the line formed in the immediate vicinity of the white dwarf (see also Stanishev et al. 2004). However, the detected variability appears in the central part of the line and is confined to $\Delta V \approx \pm$100-120 $\mathrm{km\,s^{-1}}$ from the systemic velocity. This indicates that this variability originates in the outer parts of the Hα emitting region. Assuming Keplerian motion, a 1.4 $\mathrm{M_\odot}$ white dwarf, and inclination 67^0 (i.e. Stanishev et al. 2004 and references therein) this corresponds to a distance $\geq$20-25$\mathrm{R_\odot}$.

Mass accretion in T CrB is occurring via Roche lobe overflow. As the stream of gas flows away from $\mathrm{L_1}$ it forms a ring (see Verbunt 1982). The position of the ring approximately defines the outer edge of the accretion disk. The radius of the ring can be estimated from (Hessman & Hopp 1990): $r_r/a = 0.0859(q)^{-0.426}$, where a is the semi-major axis and q is the mass ratio of giant to white dwarf. For T CrB q=0.82$\pm$0.10 and $a \approx 210$ $\mathrm{R_\odot}$ (Stanishev et al. 2004), which places the ring at 20 $\mathrm{R_\odot}$. At this location, the Keplerian velocity is about 115 $\mathrm{km\,s^{-1}}$, which is similar to ΔV of the detected variability. However, the Keplerian time scale is about 18 days, which is not comparable with the timing of our observations. This suggests that the variability is not produced by an inhomogeneous disc structure.

The observed behaviour of Hα emission from T CrB with time resolution 10-15 minutes is different from that of CH Cyg and of the variable winds observed in some CVs. We do not see ejected blobs, like those observed in CH Cyg (by Tomov et al. 1996), nor high velocity components observed in the variable disk winds of some CVs (Prinja et al. 2003). It might be that they are not detectable in our Hα profiles, even though they may exist and could be detected in the UV, where the hot component is the dominant source of radiation.

One possible explanation for the detected variability could be variable absorption from the wind of the giant or from the accretion stream. It is worth noting, that no variability in the line is observed at orbital phases where the line of sight passes through the expected position of maximum absorption from the red giant wind. Another cause could be additional emission from the area where the accretion stream hits the disk (the hot spot). It is possible that a variable component with EW$\leq$0.5Å always exists, but when the line is strong it is lost in the line (e.g. 980415).

An additional plausible explanation is that the variable continuum arising from the central part of the accretion disk (where the flickering in U arises) changes the ionisation state of the outer regions of the (flared) disk, from which the central part of the emission lines arise. This possibility deserves further exploration.

Conclusions: We searched for rapid Hα variability in the spectra of the recurrent nova T CrB. On 2 nights out of 5, we detect statistically significant variability at time resolution of 10-20 minutes. The detected variability is confined to the central part of the line profile at ± 100 km s^{-1}, which suggests that variations are produced in the outer parts of the accretion disk ($>$20 R$_\odot$). On these two nights there is evidence for variability of the total EW(Hα) (in all cases it is calculated relative to the average value, see Table 2.1) with amplitude $\pm$8% for 990106 and $\pm$6% for 990107, which is approximately five times the error of the individual measurements.

For the other 3 nights of observations we do not detect line profile changes. We place upper limits on the variability of the total EW(Hα): ΔEW(Hα) $\pm$2% for 980415, $\pm$4% for 980802 and $\pm$3% for 980803.

More extensive spectral observations with better time resolution, combined with photometry are necessary to define what influences the Hα variability and whether this variability is directly connected with the flickering.

2.2 HeII 4686 observations of T Coronae Borealis

We present spectroscopic observations of the HeIIλ4686 line of the recurrent nova T CrB. We have secured 22 spectra on 16 nights between April 1997 and January 2002 with the Coudé spectrograph of the 2.0 m RCC telescope of the Bulgarian National Astronomical Observatory "Rozhen". The spectra cover $\sim$ 100 Å (before 971010) and $\sim$ 200 Å (after 990105) around λ4686, with resolution of $\sim$ 0.2 Å pixel^{-1}. The S/N ratio achieved is 15-35. Two examples of our spectra are shown in Fig. 2.6. Journal of the observations is given in Table 2.2. The equivalent width (W) of the line is measured relative to the local continuum at $\lambda 4677 - \lambda 4690$ Å. The flux is calculated using B and V photometry. Typical errors in W and flux measurements are $\pm$15-20% and $\pm$20-30%, respectively. The radial velocity is measured at the top of the line and has an uncertainty of about $\pm$15 km s^{-1}.

T CrB consists of a red giant and a hot component (almost certainly a white dwarf). Iijima (1990) and Anupama & Mikolajewska (1999) reported the presence/absence of the HeII4686 line during the period 1987 – 1997. Combining their data with our new observations gives us the opportunity to discuss the appearance of the HeII emission during a period when the U brightness varies by more than 2 magnitudes (see Fig. 2.7). The times of HeIIλ4686 observations and detections are plotted on Fig. 2.7, together with the U band variability. We used our data, together with those of Iijima (1990) and Anupama & Mikolajewska (1999), as well as the long term light curve (Stanishev et al. 2004, and the references therein). As is apparent in Fig. 2.7, the appearance of HeIIλ4686 emission correlates with the U brightness of the object. Most of the detections clearly correspond to the short brightening in U of about ΔU$\sim$ 0.6 at JD2448050 and to the maximum at JD2450700. Variability in U reflects the changes is the mass accretion rate, provided that the spectral energy distribution does not change considerably, as is supposed from spectral fitting in high and low states (Stanishev et al. 2004).

The presence of a strong HeII line was reported in the period 1921 – 1946 (see Adams & Joy 1921, Minkowski 1943, Swings & Struve, 1943, among others). Bearing in mind that during the last decade the line was not strong and has been detected on a few occasions only, the older observations probably indicate a higher mass accretion rate during the 25 years preceding the 1946 outburst of Nova CrB (i.e. higher than the current value of about $2 \times 10^{-8}\, M_{\odot}\, yr^{-1}$ estimated by Selvelli et al. 1992).

In an attempt to detect the profile of the HeIIλ4686 line, we subtracted a template from the first 5 observations, when the line had W $>$ 1Å, and seemed blue shifted. In practise, we

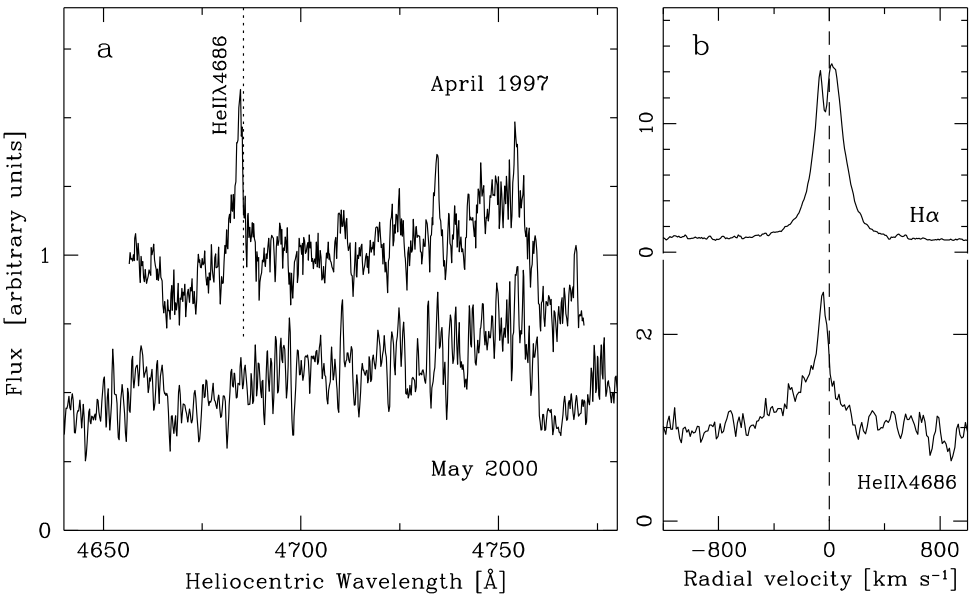

Figure 2.6: **a)** The region around the HeII line. The dotted line corresponds to the calculated radial velocity of the white dwarf (V_r=−19 km s^{-1}) **b)** Cleaned profiles of HeIIλ4686 and Hα. after the subtraction of the red giant spectrum. Both are normalised to the remaining hot component continuum, after the subtraction of the red giant spectrum. The zero of the X-axis corresponds to the calculated radial velocity of the hot component.

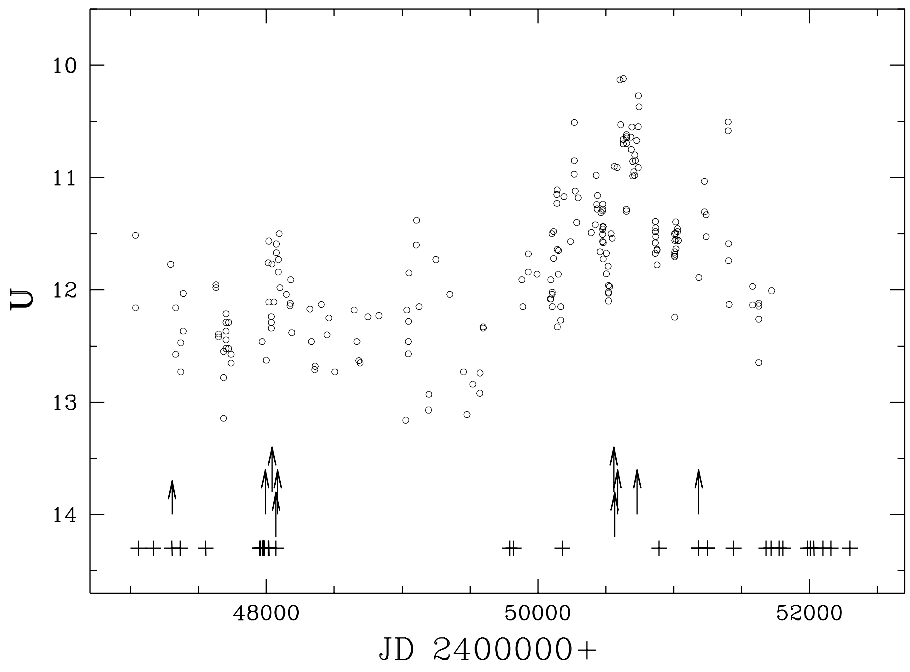

Figure 2.7: Johnson U band light curve of T CrB and observations of the HeIIλ4686 line. The arrows and crosses indicate the times of HeIIλ4686 observations. The arrows refer to detections, and crosses to non–detections of the HeIIλ4686 emission line.

used as templates epochs 000621, 010707, and 020123, where the HeII line was not detected. The upper limit ($W < 0.5$Å) was defined by comparing with (1) spectra of M giants from the library of stellar spectra of Le Borgne et al. (2003), (2) spectra of M4III stars (HD 4408 and HD 5316) observed with the same instrumental setup as T CrB.

The template was then shifted to match the observed red giant spectrum. The shifts have been calculated (i) via Fourier cross correlation, and (ii) using the orbital elements (from Stanishev et al. 2004). The shifted template has been subtracted from the 5 spectra from 970426 to 971010. Following this, the residual spectra have been shifted to the hot component velocity and averaged. The average profile of HeIIλ4686 obtained from these 5 template–subtracted spectra is plotted in Fig. 2.6b. The profile of Hα as observed in April 1997 (from Stanishev et al. 2004) is also plotted for comparison. The HeII profile is noisier than that of Hα because (i) the HeII line is weaker than Hα and (ii) the S/N of HeII spectra is lower than those in Hα.

As can be seen, the HeIIλ4686 profile is different from that of Hα. The HeII line is narrower (at half maximum), it does not exhibit double peak at the top, and it also seems to have an asymmetric profile with blue wing (Fig. 2.6b). We measured radial velocity in the higher flux regions of the line where it is practically symmetric. Part of the observational data (all cases when W > 1 Å) show that this velocity is negative relative to the orbital velocity of the hot component (the hot component orbital velocity is supposed to follow $V_h = -36.7 + 19.5\cos[2\pi(\phi - 0.563)]$ km s^{-1}, see Stanishev et al. 2004). Unfortunately, we cannot be sure whether we observe a blue wing and broad component close to the continuum level (like those detected in HeIIλ 1640 by Selvelli et al. 1992) because it is comparable with the noise and depends on the subtraction of the red giant flux. However, the blue shift at the peak and at half maximum seems to be detected. On the other two exposures (obtained on 990105) the line is weaker and its radial velocity coincides with the radial velocity of the hot component.

HeII lines are supposed to be formed in the immediate vicinity of the hot component. The blue shift of HeII4686 indicates a motion from the hot component toward the observer. The most plausible explanation is that it arises in an outflow from an accretion disk (most probably a disk wind at the high state of the system). A receding part of this outflow can also exist, but it has to be obscured by the disk itself.

In T CrB the main the accretion is the Roche lobe overflow from the giant. In addition to the flow via L_1, accretion from a stellar wind can supply about 15% of the total mass accretion rate (Selvelli et al. 1992). However, in nova–like cataclysmic variables at accretion rates $\sim 1 \times 10^{-8} \, M_{\odot} \, yr^{-1}$ (like that of T CrB) the accretion disk is expected to lose about 0.001

Table 2.2: HeIIλ4866 line observations of T CrB. The date is in the format YYMMDD. The orbital phase (ϕ) is calculated using the ephemeris $T_0 = 2447918.62 + 227.5687 \times E$ (Fekel et al. 2000). The equivalent width (W), flux of the line and radial velocity are given. The flux is in units of 10^{-13} erg cm^{-2} s^{-1}. The non–detections (nd) of the line correspond to upper limits of about $W < 0.5$ Å (equivalent to $< 0.6 \times 10^{-13}$ erg cm^{-2} s^{-1}). The calculated radial velocity of the hot component,V$_h$, is also given (see the text).

Date	HJD	ϕ	W [Å]	Flux	V$_r$ km s^{-1}	V$_h$ km s^{-1}	Date	HJD	
970426	50565.529	0.631	2.0	4.22	−67	−19.0	000516	51681.353	nd
970426	50565.543	0.631	2.7	5.70	−99	−19.0	000516	51681.368	nd
970427	50566.391	0.635	2.1	4.43	−75	−19.2	000621	51717.396	nd
971010	50732.219	0.364	1.4	3.31	−70	−30.6	000818	51775.320	nd
971010	50732.234	0.364	1.6	3.78	−75	−30.6	000917	51805.288	nd
990105	51184.632	0.352	0.9	1.78	−26	−32.0	010316	51985.438	nd
990105	51184.646	0.352	1.0	1.98	−22	−32.0	010407	52007.387	nd
990309	51247.438	0.628	nd	–	–		010502	52032.350	nd
990309	51247.452	0.628	nd	–	–		010707	52098.312	nd
990919	51441.325	0.480	nd	–	–		010904	52157.341	nd
990919	51441.343	0.480	nd	–	–		020123	52297.684	nd

- 0.15 of the accreting material via an accretion disk wind (i.e. Vitello & Shlosman 1993; Long & Knigge 2002). It is worth noting that accretion disk winds in cataclysmic variables are best visible as absorption lines and P Cyg profiles in the UV (for example Prinja et al. 2003). The available UV spectra of T CrB are however too noisy for clear detection of the UV line profiles (see Selvelli et al. 1992 and IUE archive), but the profile of HeII4686 suggests the presence of an outflow (at least in high state).

We conclude, that the appearance of the HeII emission in T CrB is connected with U band variability, and probably therefore with epochs of higher mass accretion rate. Whether we have accretion disk wind or accretion from a stellar wind (in addition to Roche lobe overflow) could be answered by careful investigation with better optical and UV spectra. This could also help us to understand when and how accretion from stellar winds, in wind-fed symbiotics, can exist together with outflows from the accreting component.

2.3 Flickering variability of T Coronae Borealis

We present electro-photometric UBV and high-speed U-band flickering observations of the recurrent nova T CrB during a period when its U brightness varies by more than 2 mag. The V band is dominated by the ellipsoidal variability of the red giant, however, the variability of the hot component also causes ~ 0.15 mag variations in V. We define a set of parameters which characterise the flickering. The Fourier spectra of all 27 nights are similar to each other. The power spectral density of the variations has a power law component ($\propto f^{-1.46}$ on average). We do not detect a dependence of the Fourier spectra and autocorrelation function on the brightness of the object. Having subtracted the contribution of the red giant, we show that the flickering amplitude correlates with the average flux of the accreting component. A comparison with CH Cyg and MWC 560 indicates that the flickering of T CrB is more stable (at least during the time of our observations), than that in the jet-ejecting symbiotic stars.

T CrB (HD 143454) is an interacting binary star which consists of a red giant and a white dwarf (Selvelli et al. 1992, and references therein). The star has undergone two nova eruptions (Nova CrB 1866, 1946) and is thus classified as a recurrent nova (and, due to the presence of the cool giant, plus emission lines seen at outburst, also as a symbiotic star). The red giant fills Roche lobe, and thus the accretion flow onto the white dwarf (WD) is via L_1, which is typical for cataclysmic variables. Sharing characteristics of three (partly overlapping) types of interacting binaries, T CrB is therefore an important object for our understanding of the different processes in interacting binaries.

Stochastic brightness variations (flickering), occurring on time scales of seconds and minutes with amplitudes ranging from a few millimagnitudes up to more than an entire magnitude are a phenomenon typical for cataclysmic variables, and it is rarely observed in symbiotic stars. For example, to-date it is detected in only 8 of the 220 known symbiotics (Dobrzycka et al. 1996; Belczyński et al 2000, Sokoloski et al. 2001). In T CrB flickering with amplitude of $\Delta U \sim 0.1$-0.5 mag has been observed on a time scale of minutes (Ianna 1964, Lawrence et al. 1967 Bianchini & Middleditch 1976, Walker 1977, Bruch 1980). The flickering amplitude is somewhat smaller in B and V bands (Raikova & Antov 1986, Hric et al. 1998). In addition, on some occasions such flickering disappears (Bianchini & Middleditch 1976, Oscanian 1983, Mikołajewski et al. 1997). In our previous investigation (Zamanov & Bruch 1998) we showed that the flickering of T CrB is indistinguishable from the flickering observed in dwarf novae, in spite of the vast difference in the geometrical size of the systems.

The exact origin of the stochastic variations is not clear, but they are considered to be a result of accretion onto the WD through a disk. The possible mechanisms include unstable mass transfer, magnetic discharges, turbulence and instability in the boundary layer (e.g. Warner 1995, Bruch 1992).

Here we present new UBV and high-speed flickering observations of T CrB, estimate the contribution of the red giant, analyse the U band variability, search for relations between the flickering quantities and the brightness of the object, and compare its behaviour with two other symbiotic stars (the "nanoquasars" CH Cyg and MWC 560).

The observations have been performed with the 60 cm telescope of NAO Rozhen equipped with a single channel photometer. The comparison stars were HD142929 and BD+26^{0}2761, the check star GSC 2037.1228 and the integration time 1 or 10 *sec*. The observations with 1 sec integration time have been binned in 10 sec. APR software (Kirov, Antov & Genkov, 1991) has been used for data processing. The accuracy of the UBV photometry is better than 0.03 mag and the results are given in Table A.1.

For the flickering observations, the reduction to the standard U band is better than ± 0.04 mag and the internal accuracy of the data (standard deviation from the average of 10 consecutive measurements) is $0.015-0.030$ mag. The control of the atmospheric conditions and performance of the system have been done by observing the check star, before and after T CrB. and carefully tracing of the comparison star counts (which has been observed every 20-30 minutes). In the subsequent data processing 2 nights has been rejected, because of "doubtful" behaviour of the comparison or/and check stars. Journal of flickering observations and the main characteristics of the U band variability for each run are summarised in Table 2.3.

The error in the magnitudes (U_{max}, U_{min}, U_{av}) are calculated dividing every run into two parts and calculating the quantities separately for each part, in this way addressing the possible errors of the run. In Fig. 2.8 is plotted the orbital modulation in V, in Fig. 2.9 the long term U band curve and the flickering observations, and in Fig. 2.10 are given two examples of the flickering.

2.3.1 Contribution of the red giant

V band: In symbiotic stars, the mass donor is a red giant. In the case of T CrB its contribution is not negligible in the UBV bands. The V band variability of T CrB is dominated by the ellipsoidal variability of the red giant (Peel 1985, Lines et al 1988). The V band data from the

Table 2.3: Journal of flickering observations in the U band. Date is given in format YYMMDD, TJD is the truncated Julian day of the start of the observation, N is the number of the points in the run, IT is the integration time [in seconds]. D is the duration of the run in minutes. U_{max}, U_{min}, and U_{aver} are the maximum brightness during the night, the minimum, and the average of this quantity, respectively. U_{av} is calculated averaging the corresponding fluxes.

Date	TJD_{start}	NxIT [sec]	D min	U_{max} [mag]	U_{min} [mag]	U_{av} [mag]
930228	49046.5117	448x10	122	12.260±0.03	12.578±0.01	12.387±0.04
940410	49453.4621	266x10	49	12.652±0.02	12.945±0.05	12.820±0.05
950613	49882.3317	242x10	45	11.713±0.11	12.222±0.07	11.952±0.08
950620	49889.3496	520x10	102	11.798±0.06	12.353±0.10	12.081±0.05
960110	50092.6671	150x10	31	11.826±0.07	12.236±0.03	12.002±0.03
960228	50141.5088	772x10	162	11.161±0.02	11.714±0.01	11.406±0.02
960229	50142.4900	9304x1	190	11.460±0.01	12.065±0.07	11.770±0.05
960325	50167.5358	3956x1	63	12.017±0.01	12.323±0.02	12.146±0.00
961216	50433.6246	2190x1	57	11.051±0.00	11.397±0.03	11.272±0.02
961218	50435.6354	1292x1	38	11.111±0.04	11.368±0.03	11.262±0.04
970128	50476.5542	674x10	128	11.181±0.05	11.632±0.10	11.456±0.07
970129	50477.5717	522x10	98	11.307±0.01	11.607±0.02	11.469±0.02
970130	50478.5983	425x10	81	11.333±0.07	11.614±0.04	11.461±0.05
970131	50479.5537	704x10	137	11.354±0.05	11.631±0.04	11.488±0.04
970201	50480.5379	8318x1	151	11.443±0.01	11.828±0.02	11.658±0.04
970721	50651.3508	547x10	119	11.200±0.02	11.457±0.01	11.326±0.01
970722	50652.3379	96x10	21	10.533±0.01	10.762±0.03	10.669±0.03
970827	50688.3313	207x10	46	10.561±0.06	10.939±0.07	10.758±0.06
980220	50864.5092	837x10	168	11.464±0.01	11.779±0.02	11.604±0.01
980224	50868.5383	407x10	81	11.296±0.06	11.700±0.07	11.505±0.05
980713	51008.3217	256x10	52	11.540±0.01	11.774±0.00	11.660±0.00
980714	51009.3188	362x10	74	11.504±0.04	11.840±0.02	11.670±0.05
980720	51015.3342	304x10	64	11.335±0.02	11.621±0.00	11.477±0.01
980721	51016.3208	319x10	64	11.435±0.03	11.770±0.05	11.613±0.02
980802	51028.3125	344x10	69	11.400±0.06	11.759±0.02	11.595±0.04
980803	51029.3217	298x10	61	11.521±0.02	11.737±0.02	11.614±0.01
990107	51185.6225	406x10	76	11.646±0.07	12.074±0.05	11.847±0.05

Table 2.3: Continuation. Date is given in format YYMMDD, σ is the standard deviation in the run. The power spectra in each night are fitted with linear fit (A and γ are the parameters of the fit, see the text). γ is the power spectrum slope in the interval 3-160 cycles/hour. The e-folding time of the ACF is given for the original run (τ_0), and after subtraction of a spline fit (τ_1).

Date	σ [mag]	A	γ	τ_0 [sec]	τ_1 [sec]
930228	0.084	3.41	−1.77	789±35	65±7
940410	0.081	3.59	−1.71	516±72	54±10
950613	0.121	3.19	−1.32	257±49	143±21
950620	0.099	2.14	−1.47	181±25	107±10
960110	0.092	3.70	−1.38	138±87	98±17
960228	0.121	2.23	−1.51	292±18	130±36
960229	0.105	1.74	−1.40	1253±82	131±12
960325	0.052	3.04	−1.68	132±30	105±21
961216	0.078	1.52	−1.06	152±21	132±18
961218	0.066	2.50	−1.41	66±6	78±7
970128	0.101	2.70	−1.45	675±89	174±10
970129	0.070	2.56	−1.47	378±47	144±22
970130	0.068	2.98	−1.54	785±204	50±8
970131	0.060	2.95	−1.67	416±25	185±13
970201	0.093	2.42	−1.54	626±61	169±17
970721	0.064	2.52	−1.43	799±38	50±5
970722	0.068	3.80	−1.73	114±13	135±16
970827	0.086	3.57	−1.67	280±60	123±22
980220	0.071	2.14	−1.40	571±44	124±12
980224	0.094	3.11	−1.58	498±45	139±23
980713	0.062	2.76	−1.28	212±25	256±46
980714	0.078	2.94	−1.43	257±216	89±10
980720	0.072	3.34	−1.67	191±14	125±18
980721	0.059	2.72	−1.41	105±14	91±11
980802	0.079	2.19	−1.09	387±118	106±14
980803	0.042	2.81	−1.38	87±25	40±10
990107	0.086	2.33	−1.40	495±144	54±5

long term light curve (see Stanishev et al. 2004 and references therein) are plotted in Fig. 2.8, folded with the orbital period. A three term truncated Fourier fit to all data gives

$$V = 10.056\,(0.003) + 0.007\,(0.004)\cos 2\pi\phi - 0.026\,(0.004)\sin 2\pi\phi - 0.161\,(0.004)\cos 4\pi\phi$$
$$-0.036\,(0.004)\sin 4\pi\phi + 0.016\,(0.004)\cos 6\pi\phi - 0.037\,(0.004)\sin 6\pi\phi, \quad (2.3)$$

where ϕ is the orbital phase (hereafter the numbers in the parentheses refer to the errors). This fit is plotted as solid line in Fig. 2.8. Typical deviation of the points from the fit line is ± 0.10 mag.

On Fig. 2.8 we have plotted with different symbols the points when the object is brighter and fainter at shorter wavelengths (open circles refer to U<12 and filled – to U≥12). It is visible that the filled circles are displaced downward slightly relative to the open ones. The U band brightness is dominated by the hot component. We can also deduce that the variability of the hot component of about 2 magnitudes in U (see also Stanishev et al. 2004) also contributes to that in V. To define this contribution we performed a simple fits (using only the main terms) to the open and filled symbols. The obtained coefficients are:

$$V = 10.157\,(0.005) - 0.194\,(0.007)\cos 4\pi\phi \quad \text{for} \quad U \geq 12 \quad (2.4)$$

$$V = 10.029\,(0.003) - 0.163\,(0.004)\cos 4\pi\phi \quad \text{for} \quad U < 12. \quad (2.5)$$

The mean values of the U band magnitudes are U=12.3±0.3 and U=11.2±0.4 for the fainter and brighter points respectively. Therefore, the increase of the system U-band brightness brightness by 1.1 mag results in an increase of the V brightness by 0.128 (Eq 2.4, Eq. 2.5). We derive a relative contribution R(V)=0.205±0.035, where R(V)=F_{hot}/F_{gM} is the relative contribution between the accreting object and the red giant at V=10.056. The corresponding orbital light curve of the red giant is plotted as a dashed line on Fig. 2.8. The calculated contribution is very similar to that obtained by Zamanov & Bruch (1998) on the basis of the average colours of the flickering source in cataclysmic variables.

Although the data in Fig. 2.8 spread over 22 years, the typical deviation of the points from the fit line is ± 0.10 mag. This points to the fact that the V band light curve has not changed in its main features over the last 22 years. This in turn indicates that the M giant is not variable. Indeed, we can put an upper limit on its possible variability of $\Delta V < 0.05 - 0.10$. The stability of the red giant is better defined in IR observations (Yudin & Munari 1993, Shahbaz et al., 1997), where a upper limit of variability $\Delta J < 0.02$ has been constrained.

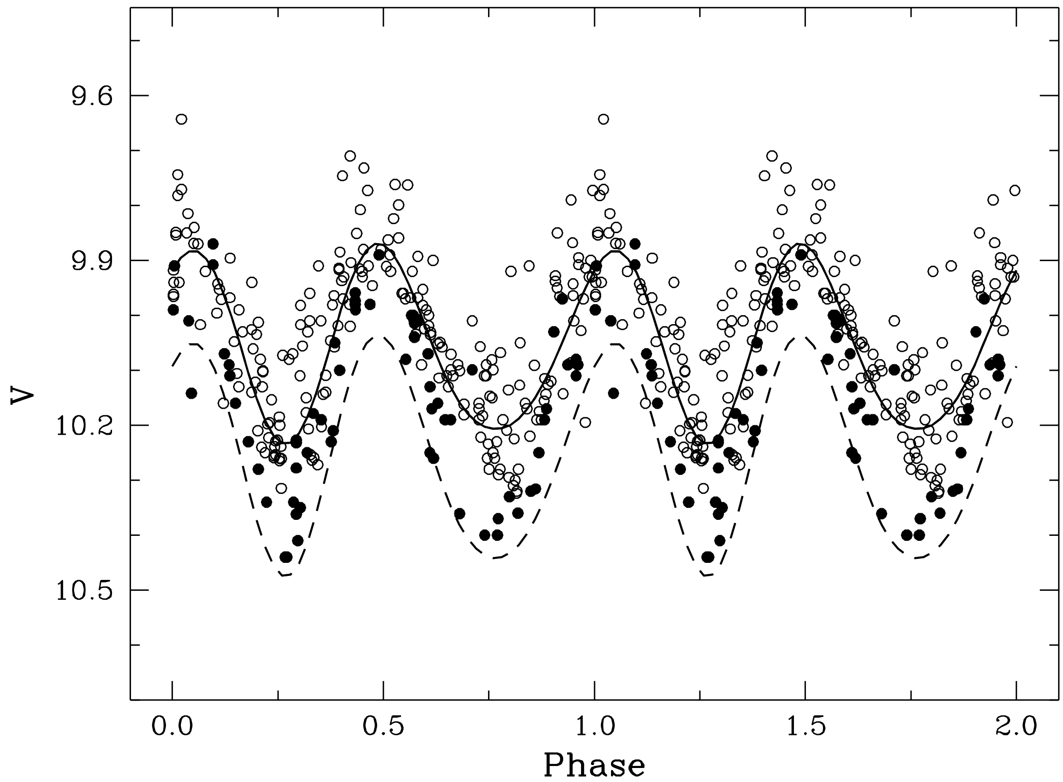

Figure 2.8: Johnson V band observations of T CrB folded with a 227 day period. The solid line is our fit to all data (Eq. 2.3). The open circles refer to the epochs when the object is brighter than U= 12 and the filled circles refer to the epochs when it is fainter than this. The dashed line is the calculated contribution of the red giant.

Red giant contribution to U band flux: The latest definitions of the spectral type of the red giant in T CrB are M4III (Zhu et al. 1999) and M4.5III (Mürset & Schmid 1999). Both are obtained on the basis of IR spectra and with typical uncertainty ±1 spectral subtype. The expected colour of a M4.5III star is (U-V)$_{M4.5III}$ $= 3.16 \pm 0.10$ (Lee 1970), (U-V)$_{M4.5III}$ $= 3.28 \pm 0.10$ (Schmidt-Kaler 1982), (U-V)$_{M4.5III}$ $= 3.25 \pm 0.10$ (calculated using the tables of Fluks et al. 1994). The New ATLAS9 model atmospheres (Pietrinferni, Cassisi, Salaris, Castelli, in preparation), for a star T$_{eff}$ =3500 K and $\log(g) = 1.0$, give (U-V)=3.18 for [Fe/H]=0.2, (U-V)=3.26 for [Fe/H]=0, and (U-V)=3.42 for [Fe/H]=-1.5.

Using R(V)=0.222 at V=10.029 (as derived in Section 2.3.1), the fit to V (Eq. 2.3), E$_{B-V}$ = 0.15, and (U-V)$_{M4.5III}$ =3.25, we can calculate the contribution of the red giant to the U band. The light curve of T CrB, our flickering observations, and the red giant contribution (as a sine wave) are plotted in Fig. 2.9.

One way to check the calculated U brightness of the red giant is IR photometry, supposing that the red giant is the only source in J band. The J brightness of T CrB varies in the interval J=5.90 – 6.19 (Kamath and Ashok 1999). Interpolations in the tables of the colours of red giants give (U-J)$_{M4.5III}$ $= 7.75 \pm 0.25$ (from Lee 1970), (U-J)$_{M4.5III}$ $= 7.14 \pm 0.2$ combining (U-V) from Schmidt-Kaler (1982) and (V-J) from Ducati et al. (2001), (U-J)$_{M4.5III}$ $= 7.34 \pm 0.2$ (from Fluks et al. 1994), where the calculated uncertainties refer to ±0.5 spectral type. The model atmospheres give (U-J)$_{[Fe/H]=0.2}$=7.24, (U-J)$_{[Fe/H]=0}$=7.13 and (U-J)$_{[Fe/H]=-1.5}$=6.52 (Pietrinferni et al. 2004).

Shahbaz et al (1999) modeled the M giant spectrum, with enhanced abundance of lithium but normal abundance of the other metals, however they used higher gravity inconsistent with the last orbital solution.

If we suppose that the red giant is the only source in J, using the above (U-J) colours and E$_{B-V}$ = 0.15 we could expect value about U$\sim$ 14.4 - 13.3, which is consistent with the calculated contribution of the red giant to the U band (U$\sim$ 14.1 - 13.6, see Fig. 2.9).

2.3.2 Flickering quantities

The U magnitudes were converted into fluxes, adopting flux for a zero magnitude star $F_0(U) = 4.194 \times 10^{-11}$ Watt m^{-2}nm^{-1} (Bessel 1979). In addition to our data, we used those from Bruch (1992) and the data of Oskanian (1983). Bruch's data are reddened with $E_{B-V} = 0.12$ and they were corrected for the difference in the adopted zero-point of the flux scale. For Oskanian's data, we assumed that the instrumental difference $\Delta u = 0$ corresponds to magnitude U=11.83.

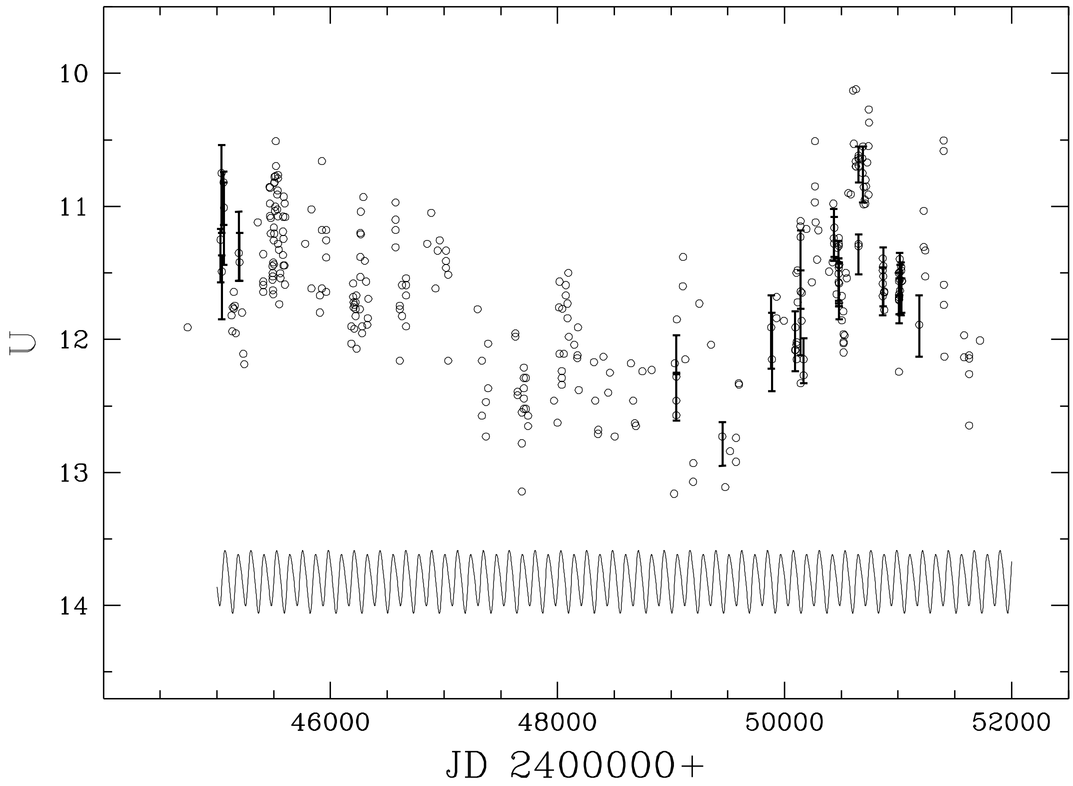

Figure 2.9: Long term variability in U band magnitudes and the flickering observations, with the corresponding amplitude. The cosine wave (bottom) is the calculated contribution of the red giant.

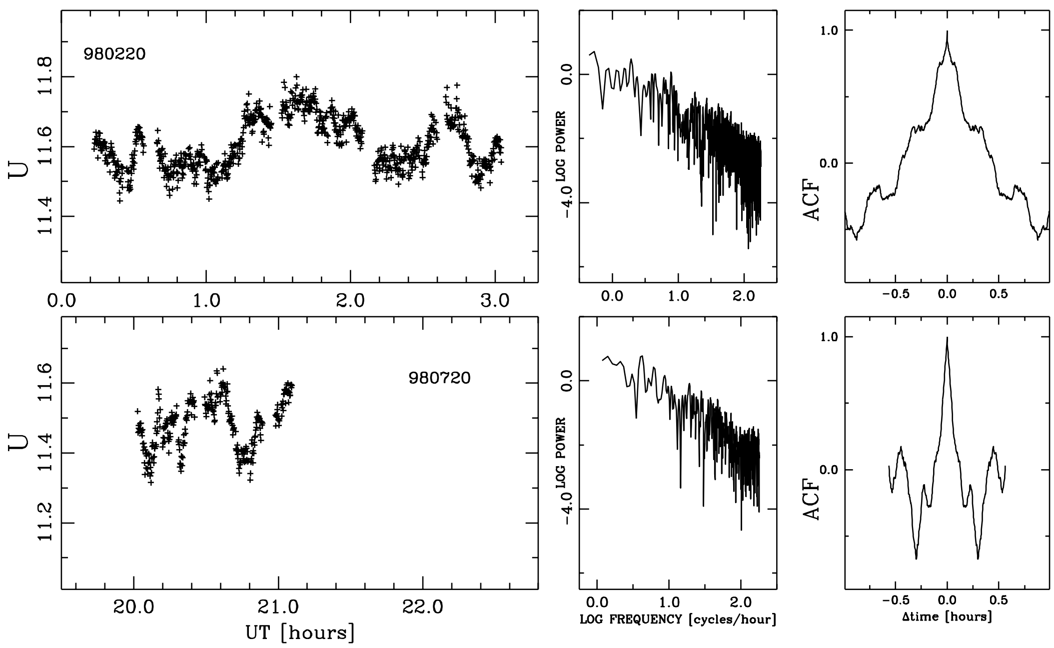

Figure 2.10: Two examples of our observations (for dates 980220 and 980720). The left panels represent the flickering behaviour of T CrB in U, mid panels the power spectra, and right panels the autocorrelation function.

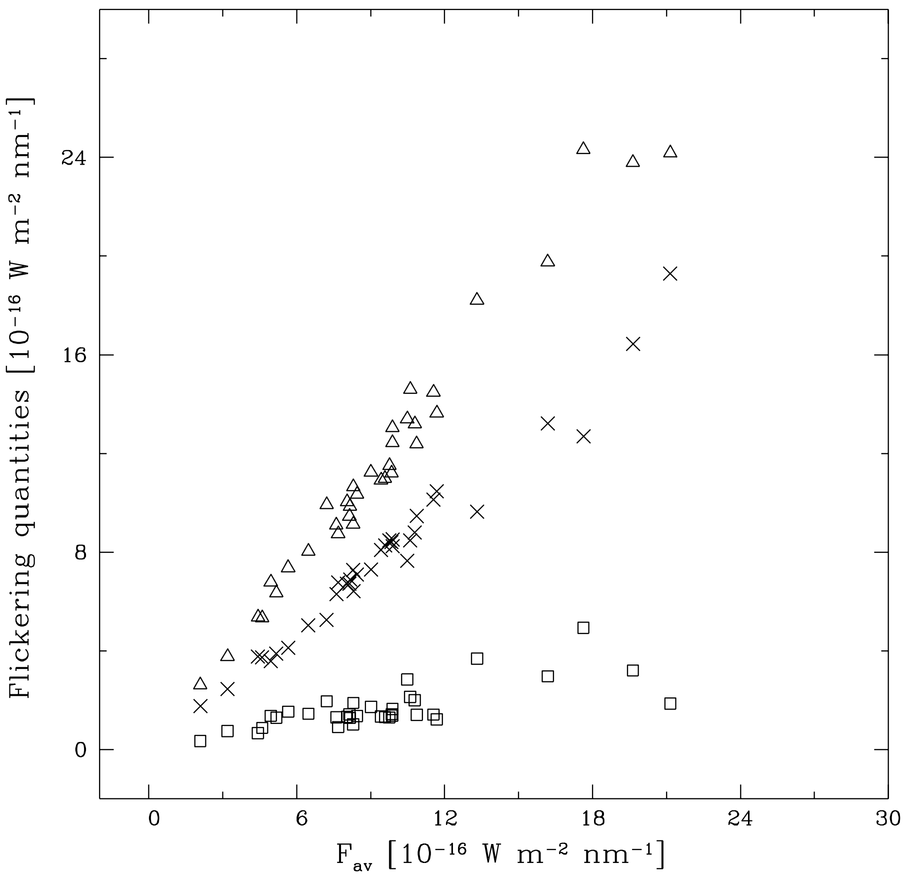

Figure 2.11: Measured flickering quantities versus the average flux F_{av} of the hot component. Triangles refer to F_{max}, crosses to F_{min} and squares to F_{fl}. The axes are in units 10^{-16} Watt $m^{-2}nm^{-1}$.

We have used only positive detections of the flickering. After the observed flux during a given night was corrected for the contribution of the red giant the following quantities were calculated:

F_{av} – the average flux of the hot component;

F_{max} – the maximum flux of the hot component;

F_{min} – the minimum flux of the hot component;

F_{fl} – the average flux of the flickering, $F_{fl} = F_{av} - F_{min}$.

In Fig. 2.11 are plotted the flickering quantities versus the average flux of the hot component. It is obvious they have to be connected, however it is not clear a priori how the different quantities will depend on each other. The least squares fits to data in Fig. 2.11 give:

$$F_{max} = -0.22\,(0.07) + 1.252\,(0.006)\ F_{av} \tag{2.6}$$

$$F_{min} = -0.32\,(0.56) + 0.858\,(0.054)\ F_{av} \tag{2.7}$$

$$F_{fl} = +0.19\,(0.42) + 0.156\,(0.042)\ F_{av} \tag{2.8}$$

Power spectra

For each run we also calculated the power spectrum and the autocorrelation function. Two examples are shown in Fig. 2.10. Over a wide range of frequencies the power spectra of T CrB light curves follow power law $P(f) \propto f^{\gamma}$, where P is the power and f is the frequency. Such a power-law shape is commonly observed in the light curves of cataclysmic variables and is attributed the flickering. The power-law index γ was determined in the frequency interval from 3 to 160 cycles/hour. Practically, we fitted the power spectra over this interval in log-log scale with least-squares linear fit: $\log(P) = A + \gamma \log(f)$. γ and A are given in Table 2.3. The typical errors are ΔA= ± 0.8 and $\Delta\gamma = \pm 0.25$. The visual comparison/inspection shows that all power spectra are very similar. This is confirmed from the fits. They give an average value of $\overline{\gamma} = -1.46 \pm 0.17$. There are two runs where γ is ≈ -1.1. In both cases two stronger flashes are visible in the variability with amplitude about ~ 0.2 mag.

The power-law spectrum of the type observed in T CrB is expected in the model of flickering proposed by Yonehara, Mineshige, & Welsh(1997). They proposed as origin of flickering self-organised critical state of the disk in which seemingly chaotic fluctuations can be produced. Such a model implies $\gamma \simeq -1 - -2$. Our observations of T CrB do not contradict to this model.

The correlation analysis shows no correlation of A and γ with U_{av} or F_{av}, ($r_P < 0.2$), indicating that the flickering is "stable", i.e. without considerable changes of the nature of the power spectrum in spite of the variability.

This is however not the situation in the symbiotic star CH Cyg, where the power spectrum changes dramatically. There are even moments when CH Cyg's power spectrum cannot be fitted with a simple power-law as a result of an unstable disk and disruption of the inner disk during the jet ejection (Sokoloski & Kenyon, 2003b). In T CrB we did not observe instabilities like those observed in CH Cyg.

Autocorrelation function (ACF)

Another objective way to investigate flickering behaviour is the ACF (see also Bruch 2000). The ACFs were calculated according to Edelson & Krolik (1988) for unevenly spaced data.

The typical time scale of the flickering may be defined as the time shift at which the ACF first reaches the value 1/e. Thus determined correlation times are influenced by the presence of periodic brightness variations or some trends in the data. As Robinson & Nather (1971) and Panek (1980) note, these correlation times can be additionally biased by the presence of weakly correlated noise and the process of trend removal (if applied).

The e-folding time is given in Table 2.3. The errors are determined from the errors of the autocorrelation coefficients. We calculated e-folding times in two different ways: (i) the e-folding time of the ACF of the original data in each run (τ_0) and (ii) after subtraction of a spline fit (τ_1). Operation (ii) has been done in order to obtain the typical time of the flickering on shorter time scales. A tension spline interpolation was undertaken. We subtracted this spline fit through the mean points in non-overlapping bins of length about ~20 minutes in a way that is identical to that applied to TT Ari by Kraicheva et al. (1999).

The e-folding time of the ACF varies over a wide interval. The average values, standard deviation of the average, and median value of the e-folding time are $\overline{\tau_0} = 394 \pm 287$, $< \tau_0 >= 292$, $\overline{\tau_1} = 115 \pm 48$, $< \tau_1 >= 123$, where all values are in seconds. The values of τ_1 are more or less similar to the values of TT Ari as defined in Kraicheva et al. (1999).

The correlation analysis showed that there are no correlations between the so-defined e-folding times and the brightness of the object, or the flickering quantities (F_{av}, F_{fl}, or the size of the boundary layer). Linear Pearson correlation coefficient and Spearman's Rank correlation give values between 0 and 0.2, indicating that there is no dependence of the time scale of variability on the luminosity of the hot component, i.e. the the characteristic time scales of the flickering are not connected with the brightness of the object.

Boundary layer

The origin of flickering is still not clear although this phenomenon is observed for many stars. Bruch (1992) and Bruch & Duschl (1993) identify the boundary layer between the accretion disk and the white dwarf as the most probable place for the origin of flickering. Bruch & Duschl (1993) consider that the ratio $\frac{F_{fl}}{F_{min}}$ is connected with the size of the boundary layer between the white dwarf and the accretion disk.

In T CrB F_{fl} is well correlated with F_{min} (see Fig. 2.12) . The Pearson's Correlation Coefficient is r_P=0.72 and Spearman's Rank Correlation r_S=0.56. Assuming that the deviation of the points from the fit lines (Fig. 2.11 and Eqs. 2.6 – 2.8) is due only to the errors of the measurements, the fits (Eqs. 2.6 – 2.8) indicate that in spite of variations in F_{av} (which we suppose is related to the mass accretion rate), the ratios F_{fl}/F_{min} and F_{max}/F_{min} do not change markedly. In terms of Bruch & Duschl (1993) this means that the size of the boundary layer remains almost constant independently of changes in the mass accretion rate. Here, adding more data (see Fig. 2.12) we confirm the conclusion of Zamanov & Bruch (1998) that F_{fl} increases linearly with the increase of F_{min}. This, within the limits of Bruch & Duschl's model, means that the size of the boundary layer in T CrB remains almost constant independently of the changes in the mass accretion rate.

2.3.3 Flickering amplitude

Flickering amplitude ($\Delta F = F_{max} - F_{min}$) is also measured in the extensive observations of CH Cyg (Mikołajewski et al., 1990) and MWC 560 (Tomov et al. 1996a). The flickering amplitude versus the average flux of the hot component, after subtraction of the red giant contribution is presented for all three stars in Fig. 2.13.

T CrB

The data in Fig. 2.13 show that the flickering amplitude depends on the average hot component flux. The correlation is well defined with $r_P = 0.72$ and $r_S = 0.56$. Searching for a dependence of the type $\Delta F \propto (F_h)^k$, we obtain a best fit for T CrB $k = 1.09 \pm 0.11$. The fit and the corresponding error have been calculated in two ways: (1) Using the errors into corresponding quantities as given in Table 2.3. (2) Bootstrapping simulations (e.g. Efron & Tibshirani, 1993) over the points plotted in Fig. 2.13, i.e. taking ∼20 subsamples from our points. Using only our own and Bruch's points (i.e. data well calibrated in U) we obtain $k = 1.03 \pm 0.09$. Using

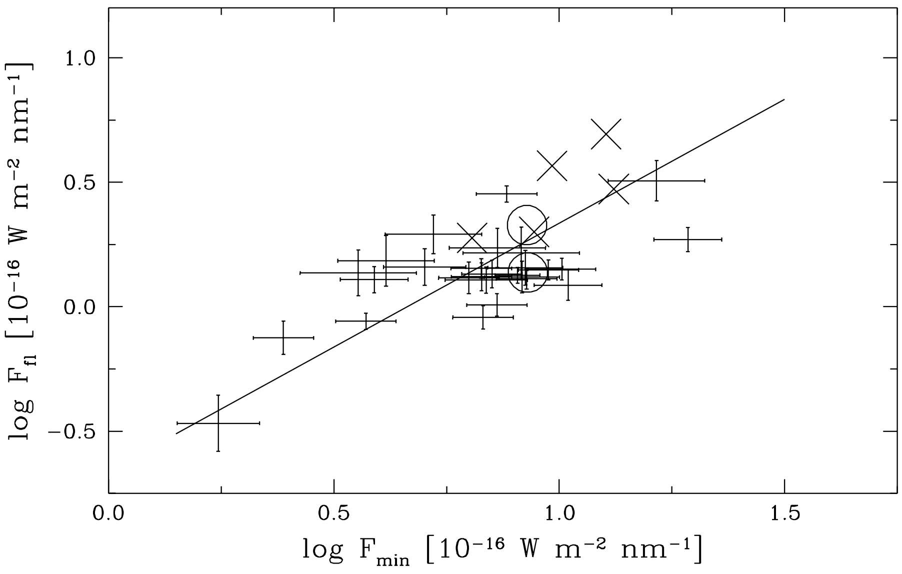

Figure 2.12: The average flux of the flickering, F_{fl}, versus the quiescent flux of the hot component in a light curve, F_{min}. The solid line is a linear least squares fit $F_{fl} \propto F_{min}^{k}$, where $k = 0.995 \pm 0.015$. Our data are plotted with the corresponding errors, the circles represent data of Bruch (1992) and crosses($\times$) - from Oskanian (1982)

different subsamples of the whole sample we obtained values $0.93 \leq k \leq 1.22$. An error in the subtraction of the M giant contribution of 25% will cause error in k of about 0.05.

CH Cyg

Dependence of the flickering amplitude on the brightness has been reported for CH Cyg by Mikołajewski et al. (1990). Their results show that the flickering amplitude in CH Cyg is a power law function of the hot component luminosity, i.e. $\Delta F \propto (F_h)^k$, where $k = 1.40 - 1.45$. Here, using their data, we subtracted the contribution of the red giant and the resulting points are plotted on Fig. 2.13. To subtract the contribution of the red giant we assume that at the minimum of V flux all the light is due only to the red giant, and it has a colour corresponding to $(U\text{-}V)_{M6III}$= 2.43 - 2.70 (Lee, 1980; Schmidt-Kaler 1982; Fluks 1994). The minimum brightness of CH Cyg is V=10.0 (Mikołajewski et al. 1996), and we adopt a contribution of the red giant of U=12.45. We will not go into details as to whether the system is triple (Hinkle et al. 1993; Skopal et al. 1998) or binary (Munari et al. 1996). Here we only note that an error of ± 0.7 mag in the subtraction of the red star(s) flux would influence the obtained slope to less than $\pm$ 0.02.

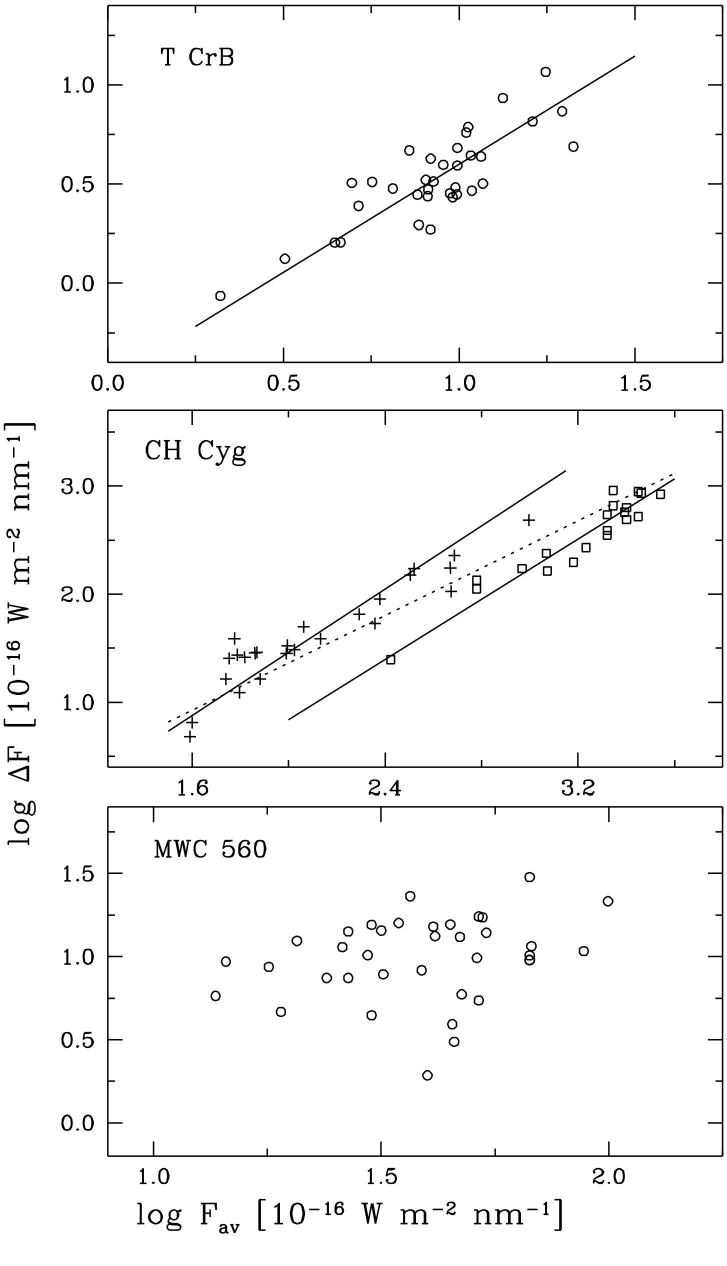

Figure 2.13: The flickering amplitude versus the flux of the hot component in U the band for T CrB (our data), CH Cyg (Mikołajewski et al. 1990, the plus signs refer to the propeller, the squares to the accretor stage), and MWC 560 (Tomov et al. 1995). The axes are in units of 10^{-16} Watt $\mathrm{m}^{-2}\mathrm{nm}^{-1}$. In all cases the contribution of the red giant has been removed. For T CrB the line is the best linear fit. For CH Cyg the solid lines are for propeller and accretor stages, and the dashed line that to all points. For MWC 560 the correlation is weak and no fit was performed.

The analysis gives a very high correlation between F_{av} and ΔF. r_P and r_S are always about 0.88-0.94 using (1) all points, (2) the propeller state observations, and (3) the accretor state (for further discussion of propeller and accretor states in CH Cyg, see Mikołajewski et al 1990).

After the subtraction of the red giant contribution we obtain $k = 1.08 \pm 0.05$ if we use all points, $k = 1.48 \pm 0.05$ for propeller state points only, and $k = 1.41 \pm 0.05$ for the accretor state only. It has to be noted that the fit $\Delta F \propto (F)^{1.08}$ obtained on the basis of all points is very similar to the value for T CrB.

MWC 560

For MWC 560 the minimum brightness is V=10.2 (Tomov et al. 1996a) and the red giant is classified as M5.5 III (Schmid et al 2001). Using $(U\text{-}V)_{M5.5III}$=2.80 - 2.95 (Lee, 1980; Schmidt-Kaler 1982; Fluks 1994), we adopt a contribution of the red giant equivalent to U$\approx$ 13.0. It deserves noting that the calculated red giant contribution in MWC 560 and CH Cyg is considerably smaller than that in T CrB, which is in accordance with the fact that in these two objects the V band variability is dominated by the hot component (not by the red giant as in T CrB).

The flickering amplitude versus F_{av} for MWC 560 is plotted in Fig. 2.13 (lower panel). The correlation is not very significant ($r_P = 0.25$ $r_S = 0.27$ – although, if we delete 3 points with $\log \Delta F < 0.6$ we can obtain a moderate correlation up to $r_P \sim 0.4$).

During the time of these observations MWC 560 is in the process of jet ejection, and the jet is even precessing (Iijima 2002). The lack of significant correlation between the flickering amplitude and hot component flux probably is a result of the outflow, i.e. the jet ejection destroys the innermost parts of the accretion disk, where the flickering is formed.

The connection between the jet and flickering is not investigated in MWC 560, however it is visible in the 1997 jet launch in CH Cyg (Sokoloski & Kenyon 2003a). The disks and jets are also connected in quasars and microquasars (see Livio, Pringle & King 2003 and references therein). In this sense the fact that the correlation between Δ F and F_{av} is loose in MWC 560, is probably due to the outflow and its connection with the accretion disk.

2.3.4 Flickering amplitude and magnetic field

In all three symbiotic stars with available data the flickering amplitude shows the same tendency to increase with increases of the hot component flux. If we accept that there are no different states in CH Cyg and all points lay on the same line it means that the obtained value of the slope is very similar to T CrB, which in terms of the Bruch & Dushl (1993) model in turn means that in both stars the size of the boundary layer remains constant (see Sect. 2.3.2). In MWC 560 the flickering is (probably) influenced by the outflow and ΔF depends weakly on F_{av}, and the correlation is not well defined.

The other possibility that the flickering amplitude of CH Cyg lays on two parallel lines would give different values of k in the relationship $\Delta F \propto (F)^k$. One of the reasons for this difference could be the magnetic field of the WD. Here we want to point out that the flickering amplitude could be connected with the magnetic field. The most probable place for the origin of the flickering is the inner parts of the accretion disk. If the flickering is a result of the turbulence in the inner parts of the disk then the energy available in the turbulence will be proportional to the density where the flickering forms (Bruch, 1992). If the white dwarf is magnetic, the inner parts of the accretion disk will be destroyed by the magnetic field. Different instabilities can appear then at the inner edge of the disk. These instabilities permit the accreting material to be absorbed from the magnetosphere as blobs. The energy releasing will be unsteady and we suppose that the amplitude of the flickering will be proportional to the typical mass of the blobs, and the mass of the blobs will in turn be proportional to the density at the inner edge of the disk. The density in the disk can be estimated as (Lipunov 1992):

$$\rho_{in} \approx \alpha^{-1} \left(\frac{R}{H}\right) \frac{\dot{M}_a}{4\pi R^{3/2}\sqrt{2GM}}, \tag{2.9}$$

where (R/H) is the ratio between the radius and the vertical size of the disk, (R/H) is usually adopted to be a constant of order 0.01–0.1. M is the mass of the white dwarf.

If the white dwarf is non-magnetic, the inner radius of the disk will be approximately equal to the white dwarf radius (for a thin boundary layer) and consequently the density at the inner edge is given by $\rho_{in} \propto \dot{M}_a$. The same relationship will be fulfilled if the boundary layer is not thin and its size does not change. If the white dwarf is magnetic the radius R_0 of the inner disk edge may be expressed as (Lamb, Pethick & Pines 1973):

$$R_0 = N(GM)^{-1/7}\mu^{4/7}\dot{M}_a{}^{-2/7}, \tag{2.10}$$

where N is a constant of order 1, and μ is the white dwarf magnetic moment. In this case (from Eqn. 2.9 and 2.10)

$$\rho_{in} \propto \dot{M}_a^k, \quad k = \frac{10}{7} \tag{2.11}$$

where $k = \frac{10}{7} = 1.43$ is in agreement with the behaviour of CH Cyg (Mikołajewski et al., 1990, see also Sect. 2.3.3), if the suppositions (1) $\Delta F \propto \rho_{in}$, and (2) accretor-propeller states in CH Cyg (Mikołajewski et al. 1990) are correct.

The data for T CrB are consistent with $k = 1$ as expected for a low or non-magnetic white dwarf, i.e. the position of the inner edge of the accretion disk does not depend on the mass accretion rate.

The presence of a magnetic WD in CH Cyg is not a certain fact. Sokoloski & Kenyon (2002a), Crocker et al. (2001), Ezuka et al. (1998) threw doubts about the presence of such a magnetic WD in CH Cyg. However, the magnetic propeller model of (Mikołajewski & Mikołajewska, 1988) still remains the most promising for the variability of this object.

If the differences in the behaviour of the flickering in T CrB, CH Cyg, and MWC 560 are not connected with the magnetic field and jet ejection, other possible reasons may be the changes of the energy distribution, or different mechanisms generating the flickering in these objects.

Conclusions: We have analysed the U band variability of the recurrent nova and symbiotic star T CrB, and compared its behaviour with two other symbiotic stars CH Cyg and MWC 560. During the period of our observations T CrB brightness varies in between U=13 and U=10 mag. The analyses we performed show that: (1) the V brightness during the last 22 years is dominated by the ellipsoidal variability of the red giant, however the hot component variability with $\Delta U \gtrsim 2$ mag, introduces a shift in V with about 0.15 mag. No signs of variability of the red giant has been detected. (2) the power spectrum of the flickering does not change during our observations, remaining always with slope $\gamma \approx -1.5$ in spite of the changes in U. We do not detect changes in the power spectrum like those observed in CH Cyg; (3) The calculated e-folding time of the ACF also does not show dependence on the changes in U; (4) The flickering amplitude is strongly correlated with the average flux of the hot component. (5) The differences in the dependence of the flickering amplitude between T CrB, CH Cyg and MWC 560 could be connected with jet ejection and the possible presence of a magnetic white dwarf in the last two. In general, in T CrB, we have observed flickering, which does not change considerably its characteristics (at least during the time of our observations).

In the future it would be very interesting to determine the behaviour of the flickering amplitude, ACF, power spectra, etc. of other symbiotic stars with flickering (in particular RS Oph, RT Cru, *o* Ceti) as well as the flickering of MWC 560 during phases without outflow, as well the connection of flickering with jet precession. Simultaneous spectral and photometric observations over a wide spectral range from UV to IR could be very useful to investigate in detail the flickering behaviour and its connection with accretion disk instabilities and jet ejections.

2.4 Rerefences to Chapter 2

Adams, W. S. & Joy, A. H., 1921, PASP, 33, 263

Anupama, G. C. & Prabhu, T. P. 1991, MNRAS, 253, 605

Anupama, G. C. & Mikołajewska, J. 1999, A&A, 344, 177

Belczyński, K., Mikołajewska, J., Munari, U., et al. 2000, A&AS, 146, 407

Bianchini, A., & Middleditch, J., 1976, IBVS 1151

Bruch, A., 1980, IBVS 1805

Bruch, A. 1992, A&A, 266, 237

Bruch, A. 2000, A&A , 359, 998

Bruch, A. & Duschl, W. J. 1993, A&A, 275, 219

Crocker, M. M., Davis, R. J., Eyres, S. P. S., et al. 2001, MNRAS, 326, 781

Dobrzycka, D., Kenyon, S. J., & Milone, A. A. E. 1996, AJ, 111, 414

Ducati, J. R., Bevilacqua, C. M., Rembold, S. B., & Ribeiro, D., 2001, ApJ, 558, 309

Edelson, R. A. & Krolik, J. H., 1988, ApJ, 333, 646

Efron B., Tibshirani R.J., 1993, "An introduction to the Bootstrap",
Monographs on Statistics and applied Probability vol.57, Chapman & Hall, New York

Ezuka, H., Ishida, M., & Makino, F., 1998, ApJ, 499, 388

Fekel, F. C., Joyce, R. R., Hinkle, K. H., & Skrutskie, M. F. 2000, AJ, 119, 1375

Fluks, M. A., Plez, B., The, P. S., et al. 1994, A&AS, 105, 311

Fullerton, A. W., Gies, D. R., & Bolton, C. T. 1996, ApJS, 103, 475

Glass I. S., Schultheis M., 2002, MNRAS, 337, 519

Hessman, F. V. & Hopp, U. 1990, A&A, 228, 387

Hinkle, K. H., Fekel, F. C., Johnson, D. S., & Scharlach, W. W. G., 1993, AJ, 105, 1074

Hric, L., Petrik, K., Urban, Z., et al. 1998, A&A, 339, 449

Ianna, P.A., 1964, ApJ, 139, 780

Iijima, T. 1990, JAAVSO, 19, 28

Iijima, T. 2002, A&A 391, 617

Kamath, U. S. & Ashok, N. M. 1999, A&AS, 135, 199

Kirov N.K., Antov A.P., Genkov V.V., 1991, C.R. Acad.Bulg.Sci. 44, 5

Kraicheva, Z., Stanishev, V., Genkov, V., & Iliev, L., 1999, A&A, 351, 607

Lamb, F. K., Pethick, C. J., & Pines, D. 1973, ApJ, 184, 271

Lawrence, G. M., Ostriker, J. P., & Hesser, J. E. 1967, ApJ 148, L161

Le Borgne, J.-F., Bruzual, G., Pello, R., et al. 2003, A&A, 402, 433

Lee, T. A. 1970, ApJ, 162, 217

Lines, H. C., Lines, R. D., & McFaul, T. G., 1988, AJ, 95, 1505

Lipunov, V. M. 1992, Astrophysics of Neutron Stars, Berlin, New York : Springer-Verlag,

Livio, M., Pringle, J. E., & King, A. R. 2003, ApJ 593, 184

Long, K. S. & Knigge, C., 2002, ApJ, 579, 725

Mikołajewski, M. & Mikołajewska, J. 1988, in "The Symbiotic Phenomenon" (IAU Colloq. 103), ASSL Vol. 145, 233

Mikołajewski, M., Tomov, T. V., Kolev, D., & Leedjarv, L., 1996, IBVS 4368

Mikołajewski, M., Tomov, T., & Kolev, D. 1997, IBVS 4428

Mikołajewski, M., Mikołajewska, J., Tomov, T., et al. 1990, Acta Astronomica, 40, 129

Minkowski, R. 1943, PASP, 55, 101

Munari, U., Yudin, B. F., Kolotilov, E. A., & Tomov, T. V. 1996, A&A, 311, 484

Mürset, U. & Schmid, H. M. 1999, A&AS, 137, 473

Oskanian, A. V. 1983, IBVS 2349

Panek, R. J., 1980, ApJ, 241, 1077

Peel, M., 1985, JAAVSO, 14, 8

Pietrinferni, A., Cassisi, S., Salaris, M., Castelli, F., 2004, ApJ, 612, 168

Prinja, R. K., Knigge, C., Ringwald, F. A., & Wade, R. A. 2000a, MNRAS, 318, 368

Prinja, R. K., Ringwald, F. A., Wade, R. A., & Knigge, C. 2000b, MNRAS, 312, 316

Prinja, R. K., Long, K. S., Froning, C. S., et al. 2003, MNRAS, 340, 551

Raikova, D. & Antov, A., 1986, IBVS 2960

Ringwald, F. A. & Naylor, T. 1998, AJ, 115, 286

Robinson, E. L. & Nather, R. E., 1979, ApJS, 39, 461

Schmidt-Kaler, T. H. 1982, in Landolt-Brnstein, New Series, Group VI, Vol. 2b, "Stars and Star Clusters", K. Schaifers & H. H. Voigt (eds.), New York: Springer

Schmid, H. M., Kaufer, A., Camenzind, M., et al. 2001, A&A, 377, 206

Selvelli, P. L., Cassatella, A., & Gilmozzi, R., 1992, ApJ, 393, 289

Shahbaz T., Somers M., Yudin B., Naylor T., 1997, MNRAS 288, 1027

Skopal, A., Bode, M. F., Lloyd, H. M., & Drechsel, H., 1998, A&A, 331, 224

Sokoloski, J. L., Bildsten, L., & Ho, W. C. G. 2001, MNRAS, 326, 553

Sokoloski, J. L., 2003, ASP Conference Series, 303, p. 202

Sokoloski, J. L. & Kenyon, S. J. 2003a, ApJ 584, 1021

Sokoloski, J. L. & Kenyon, S. J. 2003b, ApJ 584, 1027

Stanishev, V., Zamanov, R., Tomov, N., & Marziani, P. 2004, A&A, 415, 609

Swings, P. & Struve, O., 1943, ApJ, 98, 91

Tomov, T., Kolev, D., Munari, U., Sostero, G., & Lepardo, A. 1995, A&A, 300, 769

Tomov, T., Kolev D., Ivanov M., et al. 1996a, A&AS 116, 1

Tomov, T., Kolev, D., Munari, U., & Antov, A. 1996b, MNRAS, 278, 542

Verbunt, F. 1982, Space Science Reviews, 32, 379

Vitello, P. & Shlosman, I., 1993, ApJ, 410, 815

Walker, A. R., 1977, MNRAS 179, 587

Warner, B. 1995, "Cataclysmic variable stars", Cambridge University Press

Witherick, D. K., Prinja, R. K., Howell, S. B., & Wagner, R. M. 2003, MNRAS, 346, 861

Yonehara, A., Mineshige, S., & Welsh, W. F., 1997, ApJ, 486, 388

Yudin, B. & Munari, U. 1993, A&A, 270, 165

Zamanov, R. K. & Bruch, A. 1998, A&A, 338, 988

Zamanov, R. & Marti, J. 2001, IBVS 5013

Zamanov, R. K., Bode, M.F., Stanishev, V, Martí, J., 2004, MNRAS, 350, 1477

Zhu, Z. X., Friedjung, M., Zhao, G. et al. 1999, A&AS, 140, 69

Chapter 3

Variability of the recurrent nova RS Oph

3.1 Emission line variability of RS Ophiuchi

We report that the Hα emission line of RS Oph was strongly variable during our 2004 observations on a time scale of 1 month. The line consisted of both a double peaked central narrow component (FWHM$\sim$220 km s^{-1}) and a strongly variable broad one (FWHM>2000 km s^{-1}). The base of the Hα line was very broad with FWZI$\approx$4600 km s^{-1} on all spectra from 1986 to 2004. The variability of the broad component extends from -2000 to $+2000$ km s^{-1}. Most probably this is due to either blobs ejected from the white dwarf (with a typical blob mass estimated to be $\sim10^{-10}$ M$_{\odot}$) or a variable accretion disk wind. We also detected variability of the HeIIλ4686 line on a time scale shorter than 1 day. The possible origin is discussed.

Introduction: RS Ophiuchi (HD 162214) is a recurrent nova which underwent its last major outburst in 2006 (see Bode 1987, Sokoloski et al 2008, and references therein). Following Dobrzycka & Kenyon (1994), RS Oph has a binary period of 460 days with orbital inclination to the line of sight of $30^0 - 40^0$, and spectroscopic ephemeris $T_0 = JD2444999.9 \pm 29.3 + 460 \pm 10E$. The mass donor is a red giant of spectral type K4-M0 (Mürset & Schmid 1999). The nature of the hot component is unclear. Most probably it is a massive white dwarf with M$_{WD}$ $\approx$1.4 M$_{\odot}$, accreting at $\dot{M} \geq 10^{-8}$M$_{\odot}$ yr^{-1} (Hachisu & Kato, 2000). Alternatively, it has been proposed to be a B-type shell star with highly variable luminosity, which occasionally displays blue-shifted absorption features (Dobrzycka et al. 1996).

Broad, variable, emission components of the hydrogen lines were detected by Iijima et al.

(1994), Anupama & Mikołajewska (1999), and Tomov (2003). Variability of the He lines on a time scale of hours was detected by Sokoloski (2003). The origin of these changes is a mystery. Here we report that similar variability is also evident in our 2004 observations and discuss its possible origin.

We secured 8 spectra in 2004 using the ESO, La Silla, 2.2m telescope and the FEROS spectrograph. FEROS is a fibre–fed echelle spectrograph, providing a resolution of $\lambda/\Delta\lambda$ =48000, wide wavelength coverage from about 4000 Å to 8000 Å in one exposure and a high detector efficiency (Kaufer et al. 1999).

Additionally, we retrieved 4 spectra covering the region of the Hα line from the archive of the Isaac Newton Group of telescopes (ING). A journal of observations and the measured quantities are given in Table 3.1.

3.1.1 Hα emission line variability

The variability of the Hα line is immediately apparent (see Fig. 3.1 and Table 3.1). There are changes in the blue and red peaks, as well as in the wings of the line. On all spectra the base of the Hα line is very wide, the mean full width at zero intensity $\overline{\mathrm{FWZI}} = 4650 \pm 300$ km s^{-1} and the mean equivalent width of the Hα emission line $\overline{\mathrm{W}} = 112 \pm 11$ Å, which is about $1{\times}10^{-11}$ erg cm^{-2} s^{-1}. The ratio of the intensity of the blue and red peaks (V/R) varies from 0.51 to 0.87. Our data suggest that the Hα profile of RS Oph is purely in emission and consists of both a double peaked central narrow component (W$\sim$90 Å, FWHM$\sim$200-250 km s^{-1}) and a strongly variable broad one (W$\sim$20 Å, FWHM>2000 km s^{-1}).

When the spectra are obtained in the same night or in consecutive nights, the Hα profiles are effectively identical. However, changes are visible when the time difference is $\sim$1 month. To explore in more detail the velocity structure of the variability of the wings, assuming that the variability arises purely from changes in emission, we subtracted at each epoch a minimum spectrum (artificially generated by taking the minimum value from all normalized spectra at a given wavelength). The residuals are plotted in Fig. 3.2b. As can be seen, the variability of the wings extends from -2000 to $+2000$ km s^{-1}, with the most prominent additional emission around -1200 and $+1200$ km s^{-1}. On each spectrum we measured the radial velocity of the additional emission, which has equivalent width W$\leq$7 Å. The data are given in Table 3.1 along with other parameters.

A variable broad component was not detected in RS Oph's sister system T CrB (see Stanishev et al. 2004; Zamanov et al. 2005). A similar component appeared however in the 1994

Table 3.1: Hα and HeIIλ4686 observations of RS Oph. In the table are given number, date of observation, Julian Day, orbital phase, the origin of the observations. In the lower part are printed number, radial velocity of the blue peak, central dip and red peak, full width at zero intensity (FWZI) of Hα, equivalent width of Hα, equivalent width of HeIIλ4686 , the ratio between intensities of the blue and red peak, the radial velocity of the additional emission (V_{emm}), and the origin of the spectrum. The typical errors are ±1 km s^{-1} for V_{blue}, V_{dip} and V_{red}, ±250 km s^{-1} for FWZI, ±5% for $W_{H\alpha}$, ±20% for W_{4686}, ±3% for the V/R ratio, and ±150 km s^{-1} for V_{emm}.

N:	Date	JD 2400000+	ϕ	origin
1	1986-07-12	46624.425	0.53	ING
2	1986-07-13	46625.486	0.53	ING
3	1997-08-06	50667.391	0.32	ING
4	1997-08-06	50667.398	0.32	ING
5	2004-04-11	53106.384	0.62	ESO
6	2004-04-11	53106.392	0.62	ESO
7	2004-06-05	53161.223	0.74	ESO
8	2004-06-05	53161.231	0.74	ESO
9	2004-06-06	53162.284	0.74	ESO
10	2004-06-06	53162.291	0.74	ESO
11	2004-08-31	53248.043	0.93	ESO
12	2004-08-31	53248.051	0.93	ESO

N:	V_{blue}	V_{dip} [km s^{-1}]	V_{red} [km s^{-1}]	FWZI [km s^{-1}]	$W_{H\alpha}$ [km s^{-1}]	W_{4686} [Å]	V/R [Å]	V_{emm} [km s^{-1}]
1				4750	106	—	0.51	+560:
2				4940	102	—	—	+740:
3				4390	—	—	—	−1270
4				4660	—	—	—	−1130
5	-87.4	-48.9	+3.3	4940	102	<0.1	0.74	−1440, +2065
6	-86.4	-47.9	+2.9	4980	104	<0.1	0.76	−1420, +2060
7	-92.8	-55.8	+0.7	4160	125	1.9	0.53	+1110
8	-92.8	-55.9	+2.0	4210	125	3.2	0.54	+1120
9	-90.7	-54.4	+2.4	4530	127	0.7	0.60	+1150
10	-89.8	-54.9	+2.9	4300	120	0.6	0.59	+1100
11	-91.0	-46.8	+2.9	4890	110	0.2	0.86	−1180, +1750
12	-91.2	-45.6	+4.7	4850	102	0.3	0.87	−1225, +1740

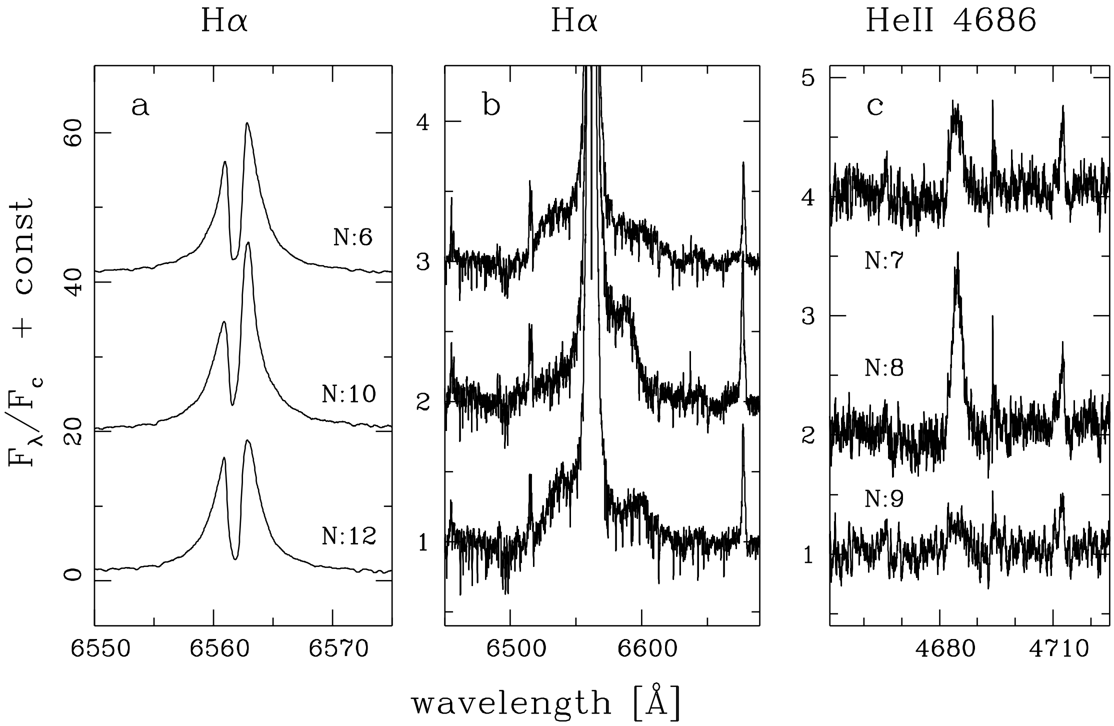

Figure 3.1: The Hα and the HeIIλ4686 emission lines of RS Oph (FEROS observations). The number against each spectrum refers to the epoch of observation as given in Table 1. All spectra are normalized to the local continuum.

a) The Hα central double peaked component with FWHM $\sim$5Å (220 km s^{-1}).

b) The same spectra as in a) but on different scales, so the Hα broad component is visible.

c) The HeIIλ4686 line. The spectrum N:8 was obtained 10 minutes after N:7, and N:9 - 24 hours later. These data demonstrate that the line is variable on a time scale $\leq$1 day.

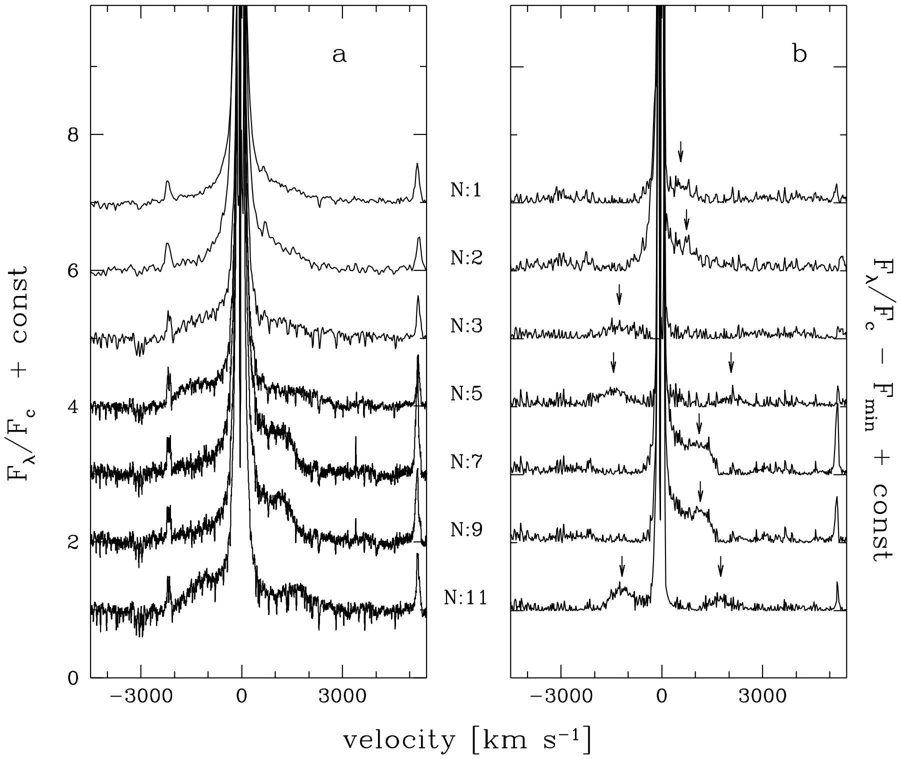

Figure 3.2: **a)** The RS Oph Hα profiles (normalized to the local continuum) for 7 different nights. The numbers again correspond to those in Table 3.1. **b)** After subtraction of the minimum spectrum, the additional emissions are visible as bumps with W$\leq$ 7 Å. The arrows indicate their measured radial velocities as given in Table 3.1.

observations of CH Cyg (Tomov et al., 1996) and the velocity range of $\pm$2000 km s^{-1}, was close to that of RS Oph. However, the time scale of appearance/disappearance was considerably shorter ($\sim$2 hours).

3.1.2 Time scale of HeIIλ4686 variability

Our spectra with numbers 7, 8 and 9 show that the HeIIλ4686 line is also variable (Fig. 3.1 and Table 3.1). The spectrum N:8 was obtained 10 minutes after N:7, and N:9 - 24 hours later. This suggests that the intensity of HeIIλ4686 changes on a time scale of minutes-hours (note that we did not detect Hα variability on such a short time scale).

The HeIIλ4686 line indicates high excitation conditions in the gas. In the case of RS Oph (see the next section) this can be related to a region located close to the boundary layer between the accretion disk and the white dwarf (Sokoloski 2003). The changes of the intensity of this line indicate changes in the region of its appearance which, in turn, is determined most probably by variable luminosity or/and temperature of the boundary layer.

3.1.3 Spectral variability of RS Oph

Our data suggest that the Hα profile of RS Oph is purely in emission and consists of both a double peaked central narrow component and a strongly variable broad one. The Balmer emission lines, appearing in the extended envelopes of symbiotic stars usually have an ordinary nebular profile with typical FWHM$\sim$100-150 km s^{-1}, for example AG Dra (Tomova & Tomov 1999). FWHM increases to 200 km s^{-1} only during the active phases. The basic mechanism determining their width is turbulence in the gas. The central narrow emission of RS Oph is very similar to the double peaked Hα line of T CrB and the two stars have practically the same FWHM of about 200-250 km s^{-1}. The Hα line of T CrB is supposed to be formed in the outer part of an accretion disk around the hot compact object (Stanishev et al. 2004). By analogy with this star we could assume that the narrow Hα component of RS Oph is formed also around its compact object. This assumption, however meets some difficulty with the fact that the peak of this component exceeds the level of the continuum by a factor of 20-25 like purely nebular lines of the symbiotic stars. This peak height differs from that one of T CrB, which exceeds the level of the continuum by a factor of 2-6 only.

While the appearance and the variability of the narrow component is relatively common in symbiotic stars (see also Ikeda & Tamura 2004 and the references therein), appearance and variability of broad component is detected in about 10 objects up to now. Fast ($\sim$1000 km s^{-1}) bipolar winds/jets were detected in Hen 3-1341 and StHα 190 (Tomov 2003). The jets in both systems appeared as satellite emission components on both sides of the strong HI Balmer and HeI emission lines, and they looked similar to the additional emission bumps in RS Oph (Fig. 3.2b). Similar profiles have been observed in the symbiotic nova RX Pup (Mikolajewska et al. 2002) and AR Pav (Quiroga et al. 2002).

At quiescence, the hot components of RS Oph and RX Pup show activity (high states) characterized by the appearance of B/A/F shell-type features and variable 'false atmosphere' together with the broad and complex emission lines and are related to the accretion flow/accretion-driven phenomena in these binaries. Other systems that show similar behaviour are CH Cyg and MWC 560 (Mikolajewska et al. 2002, 2003).

Here, we will consider three possible origins for the broad component in RS Oph:

(1) The first possible origin is related to ejection of blobs of matter. These blobs could be expelled by a rotating white dwarf magnetosphere (Tomov 2003 and references therein) or by a jet mechanism. The de-projected velocity of the ejection is ~1500-4000 km s^{-1}, having in mind V$_{emm}$ from Table 3.1 and assuming it is realized normal to the orbital plane, and also the orbital inclination is $30^0 - 40^0$. This velocity is practically the same as ejection velocities of up to 3800 km s^{-1}seen during the 1985 nova outburst (Bode 1987 and references therein).

(2) Variable disk winds with similar (to RS Oph and CH Cyg) velocities were detected in a few cataclysmic variables and the whole wind can even turn on and off. The terminal velocity of the wind in the BZ Cam system is v$_t$ ~3000 km s^{-1} and the time scale of the variability is 30-40 min (Ringwald & Naylor 1998). Indeed, their profiles bear a noticeable similarity to those in RS Oph at some epochs. For Q Cyg the terminal velocity is v$_t$ ~1500 km s^{-1} and the events last about 1.5 hours (Kafka et al. 2003). These time scales are similar to those of the Balmer line variability of CH Cyg but not to RS Oph. It is possible that the disk wind of RS Oph varies on longer time scales.

(3) If the variable broad component of RS Oph originates in an asymmetric disk, then a Keplerian velocity of 1000 km s^{-1} requires a distance from a 1.4 M$_\odot$ WD of about 2×10^{10} cm. At that distance the Keplerian period is 20 min, which is considerably different from the observed time scale of Hα variability of RS Oph.

All of the mechanisms considered are related to the loss of mass by the system. Whenever such mass-loss occurs, a question about its quantitative estimate arises. A quantitative estimate, however, is possible in those cases where the phenomenon can be related to some geometrical model. However, we have no geometrical model of loss of mass which can be related to the irregular form of the profile of the broad component. The velocity distribution of this line proposes movement of discrete regions (blobs of matter) in the emitting environment (Fig. 3.2). That is why we tried to obtain a rough estimate of the mass of one "average" blob on the basis of its emission and supposing that it is optically thin and has also a constant density within some limits. From Fig. 3.1b and Fig. 3.2, the luminous flux in Hα of such a blob is about 3×10^{-13} erg cm^{-2} s^{-1} (W≈ 3Å). This flux was corrected for interstellar reddening using E(B−V)=0.73 (Snijders 1987; Hachisu & Kato 2000, 2001) and the extinction law by Seaton (1979). A corrected flux of 1.602×10^{-12} erg cm^{-2} s^{-1} was obtained.

We will use a flux of 1.602×10^{-12} erg cm^{-2} s^{-1}, density of 10^8– 10^{10} cm^{-3} and electron temperature 20000 K, Bode (1987), gives $d = 1.6 \pm 0.3$ kpc from a variety of measures. If we adopt this distance, we obtain mass of the blob $M_{blob} \sim 2.7 \times 10^{-8} - 2.5 \times 10^{-10}$ M$_\odot$ (more details can be found in Zamanov et al. 2005, MNRAS, 363, L26)

One other estimate of the mass of the blobs can be obtained from the calculated mass accretion rate $\dot{M}_{acc} \approx 2.10^{-7} - 10^{-8}$ $M_\odot$. Assuming 1 blob per month and 10% of the mass accretion rate ejected in blobs, we calculate $M_{blob} \sim 2 \times 10^{-9} - 8 \times 10^{-11} M_\odot$ in agreement with the above estimate based on Hα emission.

Conclusions: We report that the Hα emission of RS Oph was strongly variable during our 2004 observations on time scales of ∼1 month. No variability was detected on time scales of ≤1 day. The line was always very wide at its base (FWZI≈4600 km s^{-1}) on all spectra from 1986 to 2004, consisting of narrow and broad emission components. Variable emission is detected at velocities up to ±2000 km s^{-1}. Most probably this variable emission is due to either blobs ejected from the white dwarf or a variable accretion disk wind. The approximate mass of one "average" ejected blob of matter, suggested by the variability of the broad emission component is 3.8×10^{-9}– 3.5×10^{-11} M$_\odot$. We also detected variability of HeIIλ4686 line on time scales <1 day. To understand more fully the nature of the emission line variability of RS Oph we need to acquire a set of spectra with time resolution from minutes to days.

3.2 Flickering of RS Ophiuchi

3.2.1 Disappearance of the flickering after the 2006 Outburst

In February 2006, the recurrent nova RS Oph has undergone its first outburst for this century. On February 14th, 2006 it reached $4\overset{m}{.}4$ (Narumi et al., 2006) and began to decline. In late May, the brightness of the star had already returned to its pre-outburst level of $V = 10\overset{m}{.}5$ - $11\overset{m}{.}5$ (see O'Brien et al., 2006, and AAVSO light curves for more details).

CCD photometry of this recurrent nova has been secured with the 120-cm telescope at Observatoire de Haute-Provence (France). With an 1024×1024 CCD, the field of view is 11.8×11.8 arcmin. Our aim was to investigate the variability on time scales from minutes to days after the 2006 recurrent nova outburst.

Our B, V, R (Johnson–Cousins) measurements are summarized in Table 3.2. As comparison stars we have used SAO 141899 (HD 162215, $V = 9.307, B = 10.513, R = 8.601$) and GSC 0509400061 (USNO 0825-11335145, $V = 11.494, B = 12.199, R = 11.040$). The reduction was done in a way similar to Chevalier & Ilovaisky (1991) using average extinction from June 2006. In order to search for rapid variability, we performed time-resolved differential CCD photometry in B band. This procedure involved the repeated measurement of RS Oph relative to our main comparison stars SAO 141899 and set of stars in the field. Each observational run consisted of a series of exposures in B band, with exposure time ~ 40 sec. In Table 3.3 we give the start of the run, its duration, number of the points obtained, the minimal and maximal value of B magnitude, the mean B magnitude, and the standard deviation ($\sigma_B = \sqrt{\frac{1}{(N-1)} \sum_i (B_i - \overline{B})^2}$) calculated from all points in the run. In Fig. 3.3 we plot time-resolved B magnitudes. The behaviour of σ_B for the stars in the field is illustrated in Fig. 3.4.

From Table 3.3 and Fig. 3.3, we derive upper limits of the variability: $\Delta B \leq 0.06$, and according to Table 3.2: $\Delta V \leq 0.035$, and $\Delta R \leq 0.02$. To the best of our knowledge, these are the first observations when the minute-to-day photometric variability of RS Oph in the optical is so low.

Our B band light curves (see Fig. 3.3 are considerably different from those obtained with similar setup between the 1985 and 2006 outbursts (examples of the flickering of RS Oph can be seen in Dobrzycka et al., 1996, and Sokoloski et al., 2001). The flickering of RS Oph is known since a long time. However, no systematic investigations of its properties have been made to date. The previous observations in B band (see Table 3.4), revealed strong variability on the minute-to-hour time scale.

Table 3.2: BVR magnitudes of RS Oph. Typical error of our measurement is ±0.015 mag.

Date of obs. yyyy/dd/mm	UT	JD 24.....	B	V	R
2006/06/06	22.92	53893.454	12.702	—	10.241
2006/06/09	0.53	53895.522	12.732	11.373	10.224
2006/06/09	2.02	53895.584	12.734	11.404	10.222
2006/06/09	23.99	53896.499	12.734	11.396	10.221
2006/06/10	23.44	53897.477	12.722	11.405	10.232
2006/06/11	1.73	53897.571	12.734	11.394	10.230

Table 3.3: Time-resolved B band photometry.

Date of obs. yyyy/mm/dd	UT-start h	length [h]	N_{pts}	B min/max	B mean	σ_B [mag]
2006/06/06	21.258	5.16	136	12.680/12.738	12.708	0.014
2006/06/08	20.704	5.28	144	12.680/12.730	12.706	0.011
2006/06/09	20.558	4.28	100	12.702/12.747	12.727	0.012
2006/06/10	23.515	2.47	66	12.710/12.745	12.730	0.008

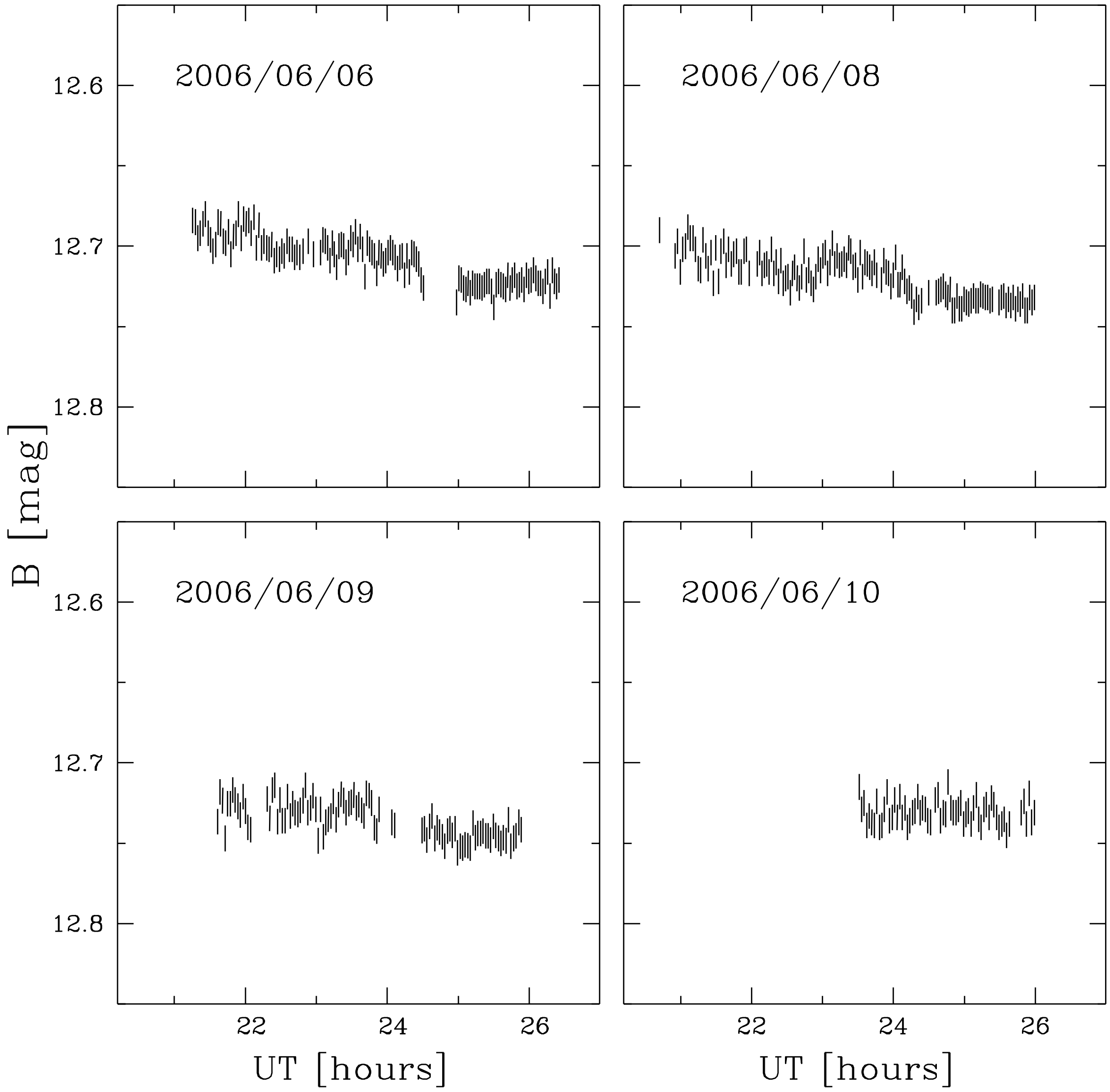

Figure 3.3: Time resolved CCD photometry of RS Oph obtained in June 2006 with the 120-cm telescope of OHP in B band. The date when the observation started is displayed in YYYY/MM/DD format. No short term variability (flickering) with total amplitude $\Delta B > 0.06$ mag has been detected on minute-to-hour time scale.

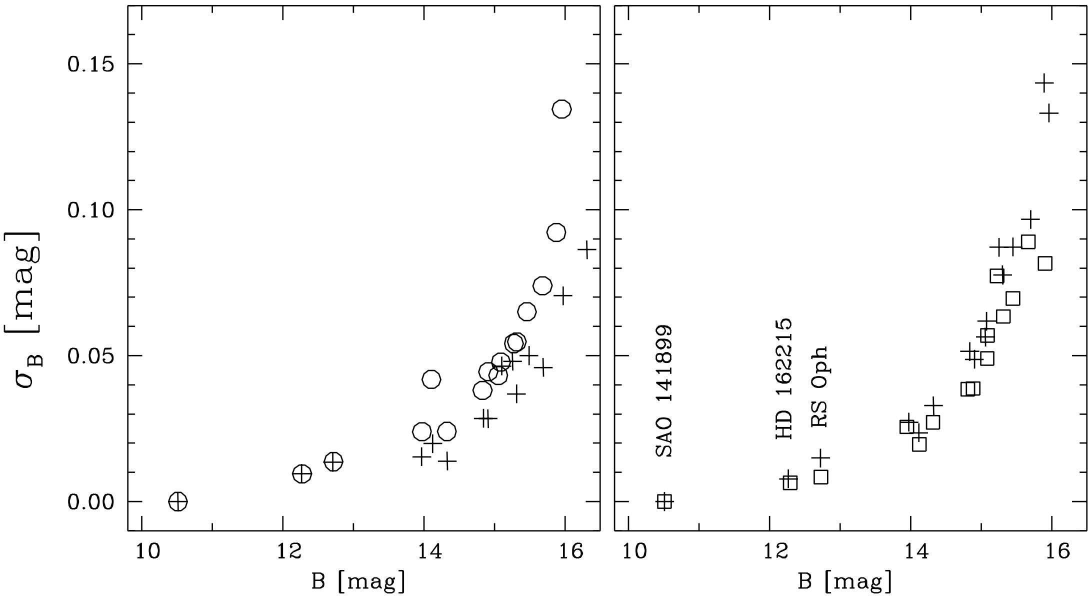

Figure 3.4: The standard deviation for the stars in the CCD field. Left panel: 2006/06/06 — crosses, 2006/06/08 — circles. Right panel: 2006/06/09 — crosses, 2006/06/10 — squares. The three brightest objects including RS Oph, are indicated on the right panel only. There is no clear departure of RS Oph from the behaviour expected for a star of constant brightness. SAO 141899 has been used as comparison star and its $\sigma_B \equiv 0$.

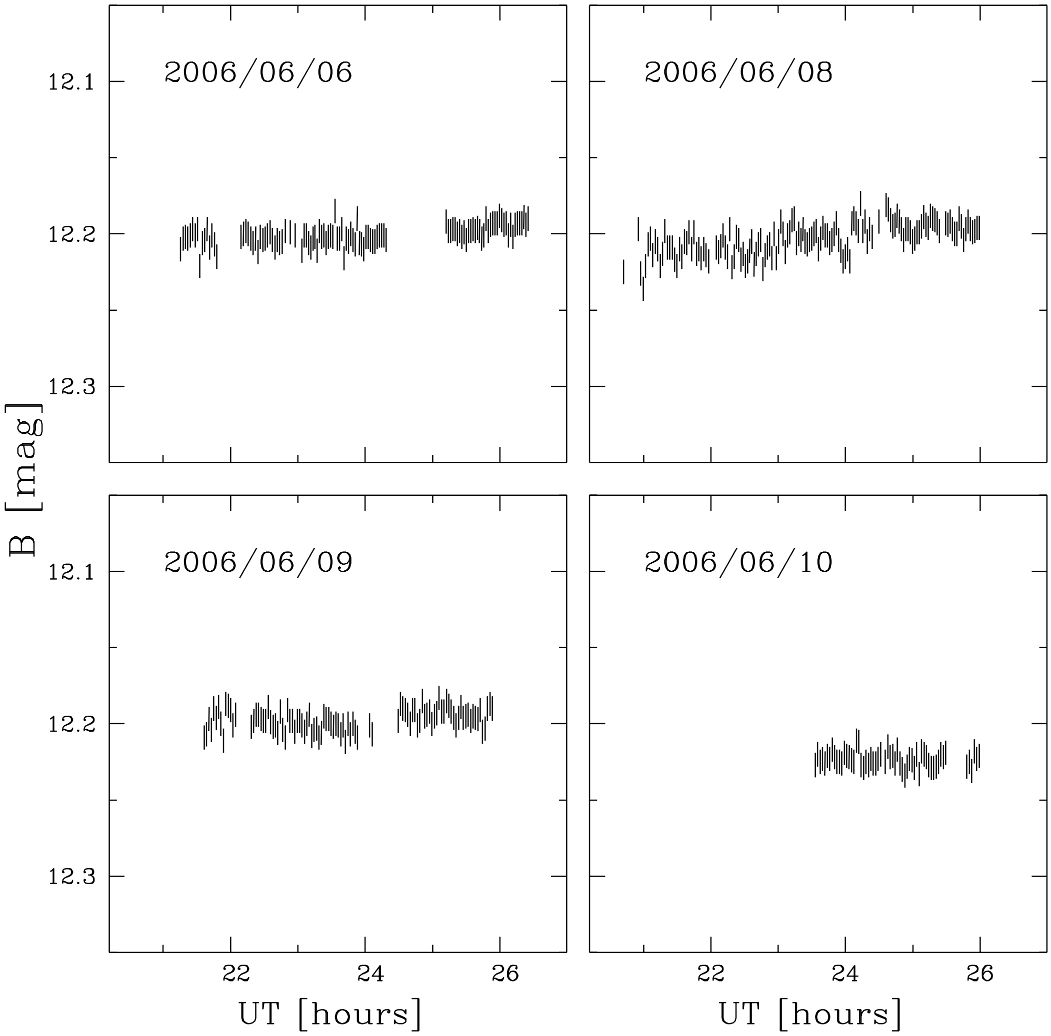

Figure 3.5: To illustrate the quality of our data, we plot the behaviour of the check star HD 162215 obtained in the same way as RS Oph's data.

Table 3.4: Observations of RS Oph in B band on minute-to-hour time scale. In the table are given the date of observations, the amplitude of the B band variability, σ_B, and the reference.

Date of obs. yyyy/mm/dd	ΔB [mag]	σ_B [mag]	Reference
1983/07/14	0.32	0.07	Bruch 1992
1983/07/18	0.38	0.06	Bruch 1992
1983/08/14	0.34	0.07	Bruch 1992
1993/06/06	0.19	0.07	Dobrzycka et al. 1996
1993/06/07	0.28	0.06	Dobrzycka et al. 1996
1993/06/09	0.24	0.05	Dobrzycka et al. 1996
1997/09/02	0.36		Sokoloski et al. 2001
2002/16/06	0.330	0.057	Gromadzki et al. 2006
2002/08/27	0.275	0.047	Gromadzki et al. 2006
2006/June	<0.05	<0.020	Zamanov et al. 2006
2008/07/06	0.23	0.051	Zamanov et al. 2010
2009/07/21	0.40	0.098	Zamanov et al. 2010
2009/07/23	0.24	0.062	Zamanov et al. 2010

Usually, the variability of RS Oph on flickering time scale has an amplitude of $\Delta B \sim 0.20 - 0.35$ magnitudes and typical $\sigma_B \sim 0.05 - 0.07$ magnitudes. During our June 2006 observations, we did not detect such a variability. On the panels for 2006/06/06 and 2006/06/08 in Fig. 3.3, one can see fading of RS Oph with $0\overset{m}{.}05$ during both nights. Our experiments have shown that this trend is probably real, although part of it can be due to the extinction. Is this fading real or not does not change our main result that the flickering of RS Oph is absent.

The disappearance of the flickering of RS Oph indicates that the accretion disk around the white dwarf has been demolished by the 2006 outburst. We can compute the approximate time to rebuild it, as the time needed the matter to cross the accretion disk (viscous time scale). An estimation of this time is $\Delta t = 2(R/H)^2 R^{3/2}/3\alpha\sqrt{GM}$, where R is the outer radius of the accretion disk, and M is the white dwarf mass. For a typical Shakura–Sunyaev accretion disk, we can use $\alpha \approx 0.1$–0.2, $(R/H) \approx 10$. Using parameters appropriate for RS Oph, $R \approx 10$–20 $R_\odot$, $M \approx 1.4\ M_\odot$, we derive $\Delta t \sim 160$–800 days.

Our estimate appeared good and Worters et al. (2007) observed resumption of the mass accretion and re-appearence of the optical flickering by the day 241 after the outburst.

3.2.2 Simultaneous UBVRI observations of the flickering of RS Oph

Abstract: We report observations of the flickering variability of the recurrent nova RS Oph at quiescence on the basis of simultaneous observations with 4 telescopes in 5 bands (UBVRI). RS Oph has flickering source with $(U\text{-}B)_0 \approx -0.70$, $(B\text{-}V)_0 \approx 0.16$, $(V\text{-}R)_0 \approx 0.22$.

Using a distance of d=1.6 kpc, we find for the flickering source a temperature $T_{eff} \approx 9500 \pm 500$ K, and luminosity $L_{fl} \sim 50\ L_{\odot}$.

We find that on a (U-B) vs (B-V) diagram the flickering of the symbiotic recurrent novae T CrB and RS Oph differs from that of the cataclysmic variables. The possible source of the flickering is discussed.

Introduction: In the symbiotic recurrent nova RS Ophiuchi (HD 162214), a near-Chandrasekhar-mass white dwarf (WD) accretes material from a red giant companion (e.g., Hachisu & Kato 2001; Sokoloski et al. 2006). It experiences nova eruptions approximately every 20 yr (Evans et al. 2008), with the most recent eruption having occurred on 2006 February 12 (Narumi et al. 2006). Fekel et al. (2000) found that RS Oph has an orbital period of 455 days and give red giant and white dwarf (WD) masses of 2.3 $M_{\odot}$ and close to 1.4 $M_{\odot}$ respectively with a separation between the components of a $= 2.68 \times 10^{13}$ cm. For the range of spectral types suggested (Worters et al. 2007) for the red giant in the RS Oph system, its radius is smaller than its Roche lobe, and accretion onto the WD may occur only from the red giant wind.

The flickering (stochastic light variations on timescale of a few minutes with amplitude a few 0.1 magnitudes) is a variability observed in the three main types of binaries that contain white dwarfs accreting material from a companion mass-donor star: cataclysmic variables (CVs), supersoft X-ray binaries, and symbiotic stars. Among ~ 200 symbiotic stars known, only 8 present flickering – RS Oph, T CrB, MWC 560, Z And, V2116 Oph, CH Cyg, RT Cru, o Cet and V407 Cyg (Belczyński et al. 2000, and references therein).

Here we investigate the flickering variability of RS Oph un the UBVRI bands and discuss its possible origin.

Observations: On the night of 2008 July 6, we observed RS Oph simultaneously with four telescopes equipped with CCD cameras. The 2m RCC telescope of the National Astronomical Observatory Rozhen equipped with a dual channel focal reducer observed in U and V bands. In the V band Photometrics CCD (1024x1024 px, pixel size 24μm, 0.89"/pixel) has been used, and in the U band a VersArray 1330B (1340x1300, 24μm, 0.89"/pixel). The 60 cm Rozhen telescope observed in the R band (equipped with a FLI PL09000 CCD with 3056 x 3056 pixels and

Table 3.5: CCD observations of RS Oph on 2008 July 6. In the table are given as follows the telescope, band, UT-start and UT-end of the run, exposure time, number of CCD images obtained, average magnitude in the corresponding band, minimum – maximum magnitudes in each band, standard deviation of the mean, typical observational error.

telescope	band	UT start-end	Exp-time [sec]	N_{pts}
2.0m Rozhen	U	19:27 - 21:26	300	20
50/70 Schmid	B	19:46 - 21:29	100,60,20	50
2.0m Rozhen	V	18:54 - 21:29	30	148
60cm Rozhen	R	19:36 - 21:33	15,20	301
60cm Belogr	I	19:42 - 21:22	60	74

band	average [mag]	min-max [mag]-[mag]	stdev [mag]	err [mag]
U	12.546	12.293 – 12.721	0.103	0.011
B	12.471	12.380 – 12.615	0.051	0.005
V	11.215	11.079 – 11.333	0.052	0.007
R	10.277	10.172 – 10.362	0.036	0.002
I	8.990	8.855 – 9.098	0.057	0.100

0.34"/pixel); the 50/70 cm Schmidt telescope of NAO Rozhen in the B band (SBIG STL11000M CCD, 4008x2672 px, 1.1"/pixel), and the 60 cm telescope of the Belogradchick Astronomical Observatory in the I band (SBIG ST8 CCD, 1530x1020px, 9μm, 3x3 binned 0.75"/pixel).

All the CCD images have been bias subtracted, flat fielded, and standard aperture photometry has been performed. The data reduction and aperture photometry are done with IRAF and have been checked with alternative software packages. The comparison stars of Henden and Munari (2006) have been used.

The results of our observations are summarized in Table 3.5 and plotted in Fig.3.6. For each run we measure the minimum, maximum, and average brightness in the corresponding band, plus the standard deviation of the run.

Our I-band data from 2008 July 6 have considerably larger observational errors due to a technical problem which gave as a consequence a variable dark current pattern of the CCD. They are therefore not used in the black body fits nor plotted in Fig.3.8.

Colour variations and colours of the flickering source

As can be seen in Fig.3.6 and Table 3.5, during our observations RS Oph exhibited variability on a time scale of 1-30 minutes with amplitude 0.19 mag (in R). The amplitude increases to shorter wavelengths up to 0.42 mag (in U).

Magnitude - Colour relation: In Fig.3.7 we plot the colours of RS Oph versus the R band magnitude. The R band is chosen because we have the shortest exposure time. The colours have been calculated over a grid with time resolution 1 minute. Linear fit (of type y=a+bx) to the data points in Fig. 3.7 give:

$$(U-R) = -8.00(\pm0.89) + 1.00(\pm0.09)R \tag{3.1}$$

$$(B-R) = -4.41(\pm1.07) + 0.64(\pm0.10)R \tag{3.2}$$

$$(V-R) = -0.79(\pm0.82) + 0.17(\pm0.08)R \tag{3.3}$$

$$\tag{3.4}$$

The errors of the coefficients are given in brackets. They are valid over the range $10.20 \leq R \leq 10.35$ mag. The Spearman's (rho) rank correlation gives $\rho = 0.85$ (significance 8.10^{-6}) for Eq.1, $\rho = 0.66$ (1.10^{-7}) for Eq.2, $\rho = 0.57$ (2.10^{-10}) for Eq.3. The significance in Eq.1-Eq.3 is always $<< 0.001$ indicating that all these correlations are highly significant and changes in the colours of RS Oph are correlated with brightness variations.

UBVRI colours of the flickering source: Bruch (1992) proposed that the light curve of CVs can be separated into two parts – constant light and flickering light source. In this

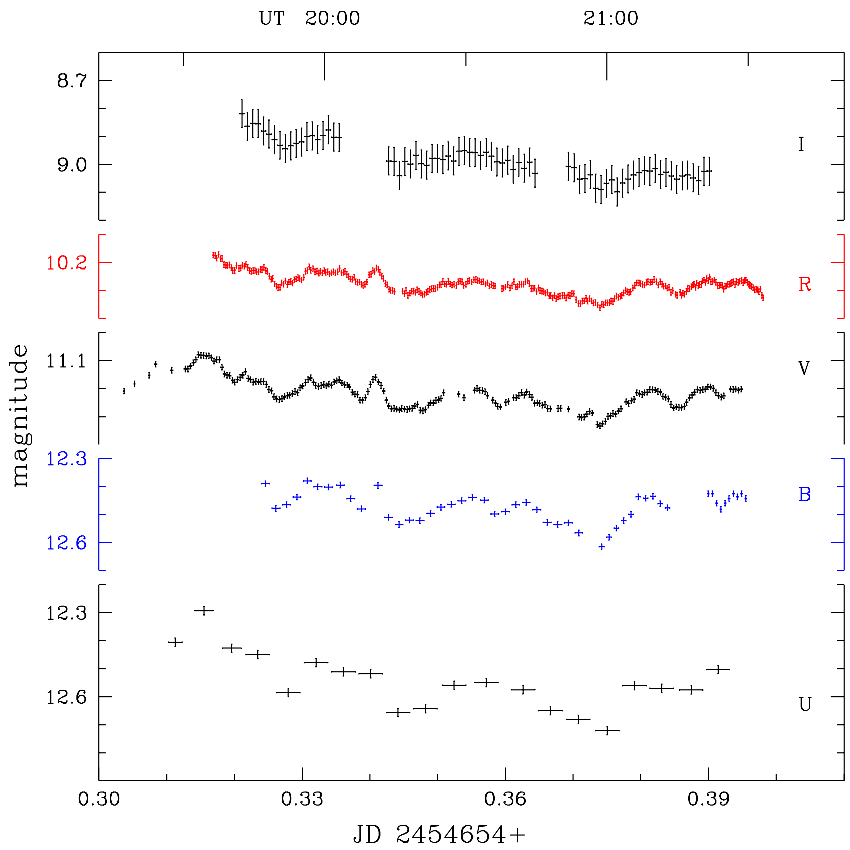

Figure 3.6: Variability of RS Oph in the UBVRI bands on 2008 July 6.

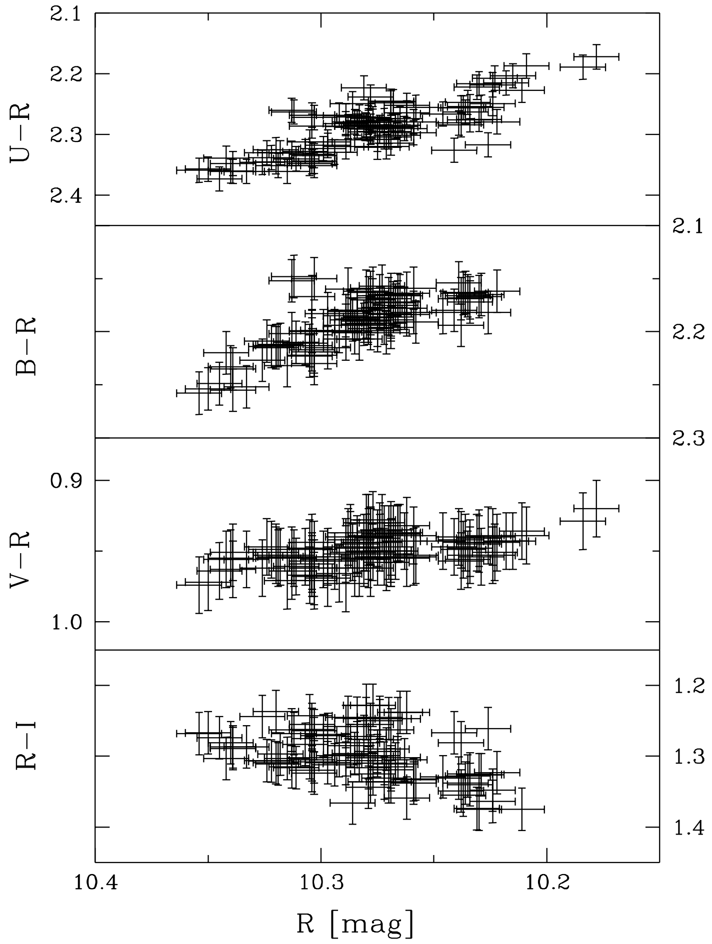

Figure 3.7: (U-R), (B-R), (V-R), and (R-I) colours of RS Oph versus R band magnitude.

supposition the flickering light source is considered 100% modulated. Following this suggestion, we calculate the flux of the flickering light source as $F_{fl} = F_{av} - F_{min}$, where F_{av} is the average flux during the run and F_{min} is the minimum flux during the run (corrected for the typical error of the observations). F_{fl} has been calculated for each band, using the values given in Table 1 and Bessel (1979) calibration for the fluxes of a zero magnitude star.

Adopting these results, we find that the flickering light source contributes about 6% of the light in the R band, 7% in V, 10% in B, and 13% in U. In other words:
Lfl/Ltot (R) =0.06
Lfl/Ltot (V) =0.07
Lfl/Ltot (B) =0.10
Lfl/Ltot (U) =0.13.

Following Snijders (1987) we assume interstellar extinction E(B-V)=0.73 ($A_V = 3.18$) and an extinction law as given in Zombeck (1990). On the basis of our observations, using each band as an independent light curve, we obtain colours of the flickering light source in RS Oph $(U-B)_0 = -0.61 \pm 0.05$, $(B-V)_0 = 0.11 \pm 0.05$, and $(V-R)_0 = 0.11 \pm 0.05$.

Using the colour relations in the interval R=10.23–10.35 mag, we obtain colours of the flickering light source in RS Oph $(\text{U-B})_0 = -0.69 \pm 0.03$, $(\text{B-V})_0 = 0.16 \pm 0.03$, $(\text{V-R})_0 = 0.22 \pm 0.21$.

These values are similar to the colours of the flickering source in 1983 July-August $(\text{U-B})_0 = -0.71$ and $(\text{B-V})_0 = 0.07 - 0.11$ (Bruch 1992).

3.2.3 Temperature and size of the flickering source

The derived $(U-B)_0$ colour corresponds to a B4V star ($T_{eff} \approx 17000$ K) and a black body with $T \approx 9000$ K. The $(B-V)_0$ colour corresponds to an A5V ($T_{eff} \approx 9000$ K) star and a black body with $T \approx 10000$ K. $(V-R)_0$ corresponds to a F8V star ($T_{eff} = 7000$ K). These estimates give an approximate temperature of the flickering light source $T_{fl} = 9000 - 12000$ K.

For the flickering light source we obtain magnitudes (corrected for interstellar extinction): 2008 July 6 : $U = 11.40$, $B = 12.06$, $V = 11.92$, $R = 11.55$ mag. In Fig.3.8c we plot all points normalized to the corresponding V band. The fit gives $T_{fl} = 9236 \pm 200$ K;

We adopt $d = 1.6 \pm 0.3$ kpc as given in Bode (1987). In Fig.3.8 we plot these magnitudes transformed to fluxes. Using a black body fit ($nfit1d$ routine of IRAF), we calculate for the flickering light source: $T_{fl} = 9492 \pm 300$ K; $R_{fl} = 2.6 \pm 0.3$ $R_\odot$; $L_{fl} \sim 50$ $L_\odot$.

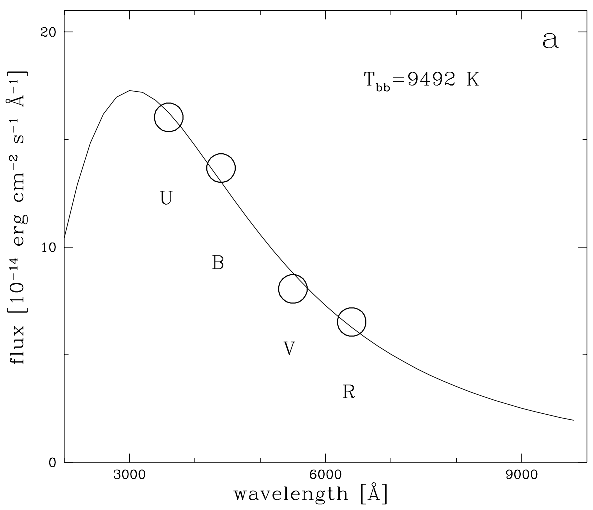

Figure 3.8: Dereddened fluxes of the flickering light source of RS Oph obtained on 2008 July 6. The solid line represents a black body fit with $T_{bb} = 9492$ K, radius $R = 2.6$ R$_\odot$, located at distance $d = 1.6$ kpc.

There are several different estimates of the mass accretion rate in RS Oph. An estimate of $\dot{M}_{acc} \approx 2.10^{-7} M_\odot$ yr^{-1} arises from the required mass accreted on to the WD to give rise to the outburst plus the latest inter-outburst time scale of 21 years (Osborne et al. 2011). Assuming $R_{WD} = 0.003$ R$_\odot$ (Starrfield et al. 1991), this results in a total accretion luminosity $L_{acc} \approx GM_{wd}\dot{M}/R_{wd} \approx 2900$ L$_\odot$. Alternatively, Walder et al. (2008) explore the hydrodynamics of wind accretion in the system and find $\dot{M}_{acc} \approx 10^{-8}$ $M_\odot$ yr^{-1}, i.e. $L_{acc} \approx 146$ L$_\odot$ (which compares to $L_{acc} \approx 190 - 740$ L$_\odot$ from IUE observations at quiescence - Snijders 1987). The spectral energy distribution of the accretion disk around the WD is similar to mid-B spectral type (Dobrzycka et al. 1996) with luminosity $100 - 600$ L$_\odot$. In practice therefore, the different estimates give $L_{acc} \sim 140 - 2800$ L$_\odot$, which means that 5%-35% of the total accretion luminosity is emitted by the flickering source (in other words $L_{fl}/L_{acc} \sim 0.05 - 0.35$).

3.3 Difference between symbiotics and CVs?

To search for difference between the flickering of symbiotic stars and CVs we performed a two-dimensional Kolmogorov-Smirnov test (Peacock 1983; Fasano & Franceschini 1987), using the data plotted on Fig.3.9. We compare colours of the flickering of the symbiotics RS Oph and

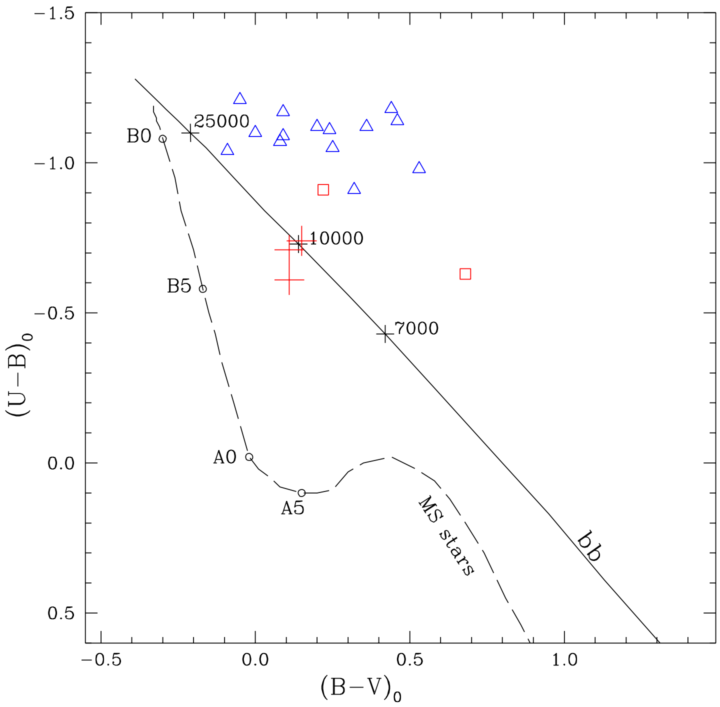

Figure 3.9: Position of the flickering light source on a (U-B) vs (B-V) diagram. The dashed line is the main sequence. The solid line is a black body, triangles - CVs (from Bruch 1992), squares - T CrB (from Bruch 1992), RS Oph is marked with red plus symbols.

T CrB with those of the CVs. The test gives a probability of 2.10^{-3} that both distribution are extracted from the same parent population. The number of points is not high, but sufficient, as shown in Fasano & Franceschini (1987), and the difference is significant. This result indicates that in this diagram there are clues to the cause of the differences between the flickering of these two classes of accreting white dwarfs.

In T CrB accretion is via L_1, but in RS Oph possibly via a stellar wind. In both stars the mass donor is red giant and the orbital periods are > 100 d. In the CVs the mass donors are late-type dwarfs and the orbital periods are ~ 1000 times shorter. To the best of our knowledge this is the first evidence that flickering differs in these two types of accreting WDs.

Origin of the flickering: Different sites for the origin of the flickering have been discussed. They are all related to the accretion process. One possible site for the origin of the flickering in RS Oph is the boundary layer between the white dwarf and accretion disk. Bruch & Duschl (1993) estimated the size of the boundary layer in RS Oph $\epsilon = 2.20$. In their model L_d/L_{bl} is connected with the size of the boundary layer (L_d is the the luminosity of the accretion disk, L_{bl} is the luminosity of the boundary layer; see Fig 1 in Bruch & Duschl 1993). If we assume $L_d + L_{bl} \approx L_{acc} \approx 110 - 2000$ L$_\odot$, and $L_{bl} \approx L_{fl} \approx 50$ L$_\odot$, then we calculate $L_d/L_{bl} = 1.2 - 40$, and the lower value agrees with the size of the boundary layer $\epsilon \sim 2$. However, the temperature of the flickering light source as derived in Sect. 3.2.3 is too low for a boundary layer.

The findings of Bruch (2000) for HT Cas, V2051 Oph, IP Peg and UX UMa demonstrated that the flickering in these CVs can originate in two regions: the innermost accretion disk with the boundary layer and the white dwarf surface, and the region of impact of the stream of transferred matter from the secondary star on the accretion disk (the bright spot).

The temperature and the size of the bright spot are derived for a number of CVs. A few examples are: (1) For OY Car Wood et al (1989) calculated black body $T = 13800 \pm 1300$ K, and color temperature T=9000 K; (2) Marsh (1988) for IP Peg - T = 11200 K; (3) Zhang & Robinson (1987) for U Gem - T $= 11600 \pm 500K$; (4) Robinson et al. (1978) give T=16000 K for the bright spot in WZ Sge;

The temperature of the flickering source of RS Oph T$_{fl}$ is similar to the temperature of the bright spot for the CVs. The mass transfer in RS Oph may not be from Roche lobe overflow (as in CVs), but via stellar wind accretion. As a result of the supersonic motion of the WD through the red giant wind there should be a shock cone and an accretion wake. Likely around the WD, an accretion disk and/or a cocoon is formed. In the place where the matter flowing through the accretion wake encounters the accretion disk/cocoon could be formed a bright spot (analogous to the bright spot formed in the case of CVs, where the mass flow from the inner Lagrangian point encounters the accretion disk).

For UU Aqr, Baptista & Bortoletto (2008) found no evidence of flickering generated in these regions. They suggested that the flickering in UU Aqr is caused by turbulence generated after the collision of disk gas with the density-enhanced spiral wave in the accretion disk.

The radial temperature profile of a steady-state accretion disk is:

$$T_{eff}^4 = \frac{3G\dot{M}_a M_{wd}}{8\pi\sigma R^3}\left[1 - \left(\frac{R_{wd}}{R}\right)^{1/2}\right] \tag{3.5}$$

Using the parameters for RS Oph, a temperature T_{fl} ~9500 K (the temperature of the flickering light source as derived in Sect. 3.2.3) should be achieved at distance R $\approx 0.5 - 1$ R$_\odot$ from the WD. This is one other site where the flickering can be produced.

After the 2006 outburst the flickering of RS Oph disappeared probably as a result of (1) destruction of the accretion disk from the nova explosion (Zamanov et al. 2006) or (2) a change in the inner disk associated with jet production (Sokoloski et al. 2008). The flickering resumed by day 241 of the outburst (Worters et al. 2007).

For the symbiotic star CH Cyg, Sokoloski & Kenyon (2003) obseved that approximately 1 yr after the jet production in 1997, the amplitude of the fastest (timescale of minutes) variations was significantly reduced, although smooth, hour-timescale variations were still present. It was proposed that the inner disk may have been disrupted, or emission from this region suppressed, in association with the mass ejection event. Observations of CH Cyg and RS Oph therefore indicate that a connection does exist between the flickering behaviour and the ejection of matter from the WD.

To understand more fully the nature of the flickering variability of RS Oph we need to acquire a set of spectra simultaneously with photometry and with time resolution ~ 30 seconds. Such spectra potentially can directly give the spectrum of the flickering light source.

Conclusions: We report our CCD observations of the flickering variability of the recurrent nova RS Oph, simultaneously with 4 telescopes in UBVRI bands. RS Oph has flickering source with $(U\text{-}B)_0 = -0.69 \pm 0.03$, $(B\text{-}V)_0 = 0.16 \pm 0.03$, $(V\text{-}R)_0 = 0.22 \pm 0.03$. For the flickering light source in RS Oph (1) we estimate $T_{eff} \approx 9500 \pm 500$ K, which is similar to the temperature of the bright spot in CVs; (2) using a distance of d=1.6 kpc, we find size $R_{fl} \approx 2.6 \pm 0.3$ $R_\odot$, and luminosity $L_{fl} \sim 50 \pm 10$ $L_\odot$.

We find clues that on (U-B) vs (B-V) diagram the flickering of the symbiotics T CrB and RS Oph differ from the flickering of the cataclysmic variables.

3.4 References to Chapter 3

Anupama, G. C., & Mikołajewska, J. 1999, A&A, 344, 177

Baptista, R., & Bortoletto, A. 2008, ApJ, 676, 1240

Belczyński, K., Mikołajewska, J., Munari, U., et al. 2000, A&AS, 146, 407

Bessell, M. S. 1979, PASP, 91, 589

Bode, M. F. (ed.) 1987, "RS Ophiuchi (1985) and the Recurrent Nova Phenomenon", VNU Science Press, Utrecht

Bruch, A. 1992, A&A, 266, 237

Bruch, A. 2000, A&A, 359, 998

Bruch, A., & Duschl, W. J. 1993, A&A, 275, 219

Chevalier, C., Ilovaisky, S.A., 1991, A&AS, 90, 225

Dobrzycka, D., & Kenyon, S. J. 1994, AJ, 108, 2259

Dobrzycka, D., Kenyon, S. J., Proga, D., et al. 1996, AJ, 111, 2090

Dobrzycka, D., Kenyon, S.J., Milone, A.A.E., 1996, AJ, 111, 414

Evans, A., Bode, M.F., O'Brien, T.J., & Darnley, M.J. (eds.) 2008, "RS Ophiuchi (2006) and the Recurrent Nova Phenomenon", ASP Conf., 401

Fasano, G., & Franceschini, A. 1987, MNRAS, 225, 155

Fekel, F. C., Joyce, R. R., Hinkle, K. H., & Skrutskie, M. F. 2000, AJ, 119, 1375

Gromadzki, M., Mikolajewski, M., Tomov, T., et al. 2006, Acta Astronomica, 56, 97

Hachisu, I., & Kato, M. 2000, ApJ, 536, L93

Hachisu, I., & Kato, M. 2001, ApJ, 558, 323

Henden, A., & Munari, U. 2006, A&A, 458, 339

Ikeda, Y., & Tamura, S. 2004, PASJ, 56, 353

Kafka, S., Tappert, C., Honeycutt, R. K., & Bianchini, A. 2003, AJ, 126, 1472

Kaufer, A., Stahl, O., Tubbesing, S., et al. 1999, The Messenger, 95, 8

Marsh, T. R. 1988, MNRAS, 231, 1117

Mikolajewska, J., Brandi, E., Garcia, L.,et al. 2002, AIP Conf. Proc. 637, 42

Mikołajewska, J. 2003, ASP Conf., 303, 9

Mürset, U., & Schmid, H. M. 1999, A&AS, 137, 473

Narumi, H., Hirosawa, K., Kanai, K., et al. 2006, IAU Circ, 8671, 2

Nussbaumer, H., & Vogel, M., 1987, A&A, 182, 51

O'Brien, T.J., Bode, M.F., Porcas, R.W., et al., 2006, *Nature*, 442, 279

Osborne, J. P., Page, K. L., Beardmore, A. P. et al. 2011, ApJ, 727, 124O

Peacock J. A., 1983, MNRAS, 202, 615

Quiroga, C., Mikołajewska, J., Brandi, E., et al. 2002, A&A, 387, 139

Robinson, E. L., Nather, R. E., & Patterson, J. 1978, ApJ, 219, 168

Ringwald, F. A., & Naylor, T., 1998, AJ, 115, 286

Seaton, M. J. 1979, MNRAS, 187, 73p

Snijders, M.A.J. 1987, in "RS Ophiuchi (1985) and the Recurrent Nova Phenomenon", M.F. Bode (ed.), VNU Science Press, p. 51

Sokoloski, J. L., Bildsten, L., & Ho, W. C. G. 2001, MNRAS, 326, 553

Sokoloski, J. L., 2003, Astronomical Society of the Pacific Conference Series, 303, p. 202

Sokoloski, J. L., Bildsten, L., & Ho, W. C. G. 2001, MNRAS, 326, 553

Sokoloski, J. L., & Kenyon, S. J. 2003, ApJ, 584, 1021

Sokoloski, J. L., Luna, G. J. M., Mukai, K., & Kenyon, S. J. 2006, Nature, 442, 276

Sokoloski, J. L., Rupen, M. P., & Mioduszewski, A. J. 2008, ApJ, 685, L137

Stanishev, V., Zamanov, R., Tomov, N., & Marziani, P. 2004, A&A, 415, 609

Starrfield, S., Truran, J.W., Sparks, W.M., & Krautter, J. 1991, in "Extreme Ultraviolet Astronomy", R. Malina & S. Bowyer (eds.), Pergamon Press, 168

Storey, P., & Hummer, D., 1995, MNRAS, 272, 41

Tomov, T., Kolev, D., Munari, U., & Antov, A. 1996, MNRAS, 278, 542

Tomov, T., 2003, ASP Conf., 303, p.376

Tomova, M. T., & Tomov, N. A. 1999, A&A, 347, 151

Vogel, M., 1993, A&A, 274, L21

Vogel, M., & Nussbaumer, H., 1994, A&A, 284, 145

Walder, R., Folini, D., & Shore, S. N. 2008, A&A, 484, L9

Wood, J. H., Horne, K., Berriman, G., & Wade, R. A. 1989, ApJ, 341, 974

Worters, H. L., Eyres, S. P. S., Bromage, G. E., & Osborne, J. P. 2007, MNRAS, 379, 1557

Zamanov, R., Gomboc, A., Bode, M. F., et al. 2005, PASP, 117, 268

Zamanov, R. K., Bode, M. F., Tomov, N. A., & Porter, J. M. 2005, MNRAS, 363, L26

Zamanov, R., Boer, M., Le Coroller, H., & Panov, K. 2006, IBVS, 5733

Zhang, E.-H., & Robinson, E. L. 1987, ApJ, 321, 813

Zombeck M., 1990, "Handbook of Space Astronomy and Astrophysics", 2nd edition, Cambridge University Press (1990)

Chapter 4

Rotational velocities of the mass donors in symbiotic stars

Introduction The Symbiotic stars (SSs – thought to comprise a white dwarf (WD) accreting from a cool giant or Mira) represent the extremum of the interacting binary star classification. They offer a unique and exciting laboratory in which to study such important processes as (i) mass loss from cool giants and the formation of Planetary Nebulae; (ii) accretion onto compact objects, (iii) photoionisation and radiative transfer in gaseous nebulae, and (iv) nonrelativistic jets and bipolar outflows (i.e. Kenyon 1986; Corradi et al. 2003).

Soker (2002) has shown theoretically that the cool companions in symbiotic systems are likely to rotate much faster than isolated cool giants or those in wide binary systems. However, there are no systematic investigations of $v \sin i$ of the mass donors in SS.

On the basis of their IR properties, SS have been classified into stellar continuum (S) and dusty (D or D') types. The D–type systems contain Mira variables as mass donors. The D'–type are characterized by an earlier spectral type (F-K) of the cool component. and lower dust temperatures.

4.1 D'-type symbiotics

Among 188 objects in the latest catalogue of symbiotic stars (Belczyński et al. 2000), there are only seven that are classified as D'–type: Wray15-157, AS 201, V417 Cen, HD 330036, AS 269, StHα 190 and Hen 3-1591 (Hen 3-1591 can be S or D'). Three of these have been studied using model atmospheres and all display rapid rotation and s-process elemental over-abundances (see Pereira et al. 2005).

Table 4.1: Journal of observations and projected rotational velocities of D' type SSs. The spectral types of the giants are from different papers (see Section 4.1.2), (B-V)$_0$ is the intrinsic colour for the corresponding spectral type. v sin i is the rotational velocity measured in this paper. The last column gives other measurements of v sin i (if available).

object	date-obs	MJD	Exp. time	
HD 330036	2004-05-22	53147.212	2×10 min	
Hen 3-1591	2004-07-19	53205.222	2×20 min	
StHα 190	2004-06-03	53159.397	2×10 min	
V417 Cen	2004-04-14	53109.280	2×10 min	
AS 201	2004-11-14	53323.330	2×10 min	
WRAY 15-157	2004-11-06	53315.327	2×10 min	

object	Cool Star Spectrum	(B-V)$_0$	v sin i [km s^{-1}]	other [km s^{-1}]
HD 330036	F8III	0.90	107.0±10	100±10[a]
Hen 3-1591	K1III	1.09	23.71±1.5	
StHα 190	G4III/IV	0.88	105.0±10	100±10[b]
V417 Cen	G9Ib-II	0.98	75.0±7.5	
AS 201	F9III	0.58	27±3	25±5[a]
WRAY 15-157	G5III	—	44±5	37±5

[a]Pereira et al.(2005); [b]Smith et al.(2001).

Our aims here are: **(1)** to measure the projected rotational velocities (v sin i) and the rotational periods (P$_{rot}$) of the giants in D' symbiotic stars, using a cross correlation function (CCF) approach; **(2)** to test the theoretical predictions that the mass donors in SSs are faster rotators than the isolated giants or those in wide binary systems; **(3)** to provide pointers to the determination of binary periods (assuming co-rotation).

4.1.1 Observations and v sin i measurement technique

The observations were performed with FEROS at the 2.2m telescope (ESO, La Silla). FEROS is a fibre-fed Echelle spectrograph, providing a high resolution of $\lambda/\Delta\lambda$ =48000, a wide wavelength coverage from about 4000 Å to 8000 Å in one exposure and a high overall efficiency (Kaufer et al. 1999). The 39 orders of the Echelle spectrum are registered on a 2k×4k EEV CCD. All spectra are reduced using the dedicated FEROS data reduction software implemented in the ESO-MIDAS system.

Radial velocities and projected rotational velocities have been derived by cross-correlating the observed spectra with a K0-type numerical mask yielding a cross-correlation function (CCF) whose centre gives the radial velocity and whose width is related to the broadening mechanisms affecting the whole spectra such as stellar rotation and turbulence. Details of the cross-correlation procedure are given in Melo et al. (2001).

In order to use the width (σ) of the CCF as an estimate of $v \sin i$ one needs to subtract the amount of broadening contributing to σ unrelated to stellar rotation (e.g., convection, instrumental profile, etc.), i.e., σ_0. Melo et al. (2001) calibrated σ_0 as a function of $(B-V)$ for FEROS spectra of stars with $0.6 < (B-V) < 1.2$. The $v \sin i$ measured from our CCFs for a set of standard stars within this $B-V$ range are in good agreement with the literature values. Therefore, for all 4 giants in Table 4.1, the Melo et al. (2001) calibration has been adopted.

For $v \sin i$ greater than about 30 km s^{-1} the shape of the CCF becomes gradually closer to the Gray rotational profile (Gray 1976). Therefore in order to correctly fit the CCF, a different approach is needed as described in Melo (2003). The CCF is then fitted by a family of functions $CCF_{V\sin i} = C - D[g_0 \otimes G(V \sin i)]$ which is the result of the convolution of the CCF of a non-rotating star g_0, which can be fairly approximated by a gaussian, and the Gray (Gray 1976) rotational profile computed for several rotational velocities $G(V \sin i)$. For each function $CCF_{V\sin i}$ we found the radial velocity V_r, the depth D and the continuum C for minimizing the quantity $\chi^2_{V\sin i}$ which is the traditional χ^2 function with $\sigma_i = 1$, where σ_i is the measurement error (see Fig. 1 of Melo 2003, for an example of the procedure). The CCFs of our objects are plotted in Fig. 1.

For $v \sin i >$ 30 km s^{-1} the typical error of our $v \sin i$ measurements is 10%. For 10 $< v \sin i \leq$ 30 km s^{-1} the error is about 1.5 km s^{-1}. Our measurements are given in Table 4.1.

4.1.2 Rotation of the mass donors

Individual objects

HD 330036 : Pereira et al. (2005) obtained L=650 $L_\odot$ for the cool component (with possible uncertainties 160$< L <$3000 $L_\odot$), T_{eff} =6200±150 K, $\log g$ = 2.4±0.7. This imply R_g = 22$R_\odot$ (using $L = 4\pi\sigma_{SB} R_g^2 T_{eff}^4$), M_g = 4.46 $M_\odot$ (using R_g and log g), and $P_{rot} \lesssim$10.4±2.4 d (using $P_{rot}\ v \sin i \leq 2\pi R_g$).

Hen 3-1591 : Medina Tanco & Steiner (1995) give spectral type K1 for the cool component. We assume that it is luminosity class III. The average radius of a K1III star is 23.9±3 $R_\odot$ and the average T_{eff} =4280±200 K (van Belle et al. 1999). A K1III star would have a mass of

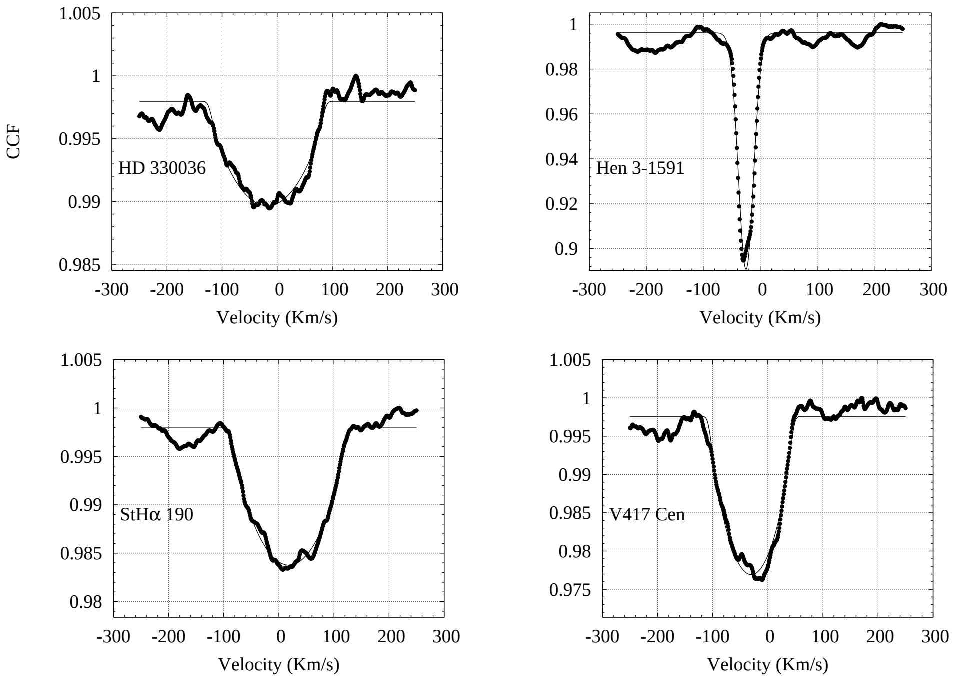

Figure 4.1: CCF relative intensity (heavy line) and the fit versus radial velocity for 4 D'-type SSs.

Table 4.2: Parameters of D'–type SS. IR types are from the catalogue of Belczyński et al.(2000), $v \sin i$ is the rotational velocity of the mass donors (as adopted here), R_g and M_g are the radius and the mass of the giant, respectively (see Sect.4.1.2). τ_{syn} is the synchronization time of the binary adopting $P_{orb} = P_{rot}$, $\tau_{syn}(100)$ is the synchronization time of the binary adopting $P_{orb} = 100$ days, $v_{\rm crit}$ is the critical rotational velocity of the giant, P_{rot} is the rotational period of the giant, a is the semimajor axis of the system calculated supposing synchronized rotation ($P_{orb} = P_{rot}$). The values in brackets for P_{rot} and a are the upper limits, supposing 10% uncertainity in $v \sin i$ and R_g.

object	IR type	Cool Star Spectrum	$v \sin i$ [km s^{-1}]	$v_{\rm crit}$ km s^{-1}	R_g [$R_\odot$]	M_g $M_\odot$
HD 330036	D'	F8III	107.0	160	22.1	4.46
Hen 3-1591	S,D'	K1III	23.7	144	23.9	3.9
StHα 190	D'	G4III/IV	105.0	191	7.88	2.25
V417 Cen	D'	G9Ib-II	75.0	105	75.0	6.45
AS 201	D'	F9III	25.0	150	24.5	4.35
WRAY 15-157	D'	G5III	44.0			

object	τ_{syn} [yr]	$\tau_{syn}(100)$ [yr]	P_{rot} [days]	a [$R_\odot$]
HD 330036	25	$2.1.10^5$	<10.4 (12.8)	35(40)
Hen 3-1591	8680	$1.3.10^5$	<51.0 (62.3)	98(112)
StHα 190	27	$1.3.10^7$	<3.78 (4.64)	15(17)
V417 Cen	36	553	<50.6 (61.8)	112(128)
AS 201	6423	$1.1.10^5$	<49.5 (60.5)	99(113)
WRAY 15-157				

3.9±0.3 $M_\odot$ (Allen 1973). The uncertainties correspond to ±0.5 spectral types. This will result in L=172 $L_\odot$(±20%) and $P_{rot} \lesssim$51.0±11.3 d.

StHα 190 : The cool component is of type G4 III/IV with T_{eff} =5300±150 K, $\log g$ = 3.0±0.5, and L=45 $L_\odot$ (Smith et al. 2001). This implies R_g = 7.9±0.4 $R_\odot$ and $P_{rot} \lesssim$3.8±1.2 days (upper limit calculated for R_g = 8.3 $R_\odot$ and $\sin i = 1.0$). The upper limit for P_{rot} is considerably shorter than the supposed orbital periods of 171 d (Munari et al. 2001) or 38 d (Smith et al. 2001).

V417 Cen : Van Winckel et al. (1994) detected a photometric period of 245 days. For the cool component they obtained G9 Ib-II, $\log L/L_\odot$ =3.5, T_{eff} =5000 K, $\log g$ = 1.5±0.5. This implies $R_g = 75 R_\odot$ and $P_{rot} \lesssim$50.6±10.2 days. P_{rot} is considerably shorter than the period obtained from photometry. However, the photometric period is not confirmed with radial velocity measurements and we do not know whether this is the orbital period.

AS 201 : Following Pereira et al. (2005), the cool component is of type F9III with T_{eff} =6000±100 K, L=700 $L_\odot$ (with possible uncertainties $300 < L < 1200$ $L_\odot$), and $\log g$ = 2.3±0.3. This imply R_g = 24.5 $R_\odot$ and $P_{rot} \lesssim$49.5±11.0 days.

$v \sin i$ **- comparision with catalogues:** There are no systematic investigations of the rotation of the mass donors in SSs. The rotational velocities of 13 S–type systems listed in Fekel et al. (2003) are between $v \sin i$= 3.6 - 10.4 km s^{-1}. All D'–type systems so far observed (see Table 4.2) rotate with $v \sin i$>20 km s^{-1}.

The catalog of de Medeiros et al. (2002) of $v \sin i$ of Ib supergiant stars contains 16 objects from spectral type G8-K0 Ib-II. All they have $v \sin i$ in the range 1-20 km s^{-1}. It means that V417 Cen is an extreme case of very fast rotation for this spectral class.

The catalogue of rotational velocities for evolved stars (de Medeiros et al. 1999) lists ∼100 K1III stars, and 90% of them rotate with $v \sin i$<8 km s^{-1}. There are only 5 with $v \sin i$>20 km s^{-1}. This means that Hen 3-1591 is a very fast rotator (in the top 5%). The same catalog contains 5 objects from spectral type F8III-F9III. They rotate with $v \sin i$ of 10-35 km s^{-1}. AS 201 is well within in this range. However HD 330036 is an extremely fast rotator. The same catalog lists 60 objects from spectral type G3,G4,G5 III-IV. They all rotate with $v \sin i < 24$ km s^{-1}. Again, this means that StHα 190 is an extremely fast rotator.

WRAY 15-157 is of spectral class G5III. The catalogue of rotational velocities for evolved stars (de Medeiros & Mayor 1999) lists 18 objects from spectral type G5III. They all rotate with $v \sin i$< 15 km s^{-1}. WRAY 15-157 with $v \sin i$= 37 ± 5 km s^{-1}, is an extremely fast rotator for this spectral class.

There are 7 D' SSs listed in the catalogue of Belczyński et al. (2000). Rotational velocities are measured for all six southern objects. Our result is: 5 out of the six southern D'–type SSs are very fast rotators. Furthermore, four of them are the fastest rotators in their spectral class.

Critical speed of rotation

There is a natural upper limit for rotation speeds, where the centripetal acceleration balances that due to gravitational attraction, often named the "critical speed", where $v_{\mathrm{crit}} = \sqrt{GM/1.5R} = 357\sqrt{M/R}$ $\mathrm{km\,s^{-1}}$ (the factor of 1.5 appears from the assumption that at critical rotation speeds the equatorial radius is 1.5 times the polar radius, R). The calculated v_{crit} is included in Table 4.2. No star can rotate faster than its critical speed, however we can see that at least three D'–type SSs are rotating at a substantial fraction of their critical speeds: $\frac{v\ \sin i}{v_{\mathrm{crit}}} \sim 0.67$ (HD 330036), ~ 0.54 (StHα 190), ~ 0.71 (V417 Cen). Probably for these three SSs the orbital inclination is high $i \geq 50^0$. For the remaining two objects we can not exclude the possibility that they also rotate very fast but are observed at low inclination ($i \lesssim 30^0$).

4.1.3 Synchronization and binary periods

Synchronization in SS: The physics of tidal synchronization for stars with convective envelopes has been analyzed several times (e.g. Zahn 1977 and also the discussion in Chapter 8 of Tassoul 2000). There are some differences in the analysis of different authors, leading to varying synchronization time-scales. Here, we use the estimate from Zahn (1977, 1989): the synchronization time-scale in terms of the period is

$$\tau_{\mathrm{syn}} \approx 800 \left(\frac{M_g R_g}{L_g}\right)^{1/3} \frac{M_g^2(\frac{M_g}{M_{WD}}+1)^2}{R_g^6} P_{orb}^4 \text{ years} \tag{4.1}$$

where M_g and M_{WD} are the masses of the giant and white dwarf respectively, and R_g and L_g are the radius and luminosity of the giant (all in Solar units). The orbital period P is measured in days.

The S–type SSs are very likely synchronized (Schild et al. 2001; Schmutz et al. 1994). Other proof of this supposition is that most of the SSs with derived orbital parameters (see Mikołajewska 2003) have orbital eccentricity $e \approx 0$. Because the circularization time of the orbits is ~ 10 times longer than the synchronization time (Schmutz et al. 1994 and the references therein), if a SS's orbit is circularized it will very likely be synchronized too.

A typical D'–type SS would have $R_g \sim 20\mathrm{R}_\odot$, $L_g \sim 500\mathrm{L}_\odot$, $M_g \sim 3\mathrm{M}_\odot$, and white dwarf mass $M_{WD} \sim 1\mathrm{M}_\odot$. For a period of 100 days for a typical D'-type SS, we find $\tau_{syn} \sim 9 \times 10^4$ years.

For the individual systems, we calculated the synchronization time (τ_{syn}) for two cases: τ_{syn} is derived assuming P_{orb} =P_{rot}, and $\tau_{syn}(100)$ assuming P_{orb} =100 days. These are given in Table 4.2. Depending on the individual parameters, the synchronization time can be from <100 yr up to >10^7 yr. This means that it is possible for a D'–type SS to be synchronized if the orbital period is short ($P_{orb} \approx P_{rot}$).

The mass of the mass donors in S–type SSs with known parameters are in the range 0.6 - 3.2 $M_\odot$ (Mikołajewska 2003). The calculated masses of the mass donors in D'–type SSs are larger. As can be seen in Table 4.2, they range from 2.2 up to 6.5 $M_\odot$.

Masses of 8 $M_\odot$ are generally considered the upper limit for evolution to planetary nebula nuclei and white dwarfs, after heavy mass loss, especially during their AGB phases. Following our calculations for the mass of the giants (Table 4.2) and assuming $M_{WD} \leq 1.4$ $M_\odot$, the total mass of the binary is about (M_g+M_{WD}) $\sim 3.5 - 8.0$ $M_\odot$, in agreement with the above upper limit of 8 $M_\odot$ for the WD progenitor.

The relevant time for a 5$M_\odot$ star to cross the Hertzsprung gap is $\approx 8\times10^5$ yr and its life time on the red giant branch is $\approx 5\times10^5$ yr (Iben 1991). For a 1.5$M_\odot$ star these times are 1.5×10^8 yr and 1.57×10^8 yr (Iben 1991). These lifetimes are longer than the calculated $\tau_{\rm syn}$ and comparable with $\tau_{\rm syn}(100)$. This means that the rotation of the mass donors in D'–type SSs could be synchronized for these lifetimes.

Clues regarding the orbital periods: Because the orbital periods of the majority of SSs are unknown, an indirect method to obtain P_{orb} is to measure $v \sin i$. If the mass donors in SSs are co-rotating (P_{rot} =P_{orb}), we can find clues for the orbital periods via the simple relation P_{orb} v_{rot} = $2\pi R_g$, where P_{orb} is the orbital period, v_{rot} and R_g are the rotational velocity and radius of the giant, respectively. It is very useful in the case of eclipsing binaries, where $\sin i \approx 1$ and $v \sin i \approx v_{rot}$. If the inclination is unknown, we can only obtain an upper limit for P_{orb}.

Using Kepler's third law [$4\pi a^3 = G(M_g + M_{WD})P^2$], we can calculate the semimajor axis of the systems. These are given in Table 4.2. The values in the brackets (for P_{rot} and a) correspond to the estimation of the upper limit of these parameters, assuming 10% errors in $v \sin i$ and R_g.

Up to now, from 188 SSs, the orbital elements and binary periods are well known for $\sim$40 objects only (and they are all S–type). The orbital periods are in the range 200 - 2000 days (Mikołajewska 2003). As can be seen in Table 4.2, if D'–type SSs are synchronized, their orbital periods would be relatively short (4-60 days) and the distance between the WD and the mass donor would be 2-5 R_g.

4.1.4 Reasons for the fast rotation and dust formation

The observation of fast rotation of D'–type SSs raises two further questions: first, what is the evolutionary history of these stars which has produced such high rotation, and second, what does the effect of high rotation have on their mass loss and subsequent dust formation?

We see three possible reasons for the fast rotation of mass donors in D'–type SSs:

(i) the rotation is synchronized with the binary period (P_{rot} = P_{orb}). In this case their orbital periods should be short $\lesssim$50 days.

However, it also could be, that they are not synchronously rotating. The possibility that $P_{rot} > P_{orb}$ has to be excluded because the orbital separations would be unreasonably small, and the synchronization time would be extremely short (they will be synchronized in 30-9000 years; see τ_{syn} in Table 4.2). If $P_{rot} < P_{orb}$, reasons for their fast rotation could be:

(ii) the current giants have been spun-up from the transfer of angular momentum. Jeffries & Stevens (1996) proposed a mechanism in which accretion of a slow massive wind from the AGB progenitor of the current white dwarf can transfer sufficient angular momentum. This also explains the chemical enrichment in s-process elements in D' SSs, that were present in the AGB wind (see also Pereira et al. 2005). Mass transfer via L_1, when the current white dwarf was the mass donor, can also spin-up the companion, as in millisecond radio pulsars (van den Heuvel 1984).

(iii) planet swallowing to spin up the giant. Rough estimation gives angular momentum transfer during a collision of a planet with mass m_p and velocity v_p to a giant of mass M_g, of the order of $\Delta\Gamma = m_p v_p R_g$. This causes a change in the giant's rotational velocity $\Delta v_g^{rot} = m_p v_p / const. M_g$, where const.$=J_g/M_g R_g^2$ depends on the internal structure of the giant. ($const.$ = 0.4 for a solid uniform density sphere, and less for a star-like centrally condensed sphere). Assuming a centrally condensed star (giant) such that $const.$ = 0.01, $v_p = \sqrt{GM_g/R} \sim 10 - 100$ km s^{-1}, $M_g = 2 - 10 M_\odot$ and $m_p = 0.01 M_\odot$ we estimate $\Delta v_g^{rot} \sim$ 1-$-$ 50 km s^{-1}, showing that in the right circumstances, the planet could spin up the giant to the rotational velocities observed in D'–type SSs.

Fast rotation, i.e. $v_{rot} \geq 0.5 v_{\rm crit}$, may change a spherical star with a spherical wind into an equatorially flattened system, with both the radius of the star and stellar wind parameters depending on the stellar latitude. Such stars will have an equatorial radius significantly larger than the polar one, and equatorially enhanced mass loss (see Lamers 2004 and references therein).

Because it seems that the majority of the giants in D'–type SSs are rapid rotators, we expect that:

(1) they have a larger mass loss rate than the slower rotating giants;

(2) their mass loss is enhanced in the equatorial regions;

(3) they could be even equatorially flattened.

It is possible, that the dusty environment in D'–type SSs is connected with rapid rotation of the mass donors. Intense mass loss in the equatorial regions can lead to the formation of an excretion disc in which the higher gas density enhances dust formation and growth. The broad IR excess in D'–type SSs can be due to the temperature stratification in the dust from such an excretion disc (Van Winckel et al. 1994). Other possible explanations for the presence of dust can be that it is left over from the formation of a planetary system, or it is a relic from a strong dusty mass loss when the present day white dwarf was on the AGB. However, we consider it is more likely that it originates in the current outflow and that this is enhanced in the equatorial regions by rapid rotation.

Conclusions Our main results are:

(1) We have measured the rotational velocities of the mass donors in D'–type symbiotic stars, using the CCF approach.

(2) Five of the six objects appeared to be very fast rotators compared with the catalogues of $v \sin i$ for the corresponding spectral types. At least four of them rotate at a substantial fraction ($\gtrsim$0.5) of the critical velocity. This means that at least in D'–type SSs, the cool components rotate faster than isolated giants (as predicted by Soker 2002).

(3) If they are tidally locked, the orbital periods should be as short as $\lesssim$10-50 days.

(4) As a result of the rapid rotation, they must have larger mass loss rates than the more slowly rotating giants, and their mass loss is probably enhanced in the equatorial regions.

To understand better these objects, we need their binary periods to be derived from radial velocity measurements and the inclination determined. In subsequent papers, we plan to explore the projected rotational velocity of the cool giants in the other types of symbiotic stars and to compare their rotational velocities with that of the isolated giants with similar mass and evolutionary stage.

4.2 Are S-type symbiotics synchronized?

4.2.1 ESO 2.2m/FEROS observations

We have observed 30 objects from the Belczyński et al.(2000) SS catalogue and have observed all S-type SSs from the catalogue with $12^h < RA < 24^h$, declination $< 2^0$, and catalogue magnitude brighter than $V < 12.5$.

The observations have been performed with FEROS at the 2.2m telescope (ESO, La Silla). FEROS is a fibre-fed echelle spectrograph, providing a high resolution of $\lambda/\Delta\lambda$ =48000, a wide wavelength coverage from about 4000 Å to 8900 Å in one exposure and a high throughput (Kaufer et al. 1999). The 39 orders of the echelle spectrum are registered with a 2k×4k EEV CCD

The present data have been collected from April to September 2004. Table 4.3 gives a log of the observations. All spectra are reduced using the dedicated FEROS data reduction software implemented in the ESO-MIDAS system (www.ls.eso.org/lasilla/sciops/2p2/E2p2M/FEROS/DRS/). A few examples of our spectra are given in the Appendix (Fig.A.1).

4.2.2 v sin i measurement techniques - CCF and FWHM

CCF method: The projected rotational velocities have been derived by cross-correlating the observed spectra with K0 numerical masks yielding a cross-correlation function whose width (σ_{obs}) is related to broadening mechanisms such as stellar rotation and turbulence.

The emission lines do have an effect in the CCF and they must be cleaned. They were cut off by fitting a continuum and replacing the emission lines by the value of the fit. Note that the exact location of the continuum is not important.

The numerical K0-mask was constructed from a K0III synthetic spectrum in the region between $\lambda\lambda$ 5000-7000 Å following the procedure described in Baranne et al. (1979) In the CORAVEL-type cross-correlation a binary mask is used as template instead a real spectrum. This binary (or CORAVEL-type) mask has been used in many different data reduction software for cross-correlation (ELODIE, CORALIE, and now HARPS). The K0-mask CCFs for the SSs observed here are plotted in the Appendix (Fig.4.1) and σ_{obs} are given in Table 4.4.

In order to use the observed width of the CCF (σ_{obs}) as an estimate of v sin i one needs to subtract the amount of broadening contributing to σ_{obs} unrelated to the stellar rotation

Table 4.3: Journal of observations. In the table are given as follows: the name of the object, date of observation (YYYY-MM-DD), the modified Julian Date (JD - 2400000.5) of the start of the observation, signal to noise ratio (S/N) around λ 8500 Å.

object	date-obs	MJD-OBS	Exp [sec]	S/N
AR Pav	2004-06-04	53160.3737	600	40
AS 255	2004-04-12	53107.3670	1200	45
AS 276	2004-04-12	53107.3967	600	45
AS 289	2004-06-05	53161.3071	600	40
AS 316	2004-06-07	53163.3600	1200	70
AS 327	2004-09-21	53269.0508	600	45
BD-21°3873	2004-04-14	53109.2903	600	80
CD-36°8436	2004-04-11	53106.3374	600	40
CD-43°14304	2004-08-30	53247.2435	1200	70
FG Ser	2004-06-03	53159.2731	1200	50
HD 319167	2004-06-07	53163.3905	600	45
Hen 2-374	2004-06-08	53164.3099	1200	40
Hen 3-1213	2004-04-12	53107.3049	1200	75
Hen 3-1341	2004-04-12	53107.3354	1200	50
Hen 3-1674	2004-06-07	53163.3103	1200	35
Hen 3-1761	2004-06-04	53160.2095	600	40
Hen 3-863	2004-04-11	53106.3067	1200	55
MWC 960	2004-06-08	53164.2738	1200	70
PN Ap 1-9	2004-06-07	53163.1986	1200	45
RS Oph	2004-04-11	53106.3849	600	50
RW Hya	2004-04-12	53107.2285	600	80
SS73 129	2004-06-29	53185.0660	1200	65
SS73 141	2004-06-29	53185.1058	1200	50
V2506 Sgr	2004-06-07	53163.2393	1200	45
V2756 Sgr	2004-06-08	53164.3968	600	40
V2905 Sgr	2004-06-28	53184.0858	1200	90
V3804 Sgr	2004-06-27	53183.9951	1200	40
V4018 Sgr	2004-08-31	53248.1800	1200	50
V4074 Sgr	2004-06-07	53163.2737	600	50
V919 Sgr	2004-06-03	53159.3108	1200	50

Table 4.4: Rotational velocities of the red giants in symbiotic stars. The spectral types are from the catalogue of Belczyński et al.(2000), $(B\text{-}V)_0$ is the intrinsic colour (from Schmidt-Kaler 1982) for the corresponding spectral type adopting luminosity class III in all cases, R_g is the adopted radius of the giant [if not otherwise indicated, this is the average radius for the corresponding spectral type taken from Table 7 of van Belle et al.(1999)]. P_{orb} is the orbital period (see Sect.4.3). $v \sin i$(FWHM) is the projected rotational velocity of the cool giant as measured with FWHM method (see Sect.3.2). σ_{obs} is the observed width of the CCF. $v \sin i$ is our measurement based on CCF method (see Sect.3.1), if other measurements of $v \sin i$ exist, they are also given in the next column. For objects with unknown orbit we give an estimation of the upper limit of the orbital period P_{ul} (i.e. we expect $P_{orb} \lesssim P_{ul}$, see Sect.4.3.2). The upper part of this table contains objects observed with FEROS, the lower part - $v \sin i$ values are taken from the literature.

object	Cool Sp.	$(B\text{-}V)_0$	R_g $R_\odot$	P_{orb} [days]	$v \sin i$ FWHM km s^{-1}	σ_{obs} CCF km s^{-1}	$v \sin i$ CCF km s^{-1}	other km s^{-1}	P_{ul} [days]
AR Pav	M5	1.59	139.6	604.5	8.8±2	6.208	8.1±1.5	11±2[e]	—
AS 255	K3	1.26	20.5		9.7±1	6.417	8.7±1.5		119
AS 276	M4.5	1.60	123.0		7.7±2	6.382	8.6±1.5		724
AS 289	M3.5	1.62	89.0	451	9.5±1	8.400	13.5±1.5	5.7±1[k]	—
AS 316	M4	1.62	105.5		9.6±1	6.843	9.8±1.5		545
AS 327	M3	1.62	71.5		7.7±1	5.847	7.1±1.5		510
BD-21°3873	K2	1.16	20.8	281.6	6.6±1	5.352	4.6±1.2	5.4±0.7[f]	—
CD-36°8436	M5.5	1.58	144.0		6.6±1.5	6.410	8.7±1.5		840
CD-43°14304	K5	1.51	38.8	1448	7.2±1	5.869	7.2±1.5	<3[g]	—
FG Ser	M5	1.59	139.6	650	9.8±1	6.756	9.6±1.5	8±1[h], 7±1[k]	—
HD 319167	M3	1.62	71.5		7.4±2	6.041	7.7±1.5		472
Hen 2-374	M5.5	1.59	144.0		8.4±1.5	5.712	6.7±1.5		1091
Hen 3-1213	M2/K4	1.54	50:?		9.1±1.5	7.236	10.8±1.5		235
Hen 3-1341	M2	1.61	57.8		7.5±1.5	6.423	8.7±1.5		336
Hen 3-1674	M5	1.59	139.6		56.0±5	.....	52.0±5.2		135
Hen 3-1761	M4	1.62	105.5		9.3±2	6.475	8.8±1.5		603
Hen 3-863	K4	1.43	45.0		7.9±1	5.811	7.0 ±1.5		326
MWC 960	K9	1.55	39.0[a]		9.0±1	6.436	8.7±1.5		225
PN Ap 1-9	K4	1.43	45.0		8.2±1	5.792	6.9±1.5		329
RS Oph	M0	1.56	59.1	455.7	13.8±1.5	7.624	11.7±1.5		—
RW Hya	M2	1.61	57.8	370.2	6.2±1	5.837	7.1±1.5	5.0±1[k]	—
SS73 129	M0	1.56	59.1		8.9±1	6.162	8.0±1.5		374
SS73 141	M5	1.59	139.6		7.9±1	6.064	7.7±1.5		914
V2506 Sgr	M5.5	1.59	144.0		7.8±1	6.284	8.3±1.5		874
V2756 Sgr	M3	1.62	71.5	243:?	4.2±1.5	4.942	3.9±1.5		932
V2905 Sgr	M5	1.59	139.6		6.6±1	5.708	6.7±1.5		1059
V3804 Sgr	M5	1.59	139.6		9.0±3	.....	.....		...
V4018 Sgr	M4	1.62	105.5		7.2±1.5	5.345	5.5±1.5		974
V4074 Sgr	M4	1.62	105.5		4.2±1.5	4.871	3.5±1.5		1508
V919 Sgr	M2	1.61	57.8		7.4±1	6.560	9.1±1.5		322
SY Mus	M5		139.6	624.5				7±1[p]	
AG Dra	K2Ib or II		30-40[b]	554				3.6±1[k], 5.9±1[q]	
BX Mon	M5III		139.6	1401				6.8±1[k]	
TX CVn	K5III		38.8	199				8.9±1[k]	
T CrB	M4IIIelips.		66±11[c]	227.57				5.4±1[k]	
V443 Her	M5.5III		144	594				4.5±1[k]	
CI Cyg	M5II or M5.5		189-236[d]	854.5				10.4±1[k]	
AG Peg	M3III		71.5	817.4				4.5±1[k]	
V1329 Cyg	M6		147.9	956.5				7.0±2[k]	
BF Cyg	M5III		75-280[r]	756.8				4.5±2[k]	

[a]-from the fit in van Belle et al.(1999); [b]Tomov, Tomova, & Ivanova (2000); [c]Belczynski & Mikolajewska(1998) [d]Kenyon et al.(1995); [e]Schild et al.(2001); [f]Smith et al.(1997); [g]Schmid et al.(1998); [h]Mürset et al.(2000); [k]Fekel et al.(2003); [p]Schmutz et al.(1994); [q]de Medeiros & Mayor (1999). [r]see Sect.4.3

(convection, instrumental profile, etc), i.e. σ_0. For FEROS spectra (see Melo et al. 2001, 2003):

$$v\ \sin i = 1.9\sqrt{\sigma_{obs}^2 - \sigma_0^2}\ \ km\ s^{-1} \tag{4.2}$$

More details of the cross-correlation procedure are given in Melo et al. (2001), and also σ_0 is calibrated as a function of the $(B-V)$ for FEROS spectra and for stars with $0.6 < (B-V) < 1.2$. For giants with $(B-V) < 1.2$ in Table 4.4, the Melo et al.(2001) calibration has been adopted. However, the stars in our sample have $(B-V)$ around 1.5 which is beyond the range of the calibration of Melo et al.(2001). For (B-V)> 1.2, we will adopt constant $\sigma_0 = 4.5$ km s^{-1}.

This value has been adopted as a result of: **(i)** CCF measurements of few objects with known $v\ \sin i$; **(ii)** bearing in mind the results of Delfosse et al. (1998). Using a similar template and method but lower resolution (which increases σ_0), Delfosse et al. (1998) have shown that σ_0 does vary over a range of $0.8 < (R-I) < 1.5$ (which corresponds to a spectral type from ∼M0 to ∼M6), decreasing from ∼ 5.1 km s^{-1} to 4.7 km s^{-1}; **(iii)** bearing in mind the calibration of CCF and FEROS spectra undertaken in Melo et al. (2001).

The errors on CCF $v\ \sin i$ measurements are dominated by systematic effects rather than by photon noise. The error on $v\ \sin i$ comes from two main sources: uncertainties on the values of σ_{obs} and σ_0. According to error estimate carried out by Melo et al.(2001), stars with $(B-V) < 1.2$ have an error on $v\ \sin i$ less than 1.2 km s^{-1}. For stars with $(B-V) > 1.2$ we adopt a constant σ_0, which leads to an increase in our errors. For such stars a conservative error of 1.5 km s^{-1} is assigned. For objects with $v\ \sin i \geq 15$ km s^{-1} the error on $v\ \sin i$ is ±10%.

For V3804 Sgr we did not get a meaningful CCF due to the numerous emission lines in the spectrum at the time of our observations. From measurements of the FeI 8689 line we obtain a rough estimate of FWHM(FeI 8689)$\approx 0.58 \pm 0.15$ Å similar to the width of this line in AR Pav and FG Ser and corresponding to $v\ \sin i \approx 9 \pm 3$ km s^{-1}.

FWHM method: Besides the cross-correlation procedure another method using full width at half maximum (FWHM) of spectral lines of observed and synthetic spectra was also applied. This procedure is similar to that described in Fekel (1997). The spectra of K5III (T_{eff}=3950 K, $\log g = 1.5$), M0III (T_{eff}=3985 K, $\log g = 1.2$), and M5III (T_{eff}=3424 K, $\log g = 0.5$), stars have been synthesized in the spectral region λ 8750-8850 Å. The value of 3 km s^{-1} was adopted for the microturbulent velocity. A grid of synthetic spectra for projected

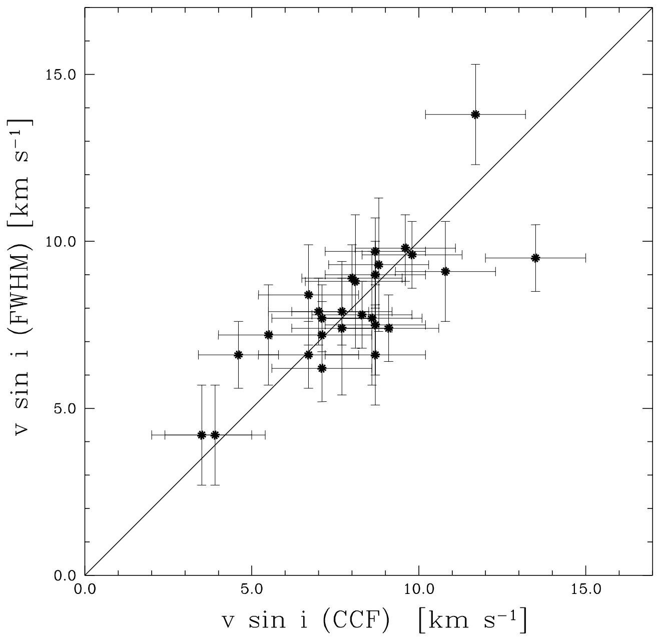

Figure 4.2: Comparison between the CCF and FWHM measurements of $v\ \sin i$. The straight line indicates $v\ \sin i$(CCF)=$v\ \sin i$(FWHM).

rotational velocities from 0 $\mathrm{km\,s^{-1}}$ to 60 $\mathrm{km\,s^{-1}}$ was calculated. The FWHM of a dozen observed spectral lines has been measured and compared to the FWHM of spectral lines from the synthetic spectra. The results are given in the sixth column of Table 4.4.

The comparison between the CCF and FHWM methods (see Fig.4.2) shows that the $v\ \sin i$ measurements agree well, with typical difference $\pm 1 - 2$ $\mathrm{km\,s^{-1}}$, as expected from the measurement errors. The only exception is AS 289 (see also Sect. 6.1).

Because the CCF method uses many more lines and a better defined mathematical procedure, in the analysis we will use $v\ \sin i$ derived with the CCF method.

4.2.3 Parameters of symbiotic stars

Synchronization timescale in SSs: The physics of tidal synchronization for stars with convective envelopes has been analyzed several times (e.g. Zahn 1977, and see the discussion in Chapter 8 of Tassoul 2000). There are some differences in the analysis of different authors, leading to varying synchronization timescales. Here, we use the estimate from Zahn (1977,

Table 4.5: The synchronization time, τ_{syn}, calculated following Eq.1 for a few representative cases. The typical values for L_g and R_g of K5 III and M4III stars are adopted following van Belle et al.(1999).

Mass donor	L_g	M_g	R_g	P_{orb}	M_2	τ_{syn}
Sp. type	$[L_\odot]$	$[M_\odot]$	$[R_\odot]$		$[M_\odot]$	[yr]
K5 III	350	2	40	200 d	1.0	7000
				1500 d	1.0	2.10^7
M4 III	1380	1	105	500 d	0.5	140
		2		500 d	1.0	700
		3		500 d	1.0	3200
		2		1500 d	1.0	60000

1989). The synchronization timescale in terms of the period is

$$\tau_{syn} \approx 800 \left(\frac{M_g R_g}{L_g} \right)^{1/3} \frac{M_g^2 (\frac{M_g}{M_2}+1)^2}{R_g^6} P_{orb}^4 \quad \text{years} \tag{4.3}$$

where M_g and M_2 are the masses of the giant and white dwarf respectively in Solar units, and R_g and L_g are the radius and luminosity of the giant, also in Solar units. The orbital period P_{orb} is measured in days.

In Table 4.5 we calculate this timescale for a few representative cases. We point out that these values serve as an estimation. From the R_g^6 dependence of τ_{syn} in Eq. 1, one can expect large uncertainties in the synchronization timescale as a result of the uncertainties in the red giant radius. There is also a P_{orb}^4 dependence, which can introduce large uncertainties, but P_{orb} is much more accurately known than R_g.

As can be seen in Table 4.5, for S–type SSs depending on the binary parameters, τ_{syn} can be as short as $< 10^4$ yr and longer than 10^7 years. Short $\tau_{\rm syn}$ can be expected when the radius of the mass donor is a significant fraction of the orbital separation.

The lifetime of the symbiotic phase for a red giant or AGB star is around 10^5year (see e.g. Yungleson et al. 1995), which is comparable with $\tau_{\rm syn}$.

Inclination and Radius of the cool component

Inclination: In our calculations, we assume that the rotational axis of the red giant is perpendicular to the orbital plane (see Fekel 1981; Hale 1994; Stawikowski 1994). To calculate

Table 4.6: Stellar radii of M giants. In column 3 are given R_g (following van Belle et al. 1999), in column 4 - mass of the M giants (from Mikołajewska 2003), in column 5 - the range of R_g for the corresponding mass and spectral type (following Dumm & Schild 1998).

Object	Mass donor	R_g	M_g	R_g
		$[R_\odot]$	$[M_\odot]$	$[R_\odot]$
1	2	3	4	5
FG Ser	M5III	140	1.7	110-150
AR Pav	M5III	140	2.5	90-240
AG Peg	M3III	72	>1.8	60-90
BX Mon	M5III	140	3-3.7	150-200
SY Mus	M5III	140	1.3	60-100
RW Hya	M2III	58	1.6	40-80
AR Pav	M5III	140	2.5-3	130-160
BF Cyg	M5III	140	1.8	110-140
AG Peg	M3III	72	$\gtrsim$1.8	60-90

the rotational periods of the mass donors (P_{rot}) we need to know the inclination of the orbit (i) and R_g.

For eclipsing binaries we can adopt inclination $i = 70^0 - 110^0$, which produces small errors in $\sin i$. For such cases we will assume that $\sin i$ is in the range 0.94-1.00. For other cases we use results from spectropolarimetric observations or radial velocity measurements.

Radius of the cool component: For a few objects, the radii of the cool components are derived from model calculations. If the radius of the giant (R_g) is not known, we will use the average radius for the corresponding spectral type taken from van Belle et al.(1999), always adopting luminosity class III and error ±5%.

For the M giants these values are similar to the stellar radii of M giants in the Hipparcos catalogue as calculated by Dumm & Schild (1998). Dumm & Schild (1998) have also shown that the radius of the M giants depends on the mass. For 9 objects included in our sample, the masses of the M giants are listed in Mikołajewska(2003). In Table 4.6, we compare the values adopted here (following van Belle et al. 1999) with the results of Dumm & Schild (1998).

As visible in most cases, the adopted radii (following van Belle et al. 1999) are in agreement with the mass-dependent radii of Dumm & Schild (1998). There are 2 cases where the adopted values are outside of this range: BX Mon and SY Mus (see Sect.4.3).

4.2.4 Results

Our measurements of $v \sin i$ together with data collected from the literature, are summarized in Table 4.4. Our sample thus contains 39 objects (29 with $v \sin i$ measured by us and 10 taken from the literature). This sample should have no biases in the rotational speed of the cool giant, even though the sample is flux limited.

In our sample of S-type SSs, the projected rotational velocities of the mass donors are from 3.5 $\mathrm{km\,s^{-1}}$ up to 52 $\mathrm{km\,s^{-1}}$. Including our data and the data from the literature, we obtain for $v \sin i$: mean=8.7 $\mathrm{km\,s^{-1}}$, median=7.7 $\mathrm{km\,s^{-1}}$, standard deviation=7.4 $\mathrm{km\,s^{-1}}$.

If we exclude the 2 slowest and the 2 fastest rotators we get: mean $v \sin i = 7.6 \pm 1.8$ $\mathrm{km\,s^{-1}}$. In effect, 90% of the mass donors in S-type SSs with measured rotation have $v \sin i$ in the interval $4.5 \leq v \sin i \leq 11.7$ $\mathrm{km\,s^{-1}}$. For the southern S-type symbiotics (29 objects, flux limited sample, FEROS observations) the values are similar: median $v \sin i$=8.1 $\mathrm{km\,s^{-1}}$, 90% of the objects in the interval $4 \leq v \sin i \leq 11.7$ $\mathrm{km\,s^{-1}}$.

4.3 S–type symbiotics with known orbital periods

In our sample, there are 17 objects with known orbital periods and 1 where this is inferred (V2756 Sgr). In this section we compare the orbital periods with the rotational periods of the mass donors object by object. The upper-lower limits of P_{rot} are calculated from:

$$P_{rot} = \frac{2\pi(R_g \pm e_1)(\sin i \pm e_2)}{v \sin i \mp e_3}, \tag{4.4}$$

where e_1, e_2, and e_3 are the corresponding errors in R_g, $\sin i$, and $v \sin i$ respectively.

In the statistical analysis (Sect.4.3.1), for P_{rot} we will use the average value between these upper-lower limits and will consider them as corresponding to $\pm 1\sigma$ error.

AR Pav is an eclipsing binary with $P_{orb} \approx 604.5$ days (Bruch et al. 1994). The giant's radius derived from the eclipse is $R_g = 137 \pm 20\ R_\odot$ (Quiroga et al. 2002), which is very close to the value adopted in Table 4.4 from the spectral type of the cool giant and to $R_g = 139 \pm 10\ R_\odot$ (Skopal 2005). We calculate $649 < P_{rot} < 1120$ days.

AS 289 (V343 Ser) has orbital period $P_{orb} = 450.5 \pm 2.2$ d, $e = 0.135 \pm 0.046$, and orbital inclination of $17^\circ - 23^\circ$ (Fekel et al. 2001). Kenyon & Fernandez-Castro (1987) gave spectral type M3.9III, but more recently M3.5 is assigned from Mürset & Schmid (1999). Assuming it is a normal M3.5III star, and using our CCF value for $v \sin i$, we obtain $159 < P_{rot} < 341$ days.

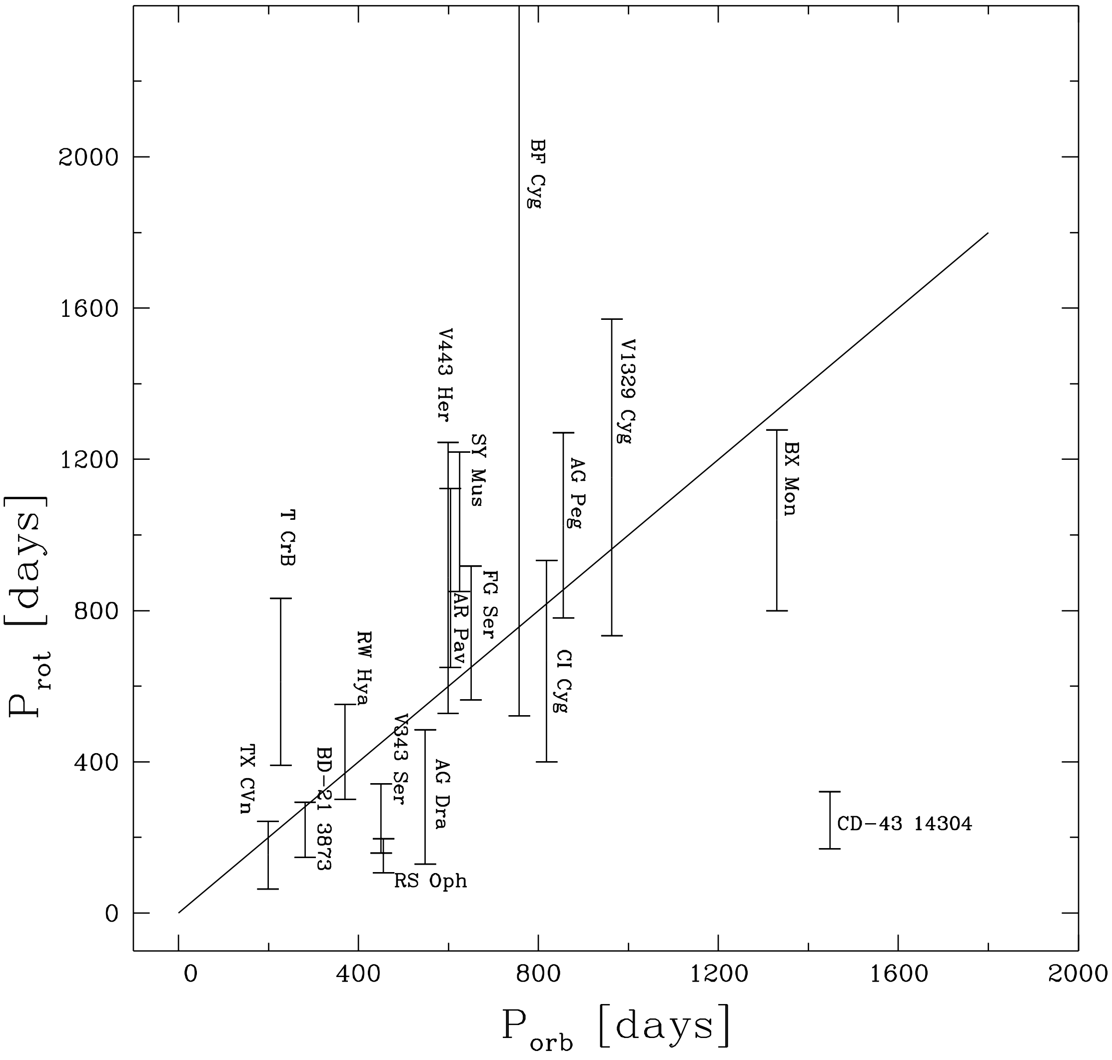

Figure 4.3: The rotational period of the red giant (P_{rot}) versus the orbital period (P_{orb}) of the 17 objects in our sample. The solid line corresponds to $P_{rot} = P_{orb}$. Most objects are close to this line, which indicates that they are synchronized. There are 2 objects which deviate considerably from that rule (RS Oph and CD-43°14304).

In a binary with an eccentric orbit the synchronization is reached at a value of $P_{rot} < P_{orb}$ (pseudosynchronization, see Hut 1981). Following Eq. 42 and Eq. 43 of Hut (1981), in AS 289 the pseudosynchronization is expected at $P_{rot} = 0.90\,P_{orb}$.

It is worth noting that Fekel et al.(2003) give a value of $v\ \sin i = 5.7 \pm 1$ km s^{-1} and our FWHM method give $v \sin i = 9.5 \pm 1$ km s^{-1}. An independent measurement of $v \sin i$ with better spectroscopic resolution will be valuable.

BD-21°3873 has $P_{orb} = 281.6 \pm 1.2$ days, sin $i = 0.87$ (Smith et al. 1997). We derive $147 < P_{rot} < 293$ days. The object is thus synchronized within the measurement errors.

RW Hya is an eclipsing binary with $P_{orb} = 370.4 \pm 0.8$ days (Schild et al. 1996). Supposing $i = 70^0 - 90^0$, we calculate that P_{rot} is in the interval 301 - 552 days. The object is thus synchronized within the measurement errors.

FG Ser (AS 296) is an eclipsing binary with $P_{orb} = 650 \pm 5$ days (Mürset et al. 2000). Supposing $i = 70^0 - 90^0$, we calculate $P_{rot} \approx 563 - 918$ days. The object is thus synchronized within the measurement errors.

Fekel, Hinkle & Joyce (2004) published values of $v\ \sin i$ for 13 S-type SSs. In this section, if not otherwise stated, we use their measurements.

SY Mus is an eclipsing binary with $i = 95^0.8 \pm 1.7^0$ (Harries & Howarth 1996, 2000), P_{orb} = 624.5 days and $v\ \sin i = 7 \pm 1$ km s^{-1} (Pereira et al.1995; Schmutz et al. 1994; Kenyon & Mikolajewska 1995). We calculate $P_{rot} \approx 830 - 1230$ days. [If we use $R_g \approx 80\ R_\odot$, we get $P_{rot} \approx 480 - 705$ days, a range which includes the orbital period.]

AG Dra is a yellow SS with spectroscopic $P_{orb} = 548.5 \pm 2$ d (Friedjung et al. 2003; Fekel et al. 2000b), and $i \approx 30^0 - 45^0$ (Mikolajewska et al.1995). The cool component is a K2 Ib or II (Zhu et al. 1999). There are two measurements of $v \sin i$: 5.9 ± 1.0 km s^{-1} (de Medeiros & Mayor 1999) and 3.6 ± 1.0 km s^{-1} (Fekel et al. 2004). We adopt $v \sin i = 4.8 \pm 1.0$ km s^{-1}. Skopal (2005) calculated $R_g = 33 \pm 11\ R_\odot$. Following Tomov, Tomova & Ivanova (2000) and the references therein we can adopt $R_g = 30 - 40\ R_\odot$. We then estimate $P_{rot} \approx 130 - 485$ days.

TX CVn has $P_{orb} = 199 \pm 3$ d, $e = 0.16 \pm 0.06$, with the cool component a normal K5III star, and inclination $20° < i < 70°$ (Kenyon & Garcia 1989). The luminosity class could also be II or Ib (Zhu et al. 1999). We calculate $P_{rot} \approx 64 - 242$ days. Pseudosynchronization (see Hut 1981) is expected at $P_{rot} = 0.87 P_{orb}$. The object is thus (pseudo)synchronized within the measurement errors.

AG Peg has $P_{orb} = 818.2 \pm 1.6$ days and $e = 0.110 \pm 0.039$ (Fekel et al. 2000a), normal M3III and $i \sim 40° - 60°$ (Kenyon et al. 1993). We calculate $P_{rot} \approx 400 - 933$ days. The object is thus synchronized within the measurement errors.

V1329 Cyg has $P_{orb} = 963.1 \pm 9.8$ days (Chochol & Wilson 2001) and inclination $i = 86^0 \pm 2^0$ (Schild & Schmid 1997). We calculate $P_{rot} \approx 734 - 1571$ days. The object is thus synchronized within the measurement errors.

T CrB has $P_{orb} = 227.57$ d (Fekel et al. 2000a), and $R_g = 66 \pm 11\ R_\odot$ (Belczynski & Mikolajewska 1998). It should be noted that Skopal (2005) gives $R_g = 75 \pm 12(d/960\text{pc})$, and that a normal M4III would have $R_g \approx 105.5 R_\odot$. The inclination of the system is $i \approx 65^0 - 70^0$ (Stanishev et al. 2004).

We calculate $P_{rot} \approx 391 - 832$ days, which differs from the expectations for synchronization. This result is unexpected, however it appears that this deviation is not statistically significant (see Table 4.7). From Eq.1 we get $\tau_{syn} < 100$ yr. The red giant in T CrB is ellipsoidally shaped (Yudin & Munari 1993). This means that the object has to be synchronized.

BX Mon The orbital parameters of this eclipsing system are:
$P_{orb} = 1401$ days, eccentricity $e = 0.49$ (Dumm et al. 1998);
P_{orb} =1259 d, $e = 0.44$ (Fekel et al. 2000a).

We calculate $P_{rot} \approx 800 - 1278$ days [if we use $R_g \approx 170\ R_\odot$ (see Sect.4.2.3), we get $P_{rot} \approx 970 - 1550$ days]. BX Mon is the only SS with considerable orbital eccentricity in our sample. SSs with $P_{orb} > 800$ days tends to eccentric orbits (Fekel et al. 2007). In a binary with $e = 0.44$, the pseudosynchronization is expected at about $P_{rot} = 0.46\ P_{orb}$ (see Hut 1981).

The time scale for synchronization in SSs is ∼10 times shorter then the circularization time (see Schmutz et al. 1994). All this implies that in this system the red giant is more or less (pseudo)synchronized, but the orbit is not circularized yet. It has therefore to be in the process of circularization.

V443 Her is not eclipsing, with $P_{orb} = 599.4 \pm 2.1$ days (Fekel et al. 2000b), viewed at an inclination $i \sim 30°$ (Dobrzycka et al. 1993). We calculate $P_{rot} = 528 - 1245$ days. The red giant is thus synchronized within the measurement errors.

CI Cyg is an eclipsing binary with orbital period 855.6 days and orbital separation $a = 2.2$ au (Kenyon et al. 1995). Kenyon et al.(1995) have shown that the mass donor is an M5II asymptotic branch giant, filling its tidal surface. They calculated from the eclipse that $R_g/a \sim 0.4 - 0.5$ which means that $R_g \approx 189 - 236\ R_\odot$. We calculate $P_{rot} = 780 - 1270$ days. The object is thus synchronized within the measurement errors.

BF Cyg is an eclipsing binary with P_{orb} = 757.3 days and inclination $i \approx 70 - 90^0$ (Pucinskas 1970, Skopal et al. 1997). If the cool component is a normal M5III giant we expect $R_g = 139.6 \pm 5\%$ $R_\odot$. Mikolajewska et al.(1989) suggested $R_g \sim 75$ $R_\odot$, however Skopal et al. (1997) give $R_g = 260 \pm 20$ $R_\odot$. Using $v \sin i = 4.5 \pm 2$ km s^{-1}, we calculate $P_{rot} \sim 560 - 5660$ days.

There are signs that the red giant is ellipsoidally shaped (Yudin et al. 2005). τ_{syn} for such an object will be short, from Eq.1 we get $\tau_{syn} < 7000$ yr. It means that the red giant has to be tidally locked and most probably the R_g is closer to a value ~ 75 $R_\odot$.

RS Oph has orbital period $P_{orb} = 455.72 \pm 0.83$ days (Fekel et al. 2000a). The inclination is about 30–40° (Dobrzycka & Kenyon1994; Dobrzycka et al. 1996). This will give a $108 < P_{rot} < 197$ days, i.e. 2–3 times less than the orbital period.

RS Oph is a peculiar SS exhibiting different types of activity – recurrent nova eruptions, jet or blob ejections, flickering (see Bode et al. 2006 and references therein).

This is one of the two objects in our sample whose deviation from synchronization is statistically significant (at confidence level >99%, see Table 4.7). The red giant in RS Oph seems to rotate faster than the orbital period, which means that it has to be in a process of deceleration (the expected $\tau_{syn} \leq 5.10^4$ yr).

While there are no doubts about P_{orb}, any of the other parameters ($v \sin i$, inclination, red giant radius) have to be checked with independent measurements.

It is noteworthy that our experiments to measure $v \sin i$ with CCF and spectra from different epochs showed that $v \sin i$ could even be higher (up to 14.5±1.5 km s^{-1}).

CD-43°14304 Schmid et al.(1998) reported a circular orbit, $P_{orb} = 1448 \pm 100$ days. They argued that the presence of phase-dependent Hα variations is attributable to occultation effects, suggesting a relatively high inclination, $i > 45^0$. Spectropolarimetry (Harries & Howarth 2000) gives two possible values for the inclination of the system $i = 57^0 \pm 5^0$ or $i = 122^0 \pm 48^0$. The second corresponds to an improbably large eccentricity for the orbit. Therefore we can accept $\sin i = 0.79 - 0.88$. With our value of $v \sin i$ we calculate $P_{rot} \approx 170 - 321$ days.

However, Schmid et al.(1998) found no evidence for rotational broadening in the cool-giant spectrum and were able to place an upper limit on $v \sin i < 3$ km s^{-1}. We measured $v \sin i =$ 7.2±1.5 km s^{-1}using CCF. The FWHM method gives a similar result. If our CCF result is wrong and that of Schmid et al.(1998) is a correct one, then the object is probably synchronized. To avoid confusion we will exclude this star from the analysis, but an independent check of $v \sin i$ would be valuable.

V2756 Sgr (Hen 2-370, SS73 145). The parameters of the system are not well known. We calculate $P_{rot} < 1595$ days. A photometric period of 243 days is supposed in Hoffleit (1970). This photometric period is not confirmed with radial velocity measurements to be that of the orbit. If this is the orbital period and the red giant is tidally locked, then the inclination of the system would be about $i \sim 15^0$.

Hen 3-1674 is the fastest rotator in our sample. The catalogues indicate that the mass donor is probably M5III star (see Table 4.4 and the references therein). A normal M5III star would have $R_g \approx 90 - 160\ R_\odot$ (van Belle et al 1999) and $M_g \approx 1 - 3\ M_\odot$, which means a break-up velocity of 30-60 $\mathrm{km\,s^{-1}}$. If our measurements and the adopted parameters of the system are correct then Hen 3-1674 rotates close to its critical velocity and has rotation similar to that of D'-type SSs (see Zamanov et al. 2006).

4.3.1 Are the mass donors in S–type symbiotics synchronized (co-rotating)?

Fig. 4.3 shows the rotational period versus the orbital period of the 17 objects in our sample, with a straight line indicating the co-rotation (i.e. P_{rot}=P_{orb}). Most objects are close to this line, which suggests that they are synchronized. In Table 4.7 are given the individual deviations as well as the corresponding probability that the deviation is random. 9 objects are synchronized within the measurement errors (1-σ level). 4 objects have deviations between 1 and 2-σ. Generally, 15 out of 17 are within the 3-σ level. The two objects that are outside of the 3-σ level are RS Oph and CD-43°14304.

The standard χ^2 test gives a probability of $p(\chi^2) < 10^{-6}$ that the co-rotation straight line fits the data points when we use all 17 objects. Here we have considered the errors of the rotational period only, the errors of P_{orb} are supposed to be small (usually they are <2%). The straight line cannot be rejected as a fit to the data at more than 90% confidence level, $p(\chi^2)$=0.127, when the two deviating objects (CD-43°14304 and RS Oph) are excluded. The χ^2 statistic tests how well the data are described by the model, assuming that all the deviations are due to measurement errors and not to intrinsic scatter.

When intrinsic scatter is allowed, as we expect to be the more realistic situation, one can apply the weighted least squares estimator (e.g. Akritas & Bershadi 1996) to find the slope (β) and the intercept (α) of a linear fit in the form

$P_{rot} = \alpha + \beta P_{orb}$ to the data points with measurement errors and non-negligible intrinsic scatter. When all objects are included, we get $\alpha = 204 \pm 49$ and $\beta = 0.14 \pm 0.07$, which is not consistent with P_{rot}=P_{orb} ($\alpha = 0$, $\beta = 1.0$). The situation changes if CD-43°14304 is removed from the sample, then $\alpha = -110 \pm 77$ and $\beta = 0.93 \pm 0.16$. When the deviating recurrent nova RS Oph is removed as well, we obtain $\alpha = -32 \pm 78$ and $\beta = 1.01 \pm 0.17$. The last result is fully consistent with P_{orb}=P_{rot} line ($\alpha = 0$, $\beta = 1$).

Although the synchronization line seems to fit well the data, we still cannot rule out the possibility that one or more outlying objects may determine a false correlation between the variables. Therefore, a rank correlation test appears appropriate. The Spearman rank correlation coefficient between the two periods is 0.61 when all 17 objects were included, and about 0.82 for 16 and 15 objects only. This result implies a significant correlation between the variables, since the p-values are less than 0.02 and 0.002 respectively. The similar Kendall-tau test gives similar results, with p-values less than 0.01 for all cases.

The objects that deviate significantly from the P_{orb}=P_{rot} line are RS Oph (a peculiar SS as noted above) and CD-43°14304 (with possible error in the v $\sin i$ measurement, see Sect.4.3). Taking into account the uncertainties of their P_{rot}, one finds that the probabilities for a random deviation are less than 0.01 for them (see Table 4.7), while for all the other 15 stars this idea cannot be rejected at the 0.01 significance level. In other words the null hypothesis that all S-type SSs with well measured v $\sin i$ are synchronized (excluding RS Oph and CD-43°14304) cannot be rejected at the 99% confidence level.

An additional test that may give some clues about the extent of synchronization of the periods is the K-S test of how much $(P_{rot} - P_{orb})/\sigma$ deviates from the normal distribution. Even when all 17 stars are included, the p-value of the K-S statistics is slightly less than 10%. When only the above 15 objects are included, the distribution becomes much narrower (mean = 0.15, σ=1.23, K-S statistics is 0.38), with a standard deviation comparable to the measurement errors of P_{rot}, $< \sigma/P_{rot} >= 0.53$. This means that the hypothesis that the sample comes from a normal distribution cannot be rejected statistically.

We see that the null hypothesis for synchronization of the red giants in symbiotic stars cannot be rejected statistically (except probably for RS Oph).

4.3.2 Clues to the orbital periods

Up to now, out of 188 SSs, the orbital elements and binary periods are well known for ∼40 objects only (and they are all S–type). The derived orbital periods are in the range 200 – 2000 days (Mikołajewska 2003).

Table 4.7: The deviations of the individual objects from the line P_{rot} =P_{orb}. In the second column the deviations are given in units of σ, where σ is the individual error of P_{rot}. The third column gives the probability for random deviation. To reject the null hypothesis (synchronization) at 99% confidence level, $p(\chi^2)$ has to be smaller than 0.01.

Object	deviation [σ]	$p(\chi^2)$
SY Mus	2.2	0.026
AG Dra	1.4	0.175
BX Mon	1.2	0.223
TX CVn	0.5	0.605
T CrB	1.7	0.082
V443 Her	0.8	0.423
CI Cyg	0.7	0.489
AG Peg	0.6	0.569
V1329 Cyg	0.5	0.651
BF Cyg	0.9	0.361
AR Pav	1.2	0.233
V343 Ser	2.2	0.028
BD-21°3873	0.8	0.399
CD-43°14304	15.9	$<10^{-6}$
FG Ser	0.5	0.610
RS Oph	6.7	$<10^{-6}$
RW Hya	0.4	0.655

Because the orbital periods of the majority of SSs are unknown, an indirect method to obtain P_{orb} is to measure $v \sin i$. If the mass donors in SSs are co-rotating ($P_{rot} = P_{orb}$), we can find clues for the orbital periods via the simple relation $P_{orb}\, v_{rot} = 2\pi R_g$, where P_{orb} is the orbital period, v_{rot} and R_g are the rotational velocity and radius of the giant, respectively. The underlying suppositions are: **(1)** corotation (see Sect. 4.3.1) and **(2)** rotational axis of the red giant perpendicular to the orbital plane (see Sect. 4.2.3 and references therein).

It could be useful in the case of eclipsing binaries, where $\sin i \approx 1$ and $v \sin i \approx v_{rot}$, however in such cases it is easy to find P_{orb} with photometry. If the inclination is unknown, we can only put an upper limit, $P_{orb} \lesssim P_{ul}$, where $P_{ul} = 2\pi R_g / v \sin i$. To see how useful this predictor is, we calculated the upper limits for the objects with known orbital periods, and we get $P_{ul}/P_{orb} \sim 0.5 - 1.5$.

For the objects with unknown periods, the upper limits for P_{orb} calculated in this way are given in the last column of Table 4.4. These upper limits are in the interval 100–1500 days. Most of them are similar to those of the measured orbital periods in S-type SSs. However, it seems that for AS 255 and Hen 3-1674, P_{orb} could be as short as $\lesssim$150 days.

4.3.3 Conclusions

We have observed 30 S-type symbiotic stars with the FEROS spectrograph. We have measured the rotational velocities of the mass donors for 29 of them by the means of the CCF method (for V3804 Sgr we did not get a meaningful CCF). The results of the CCF method have been checked by the FWHM measurements. The main results are:

(1) The projected, rotational velocities of the cool components in S-type symbiotic stars are from 3.5 $\mathrm{km\,s^{-1}}$ up to 52 $\mathrm{km\,s^{-1}}$ and 90% of them are in the interval from 4.5 $\mathrm{km\,s^{-1}}$ to 11.7 $\mathrm{km\,s^{-1}}$.

(2) In our sample of 17 S–type SSs with known orbital periods, 9 are synchronized within the measurement errors (1-σ level). If we exclude the doubtful object CD-43°14304 and the recurrent nova RS Oph, **all remaining 15 objects are synchronized within the 3-σ level**. In other words, the null hypothesis that these 15 objects are synchronized can not be rejected statistically at the 99% confidence level.

(3) Among all objects with $v \sin i$ measured by us the deviation from synchronization is statistically significant (at the 99% confidence level) only for RS Oph. The red giant in this peculiar object seems to rotate faster than the orbital period.

Table 4.8: Journal of observations and projected rotational velocities. In the table are given as follows: the name of the object, the IR type, date of observation (YYYY-MM-DD), the modified Julian Date (JD - 2400000.5) of the start of the observation, the spectral type. $v \sin i$ is the projected rotational velocity of the cool giant as measured with FWHM and CCF methods. If other measurements of $v \sin i$ exist, they are also given in the last column.

object	IR	Date-obs	MJD-obs	Sp	$v \sin i$ FWHM [$\mathrm{km\,s^{-1}}$]	$v \sin i$ CCF [$\mathrm{km\,s^{-1}}$]	other [$\mathrm{km\,s^{-1}}$]
AG Peg	S	2004-10-02	53280.0676	M4III	8.5±1.5	7.5±1.5	4.5±1[a]
BX Mon	S	2004-11-05	53314.2610	M5III	11.0±1.5	9.4±1.5	6.8±1[a]
Hen 3-905	S	2005-02-02	53403.1847	M3III	9.2±1.5	7.3±1.5	
LIN 358	S	2004-10-13	53291.0994	K5III	4.8±1.5	5.9±1.5	
PN Sa 3-22	S	2005-02-01	53402.2405	M4.5III	9.7±1.5	9.8±1.5	
V694 Mon	S	2004-11-05	53314.3158	M6III	10.3±1.5	– – –	
V840 Cen	–	2005-02-01	53402.2858	K5III	31.5±3.0	24.4±3.0	
WRAY 15-157	D'	2004-11-06	53315.3276	G5III	44±5	37±5	
AS201	D'	2004-11-14	53323.3309	F9III	27±3	29.3±3	25±5[b]

[a]Fekel et al. (2003), [b]Pereira et al. (2005).

(4) For 22 S-type SSs with unknown parameters, we give clues as to what their orbital periods could be.

4.4 Fast rotation in S-type symbiotics (Zamanov et al. 2008)

4.4.1 Data: FEROS, VLT/UVES, ELODIE, catalogs

The data have been obtained from 2004 October to 2005 February with the same set-up – the FEROS spectrograph at the 2.2m telescope of ESO (La Silla). These are S- and D'-type SSs with $0^h < RA < 12^h$, and catalogue magnitude brighter than $V < 12.5$.

The details of the observational set-up, data reduction and the techniques of $v \sin i$ measurements are given in Zamanov et al. (2006, 2007). Here we also apply two techniques of $v \sin i$ measurements: FWHM and Cross-Correlation Function (CCF).

The new data are presented in Table 4.8. Here the IR type of the objects and the spectral types of the mass donors are taken from the catalogue of Belczyński et al. (2000). This catalogue lists the spectral type of LIN 358 as a mid-K giant; we assume that it is K5III. For V694 Mon the CCF method does not give a meaningful result, due to the highly complicated emission/absorption lines in the spectrum. For this object we will use the result of the FWHM method, for all other objects the CCF measurements are more reliable.

Combining our data and data from the literature, we have $v\ \sin i$ measured for all southern S- and D'-type SSs from the Belczyński et al. (2000) catalogue with $V < 12.5$. This sample should have no biases in the rotational speed of the cool giant, even though the sample is flux limited.

Catalog data: The giants of S-type SSs with measured $v\ \sin i$ are of spectral types from K2III to K5III and from M0III to M6III.

We searched for published data of $v\ \sin i$ of giants of similar spectral type and found totally 362 giants in the interval K2-K5III in de Medeiros and Mayor (1999) and Massarotti et al. (2008). In the interval M0III-M6III we found 10 objects in Glebocki et al. (2001), 4 in Hünsch et al.(2004) and 15 in Massarotti et al. (2008).

Archive spectra: Because we have found only 29 field M giants with measured $v\ \sin i$, we searched in the archives for spectra of red giants in the interval M0III-M6III.

From the UVES Paranal Observatory Project (Bagnulo et al., 2003), we downloaded spectra of 17 M giants and from the ELODIE archive at Observatoire de Haute-Provence (Moultaka et al. 2004) we took spectra of 11 more objects. We applied the FWHM and CCF methods to measure the $v\ \sin i$ parameter in each case. The results are summarized in Table 4.9.

For the CCF measurements, the calibration of UVES values comes from an unpublished paper (Melo et al. in preparation). For ELODIE, we used the same technique as usual but using a $\sigma_0 = 4.9\ \mathrm{km\,s^{-1}}$, taken as the average value of Delfosse et al. (1998). This gives an error of $\pm 2.0\ \mathrm{km\,s^{-1}}$ in the $v\ \sin i$.

4.4.2 Statistical tests

In Fig.4.4, the projected rotational velocity ($v\ \sin i$) is plotted versus the spectral type of the giant. The error in the spectral type of SSs is adopted as ±0.5. In Fig.4.4, it is seen that in the most cases the mass donors in SSs rotate faster than the field giants. To test the visual impression, as a mathematical (statistical) approach we use the Kolmogorov-Smirnov and Mann-Whitney U-tests. These statistical tests are performed in the spectral type bins K2III-K5III, M0III-M6III, M2III-M5III. These bins are selected following the distribution of symbiotics with known $v\ \sin i$, and avoiding the interval K6III-K9III, where we do not find

Table 4.9: Projected rotational velocities of M giants, based on archive spectra from UVES and ELODIE archives. In the table are given as follows: the name of the object, the spectral type, the projected rotational velocity ($v \sin i$) as measured with FWHM and CCF methods with the corresponding errors.

object	Sp	$v \sin i$ FWHM [$\mathrm{km\,s^{-1}}$]	$v \sin i$ CCF [$\mathrm{km\,s^{-1}}$]
UVES			
Menkar	M1.5IIIa	2.5±1.5	2.8±1.5
HD 102212	M1III	1.0±1.0	1.1±1.4
HD 119149	M1.5III	2.3±1.0	1.9±1.5
HD 123934	M1III	1.0±1.0	2.3±0.9
HD 210066	M1III	1.0±1.0	0.6±2.8
HD 92305	M0III	1.7±1.5	1.2±0.7
HD 219215	M2III	1.0±1.0	0.0±1.0
HD 120052	M2III	1.5±1.5	1.0±1.5
HD 11695	M4III	2.5±1.0	3.9±0.9
HD 118767	M5III	7.5±1.5	7.7±1.0
HD 123214	M4III	3.0±1.0	4.4±0.7
HD 130328	M3III	5.5±2.0	8.2±1.7
HD 189124	M6III	5.3±1.0	9.1±0.7
HD 189763	M4III	1.5±1.5	4.5±1.9
HD 213080	M4.5III	1.5±1.5	4.5±0.8
HD 214952	M5III	2.5±1.5	6.3±2.8
HD 224935	M3III	2.5±1.5	3.9±0.6
ELODIE			
HD 006860	M0III	1.5 ±1.5	5.6±2.0
HD 018191	M6III	12.0 ±2.0	9.6±2.0
HD 042787	M2III	2.0 ±1.5	5.2±2.0
HD 046784	M0III	2.8 ±1.5	5.4±2.0
HD 097778	M3III	5.5 ±1.5	7.6±2.0
HD 167006	M3III	5.5 ±1.5	5.2±2.0
HD 168720	M1III	5.0 ±1.0	5.2±2.0
HD 184786	M4.5III	6.5 ±2.0	7.8±2.0
HD 216131	M2III	1.0 ±1.0	2.5±2.0
HD 218329	M2III	3.8 ±1.5	5.0±2.0
HD 219734	M2III	5.0 ±1.0	4.9±2.0

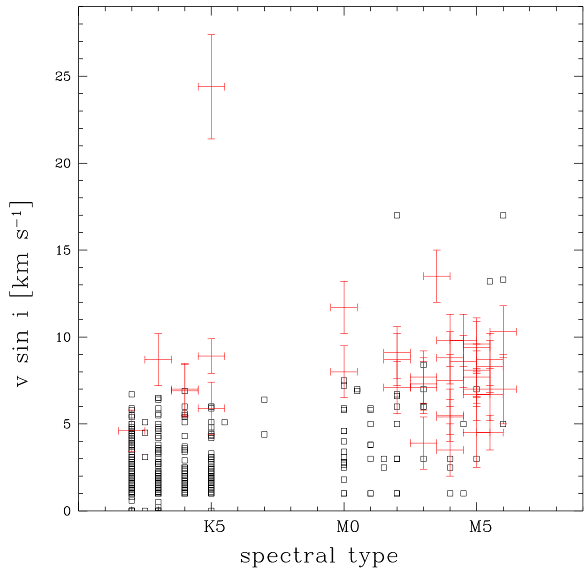

Figure 4.4: Projected rotational velocity ($v \sin i$) versus the spectral type of the giant in the spectral interval K2III-M6III. S-type SSs are indicated with error bars. The field giants are plotted with squares.

symbiotics. It deserves noting that Keenan & McNeil (1989) do not consider K6III-K9III as full spectral subclasses, therefore the lack of objects.

Bin K2-K5 giants The histograms for K giants are presented in Fig. 4.5. From Fig.4.4 and Fig.4.5, it is seen that the field giants and the giants in S–type symbiotic systems occupy different areas of $v \sin i$ values and that the K-giants in S–type SSs rotate faster than field giants.

For the field K giants typically $v \sin i < 3$ km s^{-1}. For K giants in symbiotics $4.5 \leq v \sin i \leq 25$ km s^{-1}.

For 363 field K2III-K5III giants we calculate a mean $v \sin i$=2.2 km s^{-1}, median $v \sin i$=1.8 km s^{-1}, and standard deviation of the mean $\sigma = 1.45$ km s^{-1}.

For 7 K2III-K5III giants in symbiotics, we get a mean $v \sin i$= 9.5 km s^{-1}, median $v \sin i$=7.0 km s^{-1}, and standard deviation of the mean σ =6.7 km s^{-1}. If we exclude V840 Cen from the sample we calculate a mean $v \sin i$= 7.0 km s^{-1}, median $v \sin i$=7.0 km s^{-1}, and standard deviation of the mean σ =1.6 km s^{-1}. On average SSs rotate $2-4$ times faster than the field K giants.

The Kolmogorov-Smirnov test gives a probability of only 7.10^{-6} (KS statistics =0.90) that both distributions arise from the same parent population.

The comparison of the medians (Mann-Whitney U-test) for the symbiotic and field giants gives a probability of the median $v \sin i$ of the symbiotic giants being higher than that of the

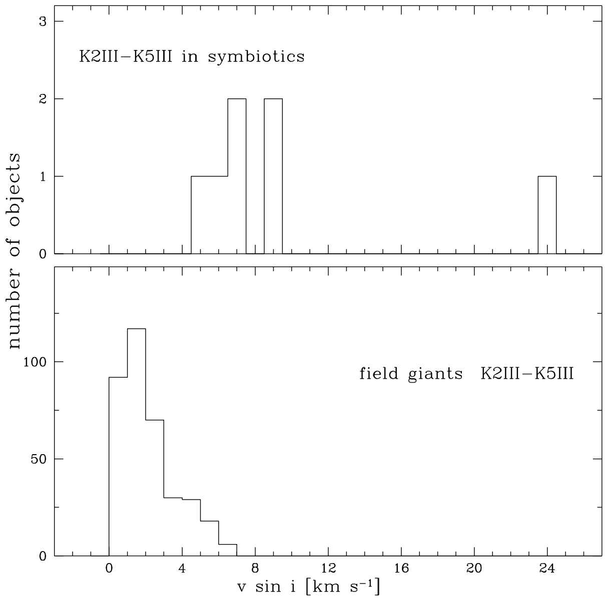

Figure 4.5: The histogram of $v \sin i$ for K2-K5 giants in symbiotics (upper panel) compared to the relevant distribution for field giants of the same spectral classes (bottom panel).

field giants > 0.99999 (U statistics = 1659).

It is therefore statistically certain that the K giants in symbiotics rotate faster than the field K giants. It has to be noted that the symbiotic V840 Cen rotates unusually fast (see Table 4.8) and it is the most rapid rotator among giants in the bin K2III-K5III known until now.

Bin M0-M6 giants: For 53 field M0III-M6III giants we calculate a mean $v \sin i$=4.8 km s^{-1}, median $v \sin i$=3.8 km s^{-1}, and standard deviation of the mean $\sigma = 3.6$ km s^{-1}.

For 32 M0III-M6III giants in symbiotics, we get a mean $v \sin i$= 9.2 km s^{-1}, median $v \sin i$=8.0 km s^{-1}, and standard deviation of the mean σ =8.1 km s^{-1}.

The fastest rotator among M giants is the symbiotic star Hen 3-1674, which rotates almost at break-up velocity. This object in not plotted on the figures because it is too far from the other values.

The distributions of $v \sin i$ in this bin are plotted in Fig.4.6. The Kolmogorov-Smirnov test gives a probability of only 3.5×10^{-7} (KS statistics =0.60) that both distributions arise from the same parent population.

The comparison of the medians (Mann-Whitney U-test) for the symbiotic and single giants gives a probability of the median $v \sin i$ of the symbiotic giants being higher than that of the

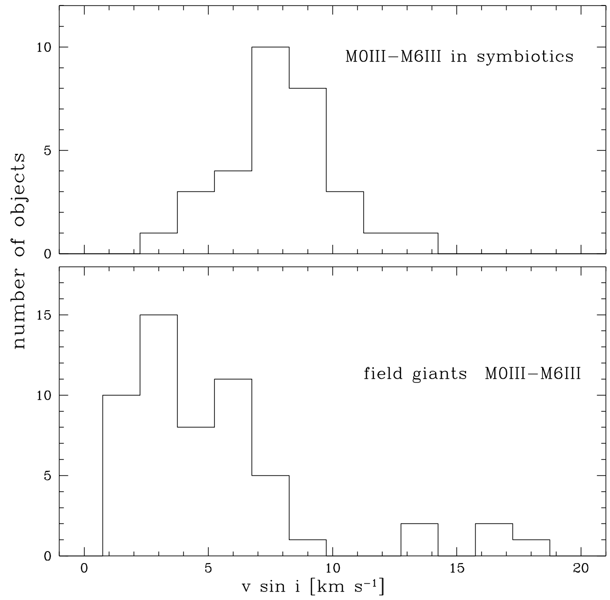

Figure 4.6: The distribution of $v \sin i$ for M0-M6 giants in symbiotic binaries (upper panel) compared to the distribution for the field M giants (bottom panel).

field giants 0.999994 (U statistics = 273).

In the above statistical test we used the FWHM measutements of the UVES and ELODIE spectra. If in the statistical test we use the CCF measurements, we obtain very similar results. The KS-test gives a probability 5×10^{-6} (KS statistics =0.57) and the U-test gives 0.9999999 (U statistics = 353.5).

Bin M2-M5 giants: This bin is selected because (1) it is in the mid of symbiotic M giants, and (2) we have 23 symbiotics and 23 field giants inside. The histograms for M2III-M5III giants are presented in Fig. 4.7. For the 23 field giants in this bin with known $v \sin i$, we calculate mean $v \sin i$= 4.8 km s^{-1}, median $v \sin i$= 5.0 km s^{-1}, and standard deviation of the mean $\sigma = 3.55$ km s^{-1}.

For 23 M giants in symbiotics we get a mean $v \sin i$= 7.7 km s^{-1}, median $v \sin i$= 7.7 km s^{-1}, and standard deviation of the mean $\sigma = 2.2$ km s^{-1}.

The Kolmogorov-Smirnov test gives a probability of 1.1×10^{-4} (K-S statistics = 0.65) that both distributions are extracted from the same parent population. The U-test gives a probability of 0.99995 (U statistics= 442.5), for the hypothesis that the median $v \sin i$ of the symbiotic M-giants is higher than the median of the single M-giants.

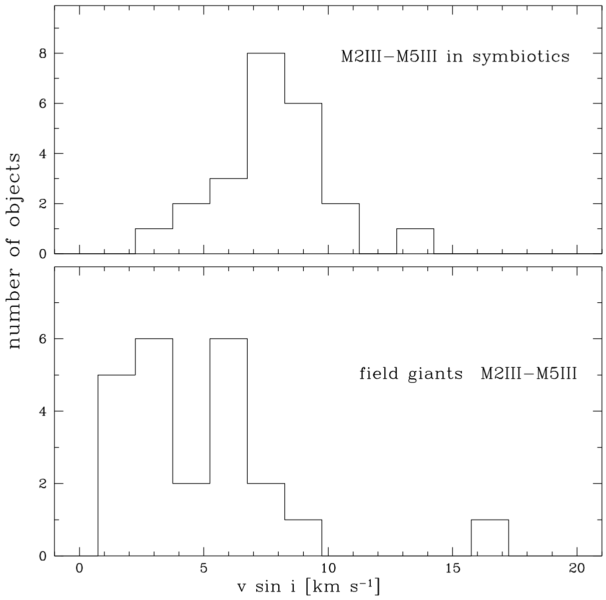

Figure 4.7: The distribution of $v\ \sin i$ for the bin M2III-M5III in symbiotic binaries (upper panel) and for the field giants (bottom panel).

If in the statistical tests we use CCF measurements for UVES and ELODIE spectra, we obtain KS-statistics=0.52, probability 10^{-9}, and U-statistics= 134.5, probaility 0.999999.

Additional checks: From Fig.4.4, it is seen that in the M0III spectral class the two fastest rotators are SSs.

As an additional check we have performed statistical test in bin M0III-M4III, where we have 16 symbiotics and 45 field giants inside. The histograms for M0III-M4III giants are presented in Fig. 4.8. The Kolmogorov-Smirnov test gives a probability of 1×10^{-9} (K-S statistics = 0.64) that both distributions are extracted from the same parent population. The U-test gives a probability of 0.999999 (U statistics= 117.5), for the hypothesis that the median $v\ \sin i$ of the symbiotic M-giants is higher than the median of the single M-giants. The statistical tests in M0III-M3III (10 SSs and 45 field giants) give 2×10^{-5} (K-S statistics = 0.83) and 0.999977 (U=38.0). In bin M4III-M6III (21 SSs and 12 field giants) the tests do not give statistically significant difference: 0.1 (KS-statistics=0.44) and 0.85 (U statistics= 98).

The mean values of $v\ \sin i$ for the M giants are presented in Table 4.10. All but one of the mean $v\ \sin i$ values of SSs are higher than those of the field giants. The majority of the field M giants rotate at about $v\ \sin i \sim 1 - 6\ \mathrm{km\,s^{-1}}$, while the symbiotic M giants rotate at $v\ \sin i$

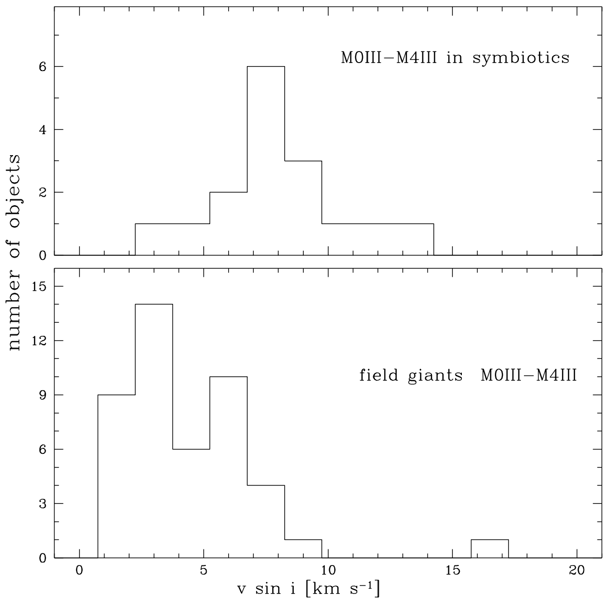

Figure 4.8: The distribution of $v\ \sin i$ for the bin M0III-M4III in symbiotic binaries (upper panel) and for the field giants (bottom panel).

Table 4.10: Projected rotational velocities of M giants. In the table are given as follows: the spectral type, the mean projected rotational velocity ($v\ \sin i$, in $\mathrm{km\,s^{-1}}$), standart deviation of the mean (σ, in $\mathrm{km\,s^{-1}}$), the number of objects. In the second column are given the values for the field M giants, in the third - for the symbiotic stars.

Sp	**field giants** mean$\pm\sigma$ (N)	**symbiotics** mean$\pm\sigma$ (N)
M0-M1 III	3.7±1.9(23)	9.9±2.6(2)
M1.5-M2 III	4.8±4.1(14)	8.3±1.1(3)
M2.5-M3 III	5.5±2.0(8)	6.5±1.8(4)
M3.5-M4 III	2.2±1.0(3)	7.7±3.3(7)
M4.5-M5 III	5.5±4.0(5)	7.9±1.7(9)
M5.5-M6 III	12.1±5.1(4)	7.6±2.0(6)

$\sim 4 - 14$ km s^{-1}

Our calculations presented above show that the M giants in symbiotics rotate faster (on average 1.5 times faster) than the field M giants, at least for the spectral interval from M0III to M5III.

4.4.3 Fast rotation – reasons and after-effects

Reasons for the fast rotation: Soker (2002) discussed in detail three possible mechanisms for speeding-up the rotation of the mass donors in SSs: **(i)** synchronization; **(ii)** accretion during the main sequence phase of what is now the red giant; **(iii)** backflowing material.

In the light of our results, the synchronization plays an important role. Other mechanisms that can also operate in single giants as well as in SSs are:

(iv) angular momentum dredge-up when the convective envelope approaches the core region of the giant (Simon & Drake 1989).

(v) planet engulfment during the giant phase.

The discovery of giant planets around solar type stars poses the question as to what happens when a MS star evolves into a giant and engulfs the planet (see Massaroti et al 2008 and references therein). Assuming for a typical M3III star $R_g = 71.5\ R_\odot$ and $M = 1.6\ M_\odot$, we calculate that an ingestion of a planet with a mass $0.01\ M_\odot$ can speed up the rotation of the giant by up to 40 km s^{-1}.

Some of the symbiotics belong to the old disk population (Wallerstein 1981). Smith et al. (1996, 1997) have shown that the symbiotics AG Dra and BD-21^{0}3873 contain metal poor giants. We have selected from Carney et al. (2003, 2008a,b) 40 metal poor K giants with $3900 \leq T_{eff} \leq 4500$ and $0.5 \leq \log g \leq 1.5$ and [Fe/H]≤ -0.8. The statistical tests do not indicate statistically significant differences between symbiotic K giants and metal poor giants. Reasons for the fast rotation (and/or line broadening) observed in the spectra of metal poor giants are considered inherited rotation, induced rotation due to a stellar or planetary companion, and more recently macroturbulence (see also Carney et al. 2003, 2008b).

Because the symbiotic stars rotate faster than the field giants, they probably can help us to understand in which cases the binarity and in which cases the planet ingestion or some other mechanism (i.e. inherited rotation, macroturbulence) is responsible for the fast rotation (or line broadening).

After-effects of the fast rotation: Fast rotation should enhance the mass loss in the equatorial regions, like the disks of the classical Be stars. The IR-disks of D'-type symbiotics are (probably) a direct result of the fast rotation. A circumstellar medium that is significantly denser in the equatorial regions of the binary than at the poles is already detected in RS Oph (Bode et al. 2007), indicating that circumbinary disks (non-dusty) can also be formed in S-type symbiotics.

Mass-loss rates for the symbiotic giants derived from cm and mm/submm radio observations (Seaquist, Krogulec & Taylor 1993; Mikołajewska, Ivison & Omont 2003) and from IRAS data (Kenyon, Fernandez-Castro & Stencel 1988) are systematically higher than those reported for field giants. The relation between rotation and mass loss is not yet exactly quantified (see Wilkinson et al 2005). Nieuwenhuijzen & de Jager (1988) find $\dot{M} \propto (v \sin i)^{2.46}$. Following this relation, we estimate that if the symbiotic giants rotate 1.5-4.0 times faster than the field giants, they should have 3-30 times larger mass loss rates. This matches the observed values (see Fig.2 in Mikolajewska, Ivison & Omont 2003) and means that the rapid rotation of the mass-donors is the likely physical reason that increases mass loss in SSs over that exhibited by normal giants.

Smith et al. (1996) point out that the Barium and CH stars are similar to symbiotics but do not trigger symbiotic like activity. Because the mass loss and/or rotation of the mass donors can be the reasons for the lack of activity, it will be interesting to measure their rotational velocities and to compare them with symbiotics and field giants.

4.4.4 Jet ejecting symbiotics

Bipolar ejections (jets) are rare phenomena for the accreting white dwarfs in symbiotics (e.g. Leedjärv 2002). Among our sample of SSs with known $v \sin i$ there are 4 objects with detected jet/blob ejection: RS Oph (Iijima et al. 1994, Zamanov et al. 2005), MWC 560 (Tomov et al. 1990, Schmid et al. 2001), StHα190 (Munari et al. 2001) and Hen 3-1341 (Tomov, Munari, & Marrese 2000).

In the recurrent nova RS Oph, the red giant probably rotates faster than the orbital period.

V694 Mon (MWC 560) is seen almost pole-on. The jet (orbit) inclination is $i < 16^0$ (Schmid et al. 2001) and probably the orbital period $P_{orb} \approx$1931 day (see Gromadzki et al. 2007 and references therein). For a typical M6III star we assume a radius of 147.9 $R_\odot$ (van Belle et al. 1999). If we assume that the rotational axis of the red giant is perpendicular to the orbital plane, we calculate a rotation period of the red giant $P_{rot} \approx 180$ d, which means that $P_{rot} << P_{orb}$.

The rotation period of StHα190 is $P_{rot} \leq 5$ d. If we assume the typical orbital period of a symbiotic binary $P_{orb} \geq 200$ d (see Mikolajewska 2003), then we get $P_{rot} << P_{orb}$.

The rotation period of Hen 3-1341 is possibly $P_{rot} \approx 168$ d (assuming $R_g = 57.8\ R_\odot$, $i \approx 30^0$), which is less than the typical orbital periods of S-type SSs.

These 4 objects point to the possibility that the jet ejections in symbiotics are detected in systems where the mass donors rotate faster than the orbital period (i.e. $P_{rot} < P_{orb}$). In this connection candidates for detection of such ejections should be considered among the fast rotating SSs V840 Cen, Hen 3-1213, Hen 3-1674, as well as all D'-type symbiotics.

4.4.5 MWC 560 – orbital eccentricity

We present projected rotational velocity measurements of the red giant in the symbiotic star MWC 560, using the high-resolution spectroscopic observations with the FEROS spectrograph. We find that the projected rotational velocity of the red giant is $v \sin i = 8.2 \pm 1.5$ km s^{-1}, and estimate its rotational period to be $P_{\rm rot} = 144$ - 306 days. Using the theoretical predictions of tidal interaction and pseudosynchronization, we estimate the orbital eccentricity $e = 0.68 - 0.82$.

Introduction: MWC 560 (V694 Mon) was discovered as an object with bright hydrogen lines (Merrill & Burwell 1943). It is a symbiotic binary system, which consists of a red giant and a white dwarf (Tomov et al. 1990; Michalitsianos et al. 1993). The orbital period is supposed to be $P_{\rm orb} \approx 5.3$ yr (Doro-shenko, Goranskij & Efimov 1993). The most spectacular features of this object are the collimated ejections of matter with velocities of up to ~ 6000 km s^{-1} (Tomov et al. 1992; Stute & Sahai 2009) and the resemblance of its emission line spectrum to that of the low-redshift quasars (Zamanov & Marziani 2002).

The jet ejections are along the line of sight and the system is seen almost pole-on ($i < 16°$). This makes it difficult to obtain the orbital parameters using the radial velocity variations, and impossible to observe effects such as eclipse or illumination.

To improve our understanding of this object, we aim here to: (1) measure the projected rotational velocity of the red giant ($v \sin i$) from high resolution spectra, and (2) use our measured $v \sin i$to find the eccentricity e of the orbit, on the basis of the theory for pseudosynchronization in binary stars.

Spectral Data and $v \sin i$ measurement

Observations: We analyzed 21 high resolution spectra of MWC 560, obtained with the FEROS spectrograph. FEROS is a fiber fed echelle spectrograph, providing high resolution of

$\lambda/\Delta\lambda = 48000$ and an wide wavelength coverage from about 4000 Å to 8900 Å in one exposure (Kaufer et al. 1999). 16 of the analyzed spectra are from our observations of the MWC 560 with the 2.2-m telescope at ESO, La Silla (ESO program 074.D-0114). The remaining spectra (5), are downloaded from FEROS Spectroscopic Database at the LSW Heidelberg www.lsw.uni-heidelberg.de/projects/instrumentation/Feros/ferosDB/ and were obtained when FEROS was mounted on the 1.52-m telescope at La Silla. A log of observations is given in Table 4.11. Details of the data processing are given in Zamanov et al. (2007). In Fig. 5.1 we show the average spectrum derived from the 16 spectra obtained by 2.2-m telescope.

Symbiotic stars have composite spectra with three main sources of radiation – red giant, hot component and nebula. Modeling of a few objects is given in Skopal (2005). Fig. 5.1 also shows a synthetic spectrum of a M5III star with parameters: $T_{\rm eff} = 3424$ K, $\log g = 0.5$, $\xi = 3$ km s^{-1}, $v \sin i = 8.2$ km s^{-1}, and 64% contribution of the giant at $\lambda = 8800$ Å (see 2.2.).

$v \sin i$ measurement: We measure $v \sin i$ by comparing the FWHM of spectral lines of observed and synthetic spectra. The procedure is similar to that described in Fekel (1997).

We synthesized spectra in the spectral region $\lambda = 8750$ - 8850 Å. Atmospheric parameters $T_{\rm eff} = 3424$ K, $\log g = 0.5$ (typical for a M5III star, see van Belle et al. 1999), the instrumental profile for our FEROS spectra, and solar abundances were the input parameters.

We adopt a microturbulent velocity $\xi = 3$ km s^{-1}. This value is the same as accepted by Fekel, Hinkle & Joyce (2004) and it is close to the values for other symbiotics.

A grid of synthetic spectra for projected rotational velocities from 0 km s^{-1} to 20 km s^{-1} was calculated. $v \sin i$ was calculated by measuring the full width at half maximum (FWHM) of twelve observed spectral lines. These were compared to the spectral line half-widths from the synthetic spectra. We thereby derive a mean $v \sin i = 8.2$ km s^{-1}, and a standard deviation of the mean $\sigma = 0.4$ km s^{-1}using all 21 spectra. we note that if we adopt a microturbulent velocity $\xi = 2$ km s^{-1} we would have measured $v \sin i = 9.4$ km s^{-1}. For the error of our measurements we adopt a conservative value ± 1.5 km s^{-1}, which also includes the uncertainty of $\xi = 3 \pm 0.5$ km s^{-1} and the error of our method. We therefore estimate our final measurement to be $v \sin i = 8.2 \pm 1.5$ km s^{-1}.

Parameters of MWC 560: Meier et al. (1996) classified the cool component of MWC 560 as M5III-M6III giant. Mürset & Schmid (1999) give M5.5III - M6III as its stellar type. According to van Belle et al. (1999), a typical M5III giant has the following pa-

Table 4.11: Spectral observations of MWC 560. The columns in the table represent: modified Julian Date (MJD) of the start of the exposure, exposure time, and the measured projected rotational velocity ($v\ \sin i$) of the mass donor.

MJD	exp-time [sec]	$v\ \sin i$ [$\mathrm{km\,s^{-1}}$]
2.2-m telescope		
53314.279	300	8.5
53314.283	300	8.6
53314.287	300	7.9
53314.291	300	7.8
53314.295	300	8.0
53314.299	300	8.2
53314.303	300	8.2
53314.308	300	8.5
53314.312	300	8.8
53314.316	300	7.8
53314.320	300	8.3
53314.324	300	7.7
53314.328	300	8.6
53314.332	300	7.9
53314.336	300	8.1
53314.340	300	8.5
1.52-m telescope		
51133.223	1200	7.8
51131.248	2400	8.9
51135.283	1200	7.8
51136.259	900	7.9
51141.315	1200	8.2

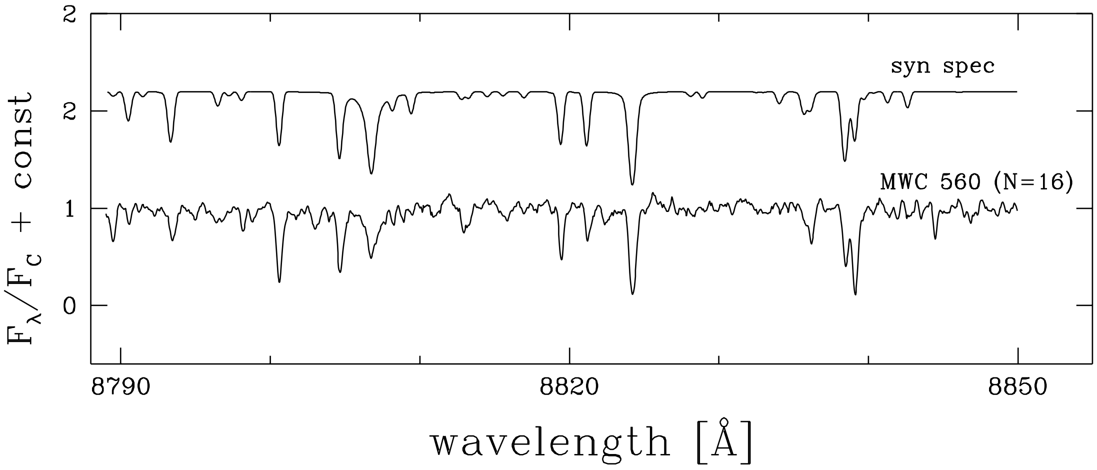

Figure 4.9: The average spectrum of MWC 560 in the range $\lambda = 8790 - 8850$ Å, obtained from 16 exposures with FEROS spectrograph at the 2.2-m telescope at La Silla, and a synthetic spectrum using $T_{\rm eff}$=3424 K, $\log g = 0.5$ $\xi = 3$ km s^{-1}, $v \sin i$= 8.2 km s^{-1}, and 64% contribution from the giant.

rameters: $R_{\rm g} = 139.6 \pm 5.6$ R$_\odot$, $T_{\rm eff} = 3424$ K, $L_{\rm g} \sim 2410$ $L_\odot$, and a typical M6III giant: $R_{\rm g} = 147.9 \pm 7.7$ $R_\odot$, $T_{\rm eff} = 3375$ K, $L_{\rm g} \sim 2560$ $L_\odot$. We adopt for the M giant in MWC 560 $R_{\rm g} = 140 \pm 7$ $R_\odot$ and $L_{\rm g} \sim 2400$ $L_\odot$.

For the masses of the red giant and white dwarf we will assume $M_{\rm g} = 1.7$ $M_\odot$ and $M_{\rm wd} = 0.65$ $M_\odot$, respectively. These values are the average masses of the components of the symbiotic stars (Mikołajewska 2003). Concerning the orbital period, we use $P_{\rm orb} = 1931 \pm 162$ day (Gromadzki et al. 2007). With the above values of the parameters assumed, we derive the semimajor axis of the orbit to be $a \approx 860$ $R_\odot$.

The jet (orbit) inclination angle to the line of sight is $i < 16^\circ$, and the white dwarf accretes at a rate $\dot{M}_{\rm acc} \approx 5 \times 10^{-7}$ $M_\odot$ (Schmid et al. 2001).

Rotation and pseudosynchronization: In a binary with a circular orbit the rotational period of the primary, $P_{\rm rot}$, reaches an equilibrium value at the orbital period, $P_{\rm rot} = P_{\rm orb}$. However, in a binary with an eccentric orbit, the tidal force acts to synchronize the rotation of the mass donor with the motion of the compact object at the periastron – the effect called pseudosynchronous rotation (Hall 1986). The corresponding equilibrium (i.e. pseudosynchronization) is reached at a value of $P_{\rm rot}$ which is *less* than $P_{\rm orb}$, the amount less being a function of the orbital eccentricity e. Hut (1981) showed that the period of pseudosynchronization, $P_{\rm ps}$, is :

$$P_{\rm ps} = \frac{(1+3e^2+\frac{3}{8}e^4)(1-e^2)^{\frac{3}{2}}}{1+\frac{15}{2}e^2+\frac{45}{8}e^4+\frac{5}{16}e^6} P_{\rm orb}. \tag{4.5}$$

When the eccentricity tends to zero, $P_{\rm ps}$ tends to $P_{\rm orb}$ ($e \to 0$ and $P_{\rm ps} \to P_{\rm orb}$).

Orbital eccentricity of MWC 560: In order to determine the orbital eccentricity of MWC 560, we need to calculate $P_{\rm rot}$ for the mass donor. We use

$$P_{\rm rot} = \frac{2\pi R_{\rm g} \sin i}{v\ \sin i}. \tag{4.6}$$

The underlying assumption is that the rotational axis of the mass donor is perpendicular to the orbital plane.

Using the value for $v \sin i = 8.2 \pm 1.5$ km s^{-1} (Sect.5.1.1), $R_{\rm g} = 140 \pm 7\ R_\odot$, and $i = 12° - 16°$ (Schmid et al. 2001), we calculate $P_{\rm rot} = 144 - 306$ days. This value is considerably less than the orbital period, $P_{\rm orb} = 1931 \pm 162$ days. MWC 560 should be close to synchronization or pseudosynchronization, and $P_{\rm rot} = P_{\rm ps}$. Finally, using Eq. 5.9 we can therefore estimate the orbital eccentricity to be $e = 0.68 - 0.82$.

It has been noted that the rotational period of the mass donor is considerably shorter than the orbital period (Zamanov et al. 2008) in a few jet-ejecting symbiotics. Our findings here pose the question whether their orbits are also eccentric.

Conclusion: We presented new measurements of the projected rotational velocity of the red giant in the symbiotic star MWC 560. We find that $v\ \sin i = 8.2 \pm 1.5$ km s^{-1}. On the basis of the theory of tidal interaction in binaries, we calculate that the orbit should be highly eccentric, with $e \gtrsim 0.7$. More details for this object can be found in the PhD thesis of K.A. Stoyanov (in preparation)

4.4.6 Conclusions

Collecting together all available data, we compare the rotation of the mass donors in symbiotic stars with the rotation of field giants of similar spectral types and find that:

(1) The symbiotic K giants included in our survey rotate on average more than twice as fast as the field K giants.

(2) The M giants in symbiotics are more rapid rotators than most of the field M giants.

(3) For the D'-type (yellow) symbiotics, 5 out of the six southern D'-type SSs are the fastest or among the fastest rotators in their spectral classes.

(4) As a result of the rapid rotation SSs should have on average ∼10 times larger mass loss rates than normal red giants.

(5) We find suggestions that in the jet-ejecting symbiotics the mass donors rotate faster than the orbital periods.

(6) We calculate that the orbit of MWC 560 should be highly eccentric, with $e \gtrsim 0.7$.

This is the first observational investigation that clearly confirms theoretical predictions that the mass donors in symbiotics are fast rotators.

4.5 References to Chapter 4

Akritas, M. G., & Bershady, M. A. 1996, ApJ, 470, 706

Allen, C. W. 1973, Astrophysical Quantities, 3rd ed., Athlone Press, London (1973)

Allen, D. A. 1982, The Nature of Symbiotic Stars, IAU Colloq. 70, 27

Bagnulo, S., Jehin, E., Ledoux, C., et al. 2003, The Messenger, 114, 10

Baranne, A., Mayor, M., & Poncet, J. L. 1979, Vistas in Astronomy, 23, 279

Belczynski, K., & Mikolajewska, J. 1998, MNRAS, 296, 77

Belczyński, K., Mikołajewska, J., Munari, U., et al. 2000, A&AS, 146, 407

Bode, M. F., O'Brien, T. J., Osborne, J. P., et al. 2006, ApJ, 652, 629

Bode, M. F., Harman, D. J., O'Brien, T. J., et al. 2007, ApJ, 665, L63

Bruch, A., Niehues, M., & Jones, A. F. 1994, A&A, 287, 829

Chochol, D., & Wilson, R. E. 2001, MNRAS, 326, 437

Corradi, R. L. M., Mikolajewska, J., & Mahoney, T. J. (eds.) 2003, "Symbiotic Stars Probing Stellar Evolution", ASP Conf. 303, 1

Delfosse, X., Forveille, T., Perrier, C., & Mayor, M. 1998, A&A, 331, 581

Doroshenko, V. T., Goranskij, V. P., Efimov, Y. S. 1993, IBVS 3824, 1

de Medeiros, J. R., & Mayor, M. 1999, A&AS, 139, 433

De Medeiros, J. R., Udry, S., Burki, G., & Mayor, M. 2002, A&A, 395, 97

Delfosse, X., Forveille, T., Perrier, C., & Mayor, M. 1998, A&A, 331, 581

Dobrzycka, D., & Kenyon, S. J. 1994, AJ, 108, 2259

Dobrzycka, D., Kenyon, S. J., Proga, D., et al. 1996, AJ, 111, 2090

Dumm, T., Muerset, U., Nussbaumer, H., et al. 1998, A&A, 336, 637

Dumm, T., & Schild, H. 1998, New Astronomy, 3, 137

Fekel, F. C., Jr. 1981, ApJ, 246, 879

Fekel, F. C. 1997, PASP, 109, 514

Fekel, F. C., Joyce, R. R., Hinkle, K. H., & Skrutskie, M. F. 2000a, AJ, 119, 1375

Fekel, F. C., Hinkle, K. H., Joyce, R. R., & Skrutskie, M. F. 2000b, AJ, 120, 3255

Fekel, F. C., Hinkle, K. H., Joyce, R. R., & Skrutskie, M. F. 2001, AJ, 121, 2219

Fekel, F. C., Hinkle, K. H., & Joyce, R. R. 2003, ASP Conference Series, 303, 113

Fekel, F. C., Hinkle, K. H., & Joyce, R. R. 2004, IAU Symposium, 215, 168

Fekel, F. C., Hinkle, K. H., Joyce, R. R., Wood, P. R., & Lebzelter, T. 2007, AJ, 133, 17

Friedjung, M., Gális, R., Hric, L., & Petrík, K. 2003, A&A, 400, 595

Glebocki, R., Gnacinski, P., & Stawikowski, A. 2001, VizieR Online Data Catalog, 3226, 0

Gromadzki, M., Mikołajewska, J., Whitelock, P. A., & Marang, F. 2007, A&A, 463, 703

Gray, D. F. 1976, "The observation and analysis of stellar photospheres", Wiley-Interscience, New York (1976)

Hale, A. 1994, AJ, 107, 306

Hut, P. 1981, A&A, 99, 126

Harries, T. J., & Howarth, I. D. 1996, A&A, 310, 235

Harries, T. J., & Howarth, I. D. 2000, A&A, 361, 139

Henry, G. W., Fekel, F. C., Henry, S. M., & Hall, D. S. 2000, ApJS, 130, 201

Hoffleit, D. 1970, IBVS, 469, 1

Hünsch, M., Konstantinova-Antova, R., Schmitt, J. H., et al. 2004, IAU Symp. 219, 223

Iben, I. J. 1991, ApJS, 76, 55

Kaufer, A., Stahl, O., Tubbesing, S., et al. 1999, The Messenger, 95, 8

Keenan, P. C., & McNeil, R. C. 1989, ApJS, 71, 245

Kenyon, S. J. 1986, The symbiotic stars, Cambridge University Press (1986)

Kenyon, S. J., & Fernandez-Castro, T. 1987, AJ, 93, 938

Kenyon, S. J., Fernandez-Castro, T., & Stencel, R. E. 1988, AJ, 95, 1817

Kenyon, S. J., & Garcia, M. R. 1989, AJ, 97, 194

Kenyon, S. J., Mikolajewska, J., Mikolajewski, M., et al. 1993, AJ, 106, 1573

Kenyon, S. J., & Mikolajewska, J. 1995, AJ, 110, 391

Keyes, C. D., & Preblich, B. 2004, AJ, 128, 2981

Lamers, H. J. G. L. M. 2004, IAU Symposium, 215, 479

Lasota, J.-P., & Soker, N. 2005, ASP Conf., 330, 117

Leedjärv, L. 2002, ASP Conference Series, 261, 353

Massarotti, A., Latham, D. W., Stefanik, R. P., & Fogel, J. 2008, AJ, 135, 209

Medina Tanco, G. A., & Steiner, J. E. 1995, AJ, 109, 1770

Meier, S. R., Rudy, R. J., Lynch, D. K., et al., 1996, AJ, 111, 476

Melo, C. H. F., Pasquini, L., & De Medeiros, J. R. 2001, A&A, 375, 851

Melo, C. H. F. 2003, A&A, 410, 269

Merrill, P. W., Burwell, C. G.: 1943, ApJ 98, 153

Michalitsianos, A. G.; Perez, M., Shore, S. N., et al.: 1993, ApJL 409, L53

Mikolajewska, J., Mikolajewski, M., & Kenyon, S. J. 1989, AJ, 98, 1427

Mikolajewska, J., Kenyon, S. J., Mikolajewski, M., et al. 1995, AJ, 109, 1289

Mikołajewska, J. 2003, ASP Conf., 303, 9

Mikołajewska, J., Ivison, R. J., & Omont, A. 2003, ASP Conf., 303, 478

Moultaka, J., Ilovaisky, S. A., Prugniel, P., & Soubiran, C. 2004, PASP, 116, 693

Munari, U., Tomov, T., Yudin, B. F., et al., 2001 A&A, 369, L1

Mürset, U., & Schmid, H. M. 1999, A&AS, 137, 473

Mürset, U., Dumm, T., Isenegger, S., et al., 2000, A&A, 353, 952

Nordström, B., et al. 2004, A&A, 418, 989

Nieuwenhuijzen, H., & de Jager, C. 1988, A&A, 203, 355

Pereira, C. B., Vogel, M., & Nussbaumer, H. 1995, A&A, 293, 783

Pereira, C. B., Smith, V. V., & Cunha, K. 2005, A&A, 429, 993

Pucinskas, A. 1970, Vilnius Astronomijos Observatorijos Biuletenis, 27, 24

Quiroga, C., Mikołajewska, J., Brandi, E., et al. 2002, A&A, 387, 139

Schild, H., Muerset, U., & Schmutz, W. 1996, A&A, 306, 477

Schild, H., Dumm, T., Mürset, U., et al. 2001, A&A, 366, 972

Schmid, H. M., Dumm, T., Murset, U., et al. 1998, A&A, 329, 986

Schmid, H. M., Kaufer, A., Camenzind, M., et al. 2001, A&A 377, 206

Schmidt-Kaler, T. H. 1982, in Landolt-Brnstein, New Series, Group VI, Vol. 2b, "Stars and Star Clusters", eds. K. Schaifers & H. H. Voigt, New York: Springer (1982)

Schmutz, W., Schild, H., Muerset, U., & Schmid, H. M. 1994, A&A, 288, 819

Skopal, A., Vittone, A., Errico, L., et al. 1997, MNRAS, 292, 703

Skopal, A. 2005, A&A, 440, 995

Smith, V. V., Cunha, K., Jorissen, A., & Boffin, H. M. J. 1997, A&A, 324, 97

Smith, V. V., Pereira, C. B., & Cunha, K. 2001, ApJ, 556, L55

Seaquist, E. R., Krogulec, M., & Taylor, A. R. 1993, ApJ, 410, 260

Schaller, G., Schaerer, D., Meynet, G., & Maeder, A. 1992, A&AS, 96, 269

Skopal, A.: 2005, A&A 440, 995

Smith, V. V., Cunha, K., Jorissen, A., & Boffin, H. M. J. 1996, A&A, 315, 179

Smith, V. V., Cunha, K., Jorissen, A., & Boffin, H. M. J. 1997, A&A, 324, 97

Smith, V. V., Pereira, C. B., & Cunha, K. 2001, ApJ, 556, L55

Schmid, H. M., Kaufer, A., Camenzind, M., et al. 2001, A&A, 377, 206

Simon, T., & Drake, S. A. 1989, ApJ, 346, 303

Soker, N. 2002, MNRAS, 337, 1038

Stanishev, V., Zamanov, R., Tomov, N., & Marziani, P. 2004, A&A, 415, 609

Stawikowski, A. 1994, Acta Astronomica, 44, 393

Stute, M., Sahai, R.: 2009, A&A 498, 209

Tassoul, J. 2000, "Stellar rotation", Cambridge University Press (2000)

Tomov, T., Kolev, D., Georgiev, L., et al. 1990, Nature, 346, 637

Tomov, T., Zamanov, R., Kolev, D., et al. 1992, MNRAS 258, 23

Tomov, T., Munari, U., & Marrese, P. M. 2000, A&A, 354, L25

Tomov, N. A., Tomova, M. T., & Ivanova, A. 2000, A&A, 364, 557

van Belle, G. T., Lane, B. F., Thompson, R. R., et al. 1999, AJ, 117, 521

van den Heuvel, E. P. J. 1984, Journal of Astrophysics and Astronomy, 5, 209

Van Winckel, H., Schwarz, H. E., Duerbeck, H. W., & Fuhrmann, B. 1994, A&A, 285, 241

Wallerstein, G. 1981, The Observatory, 101, 172

Wilkinson, M. I., Vallenari, A., Turon, C., et al. 2005, MNRAS, 359, 1306

Yudin, B., & Munari, U. 1993, A&A, 270, 165

Yudin, B. F., Shenavrin, V. I., Kolotilov, E. A. et al. 2005, Astronomy Reports, 49, 232

Yungelson, L., Livio, M., Tutukov, A., & Kenyon, S. J. 1995, ApJ, 447, 656

Zahn, J.-P. 1977, A&A, 57, 383

Zahn, J.-P. 1989, A&A, 220, 112

Zamanov, R., Marziani, P.: 2002, ApJL 571, L77

Zamanov, R. K., Bode, M. F., Tomov, N. A., & Porter, J. M. 2005, MNRAS, 363, L26

Zamanov, R. K., Bode, M. F., Melo, C. H. F., et al. 2006, MNRAS, 365, 1215

Zamanov, R. K., Bode, M. F., Melo, C. H. F., et al. 2007, MNRAS, 380, 1053

Zamanov, R. K., Bode, M. F., Melo, C. H. F., et al. 2008, MNRAS, 390, 377

Zhu, Z. X., Friedjung, M., Zhao, G., Hang, H. R., & Huang, C. C. 1999, A&AS, 140, 69

Chapter 5

Related Objects

5.1 Orbital eccentricity of the symbiotic star MWC 560

MWC 560 (V694 Mon) was discovered as an object with bright hydrogen lines (Merrill & Burwell 1943). It is a symbiotic binary system, which consists of a red giant and a white dwarf (Tomov et al. 1990; Michalitsianos et al. 1993). The orbital period is supposed to be $P_{\rm orb} \approx 5.3$ yr (Doroshenko, Goranskij & Efimov 1993). The most spectacular features of this object are the collimated ejections of matter with velocities of up to ~ 6000 km s^{-1} (Tomov et al. 1992; Stute & Sahai 2009) and the resemblance of its emission line spectrum to that of the low-redshift quasars (Zamanov & Marziani 2002).

The jet ejections are along the line of sight and the system is seen almost pole-on ($i < 16°$). This makes it difficult to obtain the orbital parameters using the radial velocity variations, and impossible to observe effects such as eclipse or illumination.

To improve our understanding of this object, we aim here to: (1) measure the projected rotational velocity of the red giant ($v \sin i$) from high resolution spectra, and (2) use our measured $v \sin i$to find the eccentricity e of the orbit, on the basis of the theory for pseudosynchronization in binary stars.

5.1.1 Spectral Data and $v \sin i$ measurement

Observations

We analyzed 21 high resolution spectra of MWC 560, obtained with the FEROS spectrograph. FEROS is a fiber fed echelle spectrograph, providing high resolution of $\lambda/\Delta\lambda = 48000$ and an wide wavelength coverage from about 4000 Å to 8900 Å in one exposure (Kaufer et al. 1999). 16 of the analyzed spectra are from our observations of the MWC 560 with the 2.2-m telescope at ESO, La Silla (ESO program 074.D-0114). The remaining spectra (5), are downloaded from FEROS Spectroscopic Database at the LSW Heidelberg[1] and were obtained when FEROS was mounted on the 1.52-m telescope at La Silla. A log of observations is given in Table 5.1. Details of the data processing are given in Zamanov et al. (2007). In Fig. 5.1 we show the average spectrum derived from the 16 spectra obtained by 2.2-m telescope.

Symbiotic stars have composite spectra with three main sources of radiation – red giant, hot component and nebula. Modeling of a few objects is given in Skopal (2005). Fig. 5.1 also shows a synthetic spectrum of a M5III star with parameters: $T_{\rm eff} = 3424$ K, $\log g = 0.5$, $\xi = 3$ km s^{-1}, $v \sin i = 8.2$ km s^{-1}, and 64% contribution of the giant at $\lambda = 8800$ Å (see 2.2.).

$v \sin i$ measurement

We measure $v \sin i$ by comparing the FWHM of spectral lines of observed and synthetic spectra. The procedure is similar to that described in Fekel (1997).

We synthesized spectra by using the code SYNSPEC (Hubeny, Lanz & Jeffery 1994) in the spectral region $\lambda = 8750$ - 8850 Å. Atmospheric parameters $T_{\rm eff} = 3424$ K, $\log g = 0.5$ (typical for a M5III star, see van Belle et al. 1999), the instrumental profile for our FEROS spectra, and solar abundances were the input parameters for the code. LTE model atmospheres were extracted from Kurucz's grid (1993). The VALD atomic line database (Kupka et al. 1999) was used to create a line list for spectrum synthesis.

We adopt a microturbulent velocity $\xi = 3$ km s^{-1}. This value is the same as accepted by Fekel, Hinkle & Joyce (2004) and it is close to the values for other symbiotics. Schmidt et al. (2006) calculated $\xi = 2.2$ km s^{-1} for CH Cyg. Wallerstein et al.(2008) used $\xi = 2.2$ km s^{-1} for T CrB. The relation between ξ and $\log g$ (Gratton, Carretta, & Castelli 1996) gives $\xi \approx$ 2.1 km s^{-1} for our case.

A grid of synthetic spectra for projected rotational velocities from 0 km s^{-1} to 20 km s^{-1} was calculated. $v \sin i$ was calculated by measuring the full width at half maximum (FWHM) of twelve observed spectral lines. These were compared to the spectral line half-widths from the synthetic spectra. We thereby derive a mean $v \sin i = 8.2$ km s^{-1}, and a standard deviation of the mean $\sigma = 0.4$ km s^{-1}using all 21 spectra. However we must also consider the contribution of systematic errors to our measurement. In particular we note that if we adopt a microturbulent

[1] www.lsw.uni-heidelberg.de/projects/instrumentation/Feros/ferosDB/

Table 5.1: Spectral observations of MWC 560. The columns in the table represent: (1) modified Julian Date (MJD) of the start of the exposure, (2) exposure time, and the (3) measured projected rotational velocity ($v\ \sin i$) of the mass donor.

MJD	exp-time [sec]	$v\ \sin i$ $[\mathrm{km\,s^{-1}}]$
2.2-m telescope		
53314.279	300	8.5
53314.283	300	8.6
53314.287	300	7.9
53314.291	300	7.8
53314.295	300	8.0
53314.299	300	8.2
53314.303	300	8.2
53314.308	300	8.5
53314.312	300	8.8
53314.316	300	7.8
53314.320	300	8.3
53314.324	300	7.7
53314.328	300	8.6
53314.332	300	7.9
53314.336	300	8.1
53314.340	300	8.5
1.52-m telescope		
51133.223	1200	7.8
51131.248	2400	8.9
51135.283	1200	7.8
51136.259	900	7.9
51141.315	1200	8.2

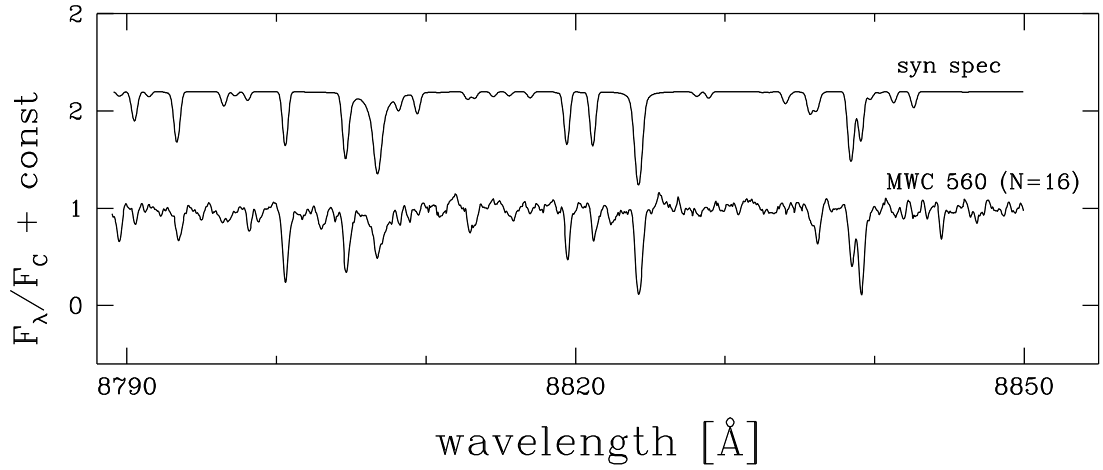

Figure 5.1: The average spectrum of MWC 560 in the range $\lambda = 8790 - 8850$ Å, obtained from 16 exposures with FEROS spectrograph at the 2.2-m telescope at La Silla, and a synthetic spectrum using $T_{\rm eff}$=3424 K, $\log g = 0.5$ $\xi = 3$ km s^{-1}, $v \sin i$= 8.2 km s^{-1}, and 64% contribution from the giant.

velocity $\xi = 2$ km s^{-1} we would have measured v sin i= 9.4 km s^{-1}. We therefore estimate our final measurement to be $= 8.2 \pm 1.0$ km s^{-1}.

5.1.2 Tidal interaction in MWC 560

Parameters of MWC 560

Meier et al. (1996) classified the cool component of MWC 560 as M5III-M6III giant. Mürset & Schmid (1999) give M5.5III - M6III as its stellar type. According to van Belle et al. (1999), a typical M5III giant has the following parameters: $R_{\rm g} = 139.6 \pm 5.6$ R$_\odot$, $T_{\rm eff} = 3424$ K, $L_{\rm g} \sim 2410$ $L_\odot$, and a typical M6III giant: $R_{\rm g} = 147.9 \pm 7.7$ $R_\odot$, $T_{\rm eff} = 3375$ K, $L_{\rm g} \sim 2560$ $L_\odot$. We adopt for the M giant in MWC 560 $R_{\rm g} = 140 \pm 7$ $R_\odot$ and $L_{\rm g} \sim 2400$ $L_\odot$.

For the masses of the red giant and white dwarf we will assume $M_{\rm g} = 1.7$ $M_\odot$ and $M_{\rm wd} = 0.65$ $M_\odot$, respectively. These values are the average masses of the components of the symbiotic stars (Mikołajewska 2003). Concerning the orbital period, we use $P_{\rm orb} = 1931 \pm 162$ day (Gromadzki et al. 2007). With the above values of the parameters assumed, we derive the semimajor axis of the orbit to be $a \approx 860$ $R_\odot$.

The jet (orbit) inclination angle to the line of sight is $i < 16^\circ$, and the white dwarf accretes at a rate $\dot{M}_{\rm acc} \approx 5 \times 10^{-7}$ $M_\odot$ (Schmid et al. 2001).

Synchronization and circularization time scales

The physics of tidal synchronization for stars with convective envelopes has been analyzed several times. There are some differences in the analysis of different authors, leading to varying synchronization timescales. We use the estimate from Zahn (1977, 1989). The synchronization timescale in terms of the period is

$$\tau_{\rm syn} \approx 800 \left(\frac{M_{\rm g} R_{\rm g}}{L_{\rm g}}\right)^{1/3} \frac{M_{\rm g}^2(\frac{M_{\rm g}}{M_{\rm wd}}+1)^2}{R_{\rm g}^6} P_{\rm orb}^4 \ \ {\rm yr}, \tag{5.1}$$

where $M_{\rm g}$ and $M_{\rm wd}$ are the masses of the giant and white dwarf respectively in Solar units, and $R_{\rm g}$, $L_{\rm g}$ are the radius and luminosity of the giant, also in Solar units. The orbital period $P_{\rm orb}$ is measured in days.

Following Hurley, Tout & Pols (2002), the circularization time scale is:

$$\frac{1}{\tau_{\rm circ}} = \frac{21}{2}\left(\frac{k}{T}\right) q_2(1+q_2)\left(\frac{R_{\rm g}}{a}\right)^8. \tag{5.2}$$

where q_2 is the mass ratio $q_2 = M_{\rm wd}/M_{\rm g}$, In Eq. 5.2, (k/T) is derived from Rasio et al. (1996):

$$\left(\frac{k}{T}\right) = \frac{2}{21}\frac{f_{\rm conv}}{\tau_{\rm conv}}\frac{M_{\rm env}}{M_{\rm g}} \ {\rm yr}^{-1}, \tag{5.3}$$

where $R_{\rm env}$ is the depth of the convective envelope, $M_{\rm env}$ is the envelope's mass, and

$$\tau_{\rm conv} = 0.4311 \left(\frac{M_{\rm env} R_{\rm env}(R_{\rm g} - \frac{1}{2}R_{\rm env})}{3L_{\rm g}}\right)^{\frac{1}{3}} {\rm yr} \tag{5.4}$$

is the eddy turnover time scale (the time scale on which the largest convective cells turnover). The numerical factor $f_{\rm conv}$ is

$$f_{\rm conv} = \min\left[1, \left(\frac{P_{\rm tid}}{2\tau_{\rm conv}}\right)^2\right], \tag{5.5}$$

where $P_{\rm tid}$ is the tidal pumping time scale given by

$$\frac{1}{P_{\rm tid}} = \left|\frac{1}{P_{\rm orb}} - \frac{1}{P_{\rm rot}}\right|. \tag{5.6}$$

For MWC 560 we assume for the red giant to have $R_{\rm env} = 0.9\ R_{\rm g}$ and $M_{\rm env} = 1.0\ M_\odot$ (Herwig 2005). Using these parameters, we calculate $P_{\rm tid} = 248$ days, $f_{\rm conv} = 1$, $\tau_{\rm conv} = 0.476$ yr, and $(k/T) = 0.12\ {\rm yr}^{-1}$. Then from Eq. 5.1 and Eq. 5.2 follows that the synchronization and circularization time scales are $\tau_{\rm sync} = 2.6 \times 10^4$ yr and $\tau_{\rm circ} = 3.1 \times 10^6$ yr respectively.

Following Hut (1981), we estimate the pseudosynchronization timescale $\tau_{\rm ps}$:

$$\tau_{\rm ps} = \frac{7}{3(\alpha-3)}\tau_{\rm circ}, \tag{5.7}$$

where α is a dimensionless quantity, representing the ratio of the orbital and rotational angular momentum:

$$\alpha = \frac{q_2}{1+q_2}\frac{1}{r_{\rm g}^2}\left(\frac{a}{R_{\rm g}}\right)^2, \tag{5.8}$$

where $r_{\rm g}$ is the gyration radius of the giant. For a red giant we adopt $r_{\rm g} \approx 0.3$ (Claret, 2004, 2007). We calculate $\alpha = 800$ and $\tau_{\rm ps} = 9.1 \times 10^3$ yr.

Lifetime of the symbiotic phase

The typical lifetime of a symbiotic star is $\tau_{\rm ss} \sim 10^5$ yr (Yungleson et al. 1995; Lü, Yungelson, & Han 2006). In the case of MWC 560, we can estimate from the rate of accretion on the white dwarf, $\dot{M}_{\rm acc} \approx 5 \times 10^{-7}$ $M_\odot$ (Schmid et al. 2001), that it will take 10^6 yr to accrete ~ 0.5 $M_\odot$ from the envelope of the red giant companion. Because the giant also losses mass via stellar wind, we find that the lifetime of the symbiotic phase of MWC 560 should be $\tau_{\rm ss} \lesssim 10^6$ yr.

For MWC 560 we have therefore the situation in which $\tau_{\rm ps} < \tau_{\rm syn} < \tau_{\rm ss} < \tau_{\rm circ}$. This means that the symbiotic phase is long enough that the tidal forces can synchronize (pseudosynchronize) the rotation of the red giant. On the other hand, the value of $\tau_{\rm circ}$ demonstrates that the symbiotic lifetime of MWC 560 is shorter than the circularization time, and therefore the orbit can be eccentric. This is in agreement with the observational evidences found by Fekel et al. (2007) that the symbiotic stars with $P_{\rm orb} > 800$ days tend to have eccentric orbits.

Schmutz et al. (1994) estimated that the timescale for circularization in SY Mus is $\sim$ 10 times longer then the synchronization time. For MWC 560, we find even higher ratio: $\tau_{\rm circ}/\tau_{\rm syn} \approx 45$.

The above implies that in MWC 560, the red giant is probably more or less synchronized, but the orbit is not circularized.

Rotation and pseudosynchronization In a binary with a circular orbit the rotational period of the primary, $P_{\rm rot}$, reaches an equilibrium value at the orbital period, $P_{\rm rot} = P_{\rm orb}$. However, in a binary with an eccentric orbit, the tidal force acts to synchronize the rotation of the mass donor with the motion of the compact object at the periastron – the effect called pseudosynchronous rotation (Hall 1986). The corresponding equilibrium (i.e. pseudosynchronization) is reached at a value of $P_{\rm rot}$ which is *less* than $P_{\rm orb}$, the amount less being a function of the orbital eccentricity e. Hut (1981) showed that the period of pseudosynchronization, $P_{\rm ps}$, is :

$$P_{\rm ps} = \frac{(1+3e^2+\frac{3}{8}e^4)(1-e^2)^{\frac{3}{2}}}{1+\frac{15}{2}e^2+\frac{45}{8}e^4+\frac{5}{16}e^6} P_{\rm orb}. \tag{5.9}$$

When the eccentricity tends to zero, $P_{\rm ps}$ tends to $P_{\rm orb}$.

5.1.3 Orbital eccentricity of MWC 560

In order to determine the orbital eccentricity of MWC 560, we first need to calculate $P_{\rm rot}$ for the mass donor. We use

$$P_{\rm rot} = \frac{2\pi R_{\rm g} \sin i}{v \, \sin i}. \tag{5.10}$$

The underlying assumption is that the rotational axis of the mass donor is perpendicular to the orbital plane.

Using the value for $v \sin i = 8.2 \pm 1.0$ km s^{-1} (Sect.5.1.1), $R_{\rm g} = 140 \pm 7 \; R_\odot$, and $i = 12° - 16°$ (Schmid et al. 2001), we calculate $P_{\rm rot} = 155 - 270$ days. This value is considerably less than the orbital period, $P_{\rm orb} = 1931 \pm 162$ days. Following the results in Sect.5.1.2, MWC 560 should be close to synchronization or pseudosynchronization, and $P_{\rm rot} = P_{\rm ps}$. Finally, using Eq. 5.9 we can therefore estimate the orbital eccentricity to be $e = 0.73 - 0.79$.

5.1.4 Discussion

In most of the symbiotics the activity of the hot components is irregular/aperiodic. However, in MWC 560 it has a periodic character. An analysis of the historical light curve (Luthardt 1991) and B-band photometry, as well as the periodogram analysis of V band and near-IR observations reveal that this periodicity has remained in-phase for over a century (Doroshenko et al. 1993; Gromadzki et al. 2007). The most natural explanation for this phenomenon is orbital modulation: around periastron, the mass accretion rate increases, which causes an increase of the accretion luminosity and the brightness of the accretion disk, which produces the observed modulation of the light curves (see also Doroshenko et al. 1993; Gromadzki et al. 2007).

With the parameters assumed above, we can calculate the distance between the components at the periastron: $r_{\rm p} = a(1-e) = 180 - 230 \; R_\odot$. It follows that the red giant fills the Roche lobe for about 10% – 30 % of the orbital period. This is in agreement with the suppositions of Gromadzki et al. (2007), that the orbital eccentricity and corresponding Roche lobe overflow at the periastron is the reason for the observed photometric variability.

It has been noted that the rotational period of the mass donor is considerably shorter than the orbital period (Zamanov et al. 2008) in a few jet-ejecting symbiotics. Our findings here pose the question whether their orbits are also eccentric.

Conclusions

We presented new measurements of the projected rotational velocity of the red giant in the symbiotic star MWC 560. We find that $v\ \sin i = 8.2 \pm 1.0\ \mathrm{km\,s^{-1}}$. On the basis of the theory of tidal interaction in binaries, we calculate that the orbit should be highly eccentric, with $e \gtrsim 0.7$. Our findings support the model that the observed photometric variability of MWC 560 is connected with high orbital eccentricity and Roche lobe overflow at periastron.

Table 5.2: Patrol observations of FY Per. In the table are given: date of observations, UT-start and UT-end of observations, number of the data points (N_{pts}), minimal and maximal brightness in B-band, standard deviation of the run (σ)

Date	UT_{start}	UT_{end}	N_{pts}	$B_{min} - B_{max}$	σ
	hh:mm	hh:mm		[mag] – [mag]	mag
18 Dec.1993	20:07	23:27	994	12.82 – 12.86	0.012
19 Dec.1993	18:43	22:20	1135	12.96 – 12.99	0.013
21 Dec.1993	22:35	22:53	88	13.08 – 13.10	0.013

Table 5.3: UBV estimates of the brightness of FY Per.

JD 2440000+	V	B-V	U-B
9340.49	12.55	0.29	-0.47
9341.45	12.68	0.30	-0.43
9343.44	12.74	0.35	-0.41
9357.42	12.53	0.30	-0.48
9366.48	12.69	0.35	-0.37

5.2 UBV photometry of FY Per

FY Per was discovered as a variable star by Morgenroth (1936). Some results of investigation of this nova-like cataclysmic variable are published by Shugarov (1980). Recently Sazonov and Shugarov (1993) have discovered that the system's light, changes with a period of 1^h33^m and an amplitude of 0.15 mag in B band.

FY Per has been observed with the 60 cm telescope and computer controlled photometer of the National Astronomical Observatory Rozhen on several occasions. BD+$50^0$1032 has been used as a comparison star. Each integration was 10 sec through the B filter. The photometric data here in were reduced using APR software system (Kirov et al., 1992). The results are summarized in Table 5.2 and Table 5.3.

In spite of the changes from night to night (see Table 5.2), the brightness has remained almost constant on the individual nights, and we have not detected any variations on a time scale of $\sim 1 - 2$ hours and amplitude larger than 0.035^m.

5.3 UBV observations of ZZ CMi

ZZ CMi (BD+09^{0}1633) is a poorly observed star. It is classified in the General Catalogue of Variable Stars as a semi-regular variable with a spectral type of M6I-IIep. On the base of 35 photographic observations covering a period of about 40 years Tshernova (1949) suggested a possible period of about 500d for the brightness variations. The spectroscopic observations of Sanford (1947) showed absorption features corresponding to a spectral class M6 and low excitation emission lines. Later Iijima (1984) noted the presence of high excitation emission lines of [OIII] and [NeIII]. Bopp (1984) reported Halpha variability and infrared photometry. Iijima (1984) and Bopp (1984) interpreted their observations as evidence that ZZ CMi is a symbiotic star. We observed ZZ CMi photoelectrically during the period January - May 1991. The observations were obtained with the 0.6m telescope of the National Astronomical Observatory Rozhen and a single channel photon counting photometer. HD58367 (V=4.996, B-V=1.002, U-B=0.783) was used as the comparison star. The data processing and reduction to the standard UBV system are made with the software of Kirov, Antov and Genkov (1991). The internal accuracy is ±0.03 in V, ±0.04 in B-V and ±0.05 in U-B.

Table 5.4 summarizes our results. Obviously the colours do not correspond to the normal M6 giants (Allen 1973). U-B is remarkably bluer and points to the presence of a hot source. A minimum in the B and V bands at the end of February 1991 (JD2448310) is detected. The amplitude of the variation in B is smaller by about 0.1 than in V. The behaviour in U is different and the changes are not so strong.

Our UBV observations are in agreement with the supposition ZZ CMi to be a symbiotic binary system. The M giant dominates the radiation in B and V and probably semi-regular variability causes the changes in these bands. The brightness in U can be influenced by a less luminous hot companion. Systematic observations are necessary to reveal the nature of this object.

Table 5.4: UBV estimates of the brightness of ZZ CMi.

HJD2440000+	V	B-V	U-B
8255.584	9.78	1.64	0.69
8262.353	9.57	1.57	0.88
8274.306	9.70	1.52	0.71
8275.529	9.74	1.54	0.71
8278.530	9.74	1.54	0.63
8291.495	9.94	1.45	0.50
8292.313	9.94	1.47	0.60
8308.356	10.13	1.45	0.43
8321.315	10.08	1.46	0.48
8337.338	9.75	1.49	0.47
8338.283	9.77	1.52	0.61
8339.360	9.76	1.50	0.44
8340.379	9.75	1.53	0.60
8341.284	9.76	1.52	0.51
8383.280	9.78	1.53	0.46

5.4 X Persei

The Be/X-ray binary X Persei is the optical counterpart of X-ray pulsar 4U 0352+30. Possible orbital period of the system is the 580 day periodicity detected in the radial velocities of the Balmer lines (Hutchings, 1977), in spite of existence of some doubts (Penrod & Vogt, 1985). The star is a known optical variable on time scales from minutes to years. The most comprehensive optical light curve over the past decades is presented by Roche et al. (1993).

X Per has been observed with 60 cm telescope and photon counting photometer of the National Astronomical Observatory Rozhen. HR 1197 (V=6.25, B−V=0.20, U−B=0.14) served as the comparison star. The APR software (Kirov et al., 1993) was used during the data reduction.

Our data are summarized in Table 5.4. Fig. 5.2 presents the V band light curve over the period 1986-1995. Our observations showed the optical low state that began in the mid-1990 finished in the spring of 1993. Since this time the star has been in optical high state. A clear similarity between the light maximum in 1987-1988 and that in 1993-1994 is visible. The displacement is about 2400 days, i.e. 4 times larger than the supposed orbital period.

The last observations indicate that the optical high state is almost over and X Per is going to a new low state now.

UBV observations of X Per

JD 2440000+	V	B−V	U−B	JD 2440000+	V	B−V	U−B
8545.57	6.81	0.09	−0.68	9341.27	6.47	0.18	−0.78
8620.52	6.76	0.08	−0.64	9343.42	6.47	0.19	−0.78
8712.29	6.78	0.11	−0.73	9357.43	6.44	0.20	−0.78
8734.26	6.76	0.05	−0.68	9366.46	6.44	0.19	−0.78
8841.52	6.75	0.13	−0.66	9572.51	6.34	0.26	−0.73
8842.56	6.76	0.11	−0.67	9573.52	6.33	0.26	−0.73
8905.56	6.78	0.09	−0.70	9597.50	6.26	0.26	−0.73
8916.42	6.78	0.09	−0.70	9598.48	6.27	0.24	−0.73
9028.22	6.78	0.05	−0.66	9715.32	6.38	0.21	−0.75
9046.26	6.76	0.06	−0.66	9748.23	6.45	0.21	−0.81
9195.55	6.45	0.21	−0.75	9772.23	6.48	0.21	−0.83
9197.54	6.42	0.21	−0.76				
9340.28	6.47	0.18	−0.79				

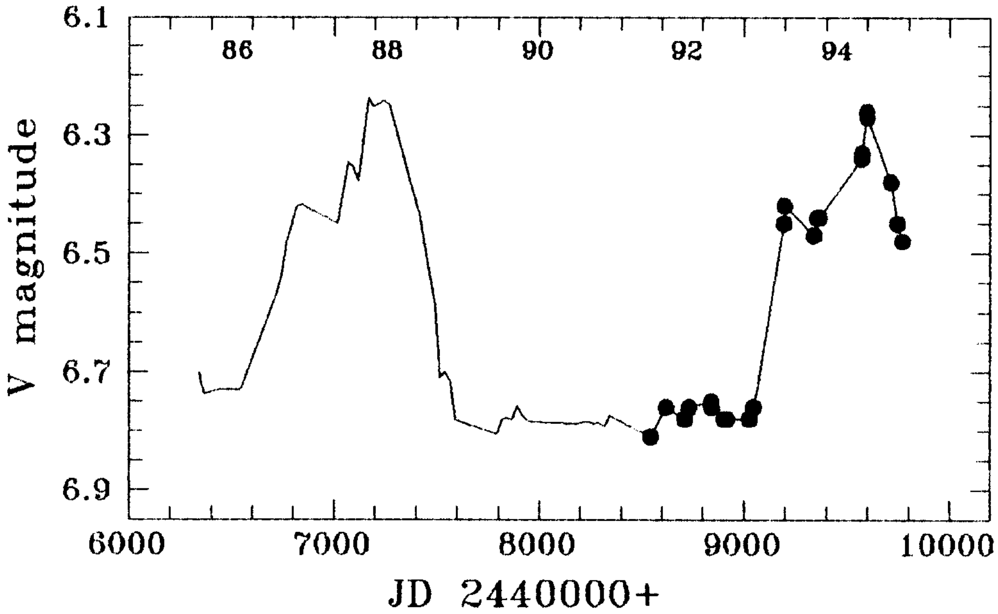

Figure 5.2: V band light curve of X Per. Circles indicate our data. The light curve before JD 2448500 is taken from Roche et al. (1993).

5.5 References to Chapter 5

Allen, C.W.: 1973, Astrophysical Quantities., The Athlone Press, London

Bopp, B.W.: 1984, Publ. Astron. Soc. Pacific, 96, 894

Claret, A.: 2004, A&A 424, 919

Claret, A.: 2007, A&A 467, 1389

Doroshenko, V. T., Goranskij, V. P., Efimov, Y. S.: 1993, IBVS 3824, 1

Fekel, F. C.: 1997, PASP 109, 514

Fekel, F. C., Hinkle, K. H., Joyce, R. R. 2004, in "Stellar Rotation", IAU Symp., 215, 168

Fekel, F. C., Hinkle, K. H., Joyce, R. R., Wood, P. R., Lebzelter, T.: 2007, AJ 133, 17

Gratton, R. G., Carretta, E., Castelli, F.: 1996, A&A 314, 191

Gromadzki, M., Mikołajewska, J., Whitelock, P. A., Marang, F.: 2007, A&A 463, 703

Hall, D. S.: 1986, ApJ 309, L83

Herwig, F.: 2005, ARA&A 43, 435

Hubeny I., Lanz T., Jeffery C.S.: 1994, in: "Newsletter on Analysis of Astronomical Spectra" No.20, C. S. Jeffery (ed.), St. Andrews University, p.30

Hurley, J. R., Tout, C. A., Pols, O. R.: 2002, MNRAS 329, 897

Hut, P.: 1981, A&A, 99, 126

Hutchings, J. B., 1977, MNRAS, 181, 619

Ijima, T.: 1984, IBVS 2491

Kaufer, A., Stahl, O., Tubbesing, S. et al. : 1999, The Messenger 95, 8

Kirov, N.K., Antov, A.P., Genkov, V.V. 1991, Compt.Rend.Acad.Bulg.Sci. 44, No 11, 5

Kupka F., Piskunov N.E., Ryabchikova T.A. et al. : 1999, A&AS 138, 119

Kurucz R.L.: 1993, ATLAS9 Stellar Atmosphere Programs, (Kurucz CD-ROM 13)

Luthardt, R.: 1991, IBVS 3563, 1

Lü, G., Yungelson, L., Han, Z.: 2006, MNRAS 372, 1389

Meier, S. R., Rudy, R. J., Lynch, D. K., et al. : 1996, AJ 111, 476

Merrill, P. W., Burwell, C. G.: 1943, ApJ 98, 153

Michalitsianos, A. G.; Perez, M., Shore, S. N., et al.: 1993, ApJL 409, L53

Mikołajewska, J.: 2003, ASP Conf. 303, p.9

Morgenroth, O., 1936, Astron. Nachr., 261, 261

Mürset, U., Schmid, H. M.: 1999, A&AS 137, 473

Penrod, G., Vogt, S., 1985, ApJ, 299, 653

Rasio, F. A., Tout, C. A., Lubow, S. H., Livio, M.: 1996, ApJ 470, 1187

Roche, P., Coe, M. J., Fabregat, J., et al., 1993, A&A, 270, 122

Sanford, R.F.: 1947, Publ. Astron. Soc. Pacific, 59, 136

Sazonov, A. V., Shugarov, S, Yu., 1993, IBVS 3744

Schmid, H. M., Kaufer, A., Camenzind, M., et al. : 2001, A&A 377, 206

Schmidt, M. R., Začs, L., Mikołajewska, J., & Hinkle, K. H.: 2006, A&A 446, 603

Schmutz, W., Schild, H., Muerset, U., Schmid, H. M.: 1994, A&A 288, 819

Shugarov, S. Yu., 1980, Astron. Tsirk, No. 1199, 3 (in Russian)

Skopal, A.: 2005, A&A 440, 995

Stute, M., Sahai, R.: 2009, A&A 498, 209

Tshernova, T.S.: 1949, Perem. Zvezdy, 7, 140

Tomov, T., Kolev, D., Georgiev, L., Zamanov, R., Antov, A., Bellas, Y., 1990, Nature 346, 637

Tomov, T., Zamanov, R., Kolev, D. et al. : 1992, MNRAS 258, 23

van Belle, G. T., Lane, B. F., Thompson, R. R. et al.: 1999, AJ 117, 521

Wallerstein, G., Harrison, T., Munari, U., Vanture, A.: 2008, PASP, 120, 492

Zahn, J.-P.: 1977, A&A 57, 383

Zahn, J.-P.: 1989, A&A 220, 112

Zamanov, R. & Marziani, P.: 2002, ApJL 571, L77

Zamanov, R. K., Bode, M. F., Melo, C. H. F., et al. 2007, MNRAS 380, 1053

Zamanov, R. K., Bode, M. F., Melo, C. H. F., et al. 2008, MNRAS 390, 377

Chapter 6

The Be/X-ray binary LSI+61^0303

6.1 Evidence of Hα periodicities in LSI+61303

We present the results of analyzing Hα spectra of the radio emitting X-ray binary LSI+61303. For the first time, the same 26.5 d radio period is clearly detected in the Hα emission line. Moreover, the equivalent width and the peak separation of the Hα emission line seem also to vary over a time scale of 1600 days. This points towards the $\sim$ 4 yr modulation, detected in the radio outburst amplitude, being probably a result of variations in the mass loss rate of the Be star and/or density variability in the circumstellar disk. In addition, the dependence of the peak separation from the equivalent width informs us that the LSI+61303 circumstellar disk is among the densest of Be-stars.

The Be/X-ray binary LSI+61303 (V615 Cas) is the optical counterpart of the highly variable radio source GT 0236+610, which exhibits radio outbursts every 26.4917 ± 0.0025 d assumed to be the orbital cycle (Taylor & Gregory 1984; Gregory et al. 1999). The radial velocity measurements of Hutchings & Crampton (1981) are consistent with this interpretation and suggest an eccentric orbit ($e \simeq 0.6$). The same 26.5 d period has been detected in the UBVRI photometric observations of Mendelson & Mazeh (1994), in the infrared (Paredes et al. 1994) and in the soft X-ray flux (Paredes et al. 1997). The amplitude of the periodic variations is $\lesssim 0.2$ magnitudes in the optical and infrared, while the X-ray luminosity of the system often evolves within the range 10^{33} to 6×10^{34} erg s^{-1} (Bignami et al. 1981; Paredes et al. 1997). LSI+61303 is also currently regarded today as a serious counterpart candidate to the γ-ray source 2CG 135+01 (Gregory & Taylor 1978; Kniffen et al. 1997; Strickman et al. 1998).

The LSI+61303 radio emission has been interpreted as synchrotron radiation from relativistic particles. The dependence of the radio outburst flux density on frequency, the time delay in the outburst peak, and the general shape of the radio light curves can be modeled as continuous injection of relativistic particles into an adiabatically expanding plasma cloud or plasmon (Paredes et al. 1991). It has been proposed that the genesis of such plasmons could be the result of the transition of the neutron star companion from the Propeller to the Ejector regime (Zamanov 1995). Alternatively, a young radio pulsar may also be responsible for the radio emission (Maraschi & Treves 1981; Tavani 1994). The ejector regime would then apply over the whole orbital period, with the flaring radio emission resulting from the variable position of the shock front between the Be star wind and the relativistic wind of the pulsar. Supercritical accretion models during the periastron passage (e.g. Taylor et al. 1992) were also widely accepted in the recent past. However, they appear now very difficult to reconcile with the confirmed sub-Eddington X-ray luminosity of LSI+61303.

On the other hand, a strong modulation in the amplitude of the 26.5 d periodic radio outbursts, on a time scale of ~ 4 yr, was noticed independently by Paredes (1987) and Gregory et al. (1989). This modulation has been recently confirmed after a Bayesian analysis of 20 yr of LSI+61303 radio data by Gregory (1999). Two possible scenarios have been considered in order to account for such a long-term variability: the precession of relativistic jets or, alternatively, the variable accretion rate due to quasi-cyclic Be-star envelope variations (Gregory et al. 1989).

The optical spectrum of LSI+61303 corresponds to a rapidly rotating B0V star with a stable equatorial disk and mass loss (Hutchings & Crampton 1981). Hα observations of this star have been discussed, among others, by Gregory et al. (1979), Paredes et al. (1994) and Zamanov et al. (1996). In these papers, it was noticed a significant variability of the red and blue humps at opposite locations of the orbit. On the other hand, the quasi simultaneous Hα and radio observations by Zamanov et al. (1996) did not indicate considerable changes in Hα close to the radio maximum. This fact is in agreement with the assumption that the Hα emission comes mainly from the Be star disk, and the radio outbursts are related to the compact object. Another interesting property of the Hα emission is its very broad wings, achieving $FWZI \sim 3000$ km s^{-1}. Unfortunately, most LSI+61303 spectra available do not have sufficient SNR to investigate this intriguing feature.

In this paper, we present 84 new Hα observations of LSI+61303 which are analyzed together with the data from Paredes et al. (1994) and Zamanov et al. (1996). We report the clear detection of a 26.5 d periodicity in some parameters of the Hα emission line. In addition, our extended spectroscopic database interestingly suggests the presence of a 1600 d modulation in the Hα equivalent width. These new Hα periods seem to match closely those known at radio wavelengths. The possible implications of all these findings are pointed out and discussed.

Observations

Our Hα spectroscopic observations of LSI+61303 were carried out using different astronomical facilities. The results of these observations are summarized in Table **??**.

A total of 60 new spectra were obtained with the Coudé spectrograph of the 2.0 m RCC telescope at the Bulgarian National Astronomical Observatory "Rozhen", between October 1993 and August 1998. An ISTA-CCD with 400×580 pixel was used as a detector. The spectrum coverage is about 110 Å, with a dispersion of 0.2 Å pixel^{-1}. Usually 2 or 3 exposures, of 20 minutes each, were always taken to improve the sensitivity and to avoid problems with eventual cosmic ray hits. The "Rozhen" observations have been processed using the 3A software (Ilyin 1997) and the IRAF package of NOAO (Tucson, Arizona). It deserves noting that the new Rozhen data from Ro931031 to Ro980805 are an uniform data set.

We have also used 17 more spectra obtained within the framework of the Southampton and Valencia Universities collaborative program on high-mass X-ray binaries (Coe et al. 1993; Reig et al. 1997a). 14 of them were obtained with the Richardson-Brearly Spectrograph at the Cassegrain focus of the Jakobus Kaptein Telescope, La Palma, Spain. Different grattings were used, giving dispersions between 0.33 and 1.34 Å pixel^{-1}. The remaining 3 spectra were obtained with the P-60 Cassegrain Echelle Spectrograph in regular gratting mode at 0.8 Å pixel^{-1}, attached to the 1.5-m telescope of the Palomar Mountain Observatory. These data were reduced using the *Figaro* (Shortridge & Meyerdicks 1996) and *Dipso* (Howarth et al. 1996) packages included in the STARLINK software collection.

Additionally, we also include 7 Hα spectra from the 2.6 m telescope at the Crimean Astrophysical Observatory. They were obtained at the Coudé focus of this instrument with a dispersion of 0.066 Å pixel^{-1} and a coverage of about 67 Å. The detector used was a Photometrics SDS-9000 with a EVV 15-11 1024×256 pixel CCD.

In order to ensure a unified post-processing of the spectra, all of them were normalized with respect to the local continuum. When possible the same continuum regions were used at 6520-6530 and 6595-6605 Å, located at the blue and red side of the Hα emission line, respectively. The underlying continuum was rectified to unity by employing a linear fit.

On each spectrum, we have measured the total equivalent width of the Hα emission line (hereafter EW(Hα)), the heliocentric radial velocities of the central dip, blue and red humps,

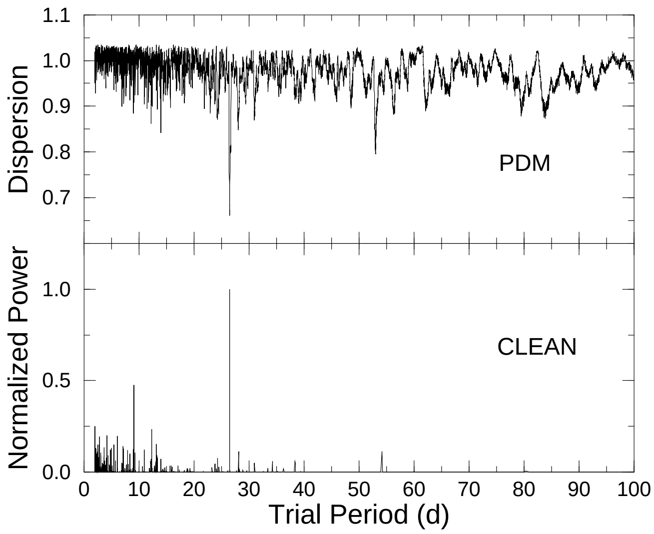

Figure 6.1: Periodograms for the ratio $EW(B)/EW(R)$ in the Hα emission line of LSI+61303 computed using the PDM (top) and CLEAN (bottom) algorithms. The 26.5 d period is independently detected in both cases as the most significant one

the ratio between the equivalent widths of the blue and red humps, the B/R ratio and the $FWHM$ of the humps. The dates of observations and the measured quantities are summarized in Table **??**. The $FWHM$ and the radial velocities were measured by employing a Gaussian fit. The $FWHM$ was corrected for the instrumental broadening. The errors depend mostly on the dispersion, and we estimate them to be about 10% for the EWs, about 1/2 pixel for the radial velocities, ± 0.04 in the B/R ratios and 1 pixel for the $FWHM$s.

Some previously published Rozhen spectra, those from Ro920903 to Ro 930909 in Table**??**, have been processed again to be used in this work. We will also include in our analysis the Hα parameters listed in the Table 4 of Paredes et al. (1994), whose $EW(R)/EW(B)$ header should be actually the inverse.

6.1.1 Detection of 26.5 day period in Hα

We have conducted a period analysis for the different Hα line parameters listed in Table**??**. The period search methods used were both the Phase Dispersion Minimization (PDM) (Stellingwerf 1978) and the CLEAN algorithm (Roberts et al. 1987). As a result, we find clear evidences that the Hα emission in LSI+61303 also displays variations with the same 26.5 d radio period. This behavior is better revealed in the line ratios such as $FWHM(B)/FWHM(R)$, $EW(B)/EW(R)$ and B/R. The periods detected are about $26.50 - 26.55$ d with typical error about ± 0.04 d. In

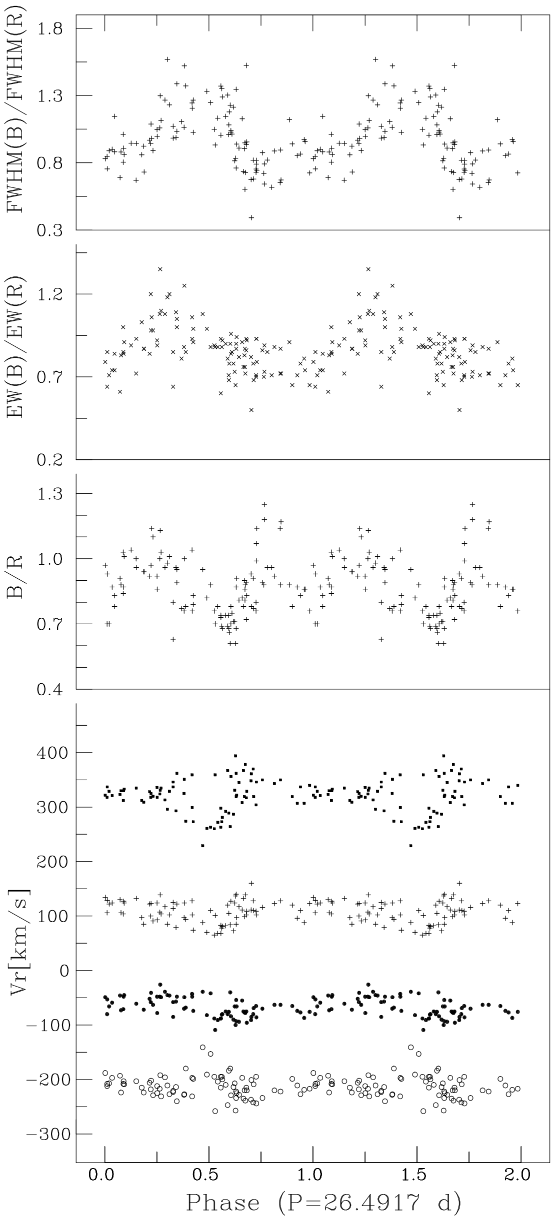

Figure 6.2: Hα line parameters of LSI+61303 folded on the 26.4917 day period and zero phase set at JD2443366.775. The panel of radial velocities contains, from the lower to the upper plot, the heliocentric radial velocities of the blue hump, $V_r(B)$ circles, the central dip, $V_r(dip)$ dots, the red hump, $V_r(R)$ plusses, and the hump separation, ΔV squares, respectively

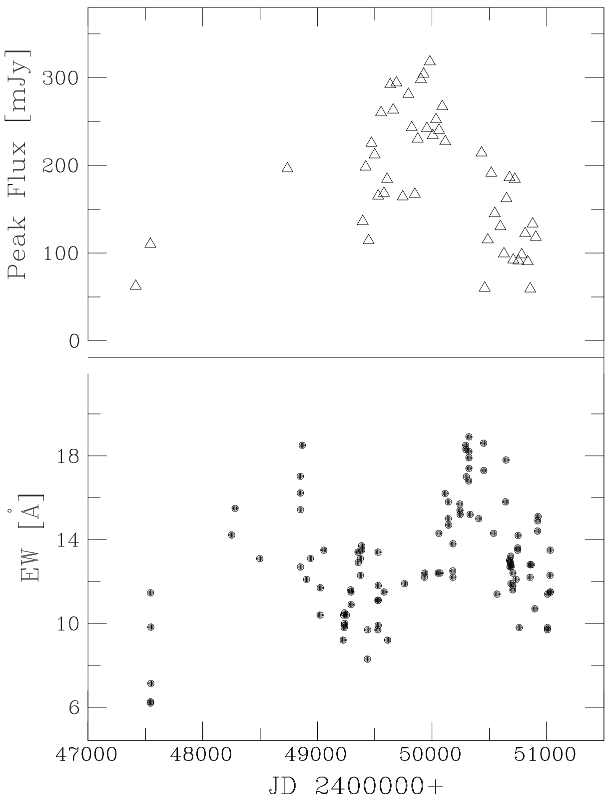

Figure 6.3: Long term behavior of the Hα equivalent width of LSI+61303. The upper panel represents the radio outburst peak flux from Gregory (1999)

Fig. 6.1 we present the PDM and CLEAN periodograms for the $EW(B)/EW(R)$ case. In this representative example, the most significant period detected in the range $2-100$ d corresponds to 26.51 ± 0.03 d and 26.53 ± 0.04 d for the PDM and CLEAN methods, respectively. The first sub-harmonic at 53 d is also clearly noticeable in the PDM panel. The periodograms for the remaining line parameters, such as radial velocities and equivalent widths alone, may also contain some power at the 26.5 d period. However, in most cases the detections are still too noisy and additional observations will be needed to confirm them.

In any case, Fig. 6.1 can be considered as a reliable proof that the signature of the LSI+61303 radio period is present in the Hα line.

The Hα parameters folded on the radio period, are displayed in Fig. 6.2 and illustrate the general trend of the Hα orbital modulation. We used for this plot the 26.4917 d period value from radio wavelengths as the best estimate of the orbital cycle currently available (Gregory et al. 1999). In the panel of the radial velocities only the Rozhen and Crimean data are included.

All data from Table **??** as well as the data from Paredes et al. (1994) are incorporated in other panels. The ratio $FWHM(B)/FWHM(R)$ achieves maximal values at radio phases $0.3-0.6$. The equivalent width ratio has one well defined maximum at phases $0.25-0.4$. In the B/R ratio at least one maximum is visible at phase 0.25, which coincides with the maximums of $FWHM(B)/FWHM(R)$ and $EW(B)/EW(R)$. A second maximum is visible at phase 0.8. It deserves noting that the appearance of this maximum is mainly due to 5 old points, which are very noisy and the presence of this maximum must be confirmed by future observations. These results proof the previous suggestions by Paredes et al. (1994) and Zamanov et al. (1996) that an orbital variability in the line ratios exists.

6.1.2 Detection of a possible ~ 4 yr modulation in Hα

Fig. 6.3 represents the long term evolution of the EW(Hα), which varies over the range 8-20 Å. These are real variations in the Hα emitted flux, because the photometric observations of Mendelson & Mazeh (1995) have shown that the R-band flux is stable with maximal deviation of the points from the average ± 0.03 magnitudes only. Two maxima in the EW(Hα) are visible, at about JD 2448850 and JD 2450300. The time interval between these two maxima is ~ 1500 d, which is remarkably close to the 1605 day period of the radio modulation as estimated by Martí (1993) and 1584 days by Gregory et al. (1999).

We have performed the period search for long term modulation. Although the values obtained are not well constrained they also point towards the four year modulation.

In Fig. 6.4 the Hα line parameters EW(Hα) and $\Delta V = V_r(R) - V_r(B)$ are plotted together with the radio parameters - the phase of the radio outburst and the maximum radio flux. The radio data are taken from Gregory (1999). All data are folded on the 1584 day period. Although the scatter of the points is considerable, the trend of this plot strongly suggests that the ~ 4 yr modulation in the Hα line is very likely to be real.

6.1.3 Other period and correlation searches

In addition to the EW(Hα), we also tried to find evidence for long term periodicities (100-2000 days) in other line parameters. The presence of B/R and related variability cycles, with periods between 4 months and 3 years, is currently regarded as a common characteristic of Be/X-ray binaries (Negueruela et al. 1998). Similar variability cycles exist in isolated Be stars, with longer periods ranging from 2 years to decades, with an average of 7 years. In those cases, the periodic variability is interpreted as due to the propagation of global density waves in the

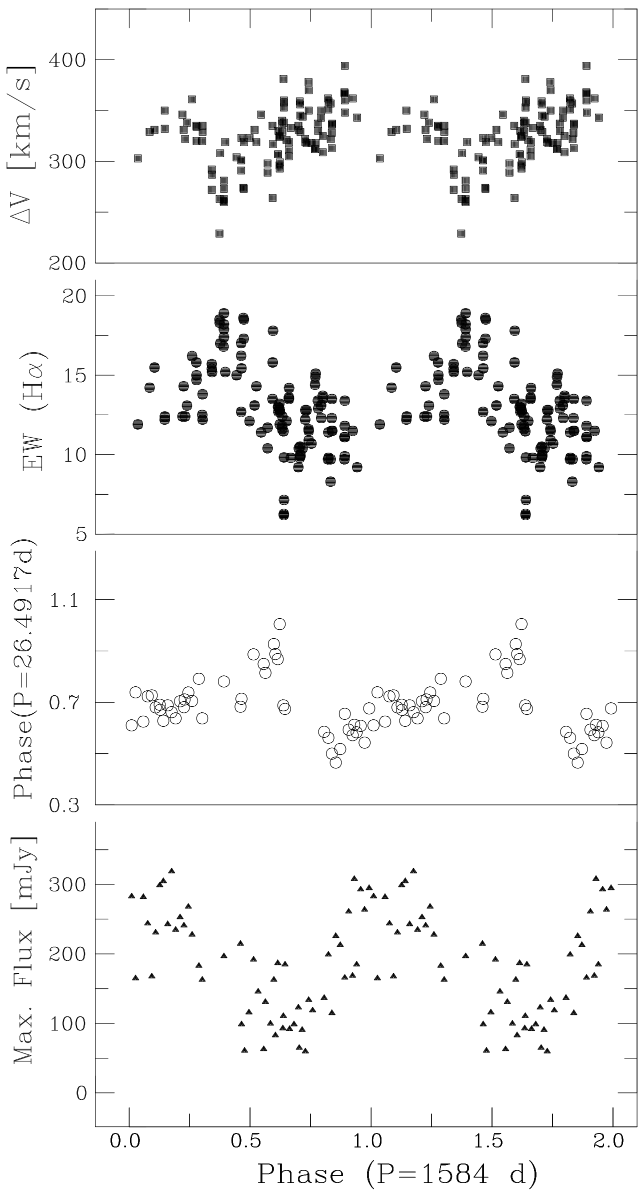

Figure 6.4: Hα and radio parameters of LSI+61303 folded on the 1584 day period with zero phase set at JD2443366.775. From up to down are plotted the hump separation of the Hα, the total $EW(\mathrm{H}\alpha)$, the phase of the radio maximum with respect to the 26.5 day period, and the maximum radio flux

circumstellar disk (Okazaki 1997). Unfortunately, the results of this search turned out to be negative. Thus, the suggestion of a ~ 4 yr Hα modulation remains present in the EW(Hα) and the hump separation measurements.

Possible correlations between the EW(Hα) and the radio outburst amplitude were investigated as well. We used for this purpose the NSF-NRAO-NASA Green Bank Interferometer data analyzed by Gregory (1999). For every Hα data point, the closest radio maximum was selected and correlations were searched for. Again, none was found in reliable way. We do not rule out that all these negative results are a consequence of the considerable scatter of the points, not to say our still short time baseline for long term period studies. It deserves noting that the radio observations are missing just about the time of the EW(Hα) maximum at JD2450300 and the Hα observations are very sparse at the maximum of the radio flux modulation (see Fig. 6.3).

6.1.4 The 26.5 day period and the Be envelope

Our spectroscopic results have provided a direct connection between the periodic radio outbursts of LSI+61303 and its Be disk environment. This connection is based on the suggestive evidence that some of the Hα emission line parameters also vary with the same 26.5 d and possibly ~ 4 yr periods previously found at radio wavelengths. Therefore, the outburst models based on the interaction between the compact object and the star Be envelope are clearly supported.

In this context, it appears likely that the 26.5 d Hα variations have to be interpreted as the neutron star perturbing the Be envelope as it was discussed by Zamanov et al. (1996). However, other alternatives cannot be completely ruled out. For instance, the detected 26.5 d period in B/R and other ratios could also be caused by the propagation of a global density wave, as it happens in many Be X-ray binaries and isolated Be stars. This scenario would then imply the shortest propagation period of the global oscillation detected so far, and the first system in which the propagation of the density wave is synchronized with the orbital period of the neutron star.

6.1.5 What causes the ~ 4 yr modulation in LSI+61303?

The Hα observations presented here can be also used to discriminate between the two previously proposed models for the ~ 4 yr modulation in the radio outburst amplitude. In the LSI+61303 case, it appears that the precessing jet model should be ruled out in favor of those based on quasi-cyclic Be-star envelope variations. Indeed, the most likely explanation of the EW(Hα)

changes, that we observe in a ~ 4 yr time scale, is a variability of the mass loss rate of the Be star.

To better assess this issue, it is instructive to obtain a estimation of how much the mass loss rate should change to account for the observed variations. We will use for this purpose the formulae of Vögel (1993) for an optically thin emission line. Of course, the Hα line is probably not thin, so it must be considered as a rough estimation of the mass loss rate variability. The flux of a wind line determined by recombination can be represented as

$$F = \frac{h\nu}{4\pi d^2} \int_{\mathcal{V}} \alpha_{\rm eff}(n_{\rm e}, T_{\rm e})\, n_{\rm e}\, n_{\rm ion}\, d\mathcal{V}, \tag{6.1}$$

where d is the distance to the star, $n_{\rm e}$ is the electron density, $n_{\rm ion}$ the density of the ion considered, $\alpha_{\rm eff}(n_{\rm e}, T_{\rm e})$ is the effective recombination coefficient of the line, and $\mathcal{V}$ the emitting volume. In the circumstellar disk of LSI+61303 the density follows the power law $\rho(r) = \rho_0(r/R_*)^{-3.25}$ (Waters et al. 1988), so the LSI+61303 flux in Hα can be expressed as

$$F = A\, \dot{M}^2_{\rm loss} \left[1 - \left(\frac{R_{\rm in}}{R_{\rm out}}\right)^{3.5}\right] \tag{6.2}$$

where $\dot{M}_{\rm loss}$ is the mass loss rate of the Be star, $R_{\rm in}$ and $R_{\rm out}$ are the inner and outer radius of the Hα emitting disk, and the constant A includes the average recombination coefficient, the helium abundance and so on (for more details e.g. Vögel, 1993; Tomov et al. 1998). We adopt that $R_{\rm in} = R_*$ and for Keplerian disk $\Delta V/(2\, v \sin i) = (R_{\rm out}/R_*)^{-1/2}$ (Hanuschik 1988), where ΔV and $v \sin i$ are the same as in Section 3.1. Since $F \propto EW$, the observed Hα parameters of LSI+61303 correspond to

$$\dot{M}_{\rm loss,max}/\dot{M}_{\rm loss,min} \simeq 1.5. \tag{6.3}$$

In this way, the variability in EW(Hα) can be explained by suggesting that the mass loss rate varies by a plausible amount of ± 25 per cent over its average value. This mechanism will also imply variations of the density over the same range.

The interaction of a neutron star with the Be star wind is critical in all suggested models for the radio outbursts of LSI+61303. The variability of the mass loss rate of the Be star causes a variability of the mass accretion rate onto the neutron star in case of accretion onto the magnetosphere. In the model of young radio pulsar, the variability of the Be star mass loss changes the position of the shock front. In ejector-propeller model it affects the moments of switching of the Ejector - at lower mass loss rate we expect the ejector to switch on earlier and the radio outburst to peak at an earlier orbital phase than at higher mass loss rate.

In Fig. 6.4, it appears that the Hα measurements are not in phase nor in anti phase with the radio data. This can be due to the bad distribution of the observations as it was noted above or to a real phase shift between the Hα and radio parameters. At this moment we are only able to say that the 1600 day modulation detected in the phase variations of the 26.5 day periodic radio outbursts and the outburst peak flux density is visible in the Hα emission line too.

In any case, it is clear that additional theoretical work and spectroscopic observations will be necessary to find out what is the exact relationship between the radio outbursts and the circumstellar disk.

Finally, if the ~ 4 yr modulation in radio and Hα is due to changes in the circumstellar disk density, it can be probably detected as well in other wavelength domains. For instance, we can expect it to be visible in the infrared bands, where the circumstellar disk contributes with an excess above the stellar continuum. The X-rays and γ-rays may also be modulated every ~ 4 yr too, since the high energy emission of the neutron star depends on the density of the surrounding matter with which it interacts.

The main results from our Hα spectroscopic observations of LSI+61303 are:

1. The circumstellar disk in LSI+61303 is among the densest of Be stars.

2. The 26.5 day period is visible in the Hα emission line. This is the first time that a clear stable periodicity is detected in the Hα emission line of a Be/X-ray binary in connection with the orbital motion of the compact object.

3. Evidences of a ~ 4 yr modulation in the Hα of LSI+61303 have been found. This favours the ~ 4 yr cycle in the radio outbursts as being related to variations of the circumstellar disk. The model of precessing jets should be consequently ruled out.

4. The ~ 4 yr modulation is also likely to be present at the infrared, X-ray and γ-ray domains.

6.2 First correlation between compact object and circumstellar disk in the Be/X-ray binaries

A remarkable correlation between the Hα emission line and the radio behaviour of LSI+61303 over its ~4 yr modulation is discovered. The radio outburst peak is shifted by a quarter of the ~4 yr modulat ion period (about 400 days) with respect to the equivalent width of the Hα emission line variability. The onset of the LSI+61303 radio outbursts varies in phase with the changes of the Hα emission line, at least during the increase of Hα equivalent width. This is the first clear correlation between the emission associated to the compact object and the Be circumstellar disk in a Be/X-ray binary system.

Introduction The Be/X-ray binaries are the major subclass of massive X-ray binary systems in which a neutron star accretes material from the wind of an early type Be star. The Be stars are known to exhibit emission in the Balmer lines and infrared excess, which are attributed to the presence of cool circumstellar disk. Correlation between the changes of the Be circumstellar envelope and the emission of the compact object can be expected, as a result of the compact object interaction with the surrounding matter. However, no clear correlation has been detected till now – only loose correlations between the optical/infrared properties of the Be circumstellar disks and the X-ray emission of the neutron star have been reported to exist (e.g. Corbet et al. 1985; Coe et al. 1994; Negueruela et al. 1998).

LSI+61303 (V615 Cas, GT 0236+610) is a radio emitting X-ray binary which exhibits radio outbursts every 26.5 d. The radio outburst peak and the outburst phase are known to vary over a time scale of ~4 yr (Gregory et al. 1989; Gregory, 1999). Hereafter, we will use the latest values reported and we will refer to these radio periods as P_1 = 26.4917 d and P_2 = 1584 d. Phase zero for both has been set at JD2443366.775 (Gregory, Peracaula & Taylor, 1999). The 26.5 d period is believed to be the orbital period. The ~4 yr modulation has been discovered on the basis of continued radio monitoring. Both relativistic jet precession or cyclic variability in the Be star envelope have been proposed as a possible origin of the long term modulation (Paredes, 1987; Gregory et al. 1989), with the second interpretation being the most likely one. This suggestion is supported by the fact that the Hα emission line varies on the same (4 yr) time scale (Zamanov et al. 1999). However, these authors were not able to derive what is the connection between the radio and Hα parameters.

In this letter we report an intriguing correlation between the synchrotron non-thermal radio emission, associated with the compact star, and the Be circumstellar disk visible in the *H*α

emission line. This is the first clear connection between the Be circumstellar disk variability and the emission from the neutron star in the Be/X-ray binaries.

6.2.1 $H\alpha$ and radio observations

The new $H\alpha$ spectroscopic observations used in this paper are obtained with the 2-m RCC telescope of the Bulgarian National Astronomical Observatory 'Rozhen' during the last two years. They are analyzed together with the previously published data (Paredes et al. 1994; Zamanov et al. 1999). The Hα parameters which vary with the $\sim$4 yr modulation are the equivalent width of Hα, EW(Hα), and the distance between the peaks, $\Delta V_{\rm peak}$ (Zamanov et al. 1999).

The radio observations during the previous 6 years were retrieved from the Green Bank Interferometer, which is a facility of the USA National Science Foundation operated by NRAO in support of the NASA High Energy Astrophysics program. From this data, we measured the radio outburst peak flux density and the beginning of every outburst. As onset of the outburst, we adopted the time when the radio flux density achieved a value equal to 1/3 of the maximum flux observed for every orbital period. Whenever possible, the onset of the outburst was measured separately from the 2.25 GHz and 8.3 GHz observations and the average value is used in the analysis.

In terms of the Ejector-Propeller model of LSI+61303, the outburst onset better represents the time of the transition of the neutron star from propeller to ejector and the appearance of the expanding radio emitting plasmon (Zamanov, 1995).

6.2.2 Relation between circumstellar disk and radio outbursts

The radio and $H\alpha$ observations obtained during the last years are plotted in Fig.6.5. It is clearly visible that all these parameters vary over a time scale of $\sim$4 yr. Following the predictions of Gregory (1999) the radio outburst peak achieved a new maximum at the end of 1999. Big changes in the radio outburst peak flux from values less than 0.150 Jy at JD2451000 to values more than 0.250 Jy at JD2451400 are observed (Fig.6.5). At the same time, the parameters of the Be circumstellar disk $EW(H\alpha)$ and $\Delta V_{\rm peak}$ do not exhibit extreme values in their behaviour. This suggests that the radio peak flux density and the $H\alpha$ parameters do not vary in phase nor in anti-phase.

To understand this behaviour we plotted all the data folded on the P_2=1584 d period. Every parameter was fitted separately with a cosine function. Our attempts to use more complicated

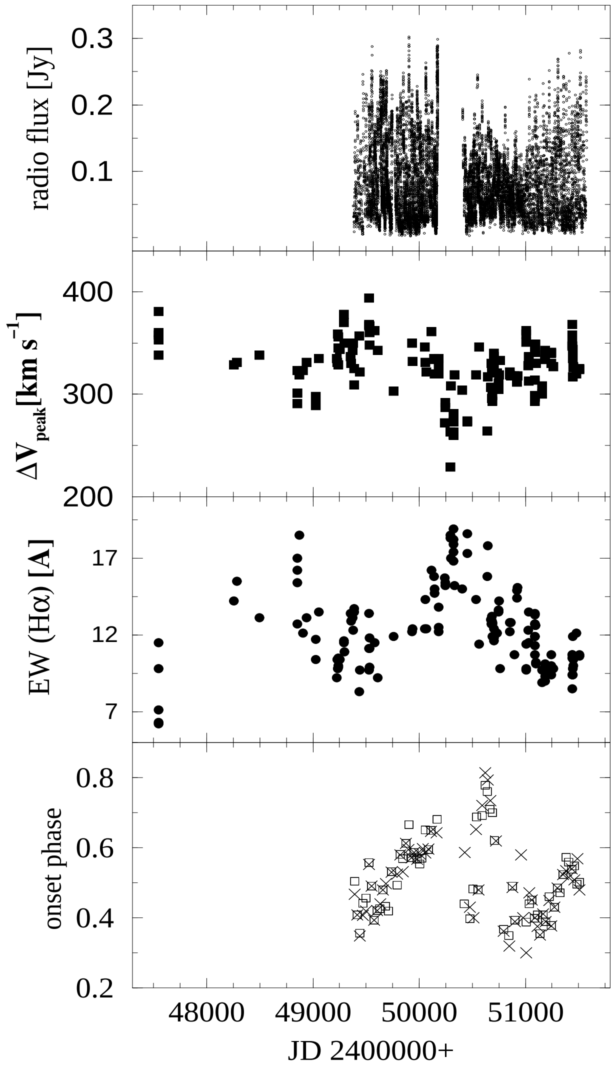

Figure 6.5: $H\alpha$ and radio observations over the period 1989 - 2000. The regular Hα observations cover more than 2500 days. From top to bottom are plotted the radio flux density at 2.25 GHz, the $\Delta V_{\rm peak}$ of Hα, the EW(Hα), and the onset phase of the outburst relatively to the orbital (P_1) period. In the bottom panel, the squares refer to 2.25 GHz and ($\times$) - to 8.3 GHz. The traces of the $\sim$4 yr modulation are visible in all panels.

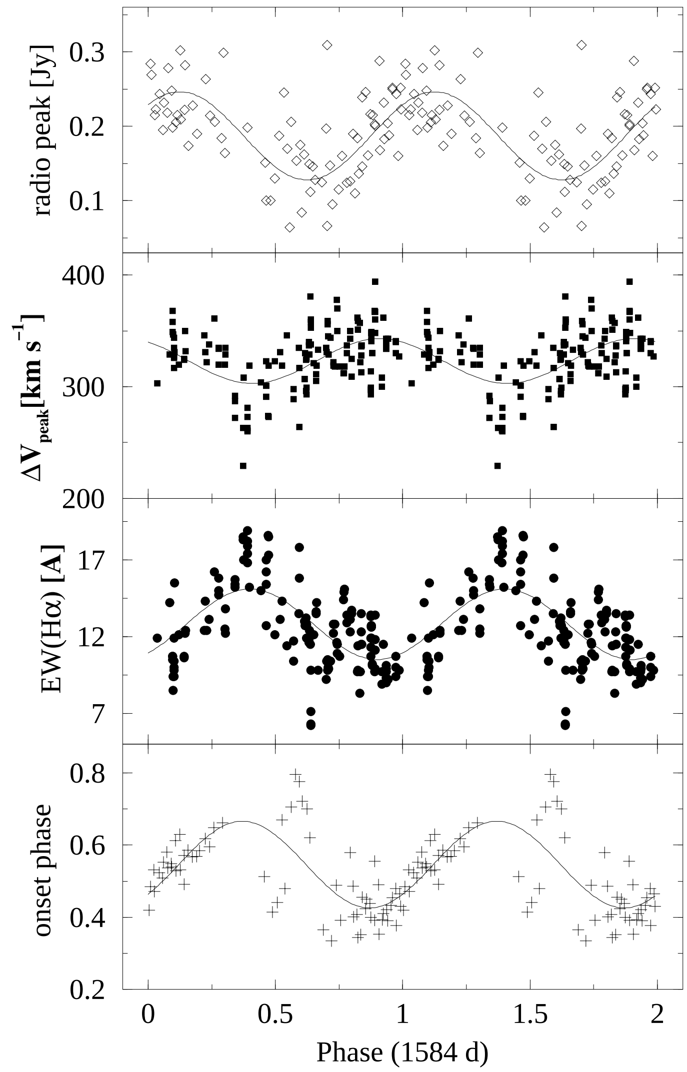

Figure 6.6: The radio and Hα parameters folded on P_2=1584 day period with phase zero at JD2443366.775. The upper panel represents the radio outburst peak flux. The Hα panels are the same as in Fig.6.5. The bottom panel represents the averaged values of the onset phase from 2.25 GHz and 8.3 GHz.

functions (e.g. three term truncated Fourier fit containing sine and cosine terms with half and quarter orbital periods) showed that, with this scatter of the points, the significance of other terms is negligible and we used simple cosine waves in the form: $y = A + B\, cos(2\pi(\phi + \phi_0))$. The best fit parameters are listed in Table 6.1 and plotted as solid lines in Fig.6.6.

From Table 6.1 and from Fig.6.6 the following correlations can be seen:

a) The Hα parameters, EW($H\alpha$) and $\Delta V_{\rm peak}$, vary in anti-phase. This is a relationship well known for the Be stars, reflecting the fact that the the size of the disk grows as the EW(Hα) increases (Hanushik, Kozok & Kaizer, 1988).

b) At the same time, a strange phase shift can be seen between the radio outburst peak flux and the Hα parameters. This shift is about 0.25 in phase. So, if the parameters really vary as simple cosine functions on average, this means that the radio peak varies with the first derivative of the $H\alpha$ emission line parameters.

c) The beginning of the radio outburst is in phase, or only slightly shifted, relative to the Hα variability, at least on the ascending branch.

Ray et al. (1997) have shown that the outburst peak is slowly shifting in phase during the time interval from JD2449400 to JD2450100. In the same interval the outburst peak flux achieved maximum values and began to decline. This is one more confirmation that the variability of the outburst peak and the time of the outburst are phase shifted one to another over the 1584 day period.

Although the scatter of the points in Fig.6.6 is considerable, all evidences (the cosine fit, the behaviour observed by Ray et al. (1997), the behaviour during the last radio outburst maximum) show that the radio outburst peak is shifted relatively to the behaviour of the circumstellar disk, although the start of the radio outburst is in phase (or almost in phase) with the circumstellar disk changes.

6.2.3 Discussion

A successful modeling of the radio outburst of LSI+61303 is based on the synchrotron radiation from relativistic particles injected into an expanding plasmon (Paredes et al. 1991). The genesis of the plasmon can be a result of the transition of the neutron star from propeller to ejector state (Zamanov, 1995), or in other words from accretion onto the magnetosphere to "young radio pulsar" every orbital period.

In such a picture, the start of the outburst will correspond to the moment when the neutron star emerges from the denser parts of the circumstellar disk. Therefore, the bigger the disk the

Table 6.1: Fitted parameters, $y = A + B\,cos(2\pi(\phi + \phi_0))$.

parameter	A	B	ϕ_0
Radio peak [Jy]	0.187±0.003	0.059±0.003	0.125±0.010
Onset phase*	0.548±0.005	0.12±0.01	0.62±0.01
EW($H\alpha$) [Å]	12.8±0.01	2.3±0.1	0.60±0.01
$\Delta V_{\rm peak}$ [km s^{-1}]	323±1	−20±2	0.59±0.01

(*) the phase of the beginning of the radio outburst calculated relative to the orbital period

later the outburst can be expected. This can be seen on Fig.6.6. At phases 0–0.25 we observe increase of the EW(Hα), decrease of the $\Delta\, V_{\rm peak}$ and slow shift of the onset of the outburst. The behaviour of the beginning of the outburst on the increasing branch (phases 0–0.25) is stable, but on the decreasing branch (phases 0.25–0.5) the scatter of the points is considerably bigger. The stable behaviour at phases 0.25–0.5 is observed twice at about JD 2449800 and JD 2451400 (Fig.6.5) so it is unlikely to be a data artifact. Probably this is a result that, during the disk build-up, the increase of the material of the Be disk is feeded only from one source - the B star equatorial region. In contrast the disk-decline can be in two directions - accretion onto the B star or slow dissipation outwards. The behaviour of the start of the outburst points that the disk build up is a stable process and the disk-decline is a more complicated and probably unstable process, or may be it suggests formation of structures like the double disk observed in X Persei (Tarasov & Roche, 1995).

In context of the propeller-ejector transition the surrounding matter will basically influence the expansion velocity of the plasmon, affecting in this way the intensity of the radio outbursts. The remaining plasmon physical parameters (initial magnetic field, injection rate of relativistic particles, etc.) are not expected to vary significantly from one to another outburst. The expanding plasmon calculations predict that there will be weaker outbursts for higher expansion velocities. By expanding faster, the energy losses of the electrons due to the adiabatic expansion are more important and less electron energy is available to be radiated. In addition, the faster decrease of the magnetic field will also contribute to less synchrotron radiation being produced. Supposing that the plasmon is a result of the propeller-ejector transition, the expanding plasmon will appear when the neutron star is receding from the periastron and the plasmon will expand outside of the Hα emitting disk. The size of this disk is about 40-65 $R_\odot$ (Zamanov & Martí 2000) and the apastron separation between components is about 150 $R_\odot$ (Hutchings & Crampton

1981). The enigmatic behaviour of the outburst peak flux density (its phase shift with 0.25 or ~400 days) indicates that the conditions outside the Hα disk vary in a different way compared to the changes inside the Hα emitting disk.

The X-ray emission of LSI+61303 is observed to exhibit maximum every orbital period and the X-ray outburst is shifted relatively to the radio outburst (Taylor et al. 1996, Harrison et al. 2000). In terms of the ejector-propeller model, the X-ray maximum is due to the propeller action and higher mass accretion rate onto the magnetosphere at the periastron passage (Zamanov & Zamanova, 1997). In this sense it will be very interesting to see what is the behaviour of the X-ray maximum observed in the high-energy emission of LSI+61303 over the ~4 yr modulation.

Another possible origin of the ~4 yr modulation may be the precession of the Be star. Lipunov & Nazin (1994) have demonstrated that this value is in rough agreement with the expected period ($\sim 10^3$d) for precession of the B star. The precession of the B star can be expected, because after the supernova kick the neutron star orbital plane may be different from the Be disk plane (e.g. Bradt & Podsiadlowski, 1995). Our attempts to model the behaviour of the outburst phase as a result of the precession are unsuccessful till now but it can be due to of insufficient data sample, because the systematic radio observations cover about 6 yr (1.5 periods) with considerable gaps and scatter inside the data set. In this context, it deserves to be noted that if the Hα variability is a result of a precessing disk seen at different inclination angles, this will imply an inclination angle $i > 60^\circ$ and a precession angle $\Delta i > 6^\circ$ (this estimate is obtained using the values from Table 6.1 and assuming everywhere an optically thick in Hα disk).

To conclude, the behaviour of LSI+61303 radio and Hα emission is evidence that the picture of the interaction between the neutron star and the circumstellar disk in the Be/X-ray binaries is not as simple as generally expected. We need long series of observations over different wavelengths to better understand the behaviour of the Be stars and the Be/X-ray binaries.

6.3 Moving component in Hα of LS I+61°303

We report our attempts to detect and confirm a narrow moving component in the $H\alpha$ emission line of LSI+61303. The existence of this spectral feature was already suspected in the past. As a result, we find that this component does exist and that its radial velocity varies in agreement with the radio period of the system. We interpret it tentatively as due to a denser region, or bulge, orbiting near the outer edge of the Hα emitting disk.

Introduction LS I+61^{0}303 (V615 Cas, GT 0236+610) is a radio emitting Be/X-ray binary, with its primary being a rapidly rotating B0V star with an equatorial disk. The secondary is a compact object, most probably a neutron star, orbiting in an eccentric orbit. The most spectacular phenomena associated with this object are its periodic non-thermal radio outbursts, repeating every ~ 26.5 d. This interval is supposed to be the orbital period of the binary.

The Hα of LSI+61303 is observed as a double peaked emission line of variable profile intensity which is not peculiar with respect to those observed in other Be stars High resolution Hα observations of this object are discussed in few papers (Paredes et al. 1994, Zamanov et al. 1999). In these papers, variability of the Hα emission line was established over time scales of days and two possible interpretations were proposed to account for it, namely: (i) an influence of the compact object onto the Be star disk; (ii) an unresolved emission line component due to gas within the system or ejected from it.

The present paper discusses $H\alpha$ observations of LSI+61303 with the aim of testing the reality of proposed unresolved component.

6.3.1 Observations, data reduction and results

The observations were obtained with the Coudé spectrograph of the 2 m telescope at the Bulgarian NAO "Rozhen". They cover about 110 Å (0.2 Å pixel^{-1}) and have a signal-to-noise ratio in the range 30-50. In order to detect a possible narrow or unresolved component we have applied the following procedure:

1. All spectra were transformed to an uniform heliocentric wavelength set.

2. The spectra were divided into 10 groups. Every group consists of 3-4 spectra, obtained in consecutive or close nights. For each group the "minimum spectrum" was generated by taking the minimum pixel intensity from all the spectra of the group over the uniform wavelength set.

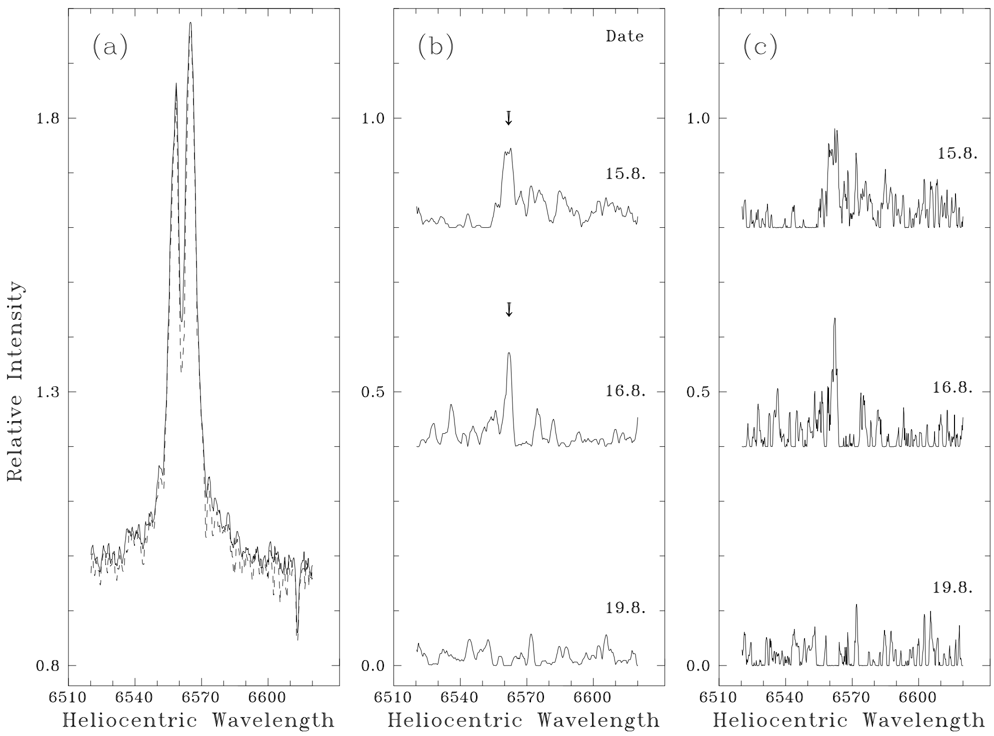

Figure 6.7: **(a)** An example of average spectrum (solid line) and the “minimum spectrum” (dashed line) obtained using the spectra from 15, 16 and 19 August 1997. **(b)** The smoothed residuals for the same group. The arrows indicate the positions of the moving component. **(c)** The unsmoothed residuals for the same spectra. The plots are offset by adding arbitrary constants identical for panels (b) and (c).

3. The “minimum spectrum” was subtracted from all spectra in the group. The residuals were smoothed with a moving average over 10-15 points (2 to 3 Å). An example is shown in Fig.6.7.

The applied procedure assumes explicitly that, if moving component exists, it must appear as a pure emission line (not absorption).

It is visible in Fig. 6.7 that a moving narrow component does exists. This feature clearly shows up in most residual plots after the “minimum spectrum” is subtracted. The typical FWHM of this moving component is 4-8 Å, with a normalized intensity about 0.1-0.2. The radial velocity of the component was determined by employing a Gaussian fit, with a typical

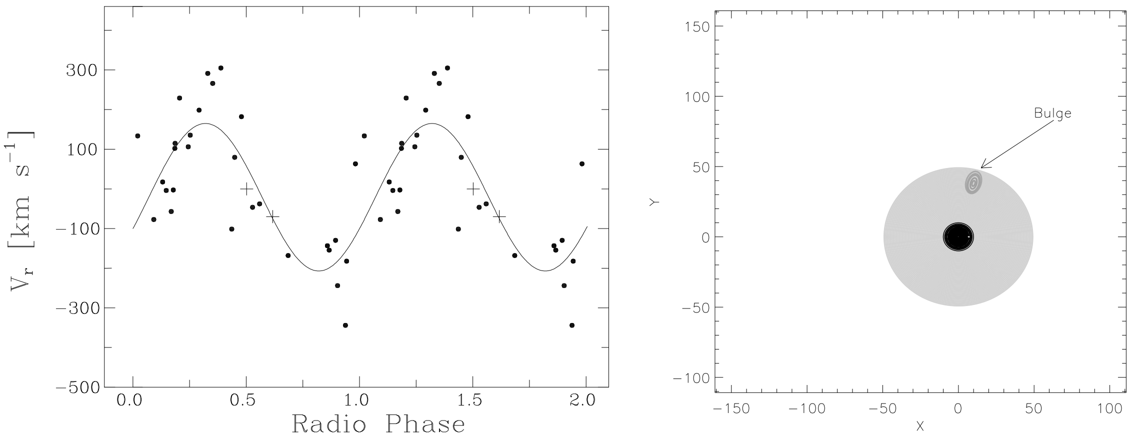

Figure 6.8: **Left panel:** Phase plot of the radial velocities of the moving component as a function of radio phase. The solid line is the best cosine fit. The dots represent our data, the crosses - from Paredes et al. (1990). **Right panel:** Schematic representation of the Be star, its Hα-emitting disk, and the bulge located near to the outer edge. The axes are in units of $R_{\odot}$.

error of ± 50 km s^{-1}. We plotted our measurements in the left panel of Fig. 6.8 folded on the radio phase of LSI+61303. The latest ephemeris by Gregory et al. (1999) was used for this purpose, with the phase origin set at JD 2443366.775 and a 26.4917 d radio period being adopted. A clear trend of the component radial velocity emerges in this figure. Indeed, a modulation with the same 26.5 d radio period and a ± 250 km s^{-1} amplitude seems to be present in the data. Such a strong radial velocity dependence gives us confidence that we are detecting a real variability, and that this is not likely to be an artifact of the applied procedure. It deserves to be noted here that the moving component was already directly visible in the high resolution spectra of Paredes et al. (1990), and without any subtraction procedure being applied. The radial velocity measurements of these authors have been incorporated in Fig. 6.8 and they are in excellent agreement with our observations.

By fitting to the data points a least squares cosine function of the form: $V_{\rm r}(\varphi) = A + B\cos[2\pi(\varphi - \varphi_0)]$, we obtain the following best fit parameters: $A = -21 \pm 14$ km s^{-1}, $B = 186 \pm 20$ km s^{-1}, and a phase shift $\varphi_0 = 0.68 \pm 0.02$ (φ is the radio phase). As it can be expected, the parameter A is near to the system velocity -55 km s^{-1} derived by Hutchings & Crampton (1981). The best fit cosine fit is plotted in Fig.6.8 as a solid line.

Table 6.2: Radial velocities of the moving component

JD2400000+	$V_r[km/s]$	Group	JD2400000+	$V_r[km/s]$	Group
49292.31	266	1	50293.55	-77	7
49293.27	305	1	50294.57	17	7
49294.53	-101	1	50298.58	–	7
49354.21	-168	2	50320.58	–	8
49356.26	–	2	50321.53	-3	8
49374.48	79	3	50322.37	-2	8
49375.25	182	3	50322.53	102	8
49385.33	-143	3	50322.56	114	8
49386.26	-129	3	50676.52	31	9
49528.45	135	4	50677.36	-26	9
49529.47	198	4	50680.56	187	9
49530.48	291	4	50685.49	-222	9
49531.42	–	4	50686.47	-260	9
50181.29	–	5	50687.55	-197	9
50182.26	–	5	50688.59	-76	9
50183.35	-344	5	50689.60	77	9
50242.53	-57	6	50703.38	-293	10
50243.52	229	6	50704.56	326	10
50244.52	106	6	50705.54	216	10

6.3.2 Origin of the moving component

What is the origin of the moving component? Among possible interpretations, one could think of a possible relationship with the compact companion in the LSI+61303 system, i.e., due to matter captured by the neutron star from the Be star wind - the material around the neutron star, or an accretion disk, or an accretion wake.

The orbital parameters of LSI+61303 are not well constrained so far. The proposed orbits by Hutchings & Crampton (1981) and Martí & Paredes (1995) are quite different. In spite of this uncertainty, the observed variations up to ± 250 km s^{-1} are significantly larger than those expected from the orbital motion of the neutron star, as well as of the Be star, in all proposed orbital solutions. Consequently a direct relationship, in the sense that the moving component is reflecting the motion of the neutron star, does not seem to apply unless the orbit is extremely eccentric, and alternative interpretations need to be considered.

The spectrally resolved interferometry of ζ Tauri by Vakili et al. (1998) has shown a bulge of emission in the disk of this Be star. These authors have interpreted their interferometric and Hα observations assuming that such a bulge follows a circular orbit in the equatorial disk plane, at a distance of about 7 stellar radii from the central star. In this context, it is thus conceivable to us that the moving Hα component in LSI+61303 is also due to a bulge region existing in the circumstellar disk.

Under the assumption that this is the case, let us find the position of the bulge. Hereafter, we will adopt the following parameters for the Be star in LSI+61303: $M_* = 10\ M_\odot$, $R_* = 10 R_\odot$, and $v \sin i = 360$ km s^{-1} (Hutchings & Crampton 1981). Assuming that the star rotates at 90% of its critical velocity (Sletteback et al. 1992), we derive $\sin i = 0.92$ and $i \simeq 67°$. Consequently, from the term B in Eq. 1 and the above assumptions we obtain that the bulge in LSI+61303 rotates at a velocity $V_{\rm bulge} = B/\sin i = 202$ km s^{-1}. This corresponds to a distance of about $\sim 4.5\ R_*$, provided that the bulge is in a Keplerian orbit around the star.

From the relationship between the separation of the Hα peaks, $\Delta V_{\rm peak}$, and the outer radius $R_{\rm out}$ of a Keplerian emitting disk: $R_{\rm out} = R_*(2v \sin i\ /\ \Delta V_{\rm peak})^2$, we find that $R_{\rm out}$ = 4.0-6.6 R_* (using $\Delta V_{\rm peak}$ = 300-360 km s^{-1}, Zamanov et al. 1999). This result compares satisfactorily to the bulge distance found above and implies that the bulge must be located near to the outer edge of the $H\alpha$ emitting disk. A schematic picture of the $H\alpha$ disk and the position of the bulge is represented in the right panel of Fig. 2.

As mentioned before, the orbital elements of the Be X-ray binary LSI+61303 are not well determined. From the 26.5 d period present in the $V_{\rm r}$ data, one could wonder if the position of the bulge should be in phase with the motion of the neutron star. However, this does not occur in any of the proposed orbital solutions. Whether at the end there is a relationship between the bulge position and that of the neutron star remains to be determined by a careful revision of orbital solutions in the future.

6.4 LSI+61^{0}303 in terms of Ejector-Propeller Model

We tested the ejector-propeller model of the Be/X-ray binary LSI+61^{0}303 by using the parameters predicted by the model in the calculations of the X-ray and radio variability. The results are: (1) in terms of the Ejector-Propeller model, the X-ray maximum is due to the periastron passage; (2) the radio outburst can be really a result of the transition from the propeller to the ejector regimes; (3) the radio outburst will delay with respect to the X-ray maximum every orbital period. The proposed scenario seems to be in good agreement with the observations.

6.4.1 Flaring behaviour of LSI+61303

LSI+61303 (V615 Cas, GT0236+620) is a well known Be/X-ray binary with periodic radio outbursts every 26.5 d, assumed to be the orbital period. After the discovery of such periodic events (Gregory & Taylor 1978; Taylor & Gregory 1982) and the first model (Maraschi & Treves, 1981), this massive system has been studied extensively since nearly two decades ago. Hereafter, we will use the late radio phase ephemeris $P = 26.4917\,d$ and phase zero at JD2443366.775 (Gregory, Peracaula & Taylor, 1999).

The flaring radio emission of LSI+61303 has been modeled by Paredes et al. (1991) as synchrotron radiation from an expanding plasmon containing relativistic particles and magnetic fields. The dependence of the radio outburst flux density on the frequency, the time delay in the outburst peak, and the general shape of the radio light curves are in general well accounted for by continuous injection of synchrotron emitting electrons into the plasmon volume. However, the formation details of such plasmon were beyond the scope of the Paredes et al. (1991) model. In fact, its initial physical properties were considered as the free parameters to be fitted. According to Zamanov (1995), the genesis of such plasmon can be interpreted as a result of a transition in the accretion regime of the neutron star as it probes different parts of the Be envelope in an eccentric orbit. The proposed transition would be from so called propeller (P) to the Ejector (E) regime. In this context, propeller means accretion onto the magnetosphere and ejector is often named “young radio pulsar”.

Our purpose here is to try to check the agreement between the plasmon parameters predicted by the theory of a PE transition and those required to reproduce the observed radio light curves using the Paredes et al. (1991) model. We advance here that the agreement seems to be good at least qualitatively, including the possibility to explain the X-ray luminosity and variability.

This agreement provides a consistent physical interpretation for the outburst mechanism in the LSI+61303 system.

6.4.2 Simultaneous Radio and X-ray observations

The variability of the source in the X-ray domain was detected in ROSAT observations (Goldoni & Mereghetti, 1995). On two occasions, the LSI+61303 flaring events have been monitored by ground based radio facilities and space X-ray satellites in a coordinated way. The results were presented in Taylor et al.(1996) and Harrison et al.(2000). The behavior observed is reproduced in Fig. 6.9, using the latest ephemeris determination. The observations during 1992 are obtained with ROSAT (0.5-2 keV) and the VLA (1.5 GHz and 4.9 GHz), and those during 1996 - with RXTE (2-10 keV) and GBI [1] (2.25 GHz and 8.3 GHz). From this figure, it is clear that in both cases the radio peak is delayed with respect to X-ray maximum.

6.4.3 Mass accretion rate

Bondi-Hoyle accretion: Usually, to estimate the mass accretion rate onto a compact object in wind fed binaries the Bondi-Hoyle-Littleton formula is used in the form:

$$\dot{M}_a = \pi \frac{(2GM_{NS})^2}{V_{rel}^3} \rho, \tag{6.4}$$

where M_{NS} is the mass of the neutron star, V_{rel} is the NS velocity relative to the surrounding matter, ρ is the density in the surrounding matter.

The structure of the Be star disks are not yet well understood, even for the most important parameters, such as the velocity and density laws, different assumptions have been proposed. Following Waters et al. (1988), we will accept a density structure in the form

$$\rho = \rho_0 (r/R_*)^{-n} \quad \text{and} \quad V_r = V_0 (r/R_*)^{n-2}, \tag{6.5}$$

where R_* is the radius of the Be star and V_r is the outward velocity. The density parameter n can take values $n = 2 - 4$ for different objects. The initial velocity, V_0 (the velocity at $r = R_*$), most probably lies between 2 and 20 km s^{-1}. Finally, a Keplerian law is adopted concerning the disk rotation:

$$V_\phi(r) = \sqrt{GM_1/r} \tag{6.6}$$

where M_1 is the mass of the primary component in the system, i.e. the Be star.

[1] The Green Bank Interferometer is a facility of the USA National Science Foundation operated by NRAO in support of the NASA High Energy Astrophysics programs.

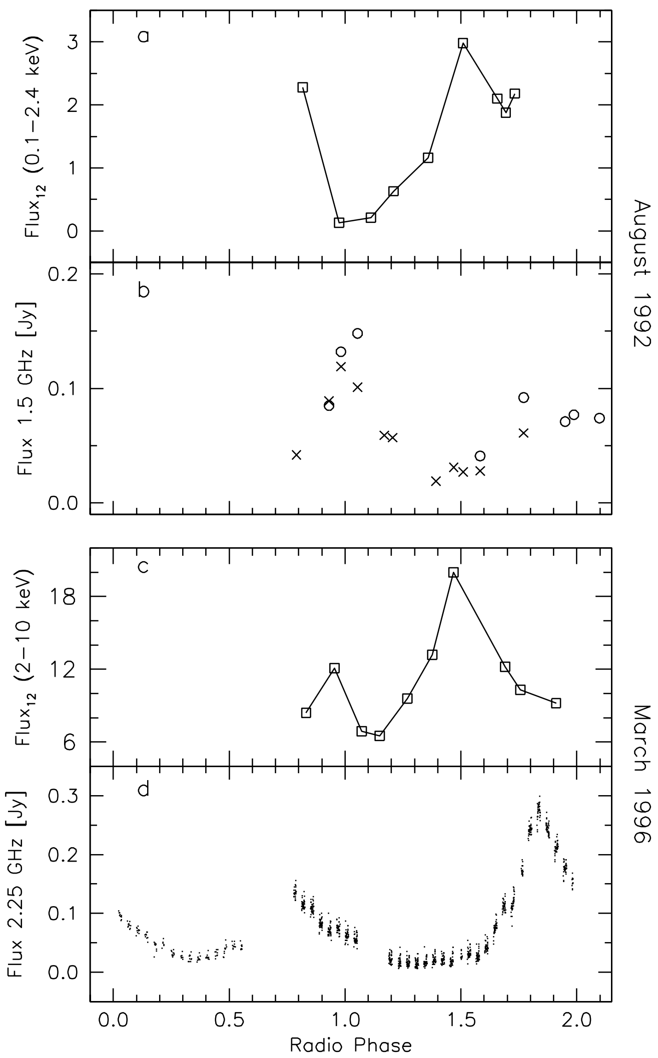

Figure 6.9: The simultaneous X-ray and radio observations:
(a) and **(b)** – August 1992, Taylor et al. (1996)
(c) and **(d)** – March 1996, Harrison et al. (2000)
A clear phase shift between X-ray and radio is visible in both cases.
In **(b)** the triangles refer to 1.5 GHz and the crosses – to 4.9 GHz flux density. The X-ray flux is everywhere in units 10^{-12} erg cm^{-2} s^{-1}.

As a result of the motion of the neutron star throw the Be circumstellar disk the mass accretion rate will vary along the orbital period. A few examples, calculated using different parameters for the Be circumstellar disk, are shown in Fig.6.10. During the calculations we assumed always an orbital eccentricity $e = 0.6$, a neutron star mass of $M_{NS} = 1.4\,M_{\odot}$, $M_1 = 10\,M_{\odot}$ and an orbital period P_{orb}=26.4917 days.

As it is visible in Fig.6.10, we can obtain very strange mass accretion rates in some cases. In Fig.6.10(b,c), the average mass accretion rate is considerably higher than the mass loss rate of the Be star. This is a false result of the used formula. The Bondi-Hoyle description is valid for accretion from infinite medium. It assumes that all the matter entering into a cylinder with radius equal to the accretion radius ($R_a = \sqrt{2GM_{NS}/V_{rel}^2}$) will be accreted. In the context of a binary star, this is only valid provided that

- the motion is high supersonic $V_{rel} >> C_s$,
- $R_a << r$,
- the whole accretion cylinder is filled with the outflowing wind.

Unfortunately these conditions are not always fulfilled in Be/X-ray binary systems.

Mass accretion rate in Be/X-ray binaries: As it was shown in the previous section the Bondi-Hoyle formulae are not giving good results in case of Be/X-ray binaries. The exact mass accretion rate could be found only if we consider simultaneously the formation of the wind and the influence of the compact object onto the wind. Here we propose a modification of the mass accretion rate formula that is appropriate for Be/X-ray binaries. In order to do so, the Bondi-Hoyle formula has to be rewritten in a way such that the accretion radius explicitly appears:

$$\dot{M}_a = \pi R_a^2\,\rho\,V_{rel}\,, \tag{6.7}$$

where the density in an outflowing wind, with disk opening angle θ, is given from the continuity equation:

$$\dot{M}_{loss} = 4\pi r^2 \sin\theta\, V_w\,\rho, \tag{6.8}$$

The wind in the disk is most probably subsonic (i.e. Okazaki, 2001). A keplerian rotation in the disk will give in many cases a low relative velocity between the NS and the wind. This means that the accretion radius depends also on the speed of sound, c_s :

$$R_a = \frac{2GM_{NS}}{V_{rel}^2 + c_s^2} \tag{6.9}$$

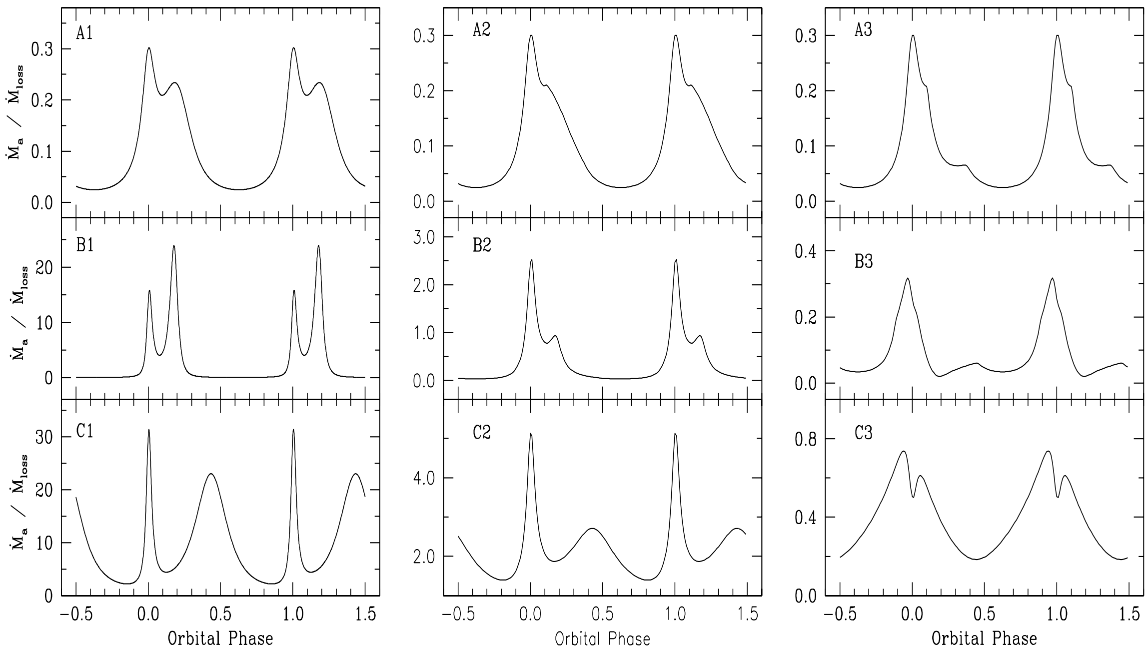

Figure 6.10: Mass accretion rate using the Bondi-Hoyle formulae. Everywhere the orbital parameters are $M_1 = 10\,M_\odot$, $M_{NS} = 1.4\,M_\odot$, P_{orb}=26.4917 d, $e = 0.6$. The wind parameters used and the calculated average mass accretion rate are :

(A1) V_0=5 km s^{-1}, $n = 3.25$, non-rotating disk, $\overline{\dot{M}_a} = 0.11\,\dot{M}_{loss}$

(B1) V_0=5 km s^{-1}, $n = 3.25$, keplerian disk, $\overline{\dot{M}_a} = 2.9\,\dot{M}_{loss}$

(C1) V_0=10 km s^{-1}, $n = 2.1$, keplerian disk, $\overline{\dot{M}_a} = 9.7\,\dot{M}_{loss}$

The use of the Bondi-Hoyle formula gives obviously false values(at least in A1 and B1) values of the average mass accretion rate:

(A2), (B2), (C2) - the same parameters, but the factor of the filling of the accretion cylinder included.

(A3), (B3), (C3) - the same parameters, but the upper limit set $R_a \leq r/4$, and the filling factor included. The corresponding average mass accretion rates are $\overline{\dot{M}_a/\dot{M}_{loss}} = 0.09$, 0.08, 0.36, for A3, B3, and C3 respectively.

Using this formula (with or without C_s^2 term), the accretion radius of a neutron star can achieve values bigger than the distance between components. However the disks in the Be/X-ray binaries are more or less similar to the disks in the "normal" Be stars (Zamanov et al. 2001) although some differences exist. This means that the accretion radius can not be very big, otherwise the NS would control the motion of the wind and this is impossible because the mass ratio is $M_1/M_{NS} > 4$ (typically $M_1 > 8\,M_\odot$ and $M_{NS} = 1.4M_\odot$) We will thus adopt here an upper limit $R_a < 0.25\,r$, where r is the distance from the Be star

Because the outflowing wind is confined in a disk, it is possible that the vertical size of the disk is less than the accretion radius. Consequently, the accretion cylinder would not entirely filled by the wind material. In case that $R_a > y$ where y is the vertical size of the outflowing disk $y = rsin\theta$, the accretion rate must be reduced with pure geometrical factor $2\pi R_a^{-2}[y\sqrt{R_a^2 - y^2} + R_a^2 \sin^{-1}(y/R_a)]$.

We believe that the proposed modifications give considerably better results concerning the mass accretion rate, i.e. the NS will accrete a fraction of the wind. The results of the calculations are demonstrated in Fig.6.10 A3,B3,C3.

6.4.4 X-ray variability in the light of Ejector-Propeller model

A sketch of the ejector-propeller model of LSI+61303 is illustrated in Fig.6.11. Following the suppositions the neutron star will act as propeller (accretion onto the magnetosphere) at periastron and as ejector (young radio pulsar) at the apastron. The transitions between the regimes will depend how material is captured in the the neutron star accretion cylinder, possible formation of accretion disk during the accretion onto the magnetosphere, and even the possible flip-flop instability of accretion (Livio et al 1991).

Following the assumptions of the ejector-propeller model, a lower mass capture rate is expected during the ejector regime. In contrast, higher mass capture rates are expected during the the propeller regime close to periastron passage. During the propeller stage the X-ray luminosity can be estimated as

$$L_X(P) = 2^{2/7}(GM)^{8/7}\mu^{-4/7}\dot{M}_a^{9/7}, \tag{6.10}$$

where G is the constant of gravitation, M is the mass of the neutron star, μ is its magnetic dipole moment (which is adopted $\mu = 2 \times 10^{30}$G cm^3), and $\dot{M}_a$ is the mass accretion rate.

During the ejector stage efficiency of conversion of the spin-down energy into high energy emission can be expected to be about 1-10% (Tavani et al. 1996). The estimated spin-down

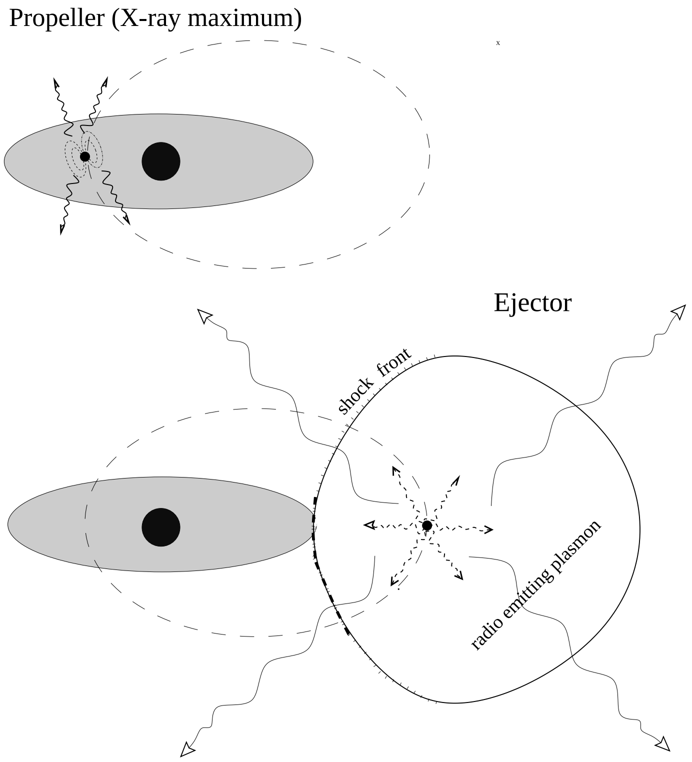

Figure 6.11: A sketch of the Ejector-propeller model. The dashed lines indicates the orbit of the neutron star. Upper - accretion onto the magnetosphere at periastron, down - ejector and the cavern around the neutron star.

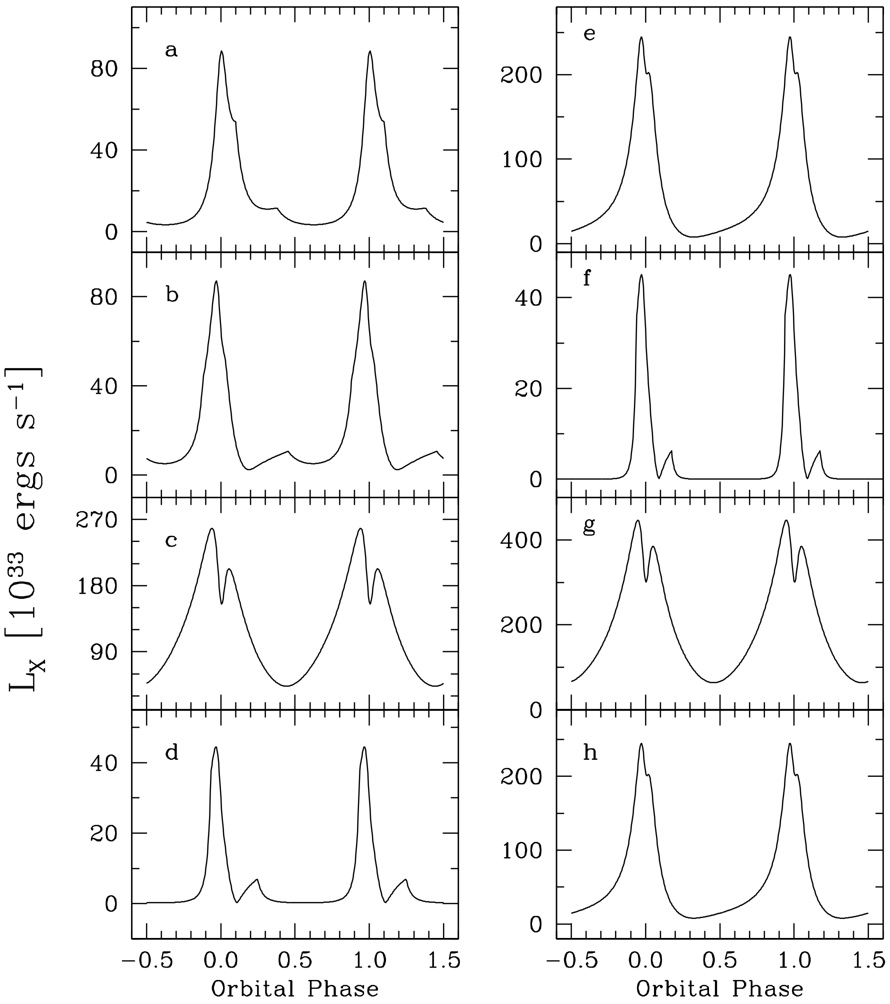

Figure 6.12: The calculated X-ray luminosity of LSI+61303 in terms of the ejector-propeller model.

luminosity of the ejector is expected about $1-5\times10^{35}$ erg s^{-1}, so as reasonable value can be adopted $L_X(E) = 2.10^{33} - 2.10^{34}$ erg s^{-1}.

The other possibility to estimate the X-ray luminosity of the expanding plasmon is to consider Bremsstrahlung emission of the shocked gas. In this case Taylor et al. (1996) also obtained 2×10^{34} erg s^{-1}. The both estimates are in good agreement and are similar to the expected values of the magnetospheric accretion.

It deserves to be noted that in case of transition between accretor and propeller a considerable luminosity gap will exist, about 100 times difference in the X-ray luminosity, is expected and observed (Corbet 1996; Raguzova & Lipunov, 1998). But this is not the case at the transition between ejector and propeller, where the X-ray luminosities are of the same order. So, we will assume that $L_X(ejector) = L_X(propeller)$ not to complicate our qualitative results.

The X-ray luminosity calculated in this way is plotted in Fig.6.12. The orbital phase zero corresponds to the periastron, the adopted mass loss rate of the Be star is $M_{loss} = 10^{-9}\,M_\odot$ yr^{-1}. The calculated X-ray variability is very similar to the observed (Fig. 6.9). The X-ray maximum is at periastron and this means that the periastron passage corresponds to radio phase ~ 0.5 using the modern radio ephemeris.

6.4.5 Plasmon parameters and radio outbursts

The switch on of the ejector will create a cavern around the neutron star. This cavern will start to expand under the pressure of the relativistic wind of the ejector and can be identified with the expanding plasmon, which radio emission successfully fit the observed radio outbursts of LSI+61303 modeled by Paredes et al. (1991). The question here is: are the parameters expected at the propeller-ejector transition appropriate for the plasmon?

The most important parameters which appeared in the radio model of Paredes et al. (1991) are initial radius (R_0), expansion velocity ($V_{\rm exp}$), initial magnetic field, injection time interval, power law index of electrons, and the injection rate. In the terms of Ejector-propeller model we can put constrains on the allowed ranges for this parameters:

- 1. The time of plasmon appearance - the plasmon will appear after the periastron passage at low mass accretion rate (for more details see Zamanov, 1995 and references therein). So it means that the radio outbursts will peak always with some phase shift after the change of the regime from propeller to ejector.

- 2. The initial radius expected at the propeller-ejector transition will be of the order of light cylinder radius, and in any case less than the accretion radius, which means that acceptable values are of the order of $0.01 - 3.0\, R_\odot$

- 3. The expansion velocity of the cavern in terms of the propeller-ejector transition can be estimated as (Zamanov, 1995):

$$V_{\rm exp} = V_{\rm w} + \sqrt{L_m V_w / (c \dot{M}_{loss})} \tag{6.11}$$

where c is the speed of light, $\dot{M}_{loss}$ and V_w are the mass loss rate and the wind velocity of the Be star respectively, L_m is magneto-dipole luminosity of the young radio pulsar. Adopting $V_w = 100\,{\rm km\,s^{-1}}$ for the disk wind and $V_w = 1000\,{\rm km\,s^{-1}}$ for the polar wind and $L_m = 1 - 5 \times 10^{35} {\rm erg\,s^{-1}}$ the cavern expansion will be with velocity $200 - 1300\,{\rm km\,s^{-1}}$. In the radio light curves we will adopt values $V_{\rm exp}$ =200, 400, 1200 $\rm km\,s^{-1}$.

- 4. Injection time interval - it is the time neutron star acts as ejector. The switch on of the ejector will be when the neutron star goes away from the B star and the switch off will be when it enters in the dense circumstellar disk approaching the periastron. From the mass accretion rate behavior (Fig. 6.10 right and Fig. 6.12) we can expect injection time interval $0.4 - 0.7 \times P_{orb}$ or in other words 10 − 20 days.

- 5. Injection rate - the total injection rate of the Crab into the nebula at a spin period of 0.033 s^{-1} is estimated to be about 10^{40}-10^{41} particles s^{-1} on base of the high-energy spectrum (De Jager & Harding, 1992). From one side the spin period of the neutron star in LSI+61303 required from the E-P model is longer than Crab. We expect $P_{spin} = 0.15 - 0.20\, s$ (see Zamanov 1995 for more details). It means $\sim 100 - 1000$ times lower rate of injected relativistic particles ($L_m \sim P_{spin}^{-4}$). From other side as a result of the magnetosphere accretion there are probably more particles for injection. We will adopt $5{\times}10^{-38}\, e^-\,{\rm s}^{-1}$

- 6. Magnetic field - the origin of magnetic field inside the plasmon will be something like to the magnetic field of the Crab nebula but some additional contribution from the B star is possible. The magnetic field referred in the "radio" figures (Fig. 6.13) are very high because they refer to the magnetic field at the initial plasmon radius. When the plasmon expands to sizes of 1 AU, as measured with VLBI, the magnetic field is then close to 1 Gauss in agreement with VLBI estimates based on equipartition arguments. (Note: Changes in the radius and the magnetic field do no alter the light curves provided that $B\,R^2$ is constant - magnetic flux conservation).

- 7. Electron power law index is adopted $p = 1.6$, in order to be consistent with observed non-thermal (i.e. negative) spectral indices when the plasmon becomes optically thin. According to synchrotron theory, the optically thin spectral index is $\alpha = (1 - p)/2$. In our case, we have then $\alpha = -0.3$ in agreement with typical observations.

- 8. Energy range of relativistic electrons:
$m_e c^2 < E < 10^{-2}\, erg$

- 9. Distance from the Earth: 2 kpc

Using the above parameters appropriate for the ejector-propeller model and the plasmon prescription we generated radio light curves. They are shown in Fig.6.13. The radio behavior (amplitude and shape) is very similar to the observed in the radio monitoring of LSI+61303.

6.4.6 Discussion & Conlusions

Using the parameters appropriate to the ejector-propeller model we calculated the X-ray and radio variability of the Be/X-ray binary LSI+61303. The general shape of the radio behavior (amplitude and shape) is very similar to the observed in the radio monitoring of LSI+61303, as it was already shown in the "plasmon" calculations by Paredes et al.(1991). The radio outbursts peak can be achieved 2-8 days after the appearance of the plasmon (see Fig.6.13). The appearance of the plasmon can be expected when the neutron star emerges from the denser part of the disk, i.e. $2-5$ days after the periastron (orbital period is 26.5 days). In the calculated X-ray curves the X-ray maximum corresponds to the periastron. The switch on of the ejector will be $0.1 - 0.4\, P_{orb}$ later. It means that the radio peak will delay with 3-13 days after the X-ray maximum. This is the behavior observed in both cases of the simultaneous radio and X-ray observations (Fig.6.9). As can be seen in Fig.6.12, the total X-ray luminosity expected in Ejector-Propeller model is of the order $1 - 200 \times 10^{33}\,\mathrm{erg\,s^{-1}}$ This is in good agreement with the observed by ASCA (Paredes et al. 1997) variability $1 - 6 \times 10^{34}\,\mathrm{erg\,s^{-1}}$ in the 2-10 keV band.

High resolution radio maps Recent high resolution radio maps have evidenced a one sided radio jet at milliarcsecond scales (Massi et al. 2001). These authors interpret it as a microquasar bipolar ejection with significant Doppler boosting effect. The ejector-propeller model, explored in this paper, provides however an alternative interpretation. Considering that the plasmon will be formed in one side of the Be star (the apastron vicinity), a one sided radio jet is naturally expected.

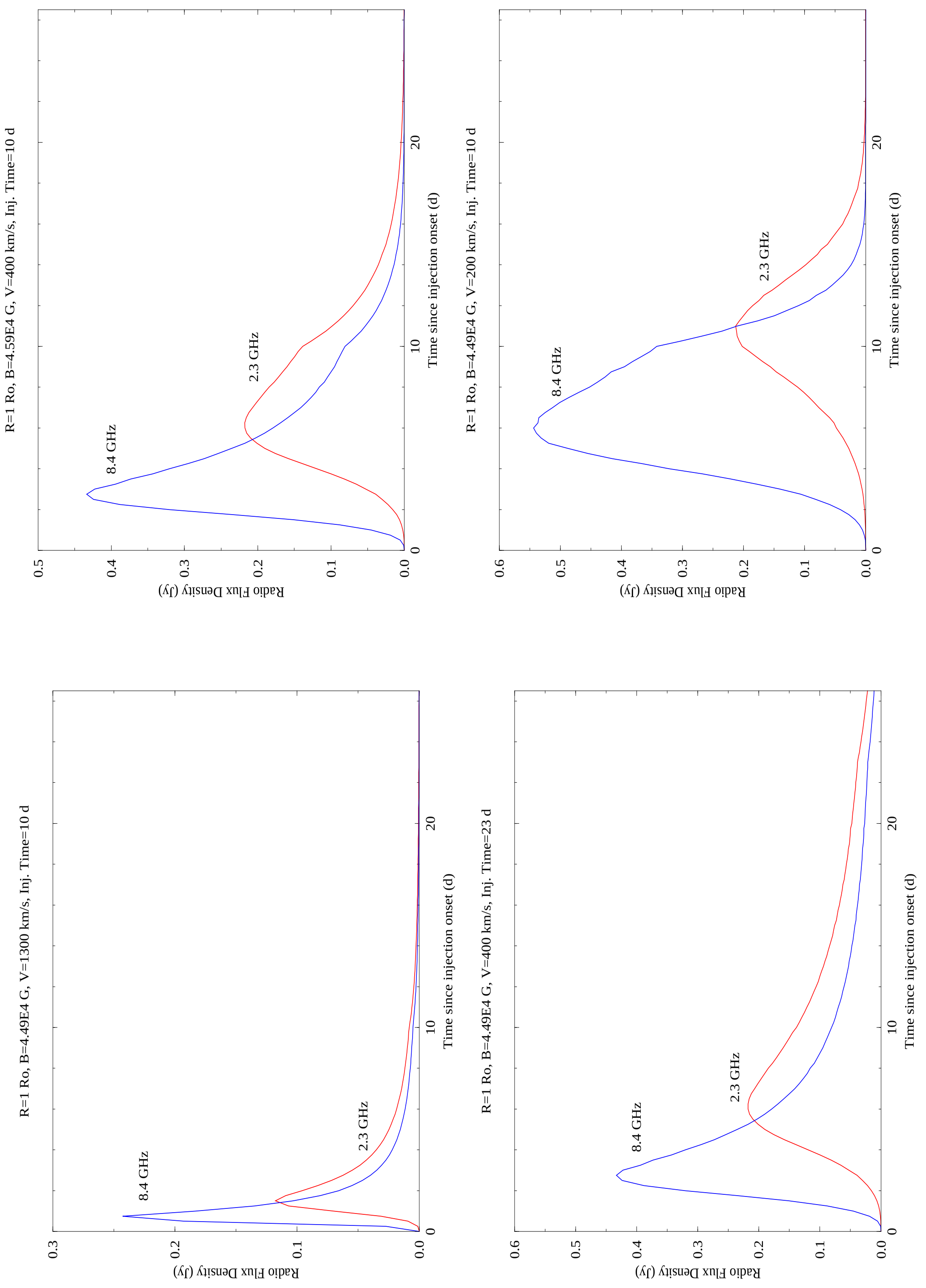

Figure 6.13: Radio Light curves generated using the expanding plasmon and setting parameters appropriate for the ejector-propeller model.

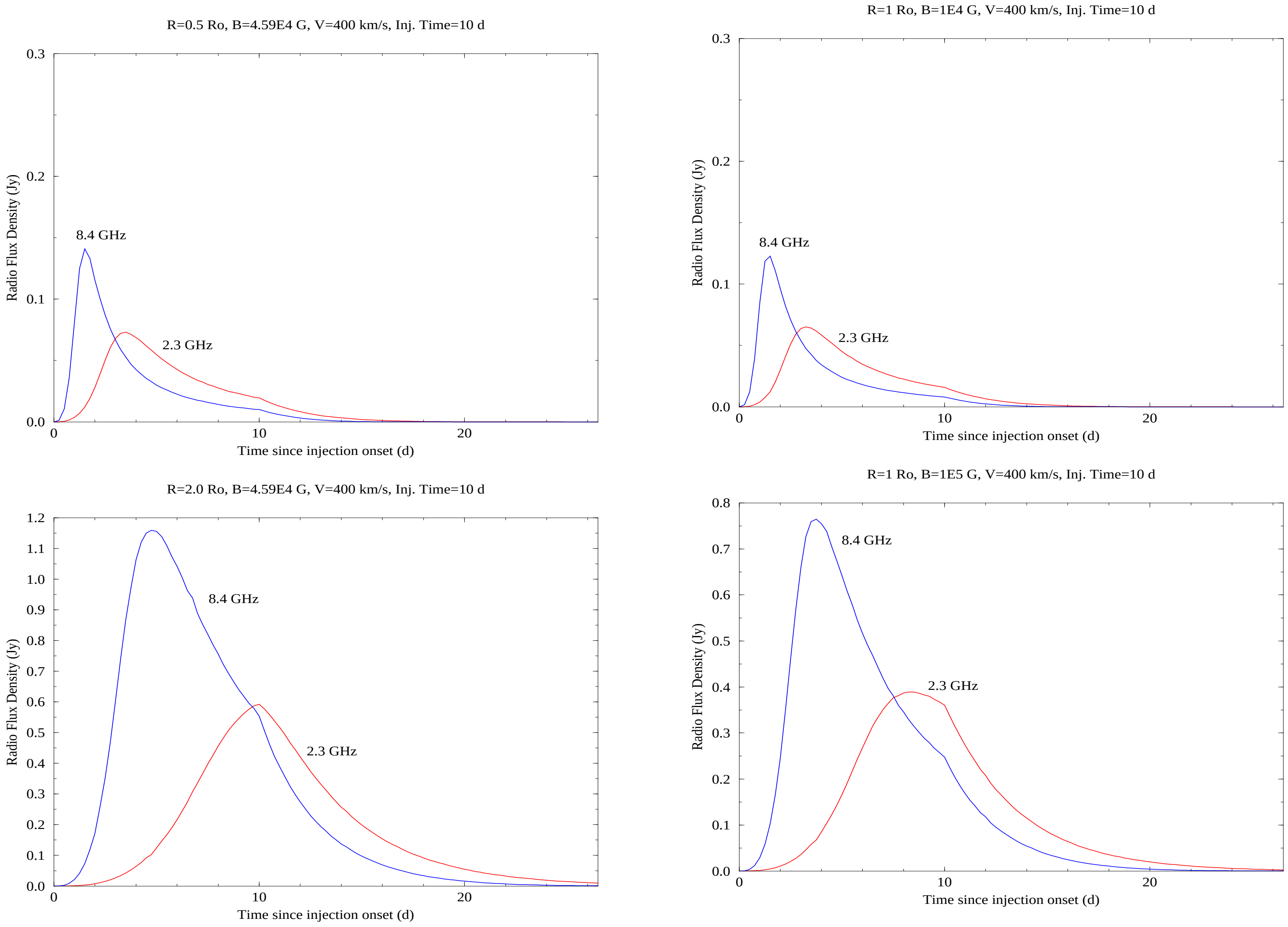

Figure 6.13: continued

Asymmetry of the cavern To model the radio light curves we assumed that the plasmon expansion is spherically symmetric. But in the real case this region will be not symmetric. Different forms of the cavern are possible - closed or open, for more details see Lipunov & Prokhorov (1984). In addition, the fact that the neutron star ejects relativistic particles at the apastron of an eccentric orbit will lead to a radio source which is elongated in the direction of apastron. In any case, the radio source formed around the ejecting neutron star will be elongated in the direction controversial to the direction to the B star.

Strong and weak radio outbursts It was discovered that radio outburst peak flux density varies over a time scale of 1600 days. On the same time scale the $H\alpha$ emission of the outflowing disk (Zamanov & Marti, 2000) varies as well, and may be even the X-ray maximum (Apparao 2001). Our preliminary tests evidenced that a slower expansion velocity and stronger magnetic field give higher radio peak flux densities and the outburst peaks later. Also a faster expansion velocity and lower magnetic field will result into lower peak flux densities and the earlier outburst peaks. These effects and their connection with the conditions in the Be disk need of careful modeling.

Multiple Outbursts A mechanism of multiple formation of caverns around an ejecting neutron star is proposed (Lipunov & Prokhorov, 1983). We can speculate that, in case of multiple peaks in the LSI+61303 radio outbursts, we may be observing such a multiple cavern formation. Another possibility is a density structure in the wind of the Be star, i.e. rings with higher density that can change the regime more than once during an orbital period.

Gamma rays During the Ejector stage the gamma ray emission is thought to originate in the shock front at the boundary of the pulsar and stellar winds (Kniffen et al. 1997). Gamma ray production is possible during the propeller action too. Possible mechanisms are double layer formation in the interblob plasma (Wynn, King & Horne, 1997) or high voltage at the boundaries of vortex structures (Wang and Robertson, 1985).

Other possibilities The fact that the radio outbursts are not exactly periodical point to they are a result of a process which has appropriate conditions to begin somewhere at radio phases 0.5-1.0, but when the process will switch on is a by-chance. We suppose that this process is the transition of the neutron star from propeller to ejector. Another alternative is the transition closed-open cavern around the ejecting neutron star (Zamanov 1995b, Harrison et al. 2000). In this case the expected magneto-dipole luminosity of the neutron star is about 6×10^{36} erg s^{-1}, i.e. 10 times more than the expected in the ejector-propeller model.

It can not be excluded that a magnetized black hole is acting in LSI+61303 (Punsly, 1999). If such a compact object does exist in LSI+61303, the microquasar scenario proposed by Massi et al. (2001) should be also considered seriously. Further observations are required in order to finally solve the true nature of this X-ray binary.

Conclusions:
We tested the ejector-propeller model for the radio-emitting Be/X-ray binary LSI+61303. The calculations show that the X-ray variability and radio outbursts can be the result of the transition from the propeller to the ejector accretion regimes every orbital period. The main results are:

- The parameters expected from the ejector-propeller model are appropriate for the radio plasmon and the calculated radio light curves are similar to the observed radio outbursts in LSI+61303.

- In terms of Ejector-Propeller model the X-ray maximum is a result of the propeller action during the periastron passage of the neutron star.

- The periastron is expected to correspond with radio phase $\sim$ 0.5 using the late radio ephemeris - i.e. the time of the X-ray maximum.

- The observed phase shift between the radio and the X-ray maxima is in agreement with the ejector-propeller model of LSI+61303. We expect that the X-ray and the radio maxima will always peak at different orbital phase.

- The total X-ray luminosity expected in terms of Ejector -Propeller model $1 - 200 \times 10^{33}\,\mathrm{erg\,s^{-1}}$ is in good agreement with the observed by ASCA (Paredes et al. 1997) variability $1 - 6 \times 10^{34}\,\mathrm{erg\,s^{-1}}$ in the 2-10 keV band.

There are a few systems where it is expected that the neutron star survives transitions from propeller to accretor and backward - A 0538-66, X 0331+53 (Raguzova & Lipunov, 1998). In our opinion, LSI+61303 is probably the first example where we observe the transition from ejector to propeller and backward to occur every orbital period.

During the lives of neutron stars in binary systems, it is believed that they evolve through different stages - ejector, propeller, accretor (Lipunov et al. 1994). Studies over systems such as LSI+61303, A 0538-66 and X 0331+53, which probably exhibit transitions between these different regimes, will give us the unique possibility to investigate these transitions over a time scale of months. This is an interval of time extremely short considering that the transitions, which are result of the neutron star evolution, occur on much longer time scales ($\sim$ 10 Myr).

New light over the evolution of the neutron stars in binary systems is expected from this kind of work.

6.5 References to Chapter 6

Apparao K.M.V., 2001, A&A 371, 672

Bignami G.F., Caraveo P.A., Lamb R.C., Markert T.H., Paul J.A.,1981, ApJ 247, L85

Brandt N., Podsiadlowski P., 1995, MNRAS 274, 461

Coe M.J., Everall C., Fabregat J., et al., 1993, A&AS 97, 245

Coe P.C., Roche P., Everall C., Fishman G., et al., 1994, A&A 289, 784

Corbet R.H.D., 1996, ApJ 457, L31

Corbet R.H.D., Charles P.A., van den Klis M., 1986, A&A 162, 117

Daugherty J.K. & Harding A.K., 1982, ApJ 252, 337

De Jager O.C., Harding A.K., 1992, ApJ 396, 161

Goldoni P., Mereghetti S., 1995, A&A 299, 751

Gregory P.C., Huang-Jian Xu, Bachhouse C.J., Reid A., 1989, ApJ 339, 1054

Gregory P.C., Taylor A.R., 1978, Nat 272, 704

Gregory P.C., Taylor A.R., Crampton D., et al., 1979, AJ 84, 1030

Gregory P.C., 1999, ApJ 520, 361

Gregory P.C., Peracaula M., Taylor A.R., 1999, ApJ 520, 376

Hanuschik R.W., 1988, A&A 190, 187

Hanuschik R.W., Kozok J.R., Kaiser D.,1988, A&A 189, 147

Harrison F.A., Ray P.S., Leahy D.A., Waltman E.B., Pooley G.G., 2000, ApJ 528, 454

Howarth I., Murray J., Mills D., et al., 1996, Starlink User Note 50, Rutherford Appleton Laboratory, U.K.

Hutchings J.B., Crampton D., 1981, PASP 93, 486

Ilyin I., 1997, Licentiate Dissertation, University of Oulu, Finland

Kniffen D., Alberts W.C.K, Bertsch D.L., et al., 1997, ApJ 486, 126

Lipunov V.M., Prokhorov M.E., 1984, Ap&SS 98, 221

Lipunov V.M., Nazin S.N., Osminkin E.Yu., Prokhorov M.E., 1994, A&A 282, 61

Lipunov V.M., Nazin S.N., A&A, 289, 822

Livio M., Soker N., Matsuda T., Anzer U., 1991, MNRAS 253, 633

Maraschi L. & Treves A., 1981, MNRAS 194, 1p

Martí J., 1993, PhD Thesis, University of Barcelona

Martí J., Paredes J.M. 1995, A&A, 298, 151

Massi M., Ribo M., Paredes J., Peracaula M., Estalella R., 2001, A&A, 376, 217

Mendelson H., Mazeh T., 1994, MNRAS 267, 1

Negueruela I., Reig, P., Coe M.J., Fabregat J., 1998, A&A 336, 251

Negueruela I., Roche P., Fabregat J., Coe M.J., 1999, MNRAS 307, 695

Okazaki A., 1997, A&A 318, 548

Okazaki A.T., 2001, PASJ 53, 119

Paredes J.M., 1987, PhD Thesis, University of Barcelona

Paredes J.M., Marziani P., Figueras F., Jordi C., Martí J., Rosselló G. et al. 1990, Boletín Astronómico del Observatorio de Madrid, v.XII, N:3, 191

Paredes J.M., Martí J., Estalella R., Sarrate J., 1991, A&A 248, 124

Paredes J.M., Marziani P., Martí J., Fabregat J., et al. 1994, A&A, 288, 519

Paredes J.M., Martí J., Peracaula M., Ribó M., 1997, A&A 320, L25

Punsly B., 1999, ApJ 519, 336

Raguzova N.V., Lipunov V.M., 1998, A&A 340, 85

Ray P.S., Foster R.S., Waltman E.B., Tavani M., Ghigo F.D., 1997, ApJ 491, 381

Reig P., Coe M.J., Stevens J.B., et al., 1997a, in 2nd INTEGRAL Workshop "The Transparent Universe", ESA SP-382, 175

Reig P., Fabregat J., Coe M.J., 1997b, A&A 322, 193

Roberts D.H., Lehar J., Dreher J.W., 1987, AJ 93, 968

Shortridge K., Meyerdicks H.,1996, Starlink User Note 50, Rutherford Appleton Laboratory, U.K.

Sletteback A., Collins II G.W., Truax R., 1992, ApJS, 81, 335

Stellingwerf R.F., 1978, ApJ 224, 953

Strickman M.S., Tavani M., Coe M.J., et al., 1998, ApJ 497, 419

Tarasov A.E., Roche P., 1995, MNRAS 276, L19

Tavani M., 1994, in *The Gamma-Ray Sky with GRO and SIGMA*, Dordrecht: Kluwer, 181

Tavani M., Hermsen W., van Dijk, R. Strickman M., Zhang S.N., Foster R.S., Ray P.S., Mattox J., Ulmer M., Purcell W., Coe M., 1996, A&AS 120C, 243

Taylor A.R., Gregory P.C., 1984, ApJ 283, 273

Taylor A.R., Kenny H.T., Spencer R.E., Tzioumis A., 1992, ApJ 395, 268

Taylor A.R., Young G., Peracaula M., Kenny H.T., Gregory P.C., 1996, A&A 305, 817

Tomov N.A., Tomova M.T., Raikova D.V., 1998, A&AS 129, 479

Vakili F., Mourard D., Stee Ph., Bonneau D., et al. 1998, A&A, 335, 261

Vögel M., 1993, A&A 274, L21

Waters L.B.F.M., Taylor A.R., van den Heuvel E.P.J., Habets G.M.H.J., Persi P., 1988, A&A 198, 200

Wang Y.-M., Robertson J.A., 1985, A&A 151, 361

Wynn G.A., King A.R., Horne K., 1995, MNRAS 286, 436

Zamanov R.K., 1995a, MNRAS 272, 308

Zamanov R.K., 1995b, Comp.Rend.Acad.bulg.Sci. 48, N: 5, 5

Zamanov R.K., Zamanova V., 1996, In: Maslev K., Kurtev R. (eds.), "100 yr Astronomical Observatory of Sofia University", Naturela, Sofia, p.109

Zamanov R.K., Martí J., Paredes J.M., Fabregat J., Ribó M., Tarasov A.E., 1999, A&A 351, 543

Zamanov R.K., Martí J., 2000, In: Smith M., Henrichs H., Fabregat J. (eds.), IAU Coll. 175, The Be Phenomenon in Early-Type Stars, ASP Conf.Ser. 214, 731

Zamanov R.K., Reig P., Marti J., Coe M.J., Fabregat J., Tomov T., Valchev T., 2001, A&A 367, 884

Chapter 7

Circumstellar disks in Be/X-ray binaries

7.1 Dense circumstellar discs in LSI+61°235 and LS I+61°303

7.1.1 LS I+61°303

It is well known that the Hα peak separation and the equivalent width correlate for the Be stars. Hanuschik et al. (1988) have derived the law

$$\log\left[\frac{\Delta V}{2\, v\, \sin i}\right] = -a\, \log\left[\frac{EW(\mathrm{H}\alpha)}{\text{Å}}\right] + b, \tag{7.1}$$

where ΔV is the peak separation, $v \sin i$ is the projected rotational velocity and $EW(\mathrm{H}\alpha)$ is expressed in Å. For stars with $EW(\mathrm{H}\alpha) > 3$ Å, the average values are $a \simeq 0.4$ and $b \simeq -0.1$. In the limit case of the most dense envelopes $b = +0.2$. Since for rotationally dominated profiles $\Delta V/(2\, v\, \sin i)$ can be regarded as a measure of the outer radius inverse of the Hα emitting disk (Hanuschik 1988), the law in Eq. 7.1 simply expresses that the outer radius grows as the $EW(\mathrm{H}\alpha)$ becomes larger.

The same quantities for LS I+61°303 are plotted in Fig. 7.1 adopting $v\, \sin i = 360$ km s^{-1} (Hutchings & Crampton 1981). The solid line represents the best linear fit over Rozhen data, from which we derive: $a = 0.38 \pm 0.04$ and $b = 0.07 \pm 0.04$. The dashed lines represent the average law ($a = 0.4$, $b = -0.1$) and the upper limit for the Be stars as obtained by Hanuschik et al. (1988). Using their formulation, our results imply that the circumstellar disk in LS I+61°303 is among the densest disks in the Be stars, i.e., roughly a factor of 2 denser than the average.

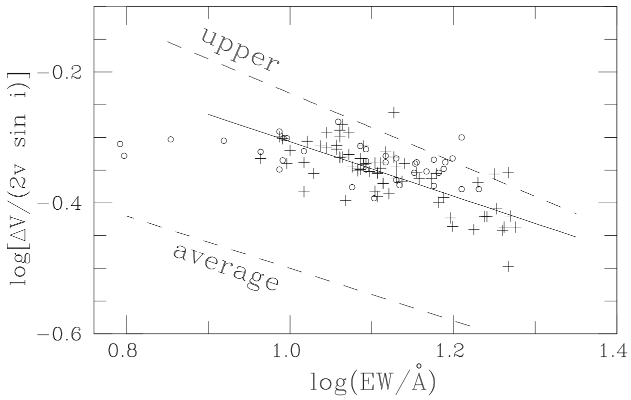

Figure 7.1: Plot of $\log\left(\Delta V/(2v\ \sin i)\right)$ versus $EW(\mathrm{H}\alpha)$ of LS I+61°303. The crosses represent the Rozhen data, the circles the other. The solid line is the best linear fit over the Rozhen data. The dashed lines are the average behavior and the upper limit for the Be stars. It is visible that all data points are shifted towards denser Be disks

Dense circumstellar disks, optically thick at infrared wavelengths, have been recently identified in other Be/X-ray binaries V0332+53 (Negueruela et al. 1999) and 4U 0115+63 (Negueruela et al. 2001). These works suggest that the disks around Be stars in X-ray binaries are denser and smaller that those in isolated Be stars. The results of Reig et al. (1997b) point towards neutron star preventing the formation of an extended disk in systems with short orbital periods, presumably due to tidal truncation (Okazaki 1998).

7.1.2 LSI+61°235

The works by Dachs et al. (1986) and Hanuschik et al. (1988) have shown that the equivalent width of Hα line emission for Be stars increases with the effective disc radius. In Eq 7.1, a least square fit to the LS I +61°235 data gave $a = -0.23 \pm 0.10$, i.e. $j \approx 0.5$ and $b = +0.1 \pm 0.1$. These values are to be compared with the average values $a = -0.4$ and $b = -0.1$ found by Hanuschik et al. (1988) for a sample of 26 isolated Be stars. The higher value of b in LSI+61°235 implies a denser disc than those of isolated Be stars.

The main (and probably only) difference between a Be/X-ray binary and an early-type isolated Be star is the presence of a neutron star in the former. It then seems natural to attribute the dissimilarity in the properties of the circumstellar envelopes to the influence of such compact companion. The neutron star trims the disc to a certain radius and prevents its free growth, making it denser. Disc truncation has been suggested in other Be/X-ray binaries like V0332+53 (Negueruela et al. 1999). This idea would support the hypothesis that the neutron star plays a fundamental role in the evolution and properties of the equatorial disc in Be/X-ray binaries, as proposed by Reig et al. (1997b).

The fact that LS I+61°303 and LSI+61°235 have circumstellar disk denser than those of normal Be stars stimulated us to compare the circumstellar disks in Be/X-ray binaries and Be stars using Hα spectroscopic observations.

7.2 Comparison of the Hα circumstellar disks in Be/X-ray binaries and Be stars

We present a comparative study of the circumstellar disks in Be/X-ray binaries and isolated Be stars based upon the Hα emission line. From this comparison it follows that the overall structure of the disks in the Be/X-ray binaries is similar to the disks of other Be stars, i.e. they are axisymmetric and rotationally supported. The factors for the line broadening (rotation and temperature) in the disks of the Be stars and the Be/X-ray binaries seem to be identical.

However, we do detect some intriguing differences between the envelopes. On average, the circumstellar disks of the Be/X-ray binaries are twice as dense as the disks of the isolated Be stars. The different distribution of the Be/X-ray binaries and the Be stars seen in the full width half maximum versus peak separation diagram indicates that the disks in Be/X-ray binaries have on average a smaller size, probably truncated by the compact object.

Introduction: The Be stars are early type non-supergiant stars surrounded by a circumstellar envelope with disk-like geometry. The circumstellar disk is visible in the Balmer (and sometimes other) line emission and also gives rise to a strong infrared excess. The physical mechanism of the disk formation is not well understood, but it is generally believed that the fast rotation of the central star plays an important role. The Be phenomenon is present in both isolated B type stars and X-ray binaries with massive B type companions. The Be/X-ray binaries represent the major subclass of massive X-ray binaries, in which the X-ray emission is due to the interaction of the compact object (usually a neutron star) with the wind of the Be star.

In this paper, we explore the existence of significative differences between the Be disks in both kinds of systems. The black hole, or neutron star, companion in an X-ray binary may be affecting the Be disk structure. Is there any observational evidence? Can we see the signature of the compact companion in the Be emission line profiles? Traditionally, the answer to this question has been negative, and it was believed that the presence of the compact object would not affect the dynamics of the Be disk. However, recent results seem to contradict this idea. Reig, Fabregat & Coe (1997) found a relationship between the properties of the disk and the orbit of the neutron star. They reported that Be stars in X-ray binary systems have, on average, a lower Hα equivalent width (EW) when compared to a complete set – those contained in the Bright Star Catalogue (Hoffleit & Jascheck 1982) – of isolated Be stars. They also discovered a possible correlation between the maximum observed EW(Hα) and the orbital period of the system, which was explained by assuming that the compact object truncates the outer parts of the Be star's disk. The idea of disk truncation, together with disk warping has been used by Negueruela et al. (2000) to explain the X-ray outburst mechanism in the Be/X-ray system 4U 0115+63 (V635 Cas).

The solution to these questions is likely to be provided by a careful and exhaustive examination of high dispersion optical and infrared (IR) spectra at high signal-to-noise ratio (S/N). The following sections are devoted to a comparative study of the circumstellar disks in the "normal" Be stars and the Be/X-ray binaries based on the best available Hα emission line spectroscopy.

7.2.1 Spectroscopic Data

In our comparative study we used the Hα equivalent width, full width at half maximum (FWHM) and the distance between the peaks (ΔV). The data for the 'normal' Be stars were taken from the high resolution, high S/N observations of Andrillat (1983), Hanuschik (1986), Hanuschik, Kozok & Kaiser (1988), Dachs, Hummel & Hanuschik (1992), Slettebak, Collins & Truax (1992). The optical counterparts of the Be/X-ray binaries have spectral classes in the range O8-B2, and represent a significantly different distribution from that of isolated Be stars (Negueruela 1998). But as far as we know there is no difference between the disk structure of the Be stars with different spectral types, so we will use all the data from the papers referred to above.

The Hα parameters corresponding to the Be/X-ray binaries were taken from the Southampton/Valencia/SAAO data base of optical and IR observations (Reig et al. 1997). This data base covers more than 10 years of observations from a variety of telescopes in both the northern and southern hemispheres. Additional observations were made from the Bulgarian National Astronomical Observatory 'Rozhen' with the Coudé spectrograph of the 2.0m RCC telescope giving a dispersion of 0.2 Å pix^{-1}. The results of our measurements are summarized in Tables 7.1 and 7.2. Our intention was to measure the EW(Hα) as defined by Dachs et al. (1981). Because traces of residual wings due to photospheric absorption were not detected, the interpolated continuum was used as baseline during the measurements.

In the case of double peak profiles the parameter FWHM is measured only when the both peaks have an intensity above the half-maximum. This is because the parameter is used to investigate the broadening in the disk and it would give unusual values if measured using only one peak, i.e. it would be sensitive to the broadening process from half of the disk only. The last column in the Tables 7.1 and 7.2 represents the reciprocal dispersion of the spectra in Å per pixel.

Additionally to these observations we used the data for 4U 1145-619 from Cook & Warwick (1987), LS I+61^{0}303 by Zamanov et al. (1999), and LS I+61^{0}235 by Reig et al. (2000). The values used for the projected rotational velocity, $v\ \sin i$, are summarized in Table 7.3.

7.2.2 Comparison of the $H\alpha$ line parameters for Be and Be/X-ray stars

In this section we present the behaviour of the Hα parameters, one versus another, for isolated Be stars and Be/X-ray binaries.

In an attempt to provide a quantitative approach to our study, we have performed two dimensional Kolmogorov-Smirnov tests (Peacock 1983, Press et al. 1994) on every figure. This test gives us the probability that both samples are compatible with each other. Usually if the indicated probability is < 0.05 the two data sets are statistically different. The Be stars atlases contain a lot of stars, each one observed one or several times. However for Be/X-ray binaries, we have merely 10 objects observed a lot of times. Therefore in the KS-test we used only 2-4 points for every Be/X-ray binary, in order to have a similar sample from each group. Thus the effective number of the data points is $\gtrsim 20$, which should give sufficient accuracy for the test.

It deserves to be noted that in general the type of the profile (double or single peak) and the V/R ratio can influence the positions in the diagrams, e.g. Dachs et al. (1992) detected a relationship between the V/R ratio and the radial velocities of the peaks. Our attempts to use only single peak profiles or only almost symmetrical profiles (V/R $\sim 1.0\pm0.2$) do not give different pictures. So in the following we will use all data independently of the Hα profile type .

The Hα parameters versus $v\ \sin i$

Fig. 7.2*a* shows the behaviour of the Hα full width at half maximum (FWHM). It is well known that the width of the Hα emission line increases linearly with $v \sin i$ (Struve 1931, Andrillat & Fehrenbach 1982, Dachs et al., 1986).

The observed points for Be/X-ray binaries are well inside the scatter of other Be stars. The KS test gives a significant probability of 0.10-0.15, that the points are extracted from the same distribution.

Table 7.1: Hα line parameters from Southampton – Valencia data base

Date (yyyymmdd)	$-EW$(Hα) (Å)	ΔV (km s^{-1})	FWHM (km s^{-1})	Disp. Å pix^{-1}
		4U1145-619/V801 Cen		
19850101	18.2	205	363	0.8
19850102	17.7	-	368	0.8
19850103	17.6	-	292	0.8
19850105	16.3	205	-	0.8
19930302	38.0	-	379	0.5
19940307	45.0	98	420	0.5
19940702	25.0	-	457	0.5
19950819	27.0	216	370	0.5
19960302	16.0	174	297	0.3
19960404	14.0	227	288	0.5
		A0535+26/V725 Tau		
19880310	14.0	-	462	2.6
19901114	9.9	140	347	1.0
19901227	8.6	167	384	0.5
19910828	9.4	198	384	0.5
19920818	7.4	218	343	0.8
19931206	13.0	-	370	0.8
19940325	9.0	-	343	1.3
19940916	9.4	199	361	1.3
19941110	12.0	228	393	0.8
19950226	8.6	212	361	0.5
19950806	8.0	230	402	0.4
19951120	6.2	244	416	0.5
19960228	7.3	233	416	0.4
		V0332+53/BQ Cam		
19900128	4.5	-	224	0.3
19900902	5.0	-	293	1.0
19901114	5.7	-	297	1.0
19910127	6.5	-	251	1.0
19910828	4.6	143	274	0.5
19911214	4.8	153	297	0.5
19920818	3.1	-	265	0.8
19921113	3.8	-	274	0.8
19970814	4.2	-	280	0.4
19971114	3.9	155	270	0.4

Table 7.1: Continuation

Date (yyyymmdd)	$-EW(\mathrm{H}\alpha)$ (Å)	ΔV (km s^{-1})	FWHM (km s^{-1})	Disp. Å pix^{-1}
		4U0115+63/V635 Cas		
19900214	6.8	182	571	1.0
19901227	4.5	400	603	0.5
19910127	9.5	-	452	1.0
19910828	3.9	453	640	0.5
19911214	5.4	497	699	0.5
19920805	4.1	425	608	1.2
19930118	7.1	406	786	0.5
19931217	5.4	362	750	0.5
19950703	3.5	448	649	1.0
19960112	11.3	215	480	1.0
19960131	8.0	292	521	1.6
19960620	7.8	321	548	1.0
19960709	6.3	404	631	1.0
19970201	3.7	470	-	1.0
		A1118-617 / Hen3-640		
19930303	70.0	106	384	0.5
19930622	68.0	106	407	0.6
19940307	62.5	100	398	0.5
19940703	62.0	59	416	0.5
19950225	65.0	59	384	0.4
19960403	62.0	82	398	0.5
19970620	69.0	65	384	0.4
		RX J0812.4–3114 / LS 992		
19980203	17.0	143	457	0.4
19990109	20.5	458	457	0.4
		4U0728-25		
19901227	9.0	-	210	0.5
19910127	7.3	-	293	1.0
19921113	5.0	176	361	0.8
19930304	5.6	-	306	0.4
19930624	6.0	115	192	0.5
19931205	5.6	-	388	0.8

Table 7.2: Hα line parameters measured on Rozhen spectra

Date (yyyymmdd)	$-EW(\mathrm{H}\alpha)$ (Å)	ΔV (km s^{-1})	FWHM (km s^{-1})	Disp. Å pix^{-1}
		XPer / HD 24534		
19920903	1.9	382	526	0.1
19920905	2.2	386	513	0.1
19970817	10.5	97	211	0.2
19980209a	12.3	133	287	0.2
19980209b	12.2	134	284	0.2
19980219a	12.1	118	286	0.2
19980219b	11.7	127	286	0.2
19981102a	9.8	142	251	0.2
19981102b	9.9	145	250	0.2
19990309a	6.7	161	283	0.2
19990309b	6.3	164	285	0.2
19990919a	8.1	146	281	0.2
19990919b	7.7	148	282	0.2
		LS I+61°303/ V615 Cas		
19980930	13.3	293	607	0.2
19980930	13.4	298	604	0.2
19981001	11.9	314	600	0.2
19981001	11.0	298	617	0.2
19981004	12.3	346	554	0.2
19981004	12.6	345	569	0.2
19981009	10.2	330	615	0.2
19981209	9.3	304	583	0.2
19990105	9.3	339	590	0.2
19990106	10.0	337	585	0.2
19990306	10.0	337	629	0.2
19990326	9.8	327	605	0.2
19990917	10.7	368	624	0.2
19990917	10.6	353	628	0.2
19990919	9.0	347	602	0.2
19990925	9.6	340	545	0.2
19990926	10.4	327	527	0.2
19991025	12.0	319	535	0.2
19991126	10.7	325	626	0.2

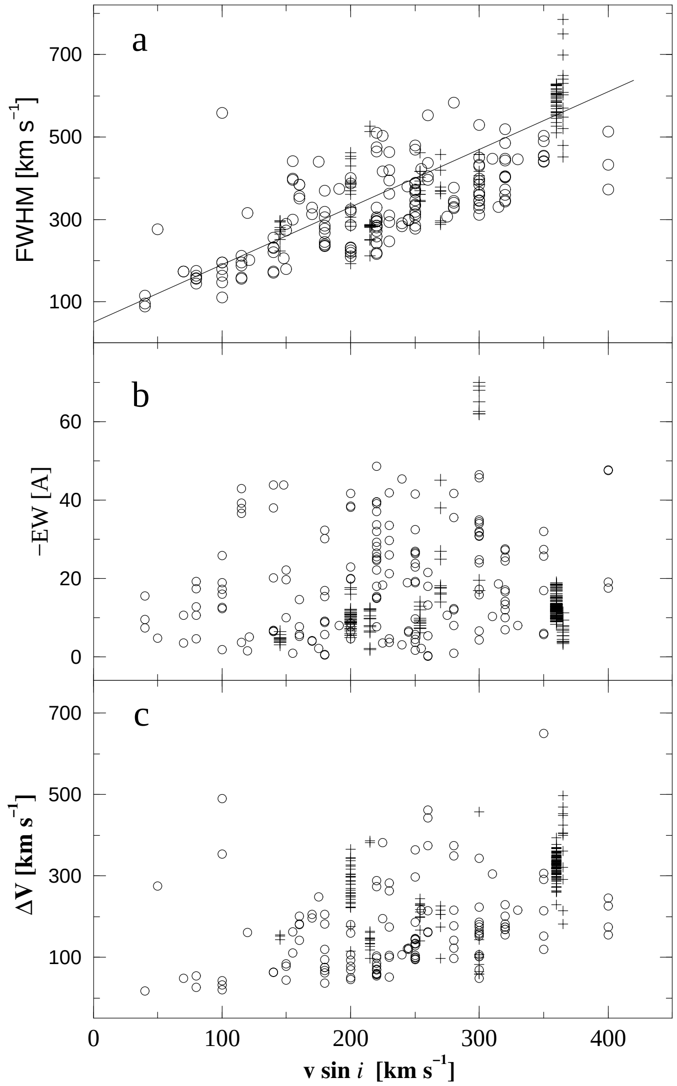

Figure 7.2: **a-c.** The Hα line parameters versus v sin i. The circles represent the Be stars, the crosses - the Be/X-ray binaries.

a FWHM versus v sin i. The solid line is $FWHM = 1.4\,v\ \sin\ i\ +\ 50\,\mathrm{km\ s^{-1}}$, which is the average behaviour of the Be stars, as defined by Hanuschik (1989).

b EW(Hα) versus v sin i.

c The distance between the peaks versus v sin i.

Table 7.3: Values of $v \sin i$ for the Be/X-ray binaries

Object	v sin i (km s^{-1})	Reference
X Per	215	Lyubimkov et al. (1997)
LS I+61°303	360	Hutchings & Crampton (1981a)
LS I+61°235	200	Reig et al. (1997)
4U 1145-619	270	van Paradijs (1995)
A 0535+26	254	Clark et al. (1998)
V 0332+53	145 *	Negueruela et al. (1999)
4U 0115+63	365	Hutchings & Crampton (1981b)
A 1118-617	300	Janot-Pacheco et al. (1981)
RX J0812-31	240	Reig et al. (2001)
4U 0728-25	200	Corbet & Mason (1984)

(*) average value on base of HeI/HeII absorption lines estimates only.

The observed correlation between stellar rotational velocities, v sin i, of the Be stars and FWHM of their emission-line profiles gives the strongest evidence for a rotationally supported disk-like circumstellar envelope and a coupling of photospheric and envelope rotation (e.g. Dachs et al. 1986; Hanuschik, 1989). The fact that the Be/X-ray binaries have a similar distribution in Fig. 7.2*a* points that, independently of the presence of compact companion, their envelopes are axisymmetric and rotationally supported, as could be expected.

In Fig. 7.2*b* and Fig. 7.2*c*, we plot the behaviour of the EW and the peak separation, ΔV, versus v sin i, respectively. In Fig. 7.2*b* the KS test gives a probability of 0.01-0.001, which suggests strongly that both samples are statistically different. Our numerical experiments suggest that this is mainly due to most Be/X-ray binaries not achieving EW(Hα) values above 25 Å. Some influence on the KS-test results has also the fact that low values of $v \sin i$ are missing among the observed Be/X-ray binaries, but this has minor contribution. Therefore, Fig. 7.2*b* supports the original result by Reig, Fabregat & Coe (1997) that the Be/X-ray binaries have, on average, a lower EW(Hα) when compared to a set of isolated Be stars.

In Fig. 7.2*c* the KS test gives a probability of 0.2-0.3, which indicates that the behaviour of the peak separation for both types is very similar. It is worth noting that (although it is not statistically significant), the peak separation of the Be/X-ray binaries does not achieve values smaller than the peak separation of the Be stars (ΔV is a measure of the disk size, see Eq.7.3).

The Hα width parameters versus the equivalent width

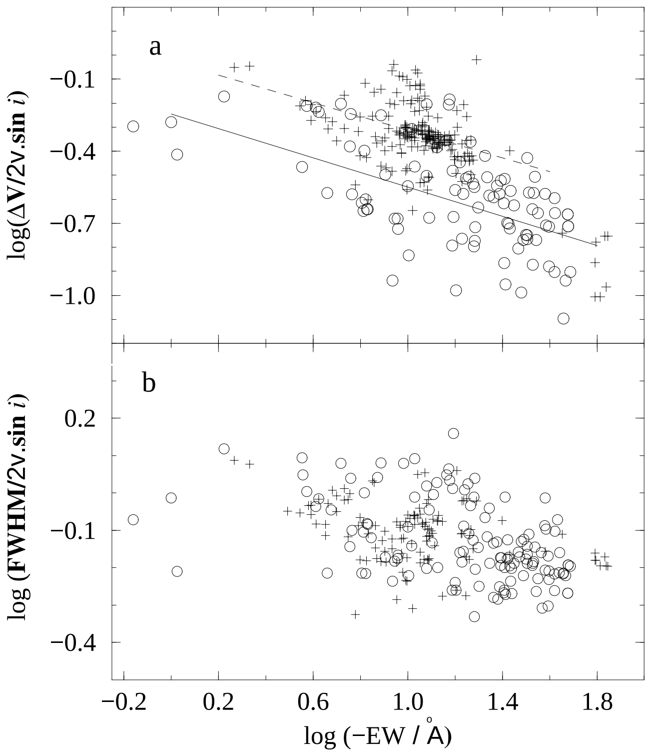

Figure 7.3: **a and b.** The Hα line parameters versus EW(Hα).
a Plot of $\log(\Delta V/(2\,v\sin i))$ versus EW(Hα). The lines represent the best linear fits: the solid line over the circles (Be stars), the dashed line over the crosses (Be/X-ray stars). The best fit line of the Be/X-ray binaries is shifted to denser circumstellar disks.
b $\log(FWHM/(2\,v\sin i))$ versus $\log EW(H\alpha)$. The Be/X-ray binaries and isolated Be stars mixed together.

In Fig.7.3 the Hα width parameters ΔV and FWHM, normalized to $v\sin i$, have been plotted as a function of the EW(Hα). In the top panel, it is clear that the Be/X-ray data points as well as their linear fit are considerably shifted relative to the behaviour of the Be stars. The KS test gives a probability of $\sim$0.001 if we use all data points, and probability $\sim$0.01 if we use only data with EW$\leq$20 Å. This fact can be interpreted as indicating the presence of denser disks and will be discussed in Sect. 7.2.3.

In the bottom panel, the KS test for EW$\leq$20 Å gives a probability of 0.20-0.40. It is also obvious that both samples occupy one and the same place at low EW. This result is not unexpected and implies that the processes relevant to the line broadening (Kepler rotation,

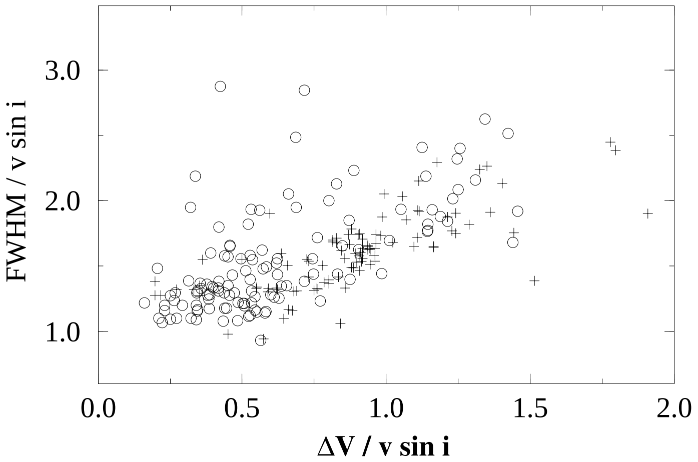

Figure 7.4: FWHM versus the peak separation, ΔV, normalized with $v \sin i$. The symbols are the same as in Fig. 7.2.

thermal broadening, non-coherent scattering) are identical in the disks of the Be and Be/X-ray stars, when the latter are non perturbed. There are several cases when one of the wings is strongly affected, and, as a result, it has an intensity below the half maximum. Probably this is an effect of global one-armed oscillations (see Negueruela et al. 1998, for a discussion of this effect). In such cases we did not measure the FWHM for the reasons mentioned in Sect. 7.2.1.

FWHM versus ΔV

In Fig.7.4 we plot the FWHM against the peak separation, both normalized to $v \sin i$. The KS test gives here a probability of about 0.001. This strongly indicates that the two samples are drawn from different distributions.

The FWHM of the Hα emission-line profiles are essentially determined by the effective rotational velocity of those regions of the envelope which are emitting an important fraction of the Hα radiation. In Fig.7.4 the crosses of the Be/X-ray binaries are shifted towards high ΔV. This implies that, at the same effective emitting size, their disks are smaller. Such a result, can be interpreted as a clear indication that in many cases the outer parts of the Be/X-ray disks are missing, probably truncated by the neutron star.

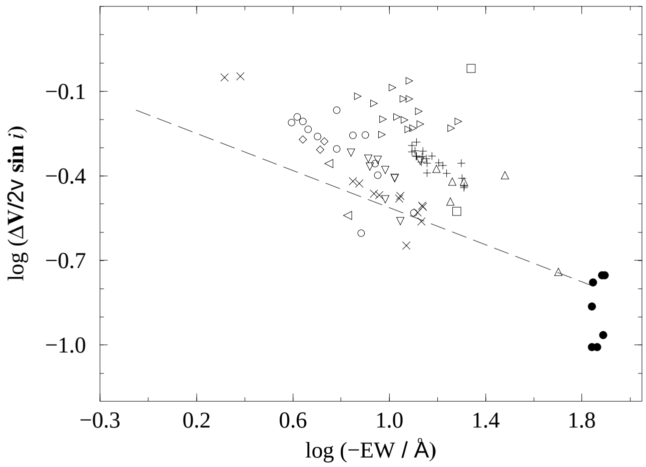

Figure 7.5: Plot of $\log(\Delta V/2v\,\sin i)$ versus $EW(\mathrm{H}\alpha)$ of Be/X-ray binaries. The dashed line represents the average behaviour of the Be stars (from Hanuschik, 1989). It is apparent that the data points for the Be/X-ray binaries are shifted up, towards denser Be disks.
Legend: pluses (+) - LS I+61°303, crosses (×) - X Per, diamonds - BQ Cam, triangles up - 4U 1145-619, triangles down - A 0535+26, triangles right - LS I+61°235, triangles left - 4U 0728-25, open circles - V635 Cas, filled circles - A 1118-617, squares - LS 992.

7.2.3 Dense circumstellar disks in the Be/X-ray binaries

It is known that the Hα peak separation and the equivalent width correlate for the Be stars (Hanuschik, Kozok & Kaiser, 1988). Hanuschik (1989) have derived the law

$$\log\left(\frac{\Delta V}{2\,v\,\sin i}\right) = -a\,\log\left(\frac{-EW(H\alpha)}{\mathring{A}}\right) + b, \tag{7.2}$$

where the average values are $a \simeq 0.32$ and $b \simeq -0.2$. It is worth noting that when using almost twice as many points we obtained practically the same values $a = 0.34 \pm 0.06$ and $b = -0.18 \pm 0.07$. The law in Eq. 7.2 expresses that the outer radius grows as the $EW(\mathrm{H}\alpha)$ becomes larger, because for rotationally dominated profiles the peak separation can be regarded as a measure of the outer radius of the Hα emitting disk (Huang, 1972):

$$\left(\frac{\Delta V}{2\,v\,\sin i}\right) = \left(\frac{R_{disk}}{R_*}\right)^{-j}, \tag{7.3}$$

with $j = 0.5$ for Keplerian rotation and $j = 1$ for conservation of angular momentum.

The same quantities for the Be/X-ray binaries are plotted in Fig. 7.5. The dashed line represent the average behaviour of Be stars as defined by Hanuschik (1989). Hanuschik, Kozok & Kaiser (1988) consider that the different electron density (N_e) is the factor responsible for the vertical scattering in this figure. They estimated that the limits for the Be stars correspond to

$$N_{e,max}/N_{e,min} \simeq 4.5. \tag{7.4}$$

From Fig. 7.5 it can be seen that almost all the data points for the Be/X-ray binaries are above the average line, i.e. they are shifted towards the denser disks. This indicates that the circumstellar disks in the Be/X-ray systems are about $\simeq 2$ times more dense than disks in isolated Be stars.

This result is very unlikely to be due to the lower resolution of the observations involving Be/X-ray binaries, because at least for three systems, X Per, LS I+61°303 and LS I+61°235, some observations had high spectral resolution (0.10 – 0.067 Å pix^{-1}) and these data do not show significant differences with respect to the lower resolution observations.

This behaviour was first discovered for LS I+61°303 (Zamanov et al. 1999) and for LS I+61°235 (Reig et al. 2000). Given the large amount of data collected for the systems LS I+61°303 and LS I+61°235 we randomly selected a subsample of their observations in order not to give too much weight to them in Fig.7.5.

The possibility that the disks in the Be/X-ray binaries are denser has already been suggested by Negueruela et al. (1998) in connection with the shorter periods of V/R variability.

7.2.4 Similarities and Differences

The Balmer emission lines that characterize the spectra of Be stars provide information about the physical conditions of the circumstellar equatorial disk. In this work we have used the Hα emission line spectral parameters to compare the properties of the disks in isolated Be stars and Be stars in Be/X-ray binaries. Our goal is to assess the possible effect of the compact object on the Be star's disk.

In our comparative study, we find similarities but also interesting differences in the physical properties of both type of systems.

Similarities: The similarities seem to be related to the overall structure of the disks, as could be expected. Firstly, the disks in Be/X-ray binaries, like those in isolated Be stars, are axisymmetric and rotationally supported. Secondly, isolated Be stars and Be stars in binaries populate the same place in the FWHM–EW diagram for low values of the EW. In other words, the line broadening processes (such as Keplerian rotation, thermal broadening, non-coherent scattering) are similar. Another similarity was presented by Telting (2000). He pointed out that the disk growth rates after a disk-loss episode for stars of similar spectral type are similar: 4×10^{-9} $M_{\odot}$ yr^{-1} for the Be/X-ray binary X Per (Telting et al. 1998) and 3.8×10^{-9} $M_{\odot}$ yr^{-1} for μ Cen (Hanuschik et al. 1993).

Differences: The differences begin to emerge when the disk develops. The results of Reig, Fabregat & Coe (1997) as well as the KS-test performed on Fig. 7.2*b* point to that the Be/X-ray binaries show smaller EW than isolated Be stars. Only the systems 4U 1145-619 and A 1118-617 (located at $v \sin i$=270km s^{-1}on Fig.7.2) and A1118-617 (at $v \sin i$=300 km s^{-1}) show EW comparable to those of isolated Be stars. The orbital period of 4U 1145-619 is 188 d and that of A 1118-617 is unknown but likely to be of the order of hundreds of days according to Corbet's diagram (Corbet 1986). With such wide orbits we would not expect the neutron star to have a strong impact on the disk evolution. In relation with this result there is the possibility that the peak separation ΔV in Be/X-ray systems tends to be larger than in Be stars (Fig 7.2*c*). Although this finding could be due, in general, to the lower resolution data for Be/X-ray binaries, if real, it can represent further evidence supporting the idea that the Be stars in X-ray binaries cannot develop extended disks because of its interaction with the neutron star (provided that ΔV can be considered as a measure of the disk radius).

The strongest evidence for a different behaviour of the circumstellar disks in Be and Be/X-ray systems is provided by Fig. 7.3*a* and Fig. 7.5. In the ΔV–EW diagram, Be/X-ray binaries are located in a higher region than isolated Be stars, indicating that they are, on average, about two times denser. Negueruela et al. (1998) noticed that the quasi periods of the V/R variability observed in Be/X-ray binaries are, on average, much shorter than those of isolated Be stars. They suppose that this difference may be caused by denser envelopes in the binary systems. Our results seem to confirm such idea. Given the tendency of Be/X-ray binaries to occupy a preferable position in this diagram it would be very interesting if we were able to find a correlation between the position of the star in this diagram and other parameters, such as the Balmer decrement, the period of V/R variability, the temperature, the rotational velocity, the chemical abundance, etc.

One possible explanation for the above mentioned differences is truncation of the Be star's disk by the compact companion. The continuous revolution of the neutron star around the Be star primary prevents the formation of an extended disk in Be/X-ray binaries. This is expected to occur for short orbital period systems. As a result of its gravitational field, the compact object not only will accrete a part of the disk material, but will distort the velocity of the particles at the outer disk. Probably a part of the material can be pushed in the inner part of the disk. This seems quite realistic especially if the neutron star acts as propeller or ejector, as it was supposed for LS I+61°303 (Zamanov, 1995).

For systems with longer orbital periods ($\geq$ 100 days) it seems unlikely that the neutron star has any influence on the Be star disk. In these systems the denser disks might be a selection effect due to the fact that the neutron star will act as X-ray pulsar only if the disk is dense. A neutron star orbiting at long distance around a Be star with low density disk will act as propeller (accretion onto the magnetosphere) or ejector (radio pulsar). If this is the case, a careful analysis of photospheric conditions of the long period Be/X-ray stars can provide us with valuable information on this issue.

The idea of disk truncation has been put on stronger theoretical grounds by Negueruela et al. (2000), who interpreted the X-ray and optical characteristics of the Be/X-ray system 4U 0115+63/V635 Cas as warping/tilting episodes of the disk. One of the best candidates to produce the high optically thick disks needed for radiation-driven warping is disk truncation.

Finally, while the compact companion does not seem to affect the formation and initial building-up stages of the circumstellar disk in Be/X-ray systems, it does seem to affect its subsequent characteristics and development.

7.2.5 Conclusions and open questions

From our comparative study between the Hα emission lines of Be/X-ray binaries and those of isolated Be stars we find that:

- The envelops in the Be/X-ray binaries are axisymmetric and rotationally supported as in isolated Be stars.

- The line broadening is similar in the isolated Be stars and the Be/X-ray binaries.

- The circumstellar disks in Be/X-ray binaries are, on average, two times denser than those in isolated Be stars.

- The relationships between the various Hα parameters (FWHM, ΔV, EW) seem to indicate the presence of smaller and denser disks in Be/X-ray binaries than in isolated Be stars, most likely truncated by the compact object.

Some of the open questions which should be addressed in the future are:

– What is the behaviour of the other emission lines in Be/X-ray binaries? The relative intensities of Balmer lines (Balmer decrement) can give more information about the temperature and electron density of the disk. The optically thin lines of FeII also can give us important information.

– What is the behaviour of the Be binary systems where the companion is not a neutron star?

– Do the physical properties of the optical companion (metallicity, instability in the photosphere induced by binary rotation, etc) contribute to producing denser disks?

7.3 References to Chapter 7

Andrillat Y., Fehrenbach Ch., 1982, A&AS 48, 93

Andrillat Y., 1983, A&AS 53, 319

Bjorkman J.E., Cassineli J.P., 1993, ApJ 409, 429

Clark J.S., Tarasov A.E., Steele I.A., Coe M.J., Roche P., Shrader C., Buckley D.A.H., Larionov V., Larionova L., Lyuty V.M., Zaitseva G.V., Grunsfeld J., Fabregat J., Parise R., 1998, MNRAS 294, 165

Cook M.C., Warwick R.S., 1987, MNRAS 227, 661

Corbet R.H.D., 1986, MNRAS 220, 1047

Corbet R.H.D., Mason K.O., 1984, A&A 131, 385

Dachs J., Eichendorf W., Schleicher H. et al., 1981, A&AS 43, 427

Dachs J., Hanuschik R., Kaiser D., et al., 1986, A&AS 63, 87

Dachs J., Hummel W., Hanuschik R.W., 1992, A&AS 95, 437

Hanuschik R.W., 1986, A&A 166, 185

Hanuschik R.W., 1989, Ap&SS 161, 63

Hanuschik R.W., Kozok J.R, Kaiser D., 1988, A&A 189, 147

Hanuschik R.W., Dachs J., Baudzus M., Thimm G., 1993, A&A 274, 356

Hoffleit D., Jascheck C., 1982, The Bright Star Catalogue, 4th Edition, Yale University

Huang S.-S., 1972, ApJ 171, 549

Hutchings J.B., Crampton D.,1981a, PASP 93, 486

Hutchings J.B., Crampton D.,1981b, ApJ 247, 222

Janot-Pacheco E., Ilovaisky S.A., Chevalier C., 1981, A&A 99, 274

Lyubimkov L.S., Rostopchin S.I., Roche P., Tarasov A.E., 1997, MNRAS 286, 549

Negueruela I., 1998, A&A 338, 505

Negueruela I., Reig P., Coe M.J., Fabregat J., 1998, A&A 336, 251

Negueruela I., Roche P., Fabregat J., Coe M.J., 1999, MNRAS 307, 695

Negueruela, I., Okazaki, A. T., Fabregat, J., Coe, M. J., Munari, U., Tomov, T., 2001, A&A,

369, 117

Okazaki, A. T., Fabregat, J., Coe, M. J., Munari, U., & Tomov, T. 2001, A&A, 369, 117

Peacock J.A., 1983, MNRAS 202, 615

Press W., Teukolsky S.A. Veterling W.T., Flannery B.P., 1993, Numerical Recipes, Cambridge University Press

Reig P., Fabregat J., Coe M.J., 1997, A&A, 322, 193

Reig, P., Coe, M. J., Stevens, J. B., et al., 1997, in "The Transparent Universe", Proceedings of the 2nd INTEGRAL Workshop, ESA SP-382

Reig P., Negueruela I., Coe M.J., Fabregat J., Tarasov A.E., Zamanov R.K., 2000, MNRAS, 317, 205

Reig P., Negueruela I., Buckley D.A.H., Coe, M. J., Fabregat, J.; Haigh, N. J., 2001, A&A, 2001, A&A, 367, 266

Roche P., Coe M.J., Fabregat J., McHardy I.M., Norton A.J., Percy J.R., Reglero V., Reynolds A., Unger S.J., 1993, A&A 270, 122

Slettebak A., Collins II G.W., Truax R., 1992, ApJS 81, 335

Stevens J.B., Reig P., Coe M.J., Buckley D.A.H., Fabregat J., Steele I.A., 1997, A&A 322, 183

Struve O., 1931, ApJ 73, 94

Telting J.H., Waters L.B.F.M., Roche P. et al., 1998, MNRAS 296, 785

Telting J.H., 2000, In: M.A.Smith H.F.Henrichs and J.Fabregat (eds.), Proc. IAU Coll. 175, The Be Phenomenon in Early Type Stars, ASP Conf. Series 214, 422

Unger S.J., Roche P., Negueruela I., Ringwald F.A., Lloyd C., Coe M.J., 1998, A&A 336, 960

Van Paradijs J., 1995, *in* X-Ray Binaries W. Lewin, J. van Paradijs, E.P.J. van den Heuvel (eds.), Cambridge University Press, p.536

Zamanov R., 1995, MNRAS 272, 308

Zamanov R., Martí J., Paredes J.M., Fabregat J., Ribó, Tarasov A.E., 1999, A&A 351, 543

Chapter 8

Active Galactic Nuclei

Introduction: Studies of emission line of the Active Galactic Nuclei (AGNs) provide the constraint on models for the nebular physics and kinematic models of the broad line emitting clouds. Ideally one would like to have high signal-to-noise ratio and good resolution. This would give possibility to measure the strongest high and low ionization lines as well as to characterize the continuum shape. The former measures have led to the Eigenvector 1 parameter space concept (Sulentic et al. 2000a,b) that is, in part, built upon foundations laid almost ten years ago (Boroson & Green 1992). The above goals are very observing time intensive but recent AGN surveys have provided an alternate method for examining quasar spectra from 1000 – 10000 Å. Average or composite spectra derived from large survey databases involving hundreds of AGN (Francis et al. 1991; Zheng et al. 1997; 1998; Brotherton et al. 2001; Vanden Berk et al. 2001) make it possible to generate the typical quasar spectrum from blueward of Lyα to Hα.

8.1 Blue "outliers" among AGNs

Kinematic Linkage Between the Broad and Narrow Line Emitting Gas in AGN – blue "outliers"

We investigate the radial velocity difference between the [O III]$\lambda\lambda$4959,5007 and Hβ lines for a sample of $\approx$ 200 low redshift AGN. We identify seven objects showing an [O III]λ5007 blueshift relative to Hβ with amplitude larger than 250 km s^{-1} (blue "outliers"). These line shifts are found in sources where the broad high ionization lines (e.g. C IVλ1549) also show a large systematic blueshift. Such blueshifts occur only in the population A region of the Eigenvector

1 parameter domain (that also contains NLSy1 sources). We suggest that [OIII]$\lambda\lambda$4959,5007 blueshifts are also associated with the high ionization outflow originating in these sources. This is a direct kinematic linkage between narrow and broad line emitting gas.

Forbidden [OIII]$\lambda\lambda$4959,5007 emission arises in the narrow line region (NLR) of Active Galactic Nuclei (AGNs). This emission has now been partly resolved in the nearest AGNs, where the geometry of the line emitting gas has been found to be far from spherically symmetric. This suggests that measures of integrated [OIII]$\lambda\lambda$4959,5007 emission may correlate with source orientation to the line of sight (Hes et al. 1993; Sulentic, Marziani & Dultzin-Hacyan 2000a, and references therein). Observations and theoretical models both (e.g., Steffen et al. 1997; Sulentic & Marziani 1999; Moiseev et al. 2001) suggest a complex interplay between (where applicable) shocks driven by radio ejection and the ionizing continuum from the nucleus.

At the same time it is generally believed that radial velocity measures of the narrow emission lines (e.g. narrow Hβ and [OIII]$\lambda\lambda$4959,5007) provide a reliable measure of the systemic, or rest-frame, velocity. [OIII]λ5007 is preferred because it is not superimposed on a much stronger broad line component. Limited HI, CO and absorption line measures of the host galaxy rest frame suggest that [OIII]$\lambda\lambda$4959,5007 usually gives consistent results within 200 km s^{-1} (de Robertis 1985; Whittle 1985; Wilson & Heckman 1985; Condon et al. 1985; Stirpe 1990; Alloin et al. 1992; Evans et al. 2001). Several observations, however, indicate that the Narrow Line Seyfert 1 (NLSy1) prototype I Zw 1 shows an [OIII]$\lambda\lambda$4959,5007 blueshift of $\Delta v_r = -500$ km s^{-1} relative to other rest frame measures (Boroson & Oke 1987). This corresponds to a 10 Å shift which is larger than any conceivable measurement or calibration errors; see Marziani et al. 1996).

We report here a study of the velocity shift of [OIII]λ5007 relative to Hβ. Our aim was to identify objects with large radial velocity disagreement between [OIII]λ5007 and Hβ and their relationship with the general population of AGNs.

Sample and Data Analysis

We measured the (narrow line) velocity difference between the peak of [OIII]λ5007 and of Hβ using our database of spectra for n= 216 AGN. The dataset includes CCD spectra obtained over the past ≈10 years for studies of the Hβ region in Seyfert 1 and low redshift (z $\lesssim$ 0.8) quasars. Spectra were obtained with the following telescopes and spectrographs: ESO 1.5m (B&Ch), San Pedro Martir 2.2m (B&Ch), Calar Alto 2.2m (B&Ch), KPNO 2.2m (Gold), and Asiago 1.82m (B&Ch). Results based on these spectra can be found in Marziani et al. (1996) and Sulentic et al. (2000a, 2002). Spectra were taken with very similar instrumental setups yielding resolution in the range 4-7 Å FWHM. The S/N of our spectra is typically in the range ≈ 20-40 (minimum 12). The high S/N and the moderate resolution make this sample appropriate for the study of line shifts because FWHM and shift measures are not significantly affected by undersampling. Our AGN sample has an average source absolute B magnitude $< M_B > \approx -23.7 \pm 2.0$ ($H_0 = 50$ km s^{-1}Mpc^{-1}, $q_0 = 0$).

We de-redshifted the spectra using an initial Hβ measurement for v$_r$ in all sources where an Hβ narrow component could be identified. Optical FeII$_{\rm opt}$ emission blends were then subtracted using the template method (Boroson & Green 1992). At this point, we measured v$_r$ for Hβ a second time, as well as v$_r$ for [OIII]λ5007. Hereafter we will consider only the difference in radial velocities Δv$_{\rm r}$ $= v_r$([OIII]λ5007)$-v_r$(Hβ) measured from the FeII$_{\rm opt}$ subtracted spectra. The measurement of Δv$_{\rm r}$ turned out to be possible for 187 sources. The 23 excluded sources include 7 with no detectable [OIII]$\lambda\lambda$4959,5007 emission and 16 with a very poorly defined Hβline peak.

8.1.1 [OIII]$\lambda\lambda$4959,5007 Line Shift Distribution

The distribution of Δv$_{\rm r}$ measures is shown in Fig. 8.1a. The values range from -950 to +280 km s^{-1} with an average $< \Delta v_r > = -30$ km s^{-1}. The sample standard deviation is $\pm$135 km s^{-1}. The median value is $\overline{\Delta v_r} = -\ 7$ km s^{-1}. 50% of the measurements fall in the interval from -49 to $+16$ km s^{-1}, so we adopt the first and third quartile as confidence limits, $\overline{\Delta v_r} = -7^{+23}_{-42}$ km s^{-1}. The central bins of our Δv$_{\rm r}$ distribution are dominated by measurement errors, with typical values estimated to be in the range 40–50 km s^{-1} at 1 σ confidence level. The continuous distribution of measures in the range -200 km s^{-1} $\lesssim \Delta$v$_{\rm r}$ $\lesssim$ +200 km s^{-1} suggests that the [OIII]λ5007 redshift measurements are consistent with Hβ to within the above range in more then 90% of the sources. The distribution of shifts is not symmetric around v$_r$= 0 km s^{-1} but is skewed toward the blue. Shifts in the range -200 $\lesssim \Delta$v$_{\rm r}$ $\lesssim$ -100 are three times more frequent than redshifts in the range 100 $\lesssim \Delta$v$_{\rm r}$ $\lesssim$ 200 km s^{-1}. The maximum shift to the red Δv$_{\rm r}$$\approx$ 280 km s^{-1} while shifts up to Δv$_{\rm r}$$\approx -1000$ km s^{-1} are observed on the blue side. The shift distribution reveals seven sources with [OIII]$\lambda\lambda$4959,5007 shift (Δv$_{\rm r}$ $\lesssim$ -250 km s^{-1}), which are listed in Table 8.1.

The relatively rare outliers, (referred to hereafter as " blue outliers"), are not randomly distributed in an Eigenvector 1 space representation of AGN diversity. Figure 8.1b plots [OIII]λ5007 shift amplitude Δv$_{\rm r}$ versus full-width half maximum of the Hβ broad component [FWHM(H$\beta_{\rm BC}$)], and Fig. 8.1c identifies the blue outlier sources in the E1 optical plane.

Fig. 8.1b and Fig. 8.1c suggest that large [OIII]λ5007 blueshifts ($\Delta v_r \lesssim$ -300 km s^{-1}) are confined to sources with FWHM(H$\beta_{\rm BC}$) $\lesssim$ 4000 km s^{-1}. The largest negative values (Δv$_{\rm r} \lesssim$ -600 km s^{-1}) is found at FWHM(H$\beta_{\rm BC}$) $\lesssim$ 2000 km s^{-1}. One radio-loud outlier PKS 0736 ($-$433 km s^{-1} blueshift) is found. It shows the largest FWHM(H$\beta_{\rm BC}$) for any of the seven identified extreme blue outliers. Figure 8.2 presents FeII subtracted spectra of the region of Hβ and [OIII]$\lambda\lambda$4959,5007 region for the 7 blue outlier sources. They also show preferentially blue Balmer line asymmetries as was previously noted for NLSy1 sources.

Are the Outliers Real ?

Even though the [OIII]$\lambda\lambda$4959,5007 emission in these sources is weak, it is difficult to doubt the detection of such large displacements in *both* [OIII]4959 and [OIII]5007 relative to the reference frame defined by Hβ. We are able to measure the radial velocity of both [OIII]λ5007 and [OIII]λ4959 including those with low equivalent width. The velocities are always consistent within 100 km s^{-1}and the equivalent width ratio of [OIII]λ5007 and [OIII]λ4959 is about 3:1 for the blue outliers, as expected (see Table 8.1). This and the fact that the shifts as well as the equivalent widths are different from sources to source, indicates that the [OIII]$\lambda\lambda$4959,5007 lines, although weak, are not strongly affected by the FeII$_{\rm opt}$ subtraction. We further cheched with subtraction of a theoretical template in the region 4800 - 5100 Å (Sigut & Pradhan, 2003), and the results are very similar.

One of the seven blue outliers (I Zw1) has reliable independent host galaxy redshift determinations based on HI 21 cm and molecular CO observations (see e.g., Schöniger & Sofue 1994). This is likely to be an accurate and reliable rest frame determination for at least three reasons: 1) the HI and CO lines profiles match very closely in shape, width and centroid velocity, 2) the profiles are symmetric and 3) the profiles are steep sided double horns. The centroid measures are consistent with the velocity of the peak of the Hβ emission line profile and not with [OIII].

Sources with FWHM(H$\beta_{\rm BC}$) $\lesssim$ 4000 km s^{-1} show a sharply peaked, Lorentzian Hβ profile. In such cases the narrow line component is uncertain because no profile inflection is seen. Even if the Hβ profile is completely ascribed to the broad component, it seems that the Hβ peak is nonetheless a good estimator of the quasar systemic velocity (this result is expected if the line comes from an extended accretion disk). We might expect to detect a *blueshifted* H$\beta_{\rm NC}$ analog to the [OIII] lines, but given the low equivalent width W([OIII]λ5007) we normally expect W([OIII]λ5007)/W(H$\beta_{\rm NC}$) $\sim$ 10), such a blueshifted component will be lost in the noise.

We also attempted to identify red outliers (there are seven objects with Δv$_{\rm r} \gtrsim$ 150 km s^{-1}which form an extended red tail in the shift distribution). In all cases, we find that the top of Hβ is complex or even multi-peaked. This means that the use of Hβ as a reference is sometimes ambiguous. Independent rest frame measures for two of these sources are consistent with an [OIII] derived radial velocity. We therefore interpret Figure 8.1a as consistent with three populations: 1) A scatter population associated in part with measurement errors; 2) a real, but relatively rare population of sources where [OIII]λ5007 shows an intrinsic large blue shift relative to the local rest frame (the blue outliers); 3) an intermediate population, in the range -250 km s^{-1} $\lesssim$ $\Delta v_r \lesssim$ -100 km s^{-1}), probably containing both sources with intrinsic blue shifts and sources with larger Hβ v_r uncertainty.

The preferred location of the blue outliers in E1 motivated us to search for corroboration among samples of phenomenologically similar (see next section) sources. Grupe, Thomas & Leighly (2001) identify a blueshift of 570 km s^{-1} in RXJ2217-59. Our quick look of other (FeII corrected) spectra (Grupe et al. 1999) revealed at least three other sources with obvious blueshifts in the range -300 to -500 km s^{-1} (RXJ1036-35, RXJ 2340-53 and MS2340-15).

Blue outliers and Eigenvector 1

Further insight and confidence about the reality of blue outliers can be gained from considering the distribution in the Eigenvector 1 diagrams (Sulentic et al. 2000b). The principal physical driver of E1 is assumed to be the luminosity-to-mass ratio ($\propto$ accretion rate) convolved with source orientation (Marziani et al. 2001) and/or the black hole mass (Boroson 2002; Zamanov & Marziani 2002). The distribution of blue outliers in the E1 optical plane Fig. 8.1c) is obviously different from that of the general AGN population. The blue outliers occupy the lower right part of the diagram and are exclusively population A/NLSy1 (FWHM(H$\beta_{\rm BC}$) $\lesssim$ 4000 km s^{-1}) sources. A 2D Kolmogorov-Smirnov (see e.g. Fasano & Franceschini, 1987) suggests that the parameter space occupation of the *blue* outliers is significantly different than the majority of AGN at a confidence level of 0.990$-$0.999. The preferred location of the blue outliers in E1 motivated us to search for other [OIII] blueshifts among samples of phenomenologically similar sources. Grupe, Thomas & Leighly (2001) identify a blueshift of 570 km s^{-1} in RXJ2217-59. Our quick look of other (FeII corrected) spectra (Grupe et al. 1999) revealed at least three other sources with obvious blueshifts in the range -300 to -500 km s^{-1} (RXJ1036-35, RXJ 2340-53 and MS2340-15).

Figure 3 in Sulentic et al (2000a) involving CIVλ1549 centroid shift vs. FWHM Hβ shows a striking similarity to Figure 8.1b of this paper. There is a HIL blueshift in the same AGN (population A) where we find all of the blue outliers. The simplest interpretation is that we are seeing a kinematic linkage between BLR and NLR HIL. A source by source comparison reveals

5 of 7 blue outliers with HST FOS archival spectra of the C IVλ1549 line. The blue outliers show CIV blueshifts (at FWHM(C IVλ1549)) between V= -503 and -1936 km s^{-1}. This motivates us to look at all sources in our full sample with CIV shift (>600 km/s) and W[OIII] (<15Å), properties similar to the blue outliers. We find 12 additional sources where: 1) no narrow Hβ peak and/or [OIII] line is observed (sometimes simply due to noisier than average spectra), 2) smaller, likely significant,[OIII] blueshifts are observed (e.g. -200 km/s for PG1444+407) and 3) a peak+blue wing structure is observed. In the numerous latter cases we see a narrow unshifted [OIII] line with a strong blue wing. In the absence of the peak we would measure a blueshift in the blue outlier velocity range. This motivates us to propose that the blue outliers represent sources where the classical extended NLR is absent or suppressed. The peak+ blue wing cases represent sources where both the (usually strong) classical and the (usually weak) blue shifted NLR components are present. The concept of two distinct NLR components is reenforced by sources like NGC7213 (Busko & Steiner 1988) and RXJ0148-27 (Grupe et al. 1999) where the unshifted and the blueshifted [OIII] components are actually resolved.

8.1.2 The Extreme of an Extreme: Large Shifts Governed by Orientation?

An obvious question involves whether or not the [O III]λ5007 blue outliers are peculiar AGN – a new, previously unknown AGN class. They do not appear to be part of a continuous distribution of [O III]λ5007 velocity shifts. However, even if the distribution of [O III]λ5007 outliers is not consistent with the other AGN in the E1 parameter plane, blue outliers lie near an extremum in the AGN occupied domain rather than outside of it. If we consider our tentative grid of expected L/M and i values in the E1 plane (Marziani et al. 2001), we see that the blue outliers may be the product of special circumstances: 1) a large L/M ratio, and 2) a small inclination (i$\rightarrow$0°). Of course these two circumstances do not explain the absence of the classical NLR. One possibility is 3) that these sources are young quasars (see below). It has been suggested that radio-quiet NLSy1 are the equivalent of BL Lacs. We infer that our blue outliers (the ones observed almost face-on, with largest C IVλ1549 and [O III]λ5007 blueshifts) may be the radio-quiet analogous of BL Lac. We note that the single RL blue outlier identified PKS0736+01 involves an optically violently variable (OVV) quasar.

We constructed a purely kinematical model in which [O III]$\lambda\lambda$4959,5007 and C IVλ1549 are both assumed to arise in a radial flow constrained in a cone of half-opening angle $\Theta_0 \approx 85°$ (e.g. a high ionization, optically thin wind) where the receding part of the flow is obscured by an optically thick accretion disk (i.e., we are able to see the approaching part of the flow and the near side of the disk which is assumed to emit Hβ). We assumed that radial motions in the gas were a fixed fraction (1.5) of the local virial velocity. We integrated over a region 100 $R_g \leq r \leq 10^5 R_g$ for CIVλ1549 and over a region 300 $R_g \leq r \leq 10^5 R_g$ for [OIII]λ5007, with emissivity power law-indices q = -2 (CIVλ1549) and q = -1 ([OIII]λ5007). Fig. 8.3 shows the resulting model profiles for a viewing angle i$\approx$ 15°. The width and shift of both lines are accounted for. We suggest, without considering this particular model as a physical one, that emission from outflowing gas, possibly associated to a disk wind, can explain the observed profiles. The occurrence of large [OIII]λ5007 shifts seems to be associated with low W([OIII]λ5007). Our model integration also consistently suggests *a very compact* NLR (r$\sim$ 1 pc for a black hole mass 10^8 solar masses). In this case, the receding part of the outflow may be more easily hidden by an optically thick disk extending to $\sim$ 1 pc (this is a requirement also to avoid double peaked profiles). The filling factor needed to explain the [OIII]λ5007 luminosity of I Zw 1 and PG 1543+489 can be reasonably small, $\sim 10^{-3}$. It is intriguing that a compact NLR complements several lines of evidence suggesting that NLSy1s are young AGN. Large W([OIII]λ5007) would imply a larger emitting volume and hence may be associated with lower [OIII]λ5007 shifts. The frequent observations of blueward asymmetry close to the [OIII]$\lambda\lambda$4959,5007 line profile base indicates that the same outflow may also be occurring in the innermost NLR of AGN with larger W([OIII]λ5007).

It is also interesting to note that Broad Absorption Line QSOs (BAL QSOs) are found more frequently in samples with low W([OIII]$\lambda\lambda$4959,5007) (Boroson & Meyers 1992; Turnshek et al. 1997). We do not find any BAL QSO among the outliers. In addition, the known low-z BAL QSO in our sample (PG 1004+13, PG 2112+059) with measurable [OIII]λ5007 (2 out of 5) show shifts $\Delta v_r \sim 0$ km s^{-1}. This is also consistent with orientation playing a role and with blue outliers being oriented predominantly "face-on." On the contrary, the CIVλ1549 absorption/emission profiles of BAL QSOs suggest that they may be observed far from pole-on.

Conclusion and References

We find that the Hβ and [OIII]λ5007 lines provide measures of the radial velocity of AGN usually consistent within $\pm$200 km s^{-1}. We identified infrequent ($\approx$ 5% in a sample of 200 sources) AGN showing $\Delta v_r \lesssim$ -250 km s^{-1}. They belong to the extreme population A sources that also show a large broad line CIVλ1549 blueshift. This kinematic coupling of the NLR and BLR HIL emission most likely involves a wind or outflow. Our analysis suggests that blue outliers are not peculiar objects, but rather AGN viewed of extreme L/M with a compact NLR.

Table 8.1: Objects with anomalous difference of the radial velocities between the [OIII]λ5007 and H_β ("blue outliers").

Name	z(Hβ)	Δv_r [km s^{-1}]	W[OIII] λ4959 [Å]	W[OIII] λ5007 [Å]	R_{FeII}	FWHM(Hβ_{BC}) [km s^{-1}]	Δ v$_r$(CIVλ1549$_{BC}$) [km s^{-1}]
I Zw 1	0.0606	-640±30	4.3	15.3	1.30	1600	-820
PKS 0736+01	0.1909	-430±60	0.6	2.6	0.70	3460	...[a]
PG 0804+761	0.1014	-305±30	3.3	10.1	0.42	2960	...[a]
Ton 28	0.3297	-680±50	1.6	3.4	0.71	1860	-1120
PG 1402+261	0.1651	-300±50	1.4	2.6	0.73	2280	-650
PG 1415+452	0.1151	-600±50	1.1	2.9	0.66	2810	-950
PG 1543+489	0.4009	-950±50	2.3	6.5	0.64	1600	-2630

[a] HST/FOS observations not available.

The typical errors are ±30% in W[λ4959], ±10% in W[λ5007], ±0.15 in R_{FeII}, ±150 km s^{-1} in FWHM(Hβ), and ±200 km s^{-1} in Δ v$_r$(CIVλ1549$_{BC}$).

A predominance of blueshifts in the sample indicates that [OIII]λ5007 peak velocity is affected by outflow motions occurring in the innermost NLR.

8.2 Influence of Black Hole Mass and Eddington Ratio

Abstract: We compute the virial mass of the central black hole (M) and the luminosity-to-mass (L/M) ratio of $\approx$ 300 low-z quasars and luminous Seyfert 1 nuclei. We analyze: (1) whether radio-quiet and radio-loud objects show systematic differences in terms of M and L/M; (2) the influence of M and L/M on the shape of the Hβ broad component line profile; (3) the significance of the so-called "blue outliers" i.e., sources showing a significant blueshift of the [OIII]$\lambda\lambda$4959,5007 lines with respect to the narrow component of Hβ which is used as an estimator of the quasar reference frame. We show that M and L/M distributions for RQ and RL sources are likely different for samples matched in luminosity and redshift, in the sense that radio-quiet sources have systematically smaller masses and larger L/M. However, the L/M ratio distributions become indistinguishable if 8.5< logM< 9.5. Line profile comparisons for median spectra computed over narrow ranges of M and L/M indicate that a Lorentz function provides a better fit for higher L/M sources and a double Gaussian for lower L/M values. A second (redshifted) Gaussian component at low L/M appears as a red asymmetry frequently observed in radio-loud and radio-quiet sources with broader (FWHM $\gtrsim$4000 km s^{-1}) Hβ broad

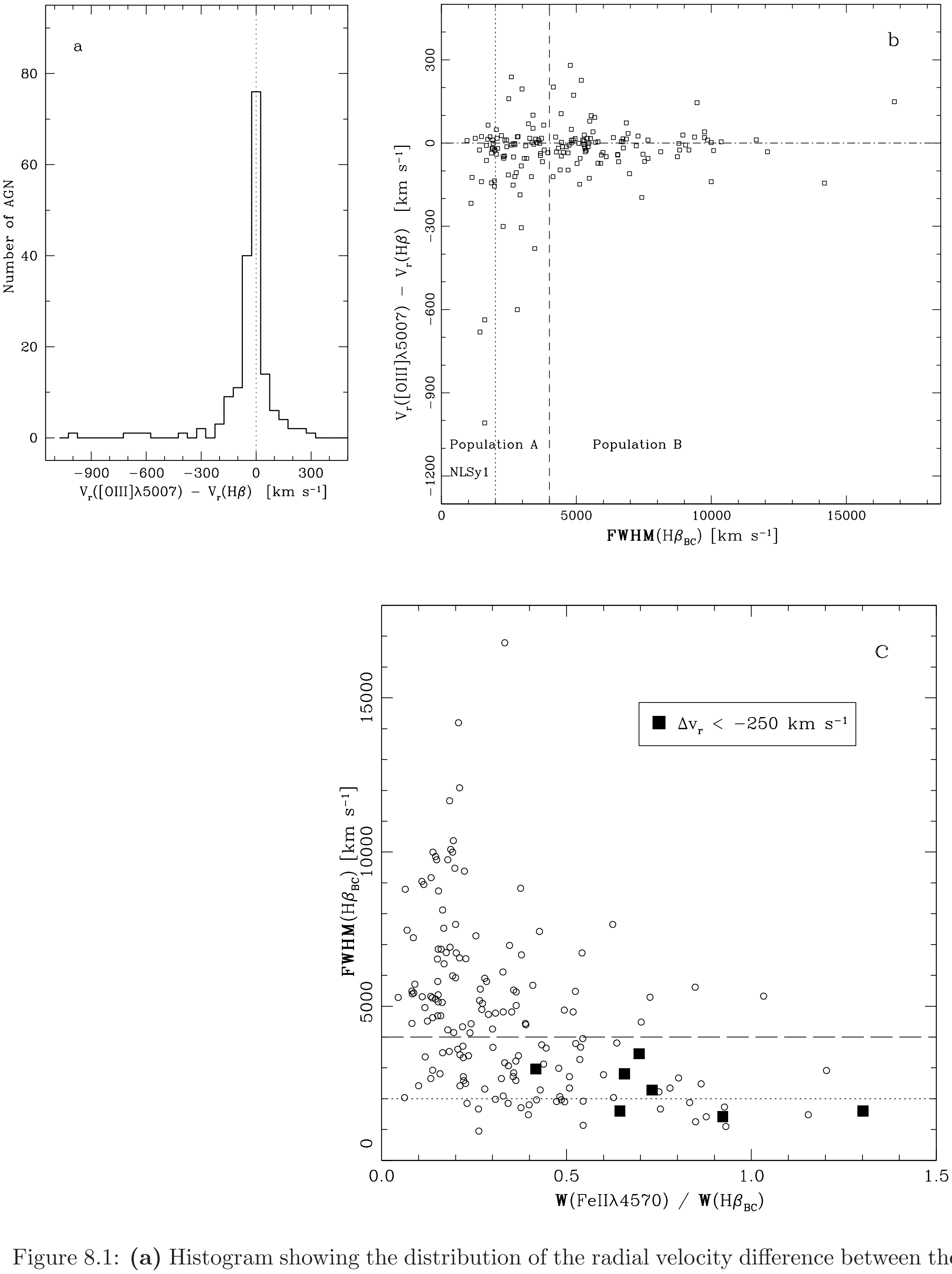

Figure 8.1: **(a)** Histogram showing the distribution of the radial velocity difference between the [OIII]λ5007 and the Hβ line. **(b)** The difference of the radial velocity between the [OIII]λ5007 and Hβ versus FWHM(H$\beta_{\rm BC}$). The vertical dotted line marks the boundary of the NLSy1 galaxies. The vertical dashed line separates Population A and B sources. Seven objects with with $\Delta v_r < -250$ km s^{-1} are visible. **(c)** Location of outliers in the FWHM(H$\beta_{\rm BC}$) vs. $R_{\rm FeII}$ diagram (the optical Eigenvector-1 diagram). Filled squares represent the "blue outliers" ($\Delta v_r <$ -250 km s^{-1}).

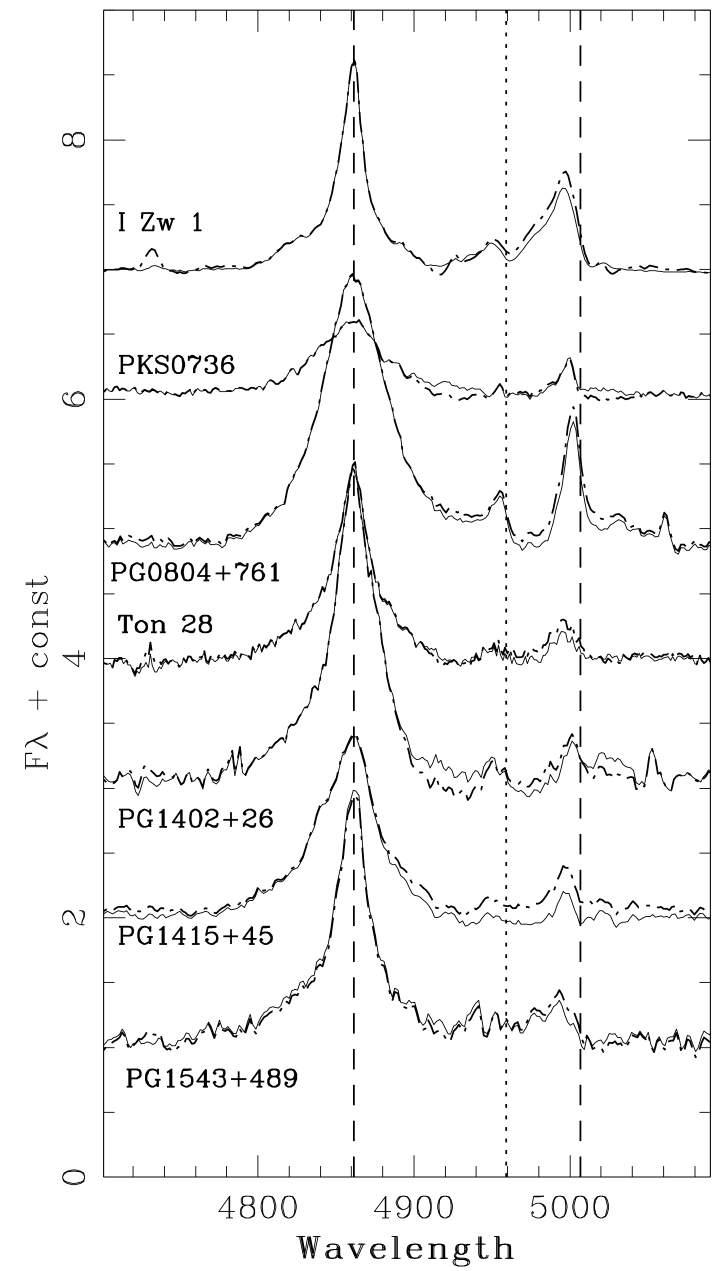

Figure 8.2: Hβ spectral region of the "blue" outliers after the deredshift and subtraction of the FeII template. The spectra are normalized with respect to the local continuum and arbitrary constant added. The solid line corresponds to the subtraction of a I Zw 1-based empirical template, the dot-dashed line to the subtraction of a theoretical template. The vertical lines indicate the position of Hβ, [OIII]λ4959 and [OIII]λ5007. The difference in the radial velocities between the [O III]λ5007 lines and Hβ is well visible.

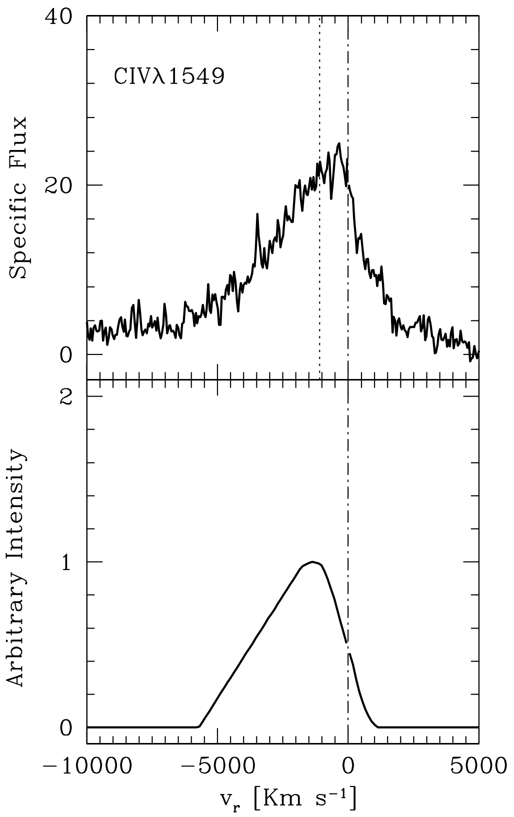

Figure 8.3: Upper panel: the CIVλ1549 and [OIII]λ5007 profile of Ton 28, a blue outlier. Lower Panel: CIVλ1549 and [OIII]λ5007 outflow model profiles, for optically thin gas moving at approximately the local escape velocity. Profiles have been computed for a cone of half-opening angle 85°, with the line of sight oriented at 15° with respect to the cone axis. The receding part of the flow is assumed to be fully obscured from the observer.

component profiles. This component becomes stronger in larger mass and lower L/M sources. No specific influence of radio loudness on the Hβ broad component profile is detected, although equivalent widths of Hβ broad component and especially of [OIII]$\lambda\lambda$4959,5007 are larger for radio-loud sources. We identify five more "blue outlier" sources. Since these sources are, on average, one magnitude brighter than other AGNs with similar mass, they are accreting at an Eddington ratio that is 2-3 times higher. We hint at evolutionary effects that explain some of these results and reinforce the "Eigenvector 1" correlations.

Introduction: Studies of emission lines play an important role in our understanding of Active Galactic Nuclei (AGN) and the physics the accretion processes, although a connection between the main theoretical parameters (i.e., black hole mass, accretion rates, black hole spin, and a viewing angle) and observed spectral parameters is, at best, just sketchy and qualitative. In recent years, a major innovation has been ascribed to the so-called "Eigenvector 1" (E1) correlations (Boroson & Green 1992). The original E1 was most closely related to the anti-correlation between Fe $\textsc{ii}_{\rm opt}$ strength and peak [OIII]λ5007 intensity, and FWHM of the Hβ broad component (Hβ_{BC}).

E1-related correlations have emerged as very robust, since they continue to appear in different low-z AGN samples, even if a set of spectral parameters partly different from the ones used for the original Principal Component Analysis (PCA) by Boroson & Green (1992) is considered.

The robustness of the E1 correlations stems probably from a series of concurring factors: (1) an Eddington ratio that may be continuously changing along the E1 sequence (e.g., Boroson, Persson & Oke 1985; Boroson & Green 1992; Murray et al. 1995; Nicastro 2000; Marziani et al. 2001; Boroson 2002); (2) outflow/wind properties which are expected to depend on Eddington ratio (e.g., Dultzin-Hacyan et al. 2000; Marziani et al. 2001); (3) orientation effects that will blur any physical correlation and displace sources in the direction of increasing Eddington ratio (Marziani et al. 2001; see also, Nagao et al. 2000, Zhou et al. 2003); (4) Broad Line Region (BLR) structural effects (Sulentic et al. 2000b, Sulentic et al. 2002; see also the Proceeding of the Nebraska meeting for the E1 relevance for the Broad Line Region structure; Gaskell et al. 1999); (5) last, but not least, evolutionary effects that will lead to an increase of black hole mass as well as of the [OIII]λ5007 rest-frame equivalent width (Zamanov et al. 2002; Boroson 2002). We will briefly discuss them in § 8.6.3 and § 9.

Even if there is not yet a consensus (see e.g., Marziani et al. 2001; Boroson 2002), the physical drivers of E1 are likely to involve the luminosity-to-black hole mass ratio (L/M $\propto$ Eddington ratio), an orientation angle, and the black hole mass (M) (Zamanov & Marziani

2002). Additional properties such as black hole spin (e.g., Wilson & Colbert 1995) or the properties of the host galaxy environment (e.g., McLure et al. 1999) are also likely to play a role in any RQ-RL dichotomy.

This paper presents a basic investigation of the influence of L/M and M on RL and RQ sample properties, on the H$\beta_{\rm BC}$ line profile, and on the occurrence of the "blue outliers", which are all major E1-dependent phenomena. In § 2 we present our quasar sample followed by (§ 3) derivation of M and L/M, (§ 4) presentation and discussion of mass – luminosity diagrams, (§ 5) a comparison of radio quiet and loud sources, (§ 6) an analysis of H$\beta_{\rm BC}$ profiles, (§ 7) as well as significance of the "blue outlier" sources. Our results are discussed in § 8. § 9 provides some concluding remarks.

Sample Definition & Measurements

We use spectra of 278 AGNs. Our AGN sample includes 215 sources and has been presented elsewhere (Marziani et al. 2003b). We added 63 soft X-ray selected sources with suitable optical spectroscopic data (Grupe et al. 1999; hereafter G99) because this turns out to be the most fertile source of "blue outliers". Inclusion of Grupe et al. data makes our sample less biased. The optical characteristics of these X-ray selected sources include: (1) relatively "narrow" broad emission lines (e.g. Narrow Line Seyfert 1 [NLSy1] sources), (2) strong optical Fe II$_{\rm opt}$ blends and (3) weak forbidden emission lines. The merged datasets provide reasonable quality spectra (S/N$\approx 20-70$) for the region near Hβ in 278 AGN ($z \lesssim 0.8$). The M03 dataset is not complete (see M03 for discussion of completeness and sample biases).

We use line parameters reported in M03 and derive the corresponding measures (using the same procedures described in M03) for the X-ray selected sample from the digital spectra made publicly available by G99. We consider here measurements of the following parameters: (a) FWHM(H$\beta_{\rm BC}$); (b) equivalent width ratio R$_{\rm FeII}$=W(FeII λ4570)/W(H$\beta_{\rm BC}$), (c) FWHM measurement of the lines in the FeII λ4570 blend (see M03 for details), (d) radial velocity difference between [OIII]λ5007 and Hβ at the line peak (without narrow component subtraction). Accuracy of the G99 wavelength calibration was evaluated by examining the distribution of radial velocity difference between [OIII]λ4959 and [OIII]λ5007. Whenever possible, [OIII]λ4363 was also used and all inter-narrow line differences were found to be comparable to our measures (cf. Zamanov et al. 2002).

Apparent (m$_{\rm V}$), and absolute B magnitudes (M$_{\rm B}$) were taken from 10$^{\rm th}$ edition of the AGN catalog (Véron-Cetty & Véron 2001). A magnitude correction +0.88 mag was applied to convert M$_{\rm B}$ from H$_0$=50 km s^{-1} Mpc^{-1} to H$_0$=75 km s^{-1} Mpc^{-1} ($q_0 = 0$) which we use throughout this paper. Galactic extinction values A$_{\rm B}$ were taken from NED following Schlegel et al. (1998). Sources were considered RL if the specific flux at 6 cm and in the B band was larger than 10, with data taken from the Véron-Cetty & Véron (2001) catalog.

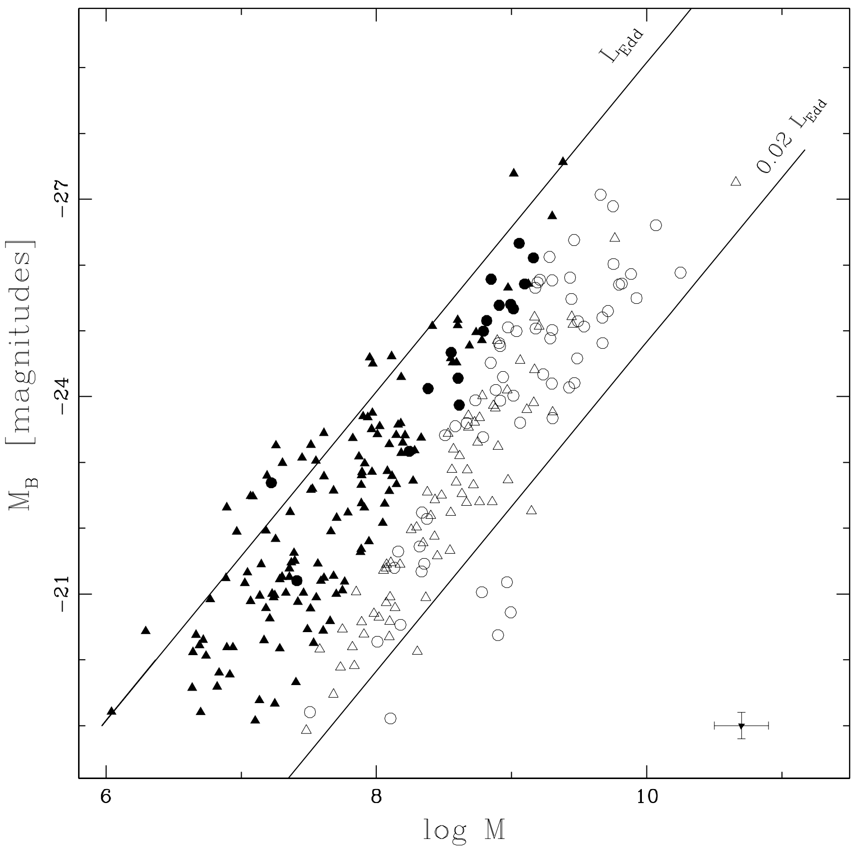

Figure 8.4: Distribution of absolute B magnitude (M_B) versus black hole mass M (in solar units) for the 278 AGN sample. M_B values are corrected for the galactic extinction. Triangles and circles indicate radio-quiet and radio-loud sources respectively. Open symbols indicate sources with FWHM(Hβ_{BC}) $\gtrsim$4000 km s^{-1}; filled symbols sources with FWHM(Hβ_{BC}) $\lesssim$4000 km s^{-1}. The bars in the lower right corner indicate typical errors.

8.3 Computation of M and L/M

8.3.1 Black Hole Masses

One can estimate the mass of the putative supermassive black hole using FWHM(H$\beta_{\rm BC}$) and a reverberation "radius" (Kaspi et al. 2000) along with the assumption of virialized motions. It is now common to estimate the mass by assuming the BLR distance from the central continuum source $r_{\rm BLR} \propto (L_{5100})^{\alpha}$ and α =0.7, as derived from the reverberation data (Kaspi et al. 2000). The virial mass is M=$r_{\rm BLR}v^2$/G, where v= $\sqrt{3}/2$ FWHM(H$\beta_{\rm BC}$) (c.f. Woo & Urry 2002), and G is the gravitational constant. We therefore can write the black hole virial mass as follows:

$$\mathrm{M} = 4.817 \times \left(\frac{\mathrm{FWHM(H}\beta_{\rm BC})}{1\ \mathrm{km\,s^{-1}}}\right)^2 \left(\frac{\lambda\,\mathrm{L}_{5100}}{10^{44}\,\mathrm{erg\,s^{-1}}}\right)^{0.7}, \qquad (8.1)$$

where M is in solar units, L_{5100} is the specific luminosity at 5100 Å (in units of ergs s^{-1} cm^{-2} Å^{-1}), and

$$\lambda\,\mathrm{L}_{5100} = 3.137 \times 10^{35-0.4(\mathrm{M_B}-\mathrm{A_B})}\ \mathrm{erg\,s^{-1}}. \qquad (8.2)$$

In order to convert the absolute B magnitude $\mathrm{M_B}$ to λL_{5100} we assumed that the specific flux is $f_\nu \propto \nu^{-0.3}$. The derived masses are thought to be reasonable estimates within a factor of about 2–3 (see also Woo & Urry 2002, Vestergaard 2002).

8.3.2 Influence of Orientation

Source viewing angle is especially important in AGN where the concepts of disk accretion/line emission and jet ejection are widely favored. In the above mass derivation formula we did not include any orientation related broadening factor. If H$\beta_{\rm BC}$ is emitted in a highly flattened structure then M can be underestimated by a factor $\approx \sin i^{-2}$ in pole-on/face-on sources (i.e., with accretion disk axis oriented along our line of sight). Unfortunately, we do not yet have a proper way to estimate the viewing angle i for each source. This is a major drawback because there is observational evidence suggesting that orientation can affect line width by a factor $\approx$ 2 (Brotherton 1996; Marziani et al. 2001; Jarvis & McLure 2002). Even though we neglected the effects of orientation in the general sample population, we considered it in computations of M and L/M the relatively rare and extreme class that is likely observed close to "pole-on": the "blue outliers" (§8.5.3).

8.3.3 The Role of the BLR Size-Luminosity Relationship

The exponent in the relationship between source luminosity L and $r_{\rm BLR}$ is assumed to be α=0.7. Any deviation from this value has quantitative effects on our results. Our sample includes many moderately luminous quasars at $0.4 < z < 0.8$, so it is important to stress that the relationship derived by Kaspi et al. (2000) is based exclusively on quasars of $z < 0.4$ and that the high (and low) luminosity ranges of the correlation are poorly sampled.

If we consider sources in the luminosity range $43.4 \lesssim \log \mathrm{L/L_\odot} \lesssim 45$ (i.e. where we have uniform luminosity sampling), the slope of the best fit is α=0.8, and could be easily as high as α

= 1 without increasing significantly the fit standard deviation. Marziani et al. (2001) considered this case which seems appropriate for the PG quasar luminosity range. One must remain open to the possibility that 0.5 $\lesssim \alpha \lesssim$1, and that α might even be a function of L. Changing α implies an L-dependent change in mass estimates; therefore the slope of the luminosity-to-mass relationship (Fig. 8.4) is affected as well as the location of points in the L/M vs. M diagram (Fig. 8.5 & Fig. 8.7). Despite these possibilities, systematic trends discussed in this paper should not be affected.

8.3.4 Bolometric Luminosity

We calculated the bolometric luminosity L from L $\approx 10\lambda\ \mathrm{L}_\lambda$(5100Å) (details can be found in Wandel, Peterson, & Malkan 1999; Elvis et al. 1994; Collin et al. 2002). Values computed in this way were used to derive the L/M ratio. The L/M ratio everywhere is expressed in solar units with the solar value $(\mathrm{L/M})_\odot = 1.92$ ergs s^{-1} g^{-1}, and the Eddington limit corresponding to logL/M = 4.53.

We neglected any possible differences in the spectral energy distribution between source subclasses. In order to test this benign neglect we considered 44 sources that are common with Woo and Urry (2002) where SEDs were constructed from archival data. Comparison of our bolometric luminosity values showed no significant systematic difference: $\overline{\Delta \log \mathrm{L}} \approx -0.06$ for all 44 sources, with a standard deviation $\sigma \approx 0.24$. RQ sources show $\overline{\Delta \log \mathrm{L}} \approx -0.06$ with $\sigma \approx 0.22$, while RL $\overline{\Delta \log \mathrm{L}} \approx -0.07$ with a slightly larger $\sigma \approx 0.26$. If we consider separately RQ and RL sources with the restriction FWHM(Hβ_{BC})$\geq$ 4000 km s^{-1}, we find $\overline{\Delta \log L} \approx -0.05$ (RQ) and $\overline{\Delta \log \mathrm{L}} \approx -0.01$ (RL). It is worth noting that the scatter is due to a minority of bad-behaving data points ($\approx$20%). If they are removed, the standard deviation becomes $\sigma \approx 0.1$ in all cases, with systematic differences always $\lesssim$0.05.

8.4 Mass - Luminosity Diagram

Fig.8.4 shows a plot of $\mathrm{M_B}$ vs. M for our combined sample which covers an absolute B magnitude range $-20 \lesssim \mathrm{M_B} \lesssim -27$ and an estimated black hole mass range $10^7 \lesssim$ M $\lesssim 10^{10}$ (M is everywhere given in $\mathrm{M}_\odot$). The data show a rather well-defined range in L/M with almost all sources lying between 0.02 $\lesssim \mathrm{L/L_{Edd}} \lesssim$1.00. RQ sources show evidence for significant Malmquist bias while RL sources show the opposite trend probably related to a bias towards selecting higher luminosity core-dominated sources likely to be beamed.

8.5 Hβ_{BC} Profile Shape

8.5.1 The Influence of M and L/M

We generated median Hβ_{BC} profiles in bins covering narrow ranges of derived M and L/M. The adopted binning is shown in Fig. 8.5. The median spectra (normalized to the local continuum)

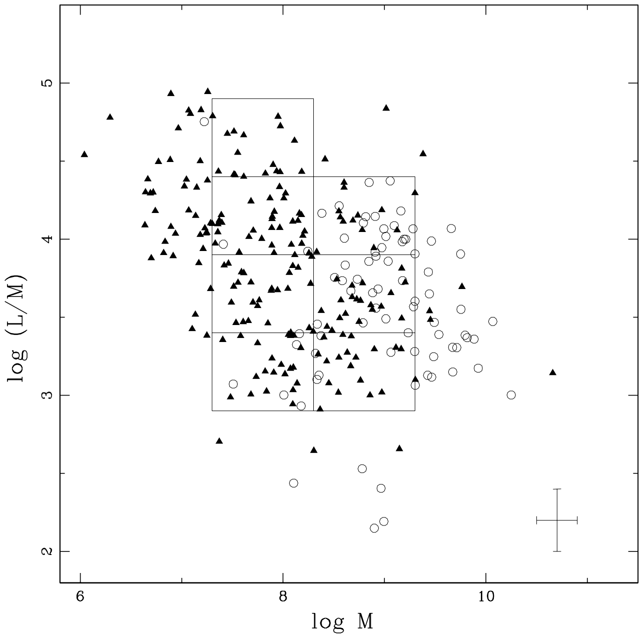

Figure 8.5: Binning of our sample in the L/M vs. M parameter space for the median spectra computations.

are plotted in Fig. 8.6.

8.5.2 The "Blue Outliers"

Spectral Properties of [OIII]$\lambda\lambda$**4959,5007 "Blue Outliers":** In a previous investigation (Zamanov et al. 2002), we identified seven objects from the M03 sample that showed an [OIII]$\lambda\lambda$4959,5007 blueshift relative to the peak of Hβ. The shift amplitudes were $\geq$ 250 km s^{-1} leaving little doubt that we are observing a significant velocity displacement. We have identified five additional AGN that show large amplitude blueshifts among the objects of G99. Some properties of all of these sources are given in Table 8.2. All of the sources show strong Fe II$_{\rm opt}$ emission. In the E1 context they show: (1) R$_{\rm FeII}$ $\gtrsim$0.5, (2) FWHM(Hβ) < 4000 km s^{-1}(i.e., they are located in spectral bins A2 and A3 of Sulentic et al. 2002); (3) a large CIVλ1549 broad component blueshift (Zamanov et al. 2002). Blue outliers show also weak [OIII]$\lambda\lambda$4959,5007 emission with W([OIII]λ5007) $\lesssim$ 20 Å, and a median value of $\approx$6 Å.

Nine out of our 12 outliers are formally NLSy1s. In general, the [OIII]$\lambda\lambda$4959,5007 lines of NLSy1s have a relatively narrow profile with often, in addition, a second broader, blueshifted component (Véron-Cetty, Véron & Gonçalves 2001). The blue-shift, is 400 – 1100 km s^{-1} when the two components can be deblended (Zheng et al. 2002). These values correspond to the blue outliers range suggesting that the latter are an extreme subset with low W([OIII]λ5007) when only the shifted component is visible.

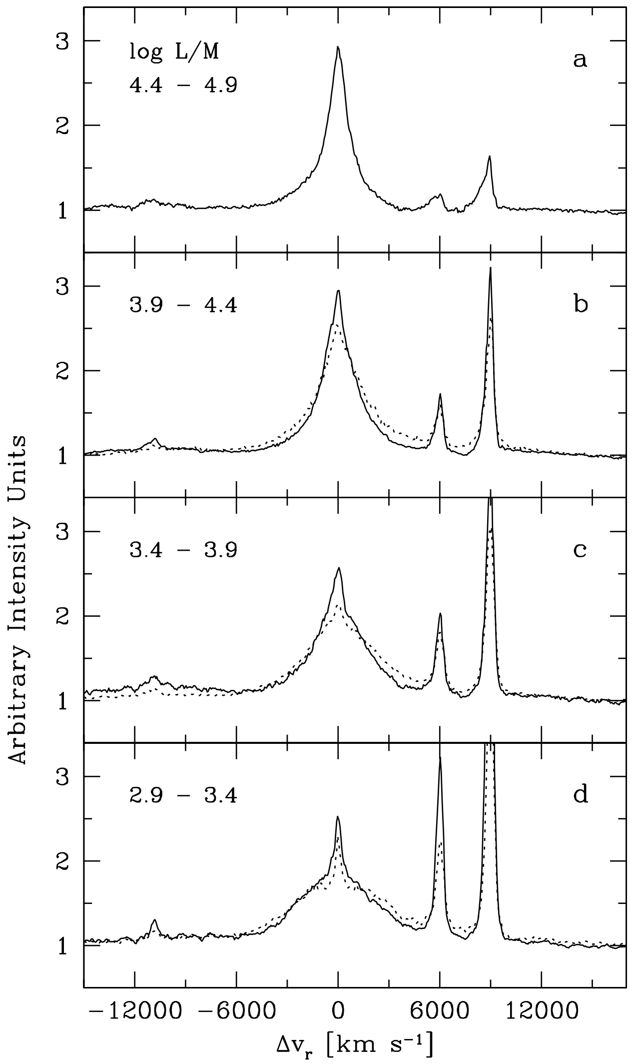

Figure 8.6: Hβ line profiles after Fe$_{\text{II}_{opt}}$ subtraction. From top to bottom the plots correspond to: **(a)** logL/M 4.4 - 4.9; **(b)** logL/M 3.9 - 4.4; **(c)** logL/M 3.4 - 3.9; **(d)** logL/M 2.9 - 3.4. Note that log L/M $\approx$4.53 corresponds to L/L$_{\rm Edd}$ $\approx$ 1. Solid lines correspond to 7.3 $\leq$ logM$\leq$ 8.3, and dashed lines to 8.3 $<$ logM$\leq$ 9.3.

FWHM of FeII$_{\rm opt}$ **and** [OIII]$\lambda\lambda$**4959,5007 lines:** Computation of M requires that H$\beta_{\rm BC}$ be separated from any narrow component so that FWHM(H$\beta_{\rm BC}$) can be properly measured. The problem is that extreme sources like the blue outliers show no profile inflection (reflected in the fact that they are well fit by a Lorentzian function). The rationale for our methodology has been detailed in M03, and will not be rediscussed here. We just remind that we normally assume (and find) that the narrow component of Hβ shows almost the same shift and width properties as the [OIII]$\lambda\lambda$4959,5007 lines. However, in blue outliers W([OIII]λ5007) is smaller than in any broad emission line AGN class and is also blueshifted relative to the peak of Hβ. We conclude that we are not measuring a narrow line component at the Lorentzian tip of the Hβ profile. Any narrow component of Hβ is assumed to be blueshifted and lost in the blue wing of the broad line (even assuming it has the same strength as [OIII]λ5007 in blue outliers it would represent less than 10% of the total line flux). Subtraction of a narrow Hβ component would have a non-negligible effect on the FWHM(H$\beta_{\rm BC}$) measurement which is needed for the M estimation.

The FeII λ4570 feature is a complex of lines thought to have FWHM similar to H$\beta_{\rm BC}$. We estimated FWHM(FeII λ4570) *independently* from FWHM(H$\beta_{\rm BC}$) by FeII$_{\rm opt}$ template fitting using the I Zw 1 spectrum (of course, only for highest S/N spectra; see M03 for details). In our sample FWHM(FeII λ4570) is similar to FWHM(H$\beta_{\rm BC}$) with few exceptions only (see Bongardo et al. 2002). Estimated FWHM(FeII λ4570) values are given in Table 8.2. No narrow FeII λ4570 component has been detected and nor is one expected given the low inferred density for the narrow line region. In principle, we can use FWHM(FeII λ4570) instead of FWHM(H$\beta_{\rm BC}$) in the mass derivations in order to avoid any error associated with a narrow line component. Use of FWHM(FeII λ4570) instead of FWHM(H$\beta_{\rm BC}$) will yield M values within $\sim$10% of ones derived from FWHM(H$\beta_{\rm BC}$).

The correlation of nuclear BH mass with stellar bulge velocity dispersion σ_* is now well established in nearby galaxies. Recent results (Nelson 2000; Boroson 2002) show that a BH mass – FWHM([OIII]λ5007) correlation is also present but with larger scatter. The FWHM([OIII]λ5007) measures given in Table 8.2 provide another way to estimate BH masses. The derived values are however considerably higher than values calculated using FWHM(H$\beta_{\rm BC}$) and source luminosity. This is not surprising because NLSy1-type AGN apparently do not follow Nelson's relation (Mathur, Kuraszkiewicz & Czerny 2001). If NLSy1s do not follow the relation then blue outliers will almost certainly show the same lack of agreement. This does not contradict our assumption that blueshifted [OIII]$\lambda\lambda$4959,5007 arises in outflowing gas (Zamanov et al. 2002), possibly associated with a disk wind. The [OIII]$\lambda\lambda$4959,5007 region in blue outliers may be very compact and its velocity field is not likely to be dynamically related to the host galaxy stellar bulge. This points to a limiting W([OIII]λ5007) ($\approx$ 20Å) below which FWHM([OIII]$\lambda\lambda$4959,5007) emission ceases to be a useful mass estimator.

8.5.3 $\mathrm{M_B}$ and L/M Ratio of [OIII] Outliers

All blue outliers lie in the region of E1 thought to be populated by highly accreting (high L/M) sources (Marziani et al. 2001). Most of them are located close to the Eddington limit ($\log \mathrm{L/M} \approx 4.53$, see Fig.8.7). This is also true if: (1) FWHM(FeII λ4570) is used instead of FWHM(Hβ_{BC}) to derive M, and (2) an orientation correction is applied. The blue outliers may be oriented close to pole-on. Since M $\propto$ FWHM^2, an inclination correction will move the "blue outliers" toward higher mass and lower L/M (see the arrows on Fig.8.7). Even with an inclination correction by a factor $\approx$4, the L/M values for blue outliers remain among the highest observed. We note that: (1) other sources should also be corrected for orientation especially if low ionization lines are emitted in a flattened configuration in all Population A sources, as suggested (Marziani et al. 1996); (2) some care is needed since we neglected a photometric correction which is basically unknown. We do not know whether any sort of continuum beaming operates for RQ AGN as $i \to 0°$ (very similar W(Hβ_{BC}) for CD and LD RL sources suggests no strong effect; Sulentic et al. 2003). Observational errors and uncertainty in the orientation correction do not allow us to determine whether some blue outliers are really super-Eddington sources as they appear in Fig.8.7.

All blue outliers show estimated masses less than $10^{8.5}\mathrm{M}_\odot$. We tried to determine if the blue outliers large L/M was a consequence of a low-mass bias by calculating the $\mathrm{M_B}$ difference between blue outliers and other sources in two mass ranges: (1) $7.15 \leq \log \mathrm{M} \leq 8.45$ (where the "blue outliers" are before the orientation correction) and (2) $7.55 \leq \log \mathrm{M} \leq 8.85$ (where they move after the orientation correction). Table 8.3 shows that the blue outliers are almost certainly ~ 1 mag brighter than other sources with similar mass implying 2–3 times higher L/M ratios.

8.6 Discussion

8.6.1 Mass-Luminosity Diagram

The ranges of M and L/M considered in this study are similar to those in other recent work (Woo & Urry 2002; Collin et al. 2002). We find that the Eddington limit defines an approximate upper boundary to the luminosity distribution (as in Woo & Urry 2002), indicating that there are no known low-z AGN accreting significantly above the Eddington limit (this depends on the adopted $\mathrm{H_0}$ value). Figure 8.4 also suggests that there may be fewer high (than low) mass sources with L/M close to the Eddington limit. This might be a selection effect or an indication that galaxies with a high mass BH may be unable to supply fuel at high L/M. In other words, the upper envelope in Figure 8.4 might be due to the Eddington limit as well as the ability of the surrounding matter to feed the accretion flow (see, e.g., Nicastro et al. 2003). The lower envelope of the luminosity distribution may be due to a selection effect (e.g. Woo & Urry 2002), or it may indicate that only sources radiating at $0.01 \lesssim (L/L_{Edd}) \lesssim 1.00$ exhibit a stable broad lines region. The latter possibility might be connected with the presence/absence of an accretion disk wind (see also Kollatschny & Bischoff 2002).

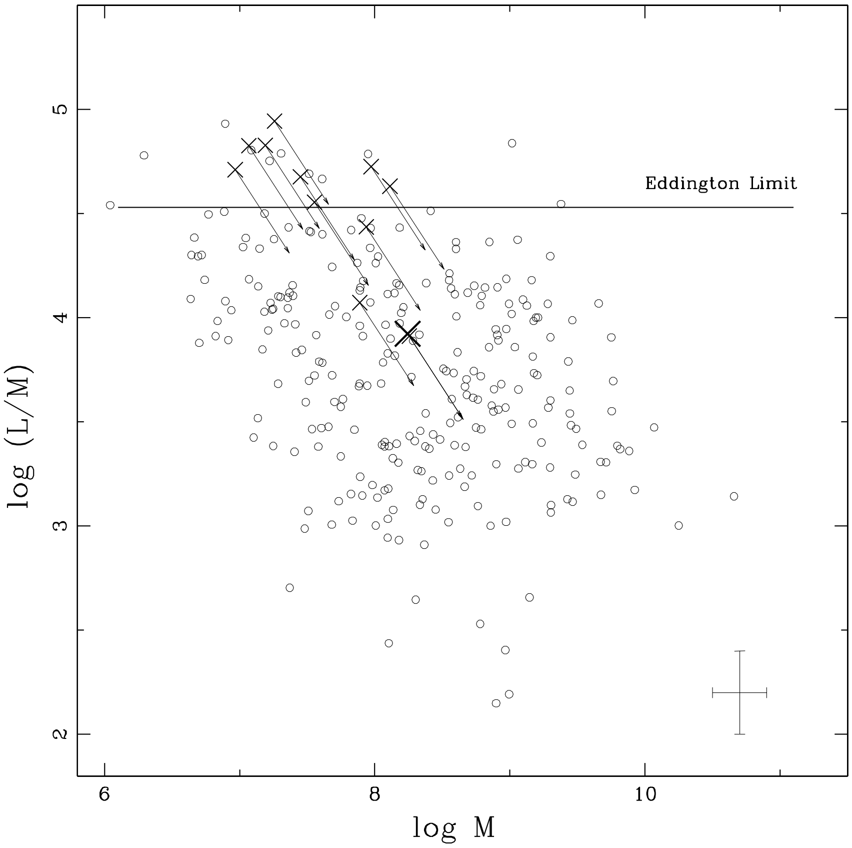

Figure 8.7: Position of blue outliers (crosses) relative to other sources in our sample (open circles). The larger cross indicates the position of PKS 0736+01 - the only known RL "blue outlier". The dashed line indicates the Eddington limit. Arrows indicate displacements of blue outliers if we apply an orientation correction ∼0.4 to the derived masses. Blue outliers are among the highest L/M sources and remain in the upper part of the diagram even after an orientation correction. One should consider that many other sources would move in the same direction of the blue outliers if a proper orientation were applied to all sources.

Table 8.2: The spectral properties of the "blue outliers": radial velocity difference between top of Hβ and [OIII]λ5007, equivalent width and FWHM of [OIII]λ5007, FWHM of FeII λ4570, the equivalent widths ratio of FeII λ4570 and Hβ_{BC} (R_{FeII}).

Name	Δv [km s^{-1}]	W[OIII] λ5007 [Å]	FWHM [OIII] [km s^{-1}]	FWHM(Hβ) [km s^{-1}]	FWHM(FeII) (FeII) [km s^{-1}]	RFe
I Zw 1	-640	15.3	1440±120	1092	1095	1.30±0.1
PKS 0736+01	-430	2.6	720±60	3258	3560	0.70±0.1
PG 0804+761	-305	10.1	780±60	3302	3067	0.42±0.1
PG 1001+291	-680	3.4	960±60	1759	1588	0.71±0.1
PG 1402+261	-300	2.6	900±180	1938	1957	0.73±0.1
PG 1415+451	-600	2.9	660±60	2555	2870	0.66±0.1
PG 1543+489	-950	6.5	—	1555	1588	0.64±0.1
RX J0136.9-3510	-380	6.0	900±60	1050	1100	1.0±0.1
RX J0439.7-4540	-580	5.0	1020±120	1020	1100	0.9±0.1
RX J2217.9-5941	-330	8.1	1140±120	1370	1588	2.0±0.2
RX J2340.6-5329	-490	21.8	780±60	1228	1588	1.3±0.1
MS 2340.9-1511	-420	5.8	780±60	969	1218	1.1±0.1

Table 8.3: M_B of the "blue outliers" (as they are given in Véron-Cetty & Véron catalog without correction for the cosmology), compared with other objects in the sample with similar mass. P_{KS} is the probability that the "blue outliers" and the other objects in the indicated mass ranges are randomly drawn from the same parent population according to Kolmogorov-Smirnov test.

	Aver.$\pm\sigma$	Med.$^{75\%}_{25\%}$	P_{KS}
blue outliers	-23.9 ± 0.8	$-23.85^{-23.45}_{-24.30}$	
$7.0 \leq$ logM≤ 8.2	-22.4 ± 0.8	$-22.20^{-21.50}_{-23.40}$	0.00035
$7.6 \leq$ logM≤ 8.8	-22.8 ± 0.8	$-22.90^{-21.80}_{-23.90}$	0.00600

8.6.2 Transition in H$\beta_{\rm BC}$ Line Profile Shape

Connecting empirical and physical parameters, we find that median profiles for H$\beta_{\rm BC}$ in Pop. A sources ($\log \mathrm{L/M} > 3.9$, and for $3.5 < \log \mathrm{L/M} < 3.9$ and $7.5 < \log \mathrm{L/M} < 8.5$) show a Lorentzian shape. In other words, if $\log \mathrm{L/M} \gtrsim 3.9$, the shape is Lorentzian for all values of M. Similarly, if $\log\mathrm{L/M} \lesssim 3.4$ (bins dominated by Pop. B surces), the profile is redward asymmetric and can be decomposed into two Gaussian components (one redshifted and the other not). This suggests that the transition from Lorentzian to double Gaussian profiles is governed by a critical L/M value (it is interesting to note that the H$\beta_{\rm BC}$ asymmetry is also one of the major correlate of the original E1 of Boroson & Green 1992). Unfortunately, the division of the bins in the L/M strip $3.4 < \log \mathrm{L/M} < 3.9$ did not make the situation clearer. We conclude that the Lorentzian – double Gaussian profile transition occurs between $3.4 \lesssim \log \mathrm{L/M} \lesssim 3.9$ ($0.08 \lesssim \mathrm{L/L_{Edd}} \lesssim 0.25$). A more precise value would require knowledge of source orientation effects and a better-constrained α value. This provides a physical basis for the phenomenological finding about profile change at FHWM(H$\beta_{\rm BC}$)$\approx$ 4000 km s^{-1}and the resulting Population A-B hypothesis (Sulentic et al. 2002).

8.6.3 On the Nature of the Blue Outliers

We observe "blue outliers" (following the simple wind model of Zamanov et al. 2002) when the [OIII]$\lambda\lambda$4959,5007 lines and the peak of Hβ arise in different regions - Hβ from a near face-on accretion disk and [OIII] from a wind with velocity of about 1000 km s^{-1}. In terms of orientation these RQ sources would be analogous to some CD RL quasars or even to BL Lac (blazars). Other nearly-as-large L/M oriented sources can/must exist in our sample but they are not "blue outliers" for at least two reasons: (i) they possess a well developed Narrow Line Region (NLR) which is unlikely to show a significant blue-shifted component; (ii) they are not oriented face-on. There are probably also lower L/M sources oriented face-on, however their L/M ratio may not be sufficient to power a wind or the wind outflow velocity may be low (roughly < 300 km s^{-1}). This could explain why the blue outliers are exclussively sources with very high L/M. It is worth noting that the only RL blue outlier, PKS 0736+01, is a flat spectrum radio source, and one of the brightest High Polarization, Optically Violently Variable sources. Its optical continuum is dominated by a "blazar" component as in BL Lac (Malkan & Moore 1986). Continuum properties suggest relativistic beaming making this a true pole-on RL source consistent with the interpretation of the "blue outliers" proposed by Zamanov et al. (2002).

In the most recent scenarios for joint AGN and galaxy evolution (e.g., Granato et al. 2001), the active nucleus and the galaxy evolve together, with BH accreting matter and the galaxy making stars and supplying fuel for the quasar. At some point, the wind from the accreting BH blows away the matter surrounding it and a quasar emerges. The central accretion source then appears as an unobscured quasar which lasts as long as there is fuel in the accretion disk (Fabian 1999). In this scenario our "blue outliers" could represent the stage when the quasar has just emerged (cf. Krongold et al. 2001 for a similar interpretation stemming from the analysis of NLSy1 host galaxies and environment). They could be in process of building of their NLR.

8.7 Conclusions

We computed virial masses and Eddington ratios for a sample of ~300 AGN. We have shown that L/M seems to govern the overall shape of the $H\beta_{BC}$, and we found an interesting dependence on M of the $H\beta_{BC}$ asymmetry. The transition between sources showing Lorentzian and double Gaussian $H\beta_{BC}$ profiles is likely associated with a critical L/M value, as suggested by Sulentic et al. (2002). L/M and M values in the range $8 \lesssim$ M $\lesssim 9.5$ and $3 \lesssim \log$ L/M $\lesssim 4.2$ are found likely for both RL and RQ AGN while others (log L/M $\gtrsim 4.2$) may very unlikely for RL sources. However, it is important to stress the existence of a radio-loud blue outlier radiating at very high L/M (log L/M$\approx$ 4.8; other RL sources radiate at logL/M $\approx$4.4). This shows that there is no physical impossibility for RL sources to be of large L/M and small M; they may be simply less likely to be that way.

We confirm that the "blue outliers" are mainly NLSy1 sources (Zamanov et al. 2002; see also Sulentic et al. 2000a). We increase the number of known "blue outliers" to 12. We show that all blue outliers are accreting at 2 times higher Eddington ratio than other sources with similar mass. The compactness of their NLR points toward very young ages (Zamanov et al. 2002), suggesting that they may be "fledgling" AGN as discussed for NLSy1 by Sulentic et al. (2000a) and Mathur (2000). An interesting issue is then whether different M and L/M distributions may point toward evolutionary effects, i.e., whether some RQ sources may be the parent population for all quasars (for example, NLSy1s, "extreme Pop. A" sources, may evolve into Pop. B RQ or even RL depending on accretion of angular momentum and/or host galaxy type/evolution).

In the future we will need of an orientation indicator for each individual AGN. This is very important for a correct evaluation of M. The CIVλ1549 line profile shows promise as an orientation indicator at least for Pop. A sources (Richards et al. 2002). It may also provide us with important clues about aspects of Broad Line Region structure and its dependence on L/M, and ultimately, with a 3D observational space to uniquely map into a 3D "physical" parameter space defined by M, L/M and orientation.

8.8 Rerefences to Chapter 8

Alloin, D., Barvainis, R., Gordon, M. A., & Antonucci, R. R. J. 1992, A&A, 265, 429
Boroson T., 2002, ApJ 565, 78
Boroson T.A., Green R.F., 1992, ApJS 80, 109
Boroson, T. A., Persson, S. E., & Oke, J. B. 1985, ApJ, 293, 120
Boroson T.A.,& Meyers, K. A., 1992, ApJ, 397, 442
Boroson, T. A. & Oke, J. B. 1987, PASP, 99, 809
Bongardo C., Zamanov R., Marziani P., Calvani M., Sulentic J. W., 2002,

"AGN5: Inflows, Outflows and Reprocessing around Black Holes", astro-ph/0211418
Brotherton, M. S., 1996, ApJS 102, 1
Brotherton, M. S., Tran, H. D., Becker, R. H., et al. 2001, ApJ, 546, 775
Busko, I. & Steiner, J. 1988,MNRAS, 232, 525
Collin, S., Boisson, C., Mouchet, M., et al., 2002, A&A 388, 771
Condon, J.J., Hutchings, J.B., & Gower, A.C. 1985, AJ, 90, 1642
de Robertis, M. 1985, ApJ, 289, 67
Dultzin-Hacyan, D., Marziani, P., & Sulentic, J. W. 2000, Revista Mexicana de Astronomia y Astrofisica Conference Series, 9, 308
Elvis, M., Wilkes, B. J., McDowell, J.C., et al. 1994, ApJS 95, 1
Evans, A. S., Frayer, D. T., Surace, J. A., & Sanders, D. B. 2001, AJ, 121, 1893
Fabian A.C., 1999, MNRAS 308, L39
Fasano G., & Franceschini A., 1987, MNRAS 225, 155
Francis, P. J., Hewett, P. C., Foltz, C. B.,et al. 1991, ApJ, 373, 465
Gaskell, C. M., Brandt, W. N., Dietrich, M., et al. 1999, ASP Conf. 175: Structure and Kinematics of Quasar Broad Line Regions
Granato, G. L., Silva, L., Monaco, P., et al. 2001, MNRAS, 324, 757
Grupe, D., Beuermann, K., Mannheim, K., Thomas, H.-C., 1999, A&A 350, 805
Grupe, D., Thomas, H.-C., Leighly, K. M., 2001 A&A, 369, 450
Jarvis, M. J., McLure, R. J., 2002, MNRAS 336, 38
Hes, R., Barthel, P. D., & Fosbury, R. A. E. 1993, Nature, 362, 326
Kaspi S., Smith P.S., Netzer H., Maoz D., Jannuzi B.T., Giveon U., 2000, ApJ 533, 631
Kollatschny W., Bischoff K., 2002, A& A, 386, 19
Krongold, Y., Dultzin-Hacyan, D., & Marziani, P. 2001, AJ, 121, 702
Malkan, M. A. & Moore, R. L. 1986, ApJ, 300, 216
Mathur, S., 2000, NewAR 44, 469
Mathur S., Kuraszkiewicz, J., Czerny B., 2001, NewA 6, 321
Marziani, P. & Sulentic, J.W. 1993, ApJ, 409, 612
Marziani, P., Sulentic, J. W., Dultzin-Hacyan, D., Calvani, M., Moles, M., 1996, ApJS 104, 37
Marziani, P., Sulentic, J. W., Zwitter, T., et al. 2001, ApJ, 558, 553
Marziani, P., Sulentic, J. W., Zamanov, R., et. al. 2003b, ApJS, 145, 199 (M03)
McLure, R. J., Kukula, M. J., Dunlop, J. S., et al. 1999, MNRAS, 308, 377
Moiseev, A. V., Afanasiev, V. L., Dodonov, S. N., et al., 2001, IAU Colloq. 184, E79
Murray, N., Chiang, J., Grossman, S. A., & Voit, G. M. 1995, ApJ, 451, 498
Nicastro, F. 2000, ApJL, 530, L65
Nicastro, F., Martocchia, A., & Matt, G. 2003, ApJL, 589, L13
Schlegel D. J., Finkbeiner D. P., & Davis M., 1998, ApJ 500, 525
Schöniger, F., & Sofue, Y. 1994, å, 283, 21
Steffen, W., Gomez, J. L., Raga, A. C., & Williams, R. J. R. 1997, ApJ, 491, L73
Stirpe, G. M. 1990, A&AS, 85, 1049
Sigut T.A.A., Pradhan A.K., 2003, ApJS, 145, 15

Sulentic, J. W. & Marziani, P. 1999, ApJ, 518, L9

Sulentic J.W., Marziani P., & Dultzin-Hacyan D., 2000a, AR A&A, 38, 521

Sulentic, J. W., Zwitter, T., Marziani, P., & Dultzin-Hacyan, D. 2000b, ApJ, 536, L5

Sulentic, J. W., Marziani, P., Zamanov, R., et al., 2002 ApJ, 566, L71

Sulentic, J. W., S. Zamfir, Marziani, P., et al., 2003 ApJ, 597, L17

Vanden Berk D.E., Richards G.T., Bauer A., et al., 2001, AJ, 122, 549

Véron-Cetty M.-P., & Véron P., 2001, A & A 374, 92

Véron-Cetty M.-P., Véron P., Gonçalves A.C., 2001, A & A 372, 730

Vestergaard, M., 2002, ApJ 571, 733

Whittle, M. 1985, MNRAS, 213, 33.

Wilson, A. S. & Colbert, E. J. M. 1995, ApJ, 438, 62

Wilson, A. S. & Heckman, T. M. 1985, "Astrophysics of Active Galaxies and Quasi-Stellar Objects", Mill Valley, CA, University Science Books, 1985, 39

Woo J.-H., Urry C.M., 2002, ApJ 579, 530

Wandel, A., Peterson, B. M., Malkan, M. A., 1999, ApJ 526, 579

Zamanov, R. & Marziani, P. 2002, ApJL, 571, L77

Zamanov R., Marziani P., Sulentic J.W., et al., 2002, ApJ 576, 9

Zheng, W., Kriss, G. A., Telfer, R. C., Grimes, J. P., & Davidsen, A. F. 1997, ApJ, 475, 469

Zheng, W., Kriss, G. A., Telfer, R. C., Grimes, J. P., & Davidsen, A. F. 1998, ApJ, 492, 855

Zheng X. Z., Xia X. Y., Mao S., Wu H., Deng Z. G., 2002, AJ 124, 18

Chapter 9

From Quasars to Symbiotic stars

9.1 The Physical Drivers of Eigenvector 1: From Quasars to Symbiotic stars

We point out an analogy between two accreting white dwarfs with jets (CH Cyg and MWC 560) and powerful quasars. In spite of the enormous difference in the mass of the central object (a factor $\sim 10^7$), the emission lines are strikingly similar to those of I Zw 1 (the prototype "Narrow Line Seyfert 1" nucleus whose spectrum is widely used as an FeII template for almost all quasars). The spectral similarity give us the unique possibility to consider the optical Eigenvector 1 diagram using objects less massive by a factor of millions. Our results reinforce the interpretation of the "Eigenvector 1 correlations" found for low redshift quasars as driven mainly by the source luminosity to central compact object mass ratio(L/M). The accreting white dwarfs CH Cyg and MWC 560, their jets and emission lines, may well represent the low energy, non relativistic end of the accretion phenomena, which encompass the most powerful quasars and the microquasars. The remarkable similarities suggest that they may be legitimately considered "nano-quasars". The accretion processes have a lot of similarities in spite of the differences in the type and the mass of the accreting object. In the last years a few microquasar sources have been discovered. They are galactic X-ray binaries in which a black hole (BH) or neutron star is accreting from the companion star, producing jets and even superluminal motion (Mirabel & Rodriguez, 1999). The accreting stellar mass compact objects give us a tool to investigate phenomena in active galactic nuclei (AGN) at much lower energy and much shorter time scale.

Our aim here is to show striking similarities between the emission lines of two accreting white dwarfs and the emission lines coming from the broad line region of the active galactic nuclei (AGN), in spite of the mass difference (a typical BH in AGN has a mass $\sim 10^6$–10^9 M_odot and the white dwarf in the interacting binaries ~ 1 M_odot). A comparison between such different objects can give us a better understanding of the accretion/ejection phenomenology, as well as of the so called "Eigenvector 1 correlations" that seem to be fundamental for AGN interpretation. We think it is appropriate to call these two accreting white dwarfs "nano-quasars" because they seem to represent the very low energy analog of quasars and microquasars.

9.1.1 Emission lines similarities

CH Cyg and MWC 560 are interacting binary stars in which a white dwarf accretes matter from the wind of a red giant. Their spectra and the spectrum of I Zw 1 are plotted in Fig. 9.1. I Zw 1 is a "Narrow-Line" Seyfert 1 (NLSy1) nucleus, well known because of his strong $\mathrm{FeII_{opt}}$ emission and relatively narrow lines (FWHM$\sim$1000 km s^{-1}), widely used as template for subtraction of the FeII complex in the Hγ - Hβ region of quasar spectra. In the upper panel of Fig. 9.1 we show the spectral region λ4200–λ4900 Å, and in the middle panel the UV region. The optical spectrum of I Zw 1 was obtained at the 1.52m ESO telescope at La Silla, and the UV was retrieved from the Hubble (HST) archive. The optical spectrum of MWC 560 is the average of the FEROS public archive spectra observed in the period November - December 1998 at ESO (Kaufer et 1999, Schmid 2001). Both optical and UV spectra of CH Cyg were obtained in 1984, when the star underwent jet activity. The optical spectrum of CH Cyg is from the plate archive of the Bulgarian National Astronomical Observatory "Rozhen" (observed on 10 July 1984). The UV spectrum have been retrieved from the International Ultraviolet Explorer database (observed on 23 Jan 1985).

A clear similarity between the emission lines can be seen in Fig. 9.1. Practically almost every emission line visible in the spectrum of I Zw 1 has corresponding features in the spectra of CH Cyg and MWC 560. An obvious similarity is visible also between the UV spectrum of CH Cyg and the one of I Zw 1. We note in passing that similar emission lines are also visible in the spectrum of XX Oph (Kolev & Tomov 1993), where the accreting object is probably a main sequence star (Evans et al. 1993). Despite the general similarity some differences are visible as well. In MWC 560 these are the absorption components in the Balmer lines. These absorptions are due to the jet coinciding with the line of sight (Tomov et al. 1990). They are also dominating the UV spectrum of MWC 560 (not shown here) making it quite different from the ones of CH Cyg and I Zw 1. In the optical spectrum of CH Cyg numerous absorptions due to the photosphere around the white dwarf are visible.

In Fig.9.1 (lower panel) the optical emission line spectra of MWC 560 and CH Cyg are shown after having been continuum subtracted, scaled and broadened. This standard procedure is widely used for the emission line measurements of AGN, using I Zw 1 itself as a template. After this processing, good identity is achieved with the spectrum of I Zw 1. Our best fit corresponds to a width FWHM(FeII_{opt})=970$\pm$90 km s^{-1}.

The hydrogen emission lines as well as the FeII emissions of AGN are emitted from the so-called broad line region (BLR). This region is thought to be within $\lesssim$1 pc from the central BH. Its structure is poorly understood as yet. The clear similarity between the emission lines means that, in objects like MWC 560 and CH Cyg, we are observing a scaled down version of the quasar BLR.

It worth noting that the interacting binaries, in which a white dwarf accretes material from the wind of a red giant (usually classified as symbiotic stars) are strongly variable objects.

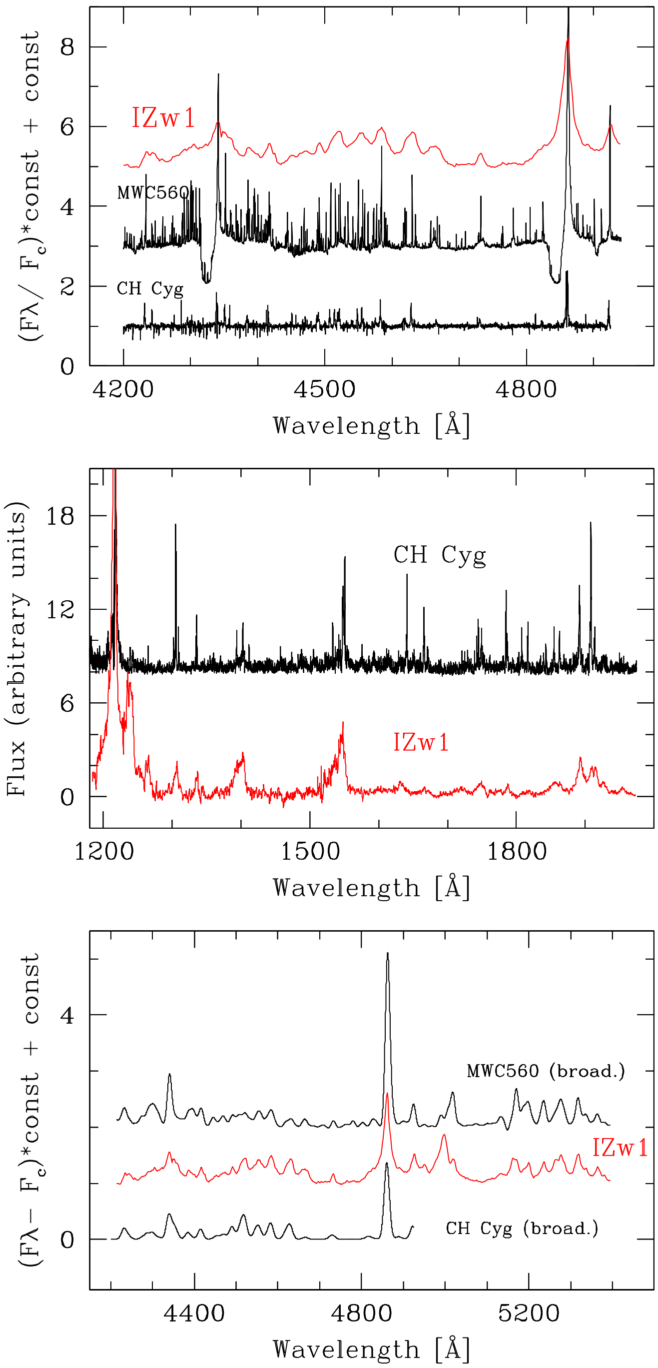

Figure 9.1: A comparison between the spectra of the interacting binaries CH Cyg, MWC 560 and the low redshift quasar I Zw 1. Upper Panel: optical spectra; Middle Panel: the UV region; Lower Panel: the optical spectra of MWC 560 and CH Cyg after broadening and scaling. A clear similarity between the emission lines is visible in all panels.

For CH Cyg and MWC 560 we show that their spectra are similar to low-redshift quasars in moments when jet activity has been detected (see § 9.2.2).

9.1.2 The Eigenvector-1 Diagram

During the last decade, several investigations of AGN emission lines emphasized the importance of a set of correlations conventionally called "Eigenvector-1" (hereafter E1) and related to principal component analysis of the properties of PG quasars Boroson & Green (1992). In the most important diagram associated to E1 (Sulentic 2000), the X-axis is the ratio between the equivalent width of the FeII complex in the range 4434–4684 Å and the equivalent width of the Hβ broad component (H$\beta_{\rm BC}$), namely R$_{FeII}$ = W(FeII)/W(H$\beta_{\rm BC}$). The Y-axis is the FWHM of H$\beta_{\rm BC}$. We measured for CH Cyg W(FeII)=4.5Å, W(Hβ)=5Å, and FWHM(Hβ)=200 km s^{-1}; and for MWC 560 W(FeII)=34Å, W(Hβ)=31Å, and FWHM(Hβ)=110 km s^{-1}.

The diagram is shown in Fig. 9.2. The left panel includes the AGN sample (marked with $\times$ and $+$) of Sulentic et al. (2002). The position of MWC 560 and CH Cyg is marked with open triangles. As could be expected, they are located outside of the AGN population, but close to the NLSy1 galaxies (marked with $+$), which are supposed to have systematically lower BH masses. The diagram of Fig. 9.2 is believed to play for AGN role similar to the one of Hertzsprung-Russell diagram for stars (Sulentic 2001). The physical drivers can be L/M ratio convolved with orientation (Marziani et al. 2001), or L/L$_{Edd}$ ($\propto$ L/M) and BH mass (Boroson 2002). Here we want to use the "nano-quasars" to understand better this correlation space. The "nano-quasars" give us the unique possibility to consider the effect of L/M along with that of varying the mass seven-eight orders of magnitude.

The reverberation mapping studies of the AGN (Kaspi et al 2001) give the following dependence of FWHM(H$\beta_{\rm BC}$) on mass and L/M:

$$FWHM(H\beta) = 4350 \left(\frac{L}{M}\right)_{su}^{-0.35} \left(\frac{M}{M_\odot}\right)^{0.15} \quad km\ s^{-1}, \tag{9.1}$$

where $(L/M)_{su}$ is the luminosity-to-mass ratio in solar units, with the solar value $(L/M)_\odot =$ 1.92 ergs s^{-1} g^{-1}.

The distance of the BLR from the central continuum source is found to depend on bolometric luminosity L:

$$r = 9.36 \times 10^8 \left(\frac{L}{L_\odot}\right)^{0.7} \quad cm\ . \tag{9.2}$$

The ionization parameter can be defined as:

$$U = \frac{Q(H)}{4\pi c r^2 n_e}\ , \tag{9.3}$$

where $Q(H) = fL/h\nu$, is the number of the hydrogen-ionizing photons, r is the distance of the broad line region from the central continuum source, f is the fraction of ionizing photons, ν the average frequency of the ionizing photons, and n_e the electron density. The appearance of the

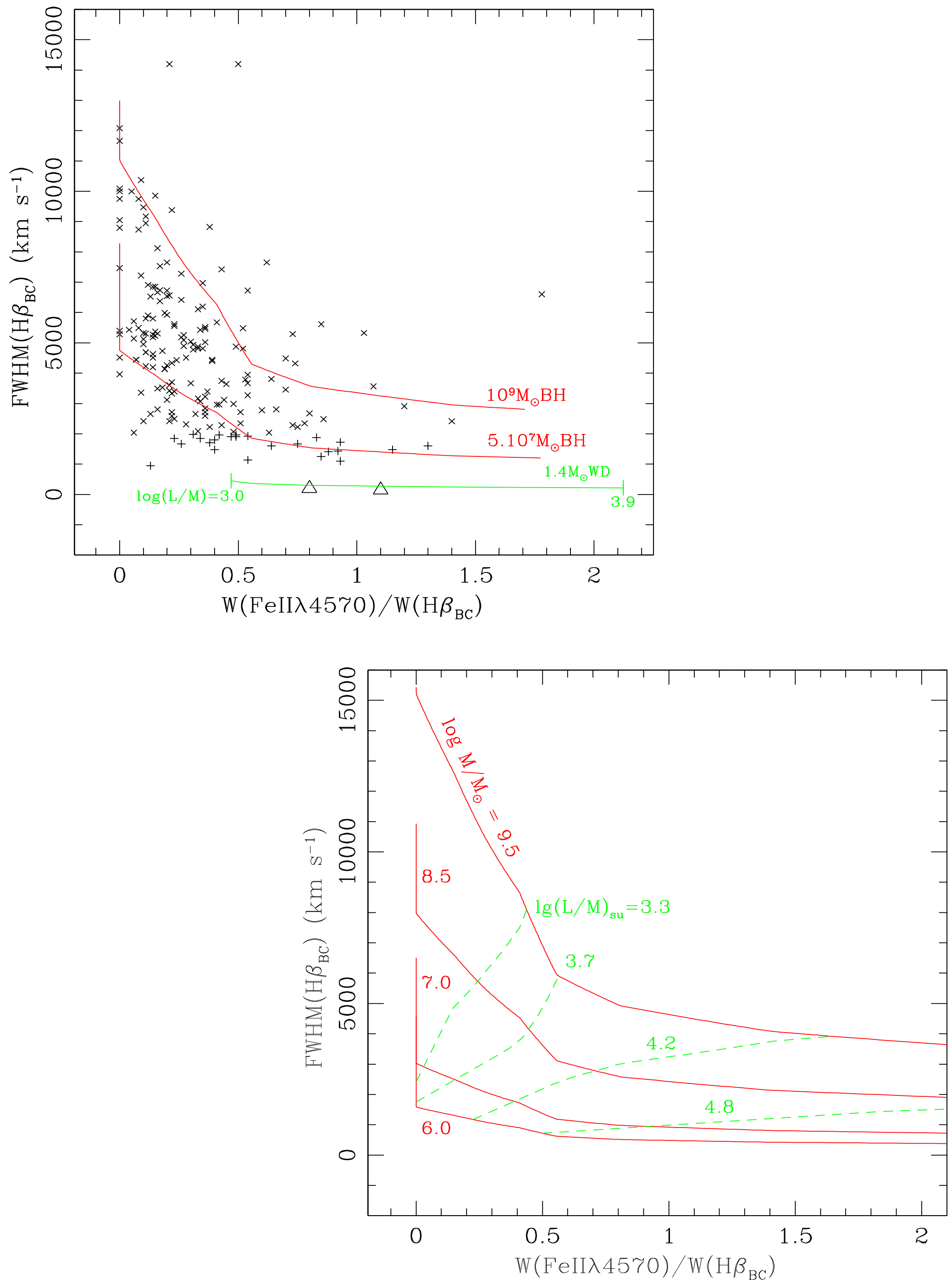

Figure 9.2: The FeII-Hβ Eigenvector-1 diagram. Abscissa is rest frame equivalent width ratio between FeII λ4570 and H$\beta_{\rm BC}$; ordinate is FWHM(H$\beta_{\rm BC}$) in km s^{-1}. Left Panel: AGN from the sample of Sulentic et al. (2002) ($\times$ and +, + refers to NLSy1s), MWC 560 (located at $\rm R_{FeII}$=1.1) and CH Cyg ($\rm R_{FeII}$=0.8) (triangles). The lines are plotted (from top to bottom) for $\rm M_{\it BH}$ = 10^9 M_odot, $\rm M_{\it BH}$ = 5×10^7 M_odot, and white dwarf mass $\rm M_{\it WD}$ = 1.4 M_odot. The line for 1.4 M_odot WD is calculated in the limits $log(L/M)_{su}$ =3.0 - 3.9. Right Panel: Theoretical grid for quasars in the optical E1 diagram. The solid lines are plotted for fixed BH mass $log(M/M_{\odot})$ =9.5, 8.5, 7.0, 6.0. The dashed lines are for fixed L/M ratio $log(L/M)_{su}$ =3.3, 3.7, 4.2, 4.8.

same lines in quasars and in symbiotic stars means that the density in the line emitting region should be similar. A relation connecting n_e and the (L/M)-ratio is (Marziani et al. 2001):

$$n_e = 5.248 \times 10^7 \left(\frac{L}{M}\right)_{su}^{\frac{2}{3}} cm^{-3} . \quad (9.4)$$

Combining the above equations we obtain:

$$U = 3.3 \times 10^6 \, f \, \left(\frac{10^{16} Hz}{\nu}\right) \left(\frac{L}{M}\right)_{su}^{-1.07} M_{su}^{-0.4} \quad (9.5)$$

A typical AGN continuum (Laor et al. 1997) yields $\nu \approx 1.22 \times 10^{16}$ Hz and $f \approx 0.39$. We can then calculate R_{FeII} following Marziani et al. (2001). On the right panel of Fig. 9.2 are shown theoretical lines covering the range of masses expected for AGN, log $(M/M_\odot) \approx 6 - 9.5$.

In symbiotic and symbiotic-like stars the ionizing photons are coming from accreting white dwarf, which effective temperature could be in the range from 6000 K up to $\gtrsim$200 000 K (Mürset & Nussbaumer 1994). In CH Cyg and MWC 560 the UV continuum shape indicates a region of extremely large column density ("cocoon") that obscures the inner disk and the hot white dwarf surface (Michalitsianos et al. 1993). The UV continuum fitting of CH Cyg during the active phase indicate temperature T_{eff}=8500 – 15000 K and temperature is the lowest at the maximum of brightness (Mikolajewska et al. 1988). Because the jet ejection is at the maximum, we will adopt T_{eff}=8500 K corresponding to $f = 1 \times 10^{-5}$ and $\nu = 3.48 \times 10^{15}$ Hz. For MWC 560 there are also no signs for temperature hotter than $15000K$ (Shore et al. 1994), and even the column density of the absorbing material is higher than in CH Cyg (Michalitsianos et al. 1993).

The resulting FWHM(Hβ) vs. R_{FeII} is plotted in Fig. 9.2. On the left panel the lines are for masses $M_{BH} = 5 \times 10^8 \ M_o dot$, $M_{BH} = 10^7 \ M_o dot$, and white dwarf mass $M_{WD} = 1.4 \ M_o dot$. We adopted f and ν following the above considerations. The L/M ratio was running in the limits $\log(L/M)_{su}$ =2.5 – 4.4 for $M_{BH} = 1 \times 10^9 \ M_o dot$, $\log(L/M)_{su}$ =2.5 – 4.9 for $M_{BH} = 10^7 \ M_o dot$, and $\log(L/M)_{su}$ =3.0-3.9 for $M_{WD} = 1.4 \ M_o dot$.

The total luminosity of the white dwarf of CH Cyg during the time of jet ejection in 1984 is L $\lesssim$1600 $L_\odot$ (Mikolajewska et al 1988) and that of MWC 560 is L≈1000 $L_\odot$ (Schmid et al. 2001). Assuming a typical white dwarf mass in symbiotic stars of $M_{WD} = 1.0 - 1.4 \ M_\odot$ (or total mass of the binary system about 3-5 $M_\odot$), we obtain $(L/M)_{su} \approx 10^3$ in agreement with parameters used to plot the lowest line in Fig. 9.2 (left panel).

If we use higher effective temperature for the ionizing continuum (i.e. $T_{eff} = 15\,000^0 K$ corresponding to $f = 6.61 \times 10^{-3}$ and $\nu = 3.66 \times 10^{15}$ Hz) to have reasonable results from Eq. 9.5 we need to go to stronger dependence like to $U \propto (L/M)^{-(1+x)} M^{-1}$ with x up to $x \approx 0.67$ (more details are given in Marziani et al. 2001). This points out that the number of ionizing photons and the shape of the UV and X-ray continuum are important in the E1 correlations. It is worth noting that the soft X-ray photon index is the third axis in E1 diagrams of Sulentic et al. (2000, 2001). The line widths, FWHM(Hβ)=100 km s^{-1} for MWC 560 and FWHM≈200 km s^{-1} for CH Cyg, are a little bit smaller than expected from Eq. 9.1, which predicts values around

300-400 km s^{-1}. It is also possible that the luminosity of CH Cyg and MWC 560 was lower (i.e. 100-500 $L_{\odot}$) at the time the spectra were obtained, if the distances used in the calculations are too large. We regard the agreement acceptable, considering the huge difference in masses and the limited range of luminosity and masses from which the relationships of Kaspi et al. (2000) and Marziani et al. (2001) were derived. The white dwarfs have lower efficiency of accretion ($\eta \approx 10^{-4}$) than expected for typical AGN ($\eta \approx 10^{-1} - 10^{-2}$). The used equations give good results without considering the effect of efficiency. This is in agreement with the interpretation of the E1 as mainly driven by L/M ratio. Efficiency, along with several other parameters, may have some (minor) influence.

Following the above equations and Fig. 9.2, a change in mass by a factor $\sim 10^7$ times changes FWHM(Hβ) by a factor $10 - 50$. A change in mass by a factor 50 (from 10^7 to $5{\times}10^8$ $M_o dot$, in the range expected for BH masses of low redshift quasars) leads to a FWHM(Hβ) change by a factor 2-3. In a sample of quasars with a limited BH mass spread, mass change may lead to second order effect which may even be smaller than the the effect of orientation (Marziani et al. 2001).

9.2 White dwarfs with jets as non-relativistic analogues of quasars and microquasars

Abstract: We explore the similarities between accreting white dwarfs (CH Cyg and MWC 560) and the much more energetic jet sources - quasars and microquasars. To-date we have identified several common attributes: (1) they exhibit collimated outflows (jets); (2) the jets are precessing; (3) these two symbiotic stars exhibit quasar-like emission line spectra; (4) there is a disk-jet connection like that observed in microquasars. Additionally they may have a similar energy source (extraction of rotational energy from the accreting object). Study of the low energy analogues could have important implications for our understanding of their higher energy cousins.

Emission line similarities As illustrated in Zamanov & Marziani (2002), there are striking similarities between the optical spectra of Active Galactic Nuclei (AGNs) and two accreting white dwarfs. Almost every emission line visible in the AGN spectrum of I Zw 1 shows a corresponding feature in the spectra of CH Cyg and MWC 560. The similarity between the UV spectrum of CH Cyg and I Zw 1 is demonstrated in Fig.9.1.

In AGN, hydrogen and FeII emission lines are emitted from the so-called Broad Line Region. This region is thought to lie within <1 pc of the central black hole. Its structure is still poorly understood. The clear similarity between the emission lines suggests that we are observing a scaled down version of the quasar Broad Line Region in galactic objects like MWC560 and CH Cyg (see also Zamanov and Marziani, 2002).

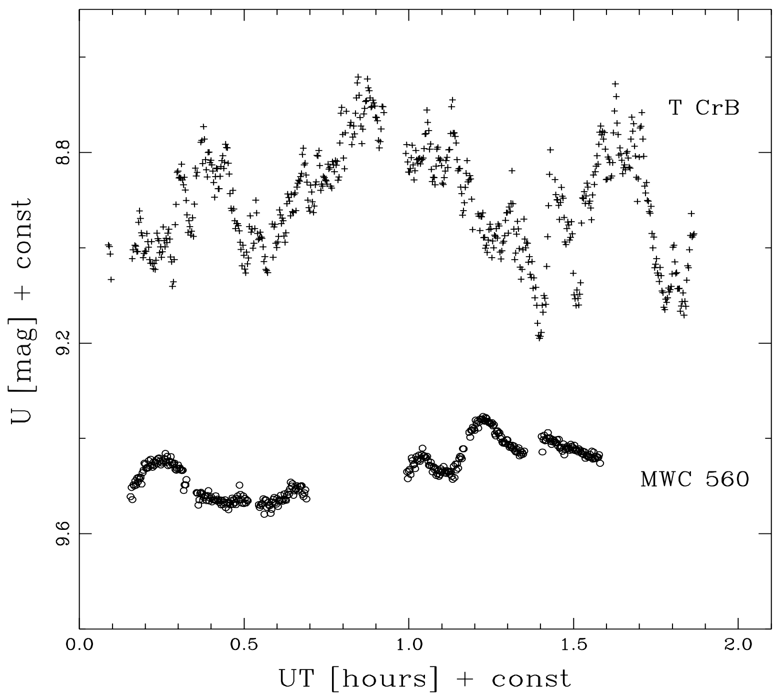

Figure 9.3: The flickering behaviour of MWC 560 and T CrB in Johnson U band. In the case of MWC 560, the short term variability (on a time scale of minutes) is missing. The observational errors are less or equal to the size of the symbols.

9.2.1 Disk-Jet connection and Precessing jets

Comparison of the flickering behaviour of T CrB (February 28, 1995) and MWC 560 (March 05, 1990) is shown on Fig. 9.3. In the case of MWC 560, the short term variability (on a time scale of minutes) is missing. Only smooth, hour-timescale variations are present. This indicates disruption of the inner part of the accretion disk during the time of jet ejection. A disruption of the inner disk (disk-jet) connection is also observed in CH Cyg (Sokoloski & Kenyon 2003). The behaviour is closely analogous to that of the microquasar GRS1915+105. This supports the view that there may be a common mechanism for jets in quasars, microquasars and symbiotic stars (see also Livio, Pringle & King 2003).

Precessing jets: The best known precessing jets in astrophysics are probably those of SS 433. In recent years precessing jets have been identified in two symbiotic stars: CH Cyg (on the basis of radio imaging by Crocker et al. 2002) and MWC 560 (from optical spectroscopy by Iijima 2002). In both cases the model of the jets of the microquasar SS 433 has been adopted to fit the evolution of the morphology of the outflows (using velocities appropriate for white dwarfs).

9.2.2 Energy Source of Jets

It is worth noting that interacting binaries, where a white dwarf accretes material from the wind of a red giant (usually classified as symbiotic stars), are strongly variable objects. We show above that the spectra of CH Cyg and MWC 560 are similar to low-redshift quasars around the times when jet activity is detected (CH Cyg - July 1984, MWC 560 - November 1990).

Jets are detected in systems quite different from those harboring black holes (for a review see Livio, 2001): young stellar objects (velocity v$\sim$200 km s^{-1}), planetary nebulae (v$\sim$200-1000 km s-1), supersoft X-ray sources (v$\sim$1000 km s^{-1}). The jet velocities observed in the accreting white dwarfs (we call them *"nanoquasars"*) are $\sim$1000 km s^{-1} in CH Cyg (Taylor et al. 1986) and 1000-6000 km s^{-1} in MWC 560 (Tomov et al. 1992). They are consistent with an overall picture in which the jet velocity is of the same order as the escape velocity from the accretor (Livio 2001).

The luminosities of MWC 560 and CH Cyg are considerably less than the Eddington limit. The mass accretion rate is about $M_{acc} \sim 0.05\ M_{Edd}$. At such mass accretion rates the most probable jet energy source involves extraction of rotational energy from the compact object. In the case of nano-quasars the extraction is probably occurring via the propeller action of a magnetic white dwarf (Mikolajewski et al. 1996). The most probable source of jet formation in quasars is the extraction of energy and angular momentum via the Blandford and Znajek (1977) mechanism. In this sense the jets in the "nanoquasars" probably represent a low energy (non-relativistic) analogue of the jets in quasars and microquasars. They involve a similar energy source - the extraction of rotational energy from the central compact object.

9.3 Conclusions and References

We think it is appropriate to call the two accreting white dwarfs discussed here "nanoquasars" because they represent the very low energy analogue of quasars and microquasars. The name is chosen by analogy with the quasar and microquasar denominations, and also because $\nu\alpha\nu o\varsigma$ (ancient greek) = nano (ital.) = dwarf(engl.).

We showed a clear similarity between the emission line spectra of the accreting white dwarfs CH Cyg and MWC 560 and low redshift quasars. Their jets may be have a similar energy source - the rotational energy of the central object. The discussed similarities have been used in this paper to aid the interpretation of the E1 diagrams for AGN. Their position in the diagram confirms the interpretation that the physical driver of the Boroson & Green's E1 is primarily the L/M ratio, and that the mass of the accreting object also plays a role. We could call the accreting white dwarfs with jets and with AGN-like spectra "nano-quasars", by analogy with the quasar and microquasar denomination (also, $\nu\alpha\nu o\varsigma$ in ancient Greek means dwarf).

In the future, the spectral similarity discussed here could be used to better understand the conditions and the structure of the BLR of quasars, and to identify numerous emission lines in the spectrum of I Zw 1 (and by extension, of the wide majority of AGN that show a $\mathrm{FeII_{opt}}$ spectrum almost identical to the one of I Zw 1). The FWHM of emission lines in AGN is $\geq$1000, which makes most $\mathrm{FeII_{opt}}$ lines blended together. In accreting white dwarfs the FWHM is a factor of ten less, making possible to identify weak lines. The diversity of symbiotic binaries properties could be used to test and to "calibrate" AGN correlations, using objects with well known mass. It will be very useful to detect a stellar mass black hole (i.e., a galactic microquasar) with similar emission lines. Discovery of an interacting binary in which a black hole accretes from the wind of a red giant will be extremely interesting, although very difficult to find from an evolutionary point of view.

Ultimately, the nano-quasars could be an important chain link in our understanding of all accreting sources. They could help us to create an unified picture of all accreting objects from cataclysmic variables and stellar-mass black holes up to the most powerful quasars.

9.4 References to Chapter 9

Blandford R., & Znajek R., 1977, MNRAS 179, 433
Boroson T.A., Green R.F., 1992, ApJS 80, 109
Boroson T., 2002, ApJ 565, 78
Crocker et al., 2002, MNRAS 335, 1100
Fender R., 2001, ApSSS 276, 69
Evans A., Albinson J.S., Barrett P., 1993, A&A 267, 161
Iijima, T., 2002, A&A 391, 617
Kaspi S., Smith P.S., Netzer H., Maoz D., Jannuzi B.T., Giveon U., 2000, ApJ 533, 631
Kaufer A., Stahl O., Tubbesing S., 1999, The ESO Messenger 95, 8
Kolev D., Tomov T., 1993, A&AS 100, 1
Laor A. Fiore F., Elvis M., Wilkes B.J., McDowell J.C., 1997, ApJ 477, 93
Livio M., 2001, ASP Conf. 224, 225
Livio M., Pringle J.E., King A.R., 2003, ApJ 593, 184
Margon B., 1984, ARA&A 22, 507
Marti J., Paredes J.M., Peracaula M., 2001, A&A 375, 476
Marziani P., Sulentic J.W., Zwitter T., Dultzin-Hacyan D., Calvani M., 2001, ApJ 558, 553
Michalitsianos A.G., et al., 1993, ApJ 409, 53
Mirabel I.F., Rodriguez L.F., 1994, Nature 371, 46
Mirabel I.F., Rodriguez L.F., 1999, ARA&A 37, 409
Mikolajewska J., Selvelli P.L., Hack M., 1988, A&A 198, 150
Mikolajewski M., Milkolajewska J., Tomov T.,IAU Symp 165, p. 451
Mürset U., Nussbaumer H., 1994, A&A 282, 586
Sulentic J.W., Marziani P., Dultzin-Hacyan D., 2000, AR A&A 38, 521
Sokoloski J. & Kenyon S., 2003, ApJ 584, 1021
Sulentic J.W., Calvani M., Marziani P. 2001, ESO Messanger 104, 25
Schmid H.M., Kaufer A., Camenzind M., Rivinius Th., 2001 A&A 377, 206
Shore S.N., Aufdenberg J.P., Michalitsianos A.G., 1994, AJ 108, 671
Taylor A.R., Seaquist E.R., Mattei J.A., 1986, Nature 319, 38
Tomov T., Kolev D., Georgiev L., Zamanov R., Antov A., Bellas Y., 1990, Nature 346, 637
Tomov T., Zamanov R., Kolev D., Georgiev L., Antov A., Mikolajewski M., Esipov V., 1992, MNRAS 258, 23
Zamanov, R., Marziani, P., 2002, ApJ 571, L77

Chapter 10

Conclusions

10.1 Results

The results presented here are based on observations obtained on the following teslescopes:

- 2.0m RCC telescope, 60 cm, and 50/70 cm Schmidt telescope of the National Astronomical Observatory Rozhen of Bulgarian Academy of Sciences,
- 60cm telescope of the Belogradchick Astronomical Observatory (Bulgaria)
- 2.2m and 3.6m telescopes of the European Southern Observatory (La Silla)
- 1.82m telescope of Asiago Observatory (Italy)
- 1.23m and 1.52m telescopes of Calar Alto (The German-Spanish Astronomical Center at Calar Alto)
- 2.0m Liverpool telescope on La Palma
- 1.2m telescope of Observatory of Heute Provance (France)
- VLT telescope of European Southern Observatory (La Paranal).

  We also used observations from the archives of VLT/UVES, ELODIE (France), Isaac Newton Group of telescopes (ING), Green Bank Interferometer (USA).

The most important results are:

Chapter 2: We performed systematic observations of the recurrent nova T CrB using the 2m and 60cm telescopes of NAO Rozhen.

- We obtained 47 spectra in 5 nights of the recurrent nova T CrB with time resolution 10–20 minutes. On two from five nights we detected statistically significant variability in the central part of the Hα emission line profile.

- We obtained 22 spectra of the HeIIλ4686 line. We conclude, that the appearance of the HeII emission in T CrB is connected with U band variability and with epochs of higher mass accretion rate.

- We secured 95 UBV estimates and 27 patrol (2349 min in total) observations in U band. during the period 1993-2004, when the brightness of the object varied in between U=13 and U=10 mag. The analyses we performed show that: **(1)** the V brightness during the last 22 years is dominated by the ellipsoidal variability of the red giant, however the hot component variability with $\Delta U \gtrsim 2$ mag, introduces a shift in V with about 0.15 mag. No signs of variability of the red giant has been detected. **(2)** the power spectrum and the e-folding time of the ACF do not change during our observations, remaining always with slope $\gamma \approx -1.5$ in spite of the changes in U. **(3)** Having subtracted the contribution of the red giant, we show that the flickering amplitude correlates with the average flux of the accreting component. A comparison with CH Cyg and MWC 560 indicates that the flickering of T CrB is more stable than that in the jet-ejecting symbiotic stars.

We argue that the presence of an accretion disc can account for most of the observed properties of T CrB. The long-term variability is (probably) caused by variations of the mass transfer rate or disk instability.

Chapter 3: We investigated the Hα and HeIIλ4686 emission lines of the recurrent nova RS Oph on base of spectra obtained on 2.2m telescope of ESO and FEROS spectrograph. We detected variability of Hα on time scale $\sim$ 1 month, which is due to ejther blobs or accretion disk wind.

We discovered that the flickering of RS Oph disappeared after the 2006 outburst.

We performed observations of the flickering variability of the recurrent nova RS Oph at quiescence on the basis of simultaneous observations in 5 bands ($UBVRI$). We derived the colours of the flickering source, its temperature, size and luminosity.

We also find that on a $(U-B)$ vs $(B-V)$ diagram the flickering of the symbiotic stars differs from that of the cataclysmic variables.

Chapter 4: We have observed 42 S– and D'-type symbiotic stars with the FEROS spectrograph at 2.2m telescope ESO and measured the projected rotational velocities of the mass donors.

- For the D'-type (yellow) symbiotics, 5 out of the six southern D'-type SSs are the fastest or among the fastest rotators in their spectral classes. At least four of them rotate at a substantial fraction (> 0.5) of the critical velocity.

- In our sample of 17 Stype symbiotics with known orbital periods, 9 are synchronized within the measurement errors ($1-\sigma$ level) and 15 objects are synchronized within the $3-\sigma$ level.

- The symbiotic K giants included in our survey rotate on average more than twice as fast as the field K giants.

- The M giants in symbiotics are more rapid rotators than most of the field M giants.
- The rapid rotation is the (likely) reason for their larger mass loss rates. We find suggestions that in the jet-ejecting symbiotics the mass donors rotate faster than the orbital periods.

Chapter 5: We performed UBV photometry of FY Per – $07h15m$ patrol observations and 5 UBV estimates in total. We did not confirm the supposition for variability on a time scale of 1 hours. For ZZ CMi we obtained 14 UBV estimates. For X Per our 24 UBV estimates demonstrated a clear similarity between the light maxima in 1987-1988 and 1993-1994. For V4641 Sgr we detected variability on time scale ∼hours.

Chapter 6: We present the results of analyzing Hα spectra of the radio emitting X-ray binary LSI+$61^0$303. For the first time, the same 26.5 d radio period is clearly detected in the Hα emission line. Moreover, the equivalent width and the peak separation of the Hα emission line vary over a time scale of 1600 days. The signs of 4.5 years modulation are visible in Hα, even during the time of lower equivalent width of Hα. This points towards the ~ 4 yr modulation, detected in the radio outburst amplitude, being probably a result of variations in the mass loss rate of the Be star and/or density variability in the circumstellar disk.

The dependence of the peak separation from the equivalent width informs us that the LSI+$61^0$303 circumstellar disk is among the densest of Be-stars.

A remarkable correlation between the Hα emission line and the radio behaviour of LSI+$61^0$303 over its 4 yr modulation is discovered. The radio outburst peak is shifted by a quarter of the 4 yr modulation period (about 400 days) with respect to the equivalent width of the Hα emission line variability. The onset of the radio outbursts varies in phase with the changes of the Hα emission line, at least during the increase of Hα equivalent width.

This is the first clear correlation between the emission associated to the compact object and the Be circumstellar disk in a Be/X-ray binary system.

Chapter 7: From our comparative study between the Hα emission lines of Be/X-ray binaries and those of isolated Be stars we find that:

- The envelops in the Be/X-ray binaries are axisymmetric and rotationally supported as in isolated Be stars.
- The line broadening is similar in the isolated Be stars and the Be/X-ray binaries.
- The circumstellar disks in Be/X-ray binaries are, on average, two times denser than those in isolated Be stars.
- The circumstellar disks are smaller and denser in Be/X-ray binaries than in isolated Be stars, most likely truncated by the compact object.

Chapter 8: We investigated a sample of 278 active galactic nuclei. We created average spectra around Hβ line in various bins.

We identified AGNs with blue shifted [OIII]λ5007 andinvestigate their nature. We find that these objects are AGNs with high accretion rate and viewed almost pole-on.

Chapter 9: We showed a clear similarity between the emission line spectra of the accreting white dwarfs CH Cyg and MWC 560 and low redshift quasars. The position of these two white dwarfs in the Eigenvector-1 diagram confirms that the physical drivers of the Boroson & Green's Eigenvector-1 are primarily the luminosity-to-mass ratio and the mass of the accreting object.

10.2 Future plans

Our future plans include:

- regular observations of interacting binary stars

- high resolution observations of northern and fainter symbiotics to expand our results on mass rotation of the mass donors

- multi-color observations of the flickering

- investigation of the flickering amplitude in symbiotic stars and cataclysmic variable

- regular spectroscopic observations of LS I+61°303 and search for correlation between variability of the circumstellar disk and gamma-rays (MAGIC data)

- investigation of the rotation of the mass donors and synchronization in High Mass X-ray binaries

- search for similarities in the accretion onto white dwarfs, neutron stars, black holes.

- search for similarities in ejection of matter from white dwarfs, neutron stars, stellar mass black holes, massive black holes.

Acknowledgements

The investigations presented here have been done mainly in:

- National Astronomical Observatory Rozhen, Bulgaria (1989 March - 2005),
- University of Jaen, Spain (October 1999 - June 2000),
- Padova Astronomical Observatory, Italy (2001 March - 2003 April),
- Liverpool John Moores University, UK (2003 - 2005),
- Institute of Astronomy, Sofia, Bulgaria (2005 – 2009).

Many thanks to all the staff of these academic institutions.

I am very grateful to:

- my first teachers in astronomy in People Astronomical Observatory in town of Stara Zagora – B. Bonev, P. Gancheva and Alexei Stoev.
- All my teachers in the University of Sofia "Kl. Ohridski" and especially to my supervisor Prof T. Tomov.
- Dr. N.A. Tomov (NAO Rozhen) for the numerous observations.
- Dr Paola Marziani and Prof Massimo Calvani (Padova, Italy) for giving me the chance to do a postdoc in Italy and the collaboration in the field of AGNs.
- Prof Mike Bode (Liverpool John Moores University, UK) for the chance to work in UK and for our fruitful collaboration in the field of symbiotic stars. **Thank you very much Mike!**
- Prof Josep Marti (University of Jaen, Spain) for our cooperation in the study of the Be/X-ray binaries. **Muchas gracias Josep!**
- The late Dr John M. Porter for the vital contribution to our succeful proposals.

Many thanks to my co-authors Claudio Melo (ESO), Rumen Bachev (Sofia), I. Stateva (Sofia), Andreja Gomboc (Ljubljana, Slovenia), J.M. Paredes (Barcelona, Spain), J. Fabregat (Valencia, Spain), A. Tarasov (Crimea, Ukraine), Albert Bruch (Germany), Pablo Reig (Spain) and many others. Without them the results presented here would be impossible to be obtained.

Appendix A

Symbiotic stars

Here we give a few examples of our spectra of symbiotic stars (Fig. A.1) and our UBV observations of T CrB.

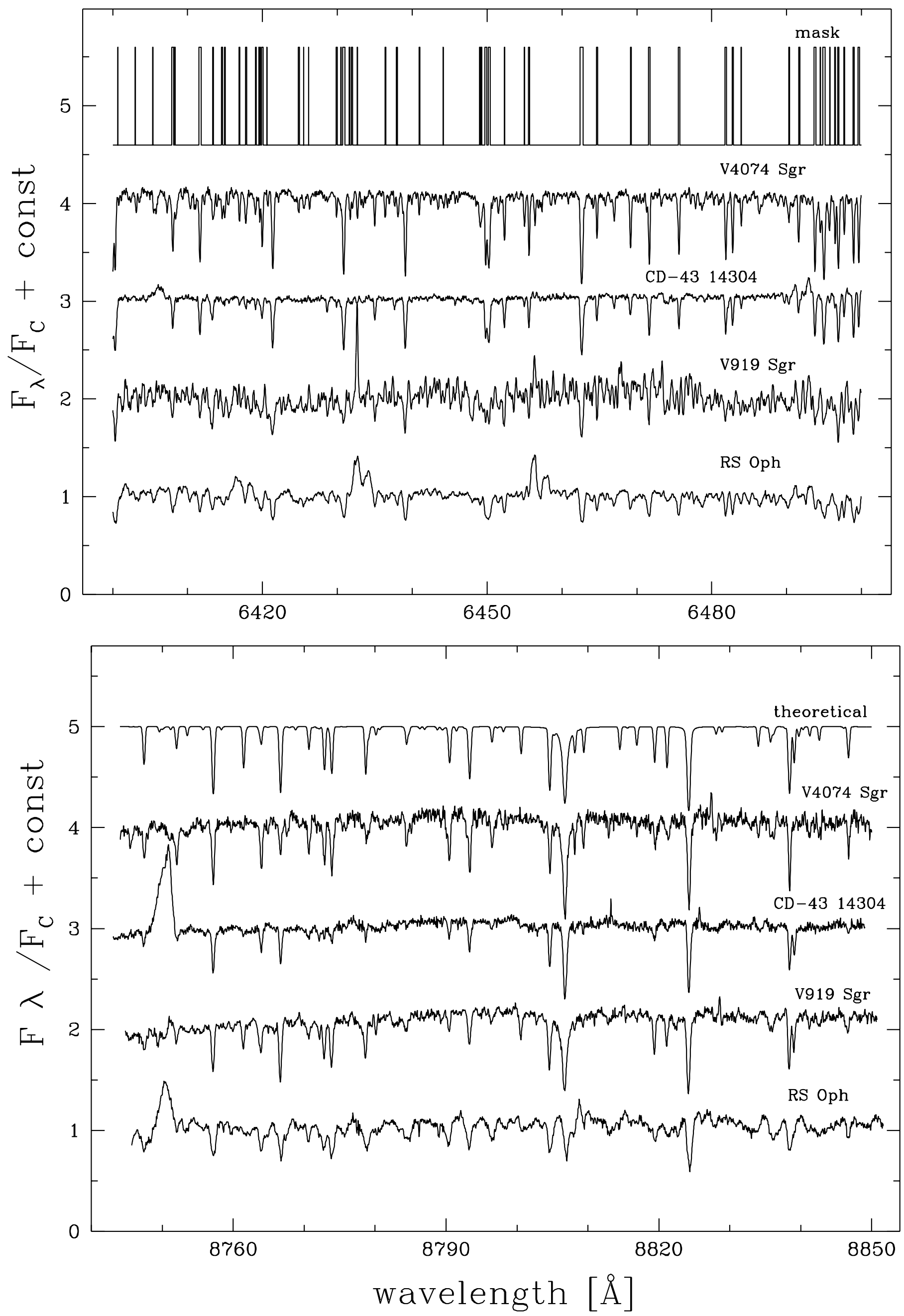

Figure A.1: A few examples of our spectra, together with the mask in the interval $\lambda\lambda 6400-6500$ Å(upper panel), and with a synthetic spectrum in the interval $\lambda\lambda 8740-8850$ Å. The spectra are plotted in increasing order of rotation: V4074 Sgr (M4III, $v \sin i$=3.5 km s^{-1}), CD-43°14304 (K5III, $v \sin i$=7.2 km s^{-1}), V919 Sgr (M2III, $v \sin i$=9.1 km s^{-1}), RS Oph (M0III, $v \sin i$=11.7 km s^{-1}). The synthetic spectrum corresponds to M0III and $v \sin i$=5 km s^{-1}.

Table A.1: UBV observations of T CrB.

JD-2400000	V	B	U	JD-2400000	V	B	U
48321.44	10.40	11.80	12.17	50652.325	9.820	10.919	10.714
49046.57	10.11	11.65	12.57	50652.329	9.785	10.919	10.730
49046.60	10.08	11.62	12.46	50654.307	9.844	10.948	10.766
49047.54	10.09	11.60	12.28	50654.311	9.733	10.908	10.811
49104.53	10.24	11.48	11.60	50698.295	10.146	11.298	11.089
49106.45	10.25	11.43	11.38	50698.301	10.142	11.269	10.979
49195.32	10.25	11.86	13.07	50739.236	9.946	10.960	10.655
49197.32	10.26	11.82	12.93	50739.242	9.943	11.075	11.105
49452.51	10.40	11.93	12.73	50741.222	9.773	10.777	10.349
49520.40	10.01	11.54	12.84	50741.227	10.036	11.950	12.671
49572.32	10.44	12.00	12.92	50828.591	10.213	11.245	11.087
49573.29	10.44	11.96	12.74	50828.595	10.188	11.217	11.144
49597.27	10.23	11.72	12.33	50864.466	10.104	11.346	11.600
49598.29	10.21	11.70	12.34	50864.470	9.852	11.226	11.508
49882.33	10.16	11.53	11.91	50865.491	10.015	11.294	11.476
49889.34	10.19	11.64	12.15	50865.499	9.993	11.280	11.406
49929.37	10.16	11.52	11.84	50867.519	9.974	11.322	11.550
49930.39	10.17	11.50	11.68	50867.523	9.958	11.313	11.484
49994.23	10.16	11.52	11.86	50877.603	9.974	11.373	11.658
50092.66	10.08	11.51	12.08	50877.609	10.023	11.387	11.660
50141.64	10.23	11.31	11.11	50877.620	10.023	11.414	11.773
50142.57	10.29	11.56	11.64	51005.484	9.841	10.828	11.412
50167.52	10.19	11.65	12.27	51005.485	9.853	10.833	11.371
50192.39	9.90	11.04	11.17	51007.487	10.095	11.390	11.691
50267.36	10.03	11.19	10.97	51007.493	10.074	11.415	12.143
50268.36	10.01	11.15	10.85	51008.310	10.090	11.440	11.715
50297.30	9.88	11.10	11.18	51008.314	10.062	11.393	11.681
50393.18	10.19	11.44	11.49	51009.304	10.026	11.318	11.574
50433.66	9.84	11.13	11.24	51009.308	10.072	11.403	11.720

Table A.1: Continuation

JD-2400000	V	B	U	JD-2400000	V	B	U
50435.66	9.87	11.16	11.28	51015.323	10.055	11.343	11.526
50476.655	10.309	11.570	11.568	51015.327	10.073	11.353	11.442
50476.659	10.311	11.564	11.620	51016.308	10.080	11.387	11.566
50477.556	10.299	11.476	11.367	51016.313	10.086	11.395	11.643
50477.559	10.280	11.507	11.496	51027.320	10.124	11.412	11.531
50478.580	10.276	11.490	11.363	51027.324	10.160	11.413	11.497
50478.583	10.274	11.446	11.314	51034.298	10.215	11.468	11.602
50479.660	10.315	11.558	11.515	51034.302	10.231	11.470	11.583
50479.663	10.311	11.579	11.517	51226.574	9.848	11.063	11.085
50480.651	10.322	11.693	11.780	51226.582	9.911	11.167	11.328
50480.654	10.370	11.615	11.639	51239.592	10.041	11.356	11.555
50504.566	10.198	11.558	11.850	51239.597	10.012	11.303	11.387
50504.572	10.162	11.425	11.676	51401.292	10.054	11.095	10.714
50520.518	10.025	11.456	12.039	51401.297	10.019	11.040	10.637
50520.524	10.040	11.433	11.970	51404.314	10.224	11.539	11.637
50628.448	9.982	11.084	10.809	51404.318	10.274	11.649	11.787
50628.453	9.972	11.048	10.766	51408.289	10.249	11.712	12.123
50651.337	9.911	11.184	11.319	51408.294	10.267	11.689	12.070
50651.342	9.906	11.191	11.328				

Appendix B

Abbreviations

Here we give abbreviations used in this work:
EW – equivalent width
BH – black hole
NS – neutron star
WD – white dwarf
RG – red giant
CV – cataclysmic variable
KS-test – Kolmogorov-Smirnov test
FWHM – full width at half maximum
AGN – active galactic nucleus
AD – accretion disk
TVS – temporal variance spectra
SS – symbiotic star
RV – radial velocity
L_1 – inner Langrangian point
M – mass
L/M – luminosity to mass ratio
M_B – absolute magnitude in B band
blue outliers – AGNs with blue shifted [OIII] lines
RL – radio loud AGN
RQ – radio quiet AGN
E1 – Eigenvector 1
ACF – autocorrelation function
FEROS – The Fiber-fed Extended Range Optical Spectrograph (ESO, La Silla)
UVES – Ultraviolet and Visual Echelle Spectrograph of the VLT
ELODIE – cross-dispersed echelle spectrograph (OHP, France)

ISAAC – ISAAC is an IR imager and spectrograph (ESO)
VLT – The ESO Very Large Telescope
ESO – European Southern Observatory
OHP – Haute-Provence Observatory, France

Appendix C

Publications

This dissertation is based on more than 50 papers.

Refereed articles:

1. Zamanov et al.(2010) 2010MNRAS.404..381
   R. K. Zamanov, S. Boeva, R. Bachev, M. F. Bode, D. Dimitrov, K. A. Stoyanov, A. Gomboc, S. V. Tsvetkova, L. Slavcheva-Mihova, B. Spassov, K. Koleva, B. Mihov, 2010 MNRAS 404, 381
   UBVRI observations of the flickering of RS Ophiuchi at Quiescence

2. Zamanov et al.(2010) 2010AN....331..282
   R. K. Zamanov, A. Gomboc, K. A. Stoyanov, I. K. Stateva, 2010, AN, 331, 282 arXiv:0910.5621
   Orbital eccentricity of the symbiotic star MWC 560

3. Stoyanov & Zamanov (2009) 2009AN....330..727S
   K. A. Stoyanov, R. K. Zamanov, 2009, AN, 330, 727
   Tidal Interaction in High Mass X-ray Binaries

4. Zamanov et al.(2008) 2008MNRAS.390..377Z
   Zamanov, R. K., Bode, M. F., Melo, C. H. F., Stateva, I. K., Bachev, R., Gomboc, A., Konstantinova-Antova, R., & Stoyanov, K. A. 2008, MNRAS, 390, 377
   Rotational velocities of the giants in symbiotic stars - III. Evidence of fast rotation in S-type symbiotics

5. Zamanov et al.(2007) 2007MNRAS.380.1053Z
   Zamanov, R. K., Bode, M. F., Melo, C. H. F., Bachev, R., Gomboc, A., Stateva, I. K., Porter, J. M., & Pritchard, J. 2007, MNRAS 380, 1053

Rotational velocities of the giants in symbiotic stars - II. Are S-type symbiotics synchronized?

6. Zamanov et al.(2007) 2007IBVS.5776....1Z
Zamanov, R. K., Stoyanov, K. A., & Tomov, N. A. 2007, Information Bulletin on Variable Stars, 5776, 1
Hα observations of the Galactic Microquasar LSI+$61^0$303

7. Zamanov et al.(2006) 2006IBVS.5733....1Z
Zamanov, R., Boer, M., Le Coroller, H., & Panov, K. 2006, Information Bulletin on Variable Stars, 5733, 1
Photometry of RS Oph after the 2006 Outburst

8. Sulentic et al.(2006) 2006RMxAA..42...23S
Sulentic, J. W., Dultzin-Hacyan, D., Marziani, P., Bongardo, C., Braito, V., Calvani, M., & Zamanov, R. 2006, Revista Mexicana de Astronomia y Astrofisica, 42, 23

9. Zamanov et al.(2006) 2006MNRAS.365.1215Z
Zamanov, R. K., Bode, M. F., Melo, C. H. F., Porter, J., Gomboc, A., & Konstantinova-Antova, R. 2006, MNRAS, 365, 1215
Rotational velocities of the giants in symbiotic stars - I. D'-type symbiotics

10. Zamanov et al.(2005) 2005MNRAS.363L..26Z
Zamanov, R. K., Bode, M. F., Tomov, N. A., & Porter, J. M. 2005, MNRAS, 363, L26
Emission line variability of RS Ophiuchi

11. Zamanov et al.(2005) 2005PASP..117..268Z
Zamanov, R., Gomboc, A., Bode, M. F., Porter, J. M., & Tomov, N. A. 2005, PASP, 117, 268
Rapid Hα Variability in T Coronae Borealis

12. Sulentic et al.(2004) 2004A&A...423..121S
Sulentic, J. W., Stirpe, G. M., Marziani, P., Zamanov, R., Calvani, M., & Braito, V. 2004, A&A, 423, 121 VLT/ISAAC spectra of the Hβ region in intermediate redshift quasars

13. Zamanov et al.(2004) 2004MNRAS.350.1477Z
Zamanov, R., Bode, M. F., Stanishev, V., & Martí, J. 2004, MNRAS, 350, 1477
Flickering variability of T Coronae Borealis

14. Martí et al.(2004) 2004A&A...418..271M
Martí, J., Luque-Escamilla, P., Garrido, J. L., Paredes, J. M., & Zamanov, R. 2004, A&A, 418, 271

15. Stanishev et al.(2004) 2004A&A...415..609S
Stanishev, V., Zamanov, R., Tomov, N., & Marziani, P. 2004, A&A, 415, 609
Hα variability of the recurrent nova T Coronae Borealis

16. Zamanov et al.(2004) 2004IBVS.5497....1Z
Zamanov, R., Bode, M. F., & Tomov, N. A. 2004, Information Bulletin on Variable Stars, 5497, 1
HeII λ4686 observations of T Coronae Borealis

17. Marziani et al.(2003) 2003MNRAS.345.1133M
Marziani, P., Zamanov, R. K., Sulentic, J. W., & Calvani, M. 2003, MNRAS, 345, 1133
Searching for the physical drivers of eigenvector 1: influence of black hole mass and Eddington ratio

18. Marziani et al.(2003) 2003ApJS..145..199M
Marziani, P., Sulentic, J. W., Zamanov, R., Calvani, M., Dultzin-Hacyan, D., Bachev, R., & Zwitter, T. 2003, ApJS, 145, 199
An Optical Spectroscopic Atlas of Low-Redshift Active Galactic Nuclei

19. Zamanov et al.(2002) 2002ApJ...576L...9Z
Zamanov, R., Marziani, P., Sulentic, J. W., Calvani, M., Dultzin-Hacyan, D., & Bachev, R. 2002, ApJL, 576, L9
Kinematic Linkage between the Broad- and Narrow-Line-emitting Gas in Active Galactic Nuclei

20. Zamanov & Marziani(2002) 2002ApJ...571L..77Z
Zamanov, R., & Marziani, P. 2002, ApJL, 571, L77
Searching for the Physical Drivers of Eigenvector 1: From Quasars to Nanoquasars

21. Sulentic et al.(2002) 2002ApJ...566L..71S
Sulentic, J. W., Marziani, P., Zamanov, R., Bachev, R., Calvani, M., & Dultzin-Hacyan, D. 2002, ApJL, 566, L71
Average Quasar Spectra in the Context of Eigenvector 1

22. Zamanov et al.(2001) 2001A&A...367..884Z
Zamanov, R. K., Reig, P., Martí, J., Coe, M. J., Fabregat, J., Tomov, N. A., & Valchev, T. 2001, A&A, 367, 884
Comparison of the Hα circumstellar disks in Be/X-ray binaries and Be stars

23. Marti et al.(2001) 2001IBVS.5036....1M
Marti, J., Zamanov, R., Paredes, J. M., & Ribo, M. 2001, IBVS, 5036
V-band Observations of V4641 Sagittarii

24. Zamanov & Marti(2001) 2001IBVS.5013....1Z
Zamanov, R., & Marti, J. 2001, Information Bulletin on Variable Stars, 5013, 1
Hα Observations of T CrB

25. Reig et al.(2000) 2000MNRAS.317..205R
Reig, P., Negueruela, I., Coe, M. J., Fabregat, J., Tarasov, A. E., & Zamanov, R. K. 2000,

MNRAS, 317, 205
Correlated V/R and infrared photometric variations in the Be/X-ray binary LSI+$61^0$235/$RX\,J$0146.9+6121

26. Zamanov & Martí(2000) 2000A&A...358L..55Z
Zamanov, R., & Martí, J. 2000, A&A, 358, L55
First correlation between compact object and circumstellar disk in the Be/X-ray binaries

27. Zamanov et al.(1999) 1999A&A...351..543Z
Zamanov, R. K., Martí, J., Paredes, J. M., Fabregat, J., Ribó, M., & Tarasov, A. E. 1999, A&A, 351, 543
Evidence of Hα periodicities in LSI+$61^0$303

28. Zamanov & Bruch(1998) 1998A&A...338..988Z
Zamanov, R. K., & Bruch, A. 1998, A&A, 338, 988
Studies of the flickering in cataclysmic variables. V. The recurrent nova T Coronae Borealis

29. Zamanov & Zamanova(1997) 1997IBVS.4461....1Z
Zamanov, R. K., & Zamanova, V. I. 1997, IBVS, 4461
UBV Observations of T CrB

30. Tomov et al.(1992) 1992MNRAS.258...23T
Tomov T., Zamanov R., Kolev D., Georgiev L., Antov A., Mikolajewski M., Esipov V., 1992, MNRAS 258, 23
MWC 560: jets or optically thick expanding envelope?

Non-refereed publications

31. Zamanov & Bachev(2007) 2007ATel.1220....1Z
Zamanov, R. K., & Bachev, R. 2007, The Astronomer's Telegram, 1220, 1

32. Zamanov et al.(2006) 2006ATel..832....1Z
Zamanov, R., Panov, K., Boer, M., & Coroller, H. L. 2006, The Astronomer's Telegram, 832, 1

33. Zamanov et al.(2005) 2005AIPC..797..655Z
Zamanov, R., Bode, M. F., Marziani, R., Davis, R. J., Eyres, S. P. S., Gomboc, A., Porter, J., & Skopal, A. 2005, Interacting Binaries: Accretion, Evolution, and Outcomes, 797, 655

34. Bode et al.(2005) 2005IAUC.8511....3B
Bode, M., Zamanov, R., Marchant, J., & O'Brien, T. J. 2005, IAU Circ, 8511, 3

35. Stirpe et al.(2004) 2004IAUS..222..539S
Stirpe, G. M., Sulentic, J. W., Marziani, P., Zamanov, R., Calvani, M., & Braito, V. 2004, The Interplay Among Black Holes, Stars and ISM in Galactic Nuclei,IAUS 222, 539

36. Zamanov et al.(2004) 2004IAUC.8415....3Z
Zamanov, R. K., Bode, M., Steele, I. A., & O'Brien, T. J. 2004, IAU Circ, 8415, 3

37. Calvani et al.(2004) 2004MSAIS...5..223C
Calvani, M., Marziani, P., Bachev, R., Sulentic, J. W., Zamanov, R. K., & Dultzin-Hacyan, D. 2004, Memorie della Societa Astronomica Italiana Supplement, 5, 223

38. Marziani et al.(2003) 2003yCat..21450199M
Marziani, P., Sulentic, J. W., Zamanov, R., Calvani, M., Dultzin-Hacyan, D., Bachev, R., & Zwitter, T. 2003, VizieR Online Data Catalog, 214, 50199

39. Zamanov & Marziani(2003) 2003whdw.conf..355Z
Zamanov, R., & Marziani, P. 2003, NATO ASIB Proc. 105: White Dwarfs, 355

40. Zamanov et al.(2003) 2003whdw.conf..353Z
Zamanov, R., Marziani, P., Stanishev, V., & Tomov, N. 2003, NATO ASIB Proc. 105: White Dwarfs, 353

41. Zamanov et al.(2003) 2003MSAIS...3..222Z
Zamanov, R., Marziani, P., Sulentic, J. W., Calvani, M., Bachev, R., Stirpe, G., & Dultzin-Hacyan, D. 2003, Memorie della Societa Astronomica Italiana Supplement, 3, 222

42. Marziani et al.(2003) 2003MSAIS...3..218M
Marziani, P., Sulentic, J. W., Zamanov, R., Calvani, M., Della Valle, M., Stirpe, G., & Dultzin-Hacyan, D. 2003, Memorie della Societa Astronomica Italiana Supplement, 3, 218

43. Zamanov et al.(2003) 2003MmSAI..74..524Z
Zamanov, R., Martí, J., & Marziani, P. 2003, Memorie della Societa Astronomica Italiana, 74, 524

44. Marziani et al.(2003) 2003MmSAI..74..492M
Marziani, P., Zamanov, R., Sulentic, J. W., Calvani, M., & Dultzin-Hacyan, D. 2003, Memorie della Societa Astronomica Italiana, 74, 492

45. Marziani et al.(2003) 2003MmSAI..74..490M
Marziani, P., Sulentic, J. W., Zamanov, R., & Calvani, M. 2003, Memorie della Societa Astronomica Italiana, 74, 490

46. Zamanov & Marziani(2003) 2003ASPC..303..308Z
Zamanov, R., & Marziani, P. 2003, Astronomical Society of the Pacific Conference Series, 303, 308

47. Marziani et al.(2003) 2003ASPC..290..231M
Marziani, P., Bongardo, C., Braito, V., Calvani, M., Zamanov, R., Sulentic, J. W., & Dultzin-Hacyan, D. 2003, Active Galactic Nuclei: From Central Engine to Host Galaxy, 290, 231

48. Marziani et al.(2003) 2003ASPC..290..229M
Marziani, P., Zamanov, R., Sulentic, J. W., Dultzin-Hacyan, D., Bongardo, C., & Calvani, M. 2003, Active Galactic Nuclei: From Central Engine to Host Galaxy, 290, 229

49. Zamanov et al.(2001) 2001cnoc.conf...50Z
Zamanov, R., Marti, J., & Marziani, P. 2001, The Second National Conference on Astrophysics of Compact Objects, 50

50. Zamanov & Martí(2000) 2000ASPC..214..731Z
Zamanov, R. K., & Martí, J. 2000, IAU Colloq. 175: The Be Phenomenon in Early-Type Stars, 214, 731

51. Zamanov & Raikova(1999) 1999ASPC..169..337Z
Zamanov, R. K., & Raikova, D. 1999, 11th European Workshop on White Dwarfs, 169, 337

52. Zamanov & Zamanova(1995) 1995IBVS.4189....1Z
Zamanov, R. K., & Zamanova, V. I. 1995, IBVS, 4189

53. Zamanov & Zamanova(1994) 1994IBVS.4081....1Z
Zamanov, R., & Zamanova, V. 1994, IBVS, 4081

54. Zamanov & Tomov(1992) 1992IBVS.3705....1Z
Zamanov, R., & Tomov, T. 1992, IBVS 3705

Appendix D

Citations

Here, I give a list of the citations of the papers from the dissertation. The total number of the citations is about 250. Self citations are not included.

Citations for 2008MNRAS.390..377Z - citations : 1.
Zamanov, R. K., Bode, M. F., Melo, C. H. F., Stateva, I. K., Bachev, R., Gomboc, A., Konstantinova-Antova, R., & Stoyanov, K. A. 2008, MNRAS, 390, 377
Rotational velocities of the giants in symbiotic stars - III. Evidence of fast rotation in S-type symbiotics

1. Lu, G., Zhu, C., Wang, Z., & Wang, N. 2009, MNRAS, 396, 1086

Citations for 2007MNRAS.380.1053Z – citations : 9.
Zamanov, R. K.; Bode, M. F.; Melo, C. H. F.; Bachev, R.; Gomboc, A.; Stateva, I. K.; Porter, J. M.; Pritchard, J. Rotational velocities of the giants in symbiotic stars - II. Are S-type symbiotics synchronized?

2. Brandi, E., Quiroga, C., Mikolajewska, J., Ferrer, O. E., & Garcia, L. G. 2009, arXiv:0902.2177
3. Hinkle, K. H., Fekel, F. C., & Joyce, R. R. 2009, ApJ, 692, 1360 (arXiv:0811.0631)
4. Barry, R. K., Mukai, K., Sokoloski, J. L., Danchi, W. C., Hachisu, I., Evans, A., Gehrz, R., & Mikolajewska, J. 2009, ASP Conference Series, 401, 52
5. Mikolajewska, J. 2009, Astronomical Society of the Pacific Conference Series, 401, 42
6. Justham, S., Wolf, C., Podsiadlowski, P., & Han, Z. 2009, A&A, 493, 1081
7. Barry, R. K., et al. 2008, ApJ, 677, 1253

8. Mikołajewska, J. 2007, Baltic Astronomy, 16, 1

9. Formiggini, L., & Leibowitz, E. M. 2006, MNRAS, 372, 1325

Citations for 2006RMxAA..42...23S – total number 4.
Sulentic, J. W.; Dultzin-Hacyan, D.; Marziani, P.; Bongardo, C.; Braito, V.; Calvani, M.; Zamanov, R. Low Redshift BAL QSOs in the Eigenvector 1 Context

10. Ballo, L., Giustini, M., Schartel, N., Cappi, M., Jiménez-Bailón, E., Piconcelli, E., Santos-Lleó, M., & Vignali, C. 2008, A&A, 483, 137

11. Trimble, V., Aschwanden, M. J., & Hansen, C. J. 2007, Space Science Reviews, 132, 1

12. Ganguly, R., Brotherton, M. S., Cales, S., Scoggins, B., Shang, Z., & Vestergaard, M. 2007, ApJ, 665, 990

13. Ganguly, R., et al. 2007, AJ, 133, 479

Citations for 2006MNRAS.365.1215Z – 6
Zamanov, R. K.; Bode, M. F.; Melo, C. H. F.; Porter, J.; Gomboc, A.; Konstantinova-Antova, R. Rotational velocities of the giants in symbiotic stars - I. D'-type symbiotics

14. Jorissen, A., Frankowski, A., Famaey, B., & Van Eck, S. 2009, A&A, 498, 489

15. Pereira, C. B., & Roig, F. 2009, AJ, 137, 118

16. Jorissen, A., & Frankowski, A. 2008, AIP Conference Series, 1057, 1

17. Pereira, C. B., Miranda, L. F., Smith, V. V., & Cunha, K. 2008, A&A, 477, 535

18. Miroshnichenko, A. S. 2007, ApJ, 667, 497

19. Angeloni, R., Contini, M., Ciroi, S., & Rafanelli, P. 2007, A&A, 472, 497

Citations for 2006IBVS.5733....1Z – 2
Zamanov, R.; Boer, M.; Le Coroller, H.; Panov, K. Photometry of RS Oph after the 2006 Outburst

20. Sokoloski, J. L., Rupen, M. P., & Mioduszewski, A. J. 2008, ApJ, 685, L137

21. Worters, H. L., Eyres, S. P. S., Bromage, G. E., & Osborne, J. P., 2007, MNRAS, 379, 1557

Citations for 2006ATel..832....1Z – 2
Zamanov, R.; Panov, K.; Boer, M.; Coroller, H. Le
RS Oph - disappearance of optical flickering after the outburst

22. Brandi, E., Quiroga, C., Mikolajewska, J., Ferrer, O. E., & Garcia, L. G. 2009, A&A, 497, 815

23. Skopal, A., Vanko, M., Komžík, R., & Chochol, D. 2009, ASP Conf., 401, 101

Citations for 2005MNRAS.363L..26Z – 1
Zamanov, R. K.; Bode, M. F.; Tomov, N. A.; Porter, J. M.
Emission line variability of RS Ophiuchi

24. Zajczyk, A., Tomov, T., Mikolajewski, M., Bull, C., Kolev, D., Cikala, M., Georgiev, L., & Galazufdinov, G. 2009, ASP Conf., 401, 106

Citations for 2005PASP..117..268Z – 1
Zamanov, R.; Gomboc, A.; Bode, M. F.; Porter, J. M.; Tomov, N. A.
Rapid Hα Variability in T Coronae Borealis

25. Anupama, G. C. 2009, ASP Conference Series, 401, 31

Citations for 2004A&A...423..121S – 8
Sulentic, J. W.; Stirpe, G. M.; Marziani, P.; Zamanov, R.; Calvani, M.; Braito, V. VLT/ISAAC spectra of the H-beta region in intermediate redshift quasars

26. D'Odorico, V., Bruscoli, M., Saitta, F., Fontanot, F., Viel, M., Cristiani, S., & Monaco, P. 2008, MNRAS, 389, 1727

27. Salviander, S., Shields, G. A., Gebhardt, K., & Bonning, E. W. 2007, ApJ, 662, 131

28. Shields, G. A., Salviander, S., & Bonning, E. W. 2006, New Astronomy Review, 50, 809

29. Salviander, S., Shields, G. A., Gebhardt, K., & Bonning, E. W. 2006, New Astronomy Review, 50, 803

30. Shields, G. A., Menezes, K. L., Massart, C. A., & Vanden Bout, P. 2006, ApJ, 641, 683

31. Wang, J., Wei, J. Y., & He, X. T. 2006, ApJ, 638, 106

32. Metcalf, R. B., & Magliocchetti, M. 2006, MNRAS, 365, 101

33. Netzer, H., Shemmer, O., Maiolino, R., Oliva, E., Croom, S., Corbett, E., & di Fabrizio, L. 2004, ApJ 614, 558

Citations for 2004MNRAS.350.1477Z – 3
Zamanov, R.; Bode, M. F.; Stanishev, V.; Mart, J. Flickering variability of T Coronae Borealis

34. Schaefer, B. E. 2009, ApJ, 697, 721
35. Gromadzki, M., Mikolajewski, M., Tomov, T., Bellas-Velidis, I., Dapergolas, A., & Galan, C. 2006, Acta Astronomica, 56, 97
36. Munari, U., Siviero, A., & Henden, A. 2005, MNRAS, 360, 1257
37. Collazzi, A. C., Schaefer, B. E., Xiao, L. et al., 2009, AJ, 138, 1846
38. Kennea, J. A., Mukai, K., Sokoloski, J. L., Luna, G. J. M., Tueller, J., Markwardt, C. B., Burrows, D. N., 2009, ApJ, 701, 1992

Citations for 2004A&A...415..609S – 2
Stanishev, V.; Zamanov, R.; Tomov, N.; Marziani, P.

39. Tutukov, A. V., & Fedorova, A. V. 2007, Astronomy Reports, 51, 291
40. Skopal, A. 2005, A&A, 440, 995

Citations for 2003MmSAI..74..492M – number citations : 2.
Marziani, P.; Zamanov, R.; Sulentic, J. W.; Calvani, M.; Dultzin-Hacyan, D. High ionization winds in the narrow line region of active galactic nuclei

41. Vignali, C., Piconcelli, E., Bianchi, S., & Miniutti, G. 2008, MNRAS, 388, 761
42. Eracleous, M., & Halpern, J. P. 2004, ApJS, 150, 181

Citations for 2003MNRAS.345.1133M – 17
Marziani, Paola; Zamanov, Radoslav K.; Sulentic, Jack W.; Calvani, Massimo Searching for the physical drivers of eigenvector 1: influence of black hole mass and Eddington ratio

43. Hu, C., Wang, J.-M., Ho, L. C., Chen, Y.-M., Zhang, H.-T., Bian, W.-H., & Xue, S.-J. 2008, ApJ, 687, 78
44. Vignali, C., Piconcelli, E., Bianchi, S., & Miniutti, G. 2008, MNRAS, 388, 761
45. Komossa, S., Xu, D., Zhou, H., Storchi-Bergmann, T., & Binette, L. 2008, ApJ, 680, 926
46. Decarli, R., Dotti, M., Fontana, M., & Haardt, F. 2008, MNRAS, 386, L15

47. Jolley, E. J. D., & Kuncic, Z. 2008, MNRAS, 386, 989

48. Kawakatu, N., Imanishi, M., & Nagao, T. 2007, ApJ, 661, 660

49. de Diego, J. A. 2007, PASP, 119, 50

50. Aoki, K., Iwata, I., Ohta, K., Ando, M., Akiyama, M., & Tamura, N. 2006, ApJ, 651, 84

51. Cirasuolo, M., Magliocchetti, M., Gentile, G., Celotti, A., Cristiani, S., & Danese, L. 2006, MNRAS, 371, 695

52. Shen, S., White, S. D. M., Mo, H. J., Voges, W., Kauffmann, G., Tremonti, C., & Anderson, S. F. 2006, MNRAS, 369, 1639

53. Wang, J., Wei, J. Y., & He, X. T. 2006, ApJ, 638, 106

54. Metcalf, R. B., & Magliocchetti, M. 2006, MNRAS, 365, 101

55. Kawakatu, N., Anabuki, N., Nagao, T., Umemura, M., & Nakagawa, T. 2006, ApJ, 637, 104

56. Greene, J. E., Ho, L. C., & Ulvestad, J. S. 2006, ApJ, 636, 56

57. Bian, W., Yuan, Q., & Zhao, Y. 2005, MNRAS, 364, 187

58. Hao, C. N., Xia, X. Y., Mao, S., Wu, H., & Deng, Z. G. 2005, ApJ, 625, 78

59. Aoki, K., Kawaguchi, T., & Ohta, K. 2005, ApJ, 618, 601

Citations for 2003ApJS..145..199M – 55
Marziani, P.; Sulentic, J. W.; Zamanov, R.; Calvani, M.; Dultzin-Hacyan, D.; Bachev, R.; Zwitter, T. An Optical Spectroscopic Atlas of Low-Redshift Active Galactic Nuclei

60. Ludwig, R.R., Wills, B., Greene, J. E., Robinson, E. L., 2009, ApJ, 706, 995

61. Bentz, M. C., Walsh, J. L., Barth, A. J., et al. 2009, ApJ, 705, 199

62. Ho, Luis C.; Kim, Minjin, 2009, ApJS, 184, 398

63. Gonzalez-Martn, O., Masegosa, J., Marquez, I., Guainazzi, M., 2009, ApJ, 704, 1570

64. Wu, Q. 2009, ApJ, 701, 95

65. Bon, E., Gavrilovic, N., La Mura, G., Popovic, L., 2009, NewAR, 53, 121

66. Marshall, Kevin, Ryle, W. T., Miller, H. R. et al., 2009, ApJ, 696, 601

67. Ponti, G., Cappi, M., Vignali, C., Miniutti, G., Tombesi, F., et al. 2009MNRAS.394.1487P

68. Kelly, B. C., Vestergaard, M., & Fan, X. 2009, ApJ, 692, 1388

69. Bianchi, S., Guainazzi, M., Matt, G., Fonseca Bonilla, N., & Ponti, G. 2009, A&A, 495, 421

70. Curran, S. J., Whiting, M. T., Wiklind, T., Webb, J. K., Murphy, M. T., & Purcell, C. R. 2008, MNRAS, 391, 765

71. Kim, M., Ho, L. C., Peng, C. Y., Barth, A. J., Im, M., Martini, P., & Nelson, C. H. 2008, ApJ, 687, 767

72. Hu, C., Wang, J.-M., Ho, L. C., Chen, Y.-M., Zhang, H.-T., Bian, W.-H., & Xue, S.-J. 2008, ApJ, 687, 78

73. Dunn, J. P., Crenshaw, D. M., Kraemer, S. B., & Trippe, M. L. 2008, AJ, 136, 1201

74. Decarli, R., Labita, M., Treves, A., & Falomo, R. 2008, MNRAS, 387, 1237

75. Ho, L. C., Darling, J., & Greene, J. E. 2008, ApJ s, 177, 103

76. Curran, S. J., Whiting, M. T., Wiklind, T., Webb, J. K., Murphy, M. T., & Purcell, C. R. 2008, 2008, MNRAS, 391, 765

77. McGill, K. L., Woo, J.-H., Treu, T., & Malkan, M. A. 2008, ApJ, 673, 703

78. Dong, X., Wang, T., Wang, J., Yuan, W., Zhou, H., Dai, H., & Zhang, K. 2008, MNRAS, 383, 581

79. Salviander, S., Shields, G. A., Gebhardt, K., & Bonning, E. W. 2007, ApJ, 662, 131

80. Wang, J.-M., Chen, Y.-M., Yan, C.-S., Hu, C., & Bian, W.-H. 2007, ApJ l, 661, L143

81. Maiolino, R., Shemmer, O., Imanishi, M., Netzer, H., Oliva, E., Lutz, D., & Sturm, E. 2007, A&A, 468, 979

82. Wang, J.-M., & Zhang, E.-P. 2007, ApJ, 660, 1072

83. Bonning, E. W., Cheng, L., Shields, G. A., Salviander, S., & Gebhardt, K. 2007, ApJ, 659, 211

84. Ohta, K., Aoki, K., Kawaguchi, T., & Kiuchi, G. 2007, ApJ s, 169, 1

85. Punsly, B. 2007, ApJ l, 657, L9

86. Punsly, B. 2007, MNRAS, 374, L10

87. Dimitrijević, M. S., Popović, L. Č., Kovačević, J., Dačić, M., & Ilić, D. 2007, MNRAS, 374, 1181

88. Kelly, B. C., & Bechtold, J. 2007, ApJ s, 168, 1

89. Lobanov, A., & Zensus, J. A. 2007, Exploring the Cosmic Frontier: Astrophysical Instruments for the 21st Century, 147

90. Fine, S., et al. 2006, MNRAS, 373, 613

91. Labita, M., Treves, A., Falomo, R., & Uslenghi, M. 2006, MNRAS, 373, 551

92. Zhang, E.-P., & Wang, J.-M. 2006, ApJ, 653, 137

93. Salviander, S., Shields, G. A., Gebhardt, K., & Bonning, E. W. 2006, New Astronomy Review, 50, 803

94. Strateva, I. V., Brandt, W. N., Eracleous, M., Schneider, D. P., & Chartas, G. 2006, ApJ, 651, 749

95. Chiaberge, M., Gilli, R., Macchetto, F. D., & Sparks, W. B. 2006, ApJ, 651, 728

96. Zhang, X.-G., Dultzin-Hacyan, D., & Wang, T.-G. 2006, MNRAS, 372, L5

97. Trump, J. R., et al. 2006, ApJ s, 165, 1

98. Woo, J.-H., Treu, T., Malkan, M. A., & Blandford, R. D. 2006, ApJ, 645, 900

99. Rigby, J. R., Rieke, G. H., Donley, J. L., Alonso-Herrero, A., & Pérez-González, P. G. 2006, ApJ, 645, 115

100. Véron-Cetty, M.-P., Joly, M., Véron, P., Boroson, T., Lipari, S., & Ogle, P. 2006, A&A, 451, 851

101. Nandra, K. 2006, MNRAS, 368, L62

102. McLure, R. J., Jarvis, M. J., Targett, T. A., Dunlop, J. S., & Best, P. N. 2006, MNRAS, 368, 1395

103. Vestergaard & Peterson(2006)]2006ApJ...641..689V Vestergaard, M., & Peterson, B. M. 2006, ApJ, 641, 689

104. Shields, G. A., Menezes, K. L., Massart, C. A., & Vanden Bout, P. 2006, ApJ, 641, 683

105. Landt, H., Perlman, E. S., & Padovani, P. 2006, ApJ, 637, 183

106. Nandra, K., O'Neill, P. M., George, I. M., Reeves, J. N., & Turner, T. J. 2006, Astronomische Nachrichten, 327, 1039

107. Bian, W., Yuan, Q., & Zhao, Y. 2005, MNRAS, 364, 187

108. Bonning, E. W., Shields, G. A., Salviander, S., & McLure, R. J. 2005, Revista Mexicana de Astronomia y Astrofisica Conference Series, 23, 109

109. Ho, L. C. 2005, ApJ, 629, 680

110. Kaspi, S., Maoz, D., Netzer, H., Peterson, B. M., Vestergaard, M., & Jannuzi, B. T. 2005, ApJ, 629, 61

111. Bonning, E. W., Shields, G. A., Salviander, S., & McLure, R. J. 2005, ApJ, 626, 89

112. Zhou, X.-L., & Wang, J.-M. 2005, ApJL, 618, L83

113. Aoki, K., Kawaguchi, T., & Ohta, K. 2005, ApJ, 618, 601

114. Arshakian, T. G., Chavushyan, V. H., Ros, E., Kadler, M., & Zensus, J. A. 2005, Memorie della Societa Astronomica Italiana, 76, 35

115. Czerny, B., Różańska, A., & Kuraszkiewicz, J. 2004, A&A, 428, 39

116. Treu, T., Malkan, M. A., & Blandford, R. D. 2004, ApJ l, 615, L97

117. Peterson, B. M., et al. 2004, ApJ, 613, 682

118. McLure, R. J., & Dunlop, J. S. 2004, MNRAS, 352, 1390

119. Kawaguchi, T., Aoki, K., Ohta, K., & Collin, S. 2004, A&A, 420, L23

120. Grupe, D. 2004, AJ, 127, 1799

121. Page, K. L., O'Brien, P. T., Reeves, J. N., & Turner, M. J. L. 2004, MNRAS, 347, 316

122. Crenshaw, D. M., Kraemer, S. B., & Gabel, J. R. 2003, AJ, 126, 1690

Citations for 2002ApJ...576L...9Z – number 23.
Zamanov, R.; Marziani, P.; Sulentic, J. W.; Calvani, M.; Dultzin-Hacyan, D.; Bachev, R. Kinematic Linkage between the Broad- and Narrow-Line-emitting Gas in Active Galactic Nuclei

123. Comerford, J.M., Gerke, B. F., Newman, J. A., et al. 2009, ApJ, 698, 956

124. Vignali, C., Piconcelli, E., Bianchi, S., & Miniutti, G. 2008, MNRAS, 388, 761

125. Komossa, S., Xu, D., Zhou, H., Storchi-Bergmann, T., & Binette, L. 2008, ApJ, 680, 926

126. Komossa, S. 2008, Revista Mexicana de Astronomia y Astrofisica Conference Series, 32, 86

127. Xu, D., Komossa, S., Zhou, H., Wang, T., & Wei, J. 2007, ApJ, 670, 60

128. Komossa, S., & Xu, D. 2007, ApJ l, 667, L33

129. Shang, Z., Wills, B. J., Wills, D., & Brotherton, M. S. 2007, AJ, 134, 294

130. Aoki, K., Iwata, I., Ohta, K., Ando, M., Akiyama, M., & Tamura, N. 2006, ApJ, 651, 84

131. Zhou, H., Wang, T., Yuan, W., Lu, H., Dong, X., Wang, J., & Lu, Y. 2006, ApJS, 166, 128

132. Grupe, D., Leighly, K. M., Komossa, S., Schady, P., O'Brien, P. T., Burrows, D. N., & Nousek, J. A. 2006, AJ, 132, 1189

133. Collin, S., Kawaguchi, T., Peterson, B. M., & Vestergaard, M. 2006, A&A, 456, 75

134. Holt, J., Tadhunter, C., Morganti, R., Bellamy, M., González Delgado, R. M., Tzioumis, A., & Inskip, K. J. 2006, MNRAS, 370, 1633

135. Wang, J., Wei, J. Y., & He, X. T. 2006, ApJ, 638, 106

136. Bian, W., Yuan, Q., & Zhao, Y. 2005, MNRAS, 364, 187

137. Boroson, T. 2005, AJ, 130, 381

138. Wang, J., Wei, J. Y., & He, X. T. 2005, A&A, 436, 417

139. Wang, J., Wei, J. Y., & He, X. T. 2005, New Astronomy, 10, 353

140. Aoki, K., Kawaguchi, T., & Ohta, K. 2005, ApJ, 618, 601

141. Popović, L. Č., Mediavilla, E., Bon, E., & Ilić, D. 2004, A&A, 423, 909

142. Grupe, D. 2004, AJ, 127, 1799

143. Dopita, M. A. 2003, Ap&SS, 284, 569

144. Dopita, M. A., Bicknell, R. S., Sutherland, R. S., & Saxton, C. J. 2003, Revista Mexicana de Astronomia y Astrofisica Conference Series, 15, 323

145. Schmidt, G. D., Smith, P. S., Foltz, C. B., & Hines, D. C. 2002, ApJ l, 578, L99

Citations for 2002ApJ...571L..77Z – number citations : 12
Zamanov, R.; Marziani, P. Searching for the Physical Drivers of Eigenvector 1: From Quasars to Nanoquasars

146. Wang, J., Mao, Y. F., & Wei, J. Y. 2009, AJ, 137, 3388

147. Luna, G. J. M., & Sokoloski, J. L. 2007, ApJ, 671, 741

148. de Diego, J. A. 2007, PASP, 119, 50

149. Wang, J., Wei, J. Y., & He, X. T. 2006, ApJ, 638, 106

150. Weisskopf, M. C., et al. 2006, ApJ, 637, 682

151. Wang, J., Wei, J. Y., & He, X. T. 2005, A&A, 436, 417

152. Zakharov, A. F., Ma, Z., & Bao, Y. 2004, New Astronomy, 9, 663

153. Leedjärv, L. 2004, Baltic Astronomy, 13, 109

154. Zakharov, A. F., Kardashev, N. S., Lukash, V. N., & Repin, S. V. 2003, MNRAS, 342, 1325

155. Trimble, V., & Aschwanden, M. J. 2003, PASP, 115, 514

156. Sigut, T. A. A., & Pradhan, A. K. 2003, ApJs, 145, 15

157. Sokoloski, J. L., & Kenyon, S. J. 2003, ApJ, 584, 1021

**Citations for 2002ApJ...566L..71S Total number citations : 16.
Sulentic, J. W.; Marziani, P.; Zamanov, R.; Bachev, R.; Calvani, M.; Dultzin-Hacyan, D. Average Quasar Spectra in the Context of Eigenvector 1**

158. Husemann, B., Wisotzki, L., Sánchez, S. F., & Jahnke, K. 2008, A&A, 488, 145

159. Hu, C., Wang, J.-M., Ho, L. C., Chen, Y.-M., Bian, W.-H., & Xue, S.-J. 2008, ApJL, 683, L115

160. Komossa, S. 2008, Revista Mexicana de Astronomia y Astrofisica Conference Series, 32, 86

161. Xu, D., Komossa, S., Zhou, H., Wang, T., & Wei, J. 2007, ApJ, 670, 60

162. Bennert, N., Jungwiert, B., Komossa, S., Haas, M., & Chini, R. 2006, A&A, 459, 55

163. Komossa, S., Voges, W., Xu, D., Mathur, S., Adorf, H.-M., Lemson, G., Duschl, W. J., & Grupe, D. 2006, AJ, 132, 531

164. Komossa, S., Voges, W., Adorf, H.-M., Xu, D., Mathur, S., & Anderson, S. F. 2006, ApJ, 639, 710

165. Wang, J., Wei, J. Y., & He, X. T. 2006, ApJ, 638, 106

166. Weisskopf, M. C., et al. 2006, ApJ, 637, 682

167. Nagao, T., Marconi, A., & Maiolino, R. 2006, A&A, 447, 157

168. López-Corredoira, M., & Gutiérrez, C. M. 2004, A&A, 421, 407

169. Grupe(2004)]2004AJ....127.1799G Grupe, D. 2004, AJ, 127, 1799

170. Grupe, D., Wills, B. J., Leighly, K. M., & Meusinger, H. 2004, AJ, 127, 156

171. Richards, G. T., et al. 2003, AJ, 126, 1131

172. Constantin, A., & Shields, J. C. 2003, PASP, 115, 592

173. Nagao, T., Murayama, T., Shioya, Y., & Taniguchi, Y. 2002, ApJ, 575, 721

Citations for 2001A&A...367..884Z - number citations : 23.
Zamanov, R. K.; Reig, P.; Mart, J.; Coe, M. J.; Fabregat, J.; Tomov, N. A.; Valchev, T. Comparison of the H-alpha circumstellar disks in Be/X-ray binaries and Be stars

174. Kanaan, S., Meilland, A., Stee, P., Zorec, J., Domiciano de Souza, A., Frémat, Y., & Briot, D. 2008, A&A, 486, 785

175. Zdziarski, A. A., Neronov, A., & Chernyakova, M. 2010, MNRAS, 403, 1873

176. Martayan, C., Floquet, M., Hubert, A. M., Gutiérrez-Soto, J., Fabregat, J., Neiner, C., & Mekkas, M. 2007, A&A, 472, 577

177. Uytterhoeven, K., Poretti, E., Rodríguez, E., De Cat, P., Mathias, P., Telting, J. H., Costa, V., & Miglio, A. 2007, A&A, 470, 1051

178. Grundstrom, E. D., et al. 2007, ApJ, 660, 1398

179. Okazaki, A. T., & Hayasaki, K. 2007, ASP Conf., 361, 395

180. Negueruela, I. 2007, ASP Conf., 361, 376

181. Grundstrom, E. D., et al. 2007, ApJ, 656, 437

182. Okazaki, A. T. 2007, ASP Conf. 367, 485

183. Negueruela, I. 2007, ASP Conf. 367, 477

184. Coe, M. J., Reig, P., McBride, V. A., Galache, J. L., & Fabregat, J. 2006, MNRAS, 368, 447

185. Martayan, C., Hubert, A. M., Floquet, M., Fabregat, J., Frémat, Y., Neiner, C., Stee, P., & Zorec, J. 2006, A&A, 445, 931

186. Okazaki, A. T. 2005, ASP Conf., 337, 285

187. Okazaki, A. T., & Hayasaki, K. 2004, Revista Mexicana de Astronomia y Astrofisica Conference Series, 20, 144

188. Schmidtke, P. C., Cowley, A. P., Levenson, L., & Sweet, K. 2004, AJ, 127, 3388

189. Zhang, F., Li, X.-D., & Wang, Z.-R. 2004, ApJ, 603, 663

190. Porter, J. M., & Rivinius, T. 2003, PASP, 115, 1153

191. Miroshnichenko, A. S., et al. 2003, A&A, 408, 305

192. Okazaki, A. T., Bate, M. R., Ogilvie, G. I., & Pringle, J. E. 2002, MNRAS, 337, 967

193. Gregory, P. C., & Neish, C. 2002, ApJ, 580, 1133

194. Trimble, V., & Aschwanden, M. J. 2002, PASP, 114, 475

195. Covino, S., Negueruela, I., Campana, S., Israel, G. L., Polcaro, V. F., Stella, L., & Verrecchia, F. 2001, A&A, 374, 1009

196. Roberts, M. S. E., Michelson, P. F., Leahy, D. A., Hall, T. A., Finley, J. P., Cominsky, L. R., & Srinivasan, R. 2001, ApJ, 555, 967

Citations for 2000A&A...358L..55Z – 7
Zamanov, R.; Mart, J. First correlation between compact object and circumstellar disk in the Be/X-ray binaries

197. Zdziarski, A. A., Neronov, A., & Chernyakova, M. 2010, MNRAS, 403, 1873

198. Grundstrom, E. D., et al. 2007, ApJ, 656, 437

199. Martocchia, A., Motch, C., & Negueruela, I. 2005, A&A, 430, 245

200. Massi, M. 2004, A&A, 422, 267

201. Massi, M. 2004, European VLBI Network on New Developments in VLBI Science and Technology, 215 2004evn..conf..215M

202. Gregory, P. C. 2002, ApJ, 575, 427

203. Apparao, K. M. V. 2001, A&A, 371, 672

Citations for 1999A&A...351..543Z – Total number citations : 13.
Zamanov, R. K.; Mart, J.; Paredes, J. M.; Fabregat, J.; Rib, M.; Tarasov, A. E. Evidence of Halpha periodicities in LS I+61deg303

204. Albert, J., et al. 2009, ApJ, 693, 303

205. Nagae, O., Kawabata, K. S., Fukazawa, Y., Okazaki, A., Isogai, M., & Yamashita, T. 2009, AJ, 137, 3509

206. Zdziarski, A. A., Neronov, A., & Chernyakova, M. 2010, MNRAS, 403, 1873

207. Esposito, P., Caraveo, P. A., Pellizzoni, A., de Luca, A., Gehrels, N., & Marelli, M. A. 2007, A&A, 474, 575

208. Grundstrom, E. D., et al. 2007, ApJ, 660, 1398

209. Grundstrom, E. D., et al. 2007, ApJ, 656, 437

210. Nagae O., Kawabata K. S., Fukazawa Y., et al. 2006, PASJ, 58, 1015

211. Sidoli, L., Pellizzoni, A., Vercellone, S., Moroni, M., Mereghetti, S., & Tavani, M. 2006, A&A, 459, 901

212. Liu, Q. Z., & Yan, J. Z. 2005, New Astronomy, 11, 130

213. Zaitseva, G. V., & Borisov, G. V. 2003, Astronomy Letters, 29, 188

214. Liu, Q. Z., van Paradijs, J., & van den Heuvel, E. P. J. 2000, A&AS, 147, 25

215. Liu, Q. Z., Hang, H. R., Wu, G. J., Chang, J., & Zhu, Z. X. 2000, A&A, 359, 646

216. Apparao, K. M. V. 2000, A&A, 356, 972

Citations for 1998A&A...338..988Z – number citations : 6.
Zamanov, R. K.; Bruch, A. Studies of the flickering in cataclysmic variables. V. The recurrent nova T Coronae Borealis

217. Tamburini, F., De Martino, D., & Bianchini, A. 2009, A&A, 502, 1

218. Worters, H. L., Eyres, S. P. S., Bromage, G. E., & Osborne, J. P. 2007, MNRAS, 379, 1557

219. Sokoloski, J. L., & Kenyon, S. J. 2003, ApJ, 584, 1027

220. Sokoloski et al.(2001)]2001MNRAS.326..553S Sokoloski, J. L., Bildsten, L., & Ho, W. C. G. 2001, MNRAS, 326, 553

221. Hachisu & Kato(2001)]2001ApJ...558..323H Hachisu, I., & Kato, M. 2001, ApJ, 558, 323

222. Anupama, G. C., & Mikołajewska, J. 1999, A&A, 344, 177

Citations for 1997IBVS.4461....1Z – number citations : 1.
Zamanov, R. K.; Zamanova, V. I. UBV Observations of T CrB

223. Hric, L., Petrik, K., Urban, Z., Niarchos, P., & Anupama, G. C. 1998, A&A, 339, 449

Citations for 1995IBVS.4189....1Z – number citations : 5.
Zamanov, R. K.; Zamanova, V. I. : X Persei

224. Liu, Q.-Z., & Hang, H.-R. 2001, Ap&SS, 275, 401

225. Kolka, I., Eenme, T., Puss, A., & Leedjru, L., 2000, ASP Conf. Ser. 214, 593

226. Piccioni, A., Bartolini, C., Bernabei, S., Galleti, S., Guarnieri, A., & Valentini, G. 2000, IAU Colloq. 175: The Be Phenomenon in Early-Type Stars, 214, 585

227. Roche, P., et al. 1997, A&A, 322, 139

228. Engin, S., & Yuce, K. 1997, IBVS, 4454, 1

Citations for 1995MNRAS.272..308Z – number citations : 10
Zamanov, R. K., An ejector-propeller model for LSI+61303

229. Romero, G. E., Okazaki, A. T., Orellana, M., & Owocki, S. P. 2007, A&A, 474, 15

230. Ekşİ, K. Y., & Alpar, M. A. 2005, ApJ, 620, 390

231. Zhang, F., Li, X.-D., & Wang, Z.-R. 2004, ApJ, 603, 663

232. Gregory, P. C., & Neish, C. 2002, ApJ, 580, 1133

233. Massi, M., Ribó, M., Paredes, J. M., Peracaula, M., & Estalella, R. 2001, A&A, 376, 217

234. Apparao, K. M. V. 2001, A&A, 371, 672

235. Gregory, P. C., Peracaula, M., & Taylor, A. R. 1999, ApJ, 520, 376

236. Ray, P. S., Foster, R. S., Waltman, E. B., Tavani, M., & Ghigo, F. D. 1997, ApJ, 491, 381

237. Peracaula, M., Marti, J., & Paredes, J. M. 1997, A&A, 328, 283

238. Paredes, J. M., Marti, J., Peracaula, M., & Ribo, M. 1997, A&A, 320, L25

Citations for 1992MNRAS.258...23T – 15
Tomov, T.; Zamanov, R.; Kolev, D.; Georgiev, L.; Antov, A.; Mikolajewski, M.; Esipov, V. MWC 560 - Jets or optically thick expanding envelope?

239. Arrieta, A., Torres-Peimbert, S., & Georgiev, L. 2005, ApJ, 623, 252

240. Hillwig, T., Livio, M., & Honeycutt, R. K. 2004, PASP, 116, 397

241. Iijima, T. 2002, A&A, 391, 617

242. Leedjärv, L. 2002, ASP Conf. 261, 353

243. Schmid, H. M., Kaufer, A., Camenzind, M., Rivinius, T., Stahl, O., Szeifert, T., Tubbesing, S., & Wolf, B. 2001, A&A, 377, 206

244. Sokoloski, J. L., Bildsten, L., & Ho, W. C. G. 2001, MNRAS, 326, 553

245. Ishioka, R., Uemura, M., & Kato, T. 2001, IBVS, 5028, 1

246. Iijima, T. 2001, ASP Conf. 242, 187

247. Iijima, T. 2000, ASP Conf., 204, 359

248. Sokoloski, J. L., & Bildsten, L. 1999, ApJ, 517, 919

249. Ringwald, F. A., & Naylor, T. 1998, AJ, 115, 286

250. Ferrer, O. E., Brandi, E., García, L., & Barbá, R. 1997, Boletin de la Asociacion Argentina de Astronomia La Plata Argentina, 41, 45

251. Meier, S. R., Rudy, R. J., Lynch, D. K., Rossano, G. S., Erwin, P., & Puetter, R. C. 1996, AJ, 111, 476

252. Dobrzycka, D., Kenyon, S. J., & Milone, A. A. E. 1996, AJ, 111, 414

253. Shore, S. N., Aufdenberg, J. P., & Michalitsianos, A. G. 1994, AJ, 108, 671

Citations for 1992IBVS.3705....1Z citations : 2.
Zamanov, R.; Tomov, T. : UBV Observations of ZZ CMi

254. Taranova, O. G., & Shenavrin, V. I. 2001, Astronomy Letters, 27, 338

255. Belczyński, K., Mikołajewska, J., Munari, U., Ivison, R. J., & Friedjung, M. 2000, A&AS, 146, 407